UNDERSTANDING HURRICANE MOVEMENT FROM A POTENTIAL VORTICITY PERSPECTIVE: A NUMERICAL MODEL AND AN OBSERVATIONAL STUDY

by
Chun-Chieh Wu
B.S., Atmospheric Sciences, National Taiwan University
(1986)

Submitted to the Department of Earth, Atmospheric and Planetary Sciences in partial fulfillment of the requirements for the degree of

DOCTOR OF PHILOSOPHY IN METEOROLOGY
at the
MASSACHUSETTS INSTITUTE OF TECHNOLOGY
May 1993

Signature of Author _____
Center for Meteorology and Physical Oceanography
17 May 1993

Certified by _____
Kerry A. Emanuel, Thesis Supervisor

Accepted by ___ _____
Thomas H. Jordan, Department Chairman

UNDERSTANDING HURRICANE MOVEMENT FROM A POTENTIAL VORTICITY PERSPECTIVE: A NUMERICAL MODEL AND AN OBSERVATIONAL STUDY

by
Chun-Chieh Wu

Submitted to the Department of Earth, Atmospheric and Planetary Sciences on May 17, 1993 in partial fulfillment of the requirements for the degree of Doctor of Philosophy in Meteorology

ABSTRACT

Most extant studies of tropical cyclone movement consider a barotropic vortex on a β plane. However, observations have shown that real tropical cyclones are strongly baroclinic, with broad anticyclones aloft. Also, the distribution of the large-scale potential vorticity gradient in the tropical atmosphere is very nonuniform. These properties may substantially influence the movement of such storms.

Note that the anticyclone above a hurricane can interact with the lower hurricane vortex and induce storm motion. Such interaction can be caused by both the direct effect of ambient vertical shear and the effect of vertical variation of the background potential vorticity gradient. In the first part of this thesis, we attempt to isolate the effect of background vertical shear. The hurricane is represented in a two-layer quasigeostrophic model as a point source of mass and zero potential vorticity air in the upper layer, collocated with a point cyclone in the lower layer. The model is integrated by the method of contour dynamics and contour surgery.

The model results show that Northern Hemisphere tropical cyclones should have a component of drift relative to the mean flow in a direction to the left of the background vertical shear. The effect of weak shear is found to be at least as strong as the β effect, and the effect is maximized by a certain optimal ambient shear. The behavior of the model is sensitive to the thickness ratio of the two layers and is less sensitive to the ratio of the vortices' horizontal scale to the radius of deformation. Storms with stronger negative potential vorticity anomalies tend to exhibit more vortex drift.

The validity of balance dynamics in the tropics also allows us to explore the dynamics of hurricanes using the potential vorticity (PV) framework. In the second part of this thesis, three observational case studies (Hurricane Bob and Tropical Storm Ana of 1991, and Hurricane Andrew of 1992) have been performed to demonstrate the use of PV diagnostics of hurricane movement from the twice-daily National Meteorological Center Northern Hemisphere final analyses gridded datasets. Using the seasonal climatology as the mean reference state, piecewise potential vorticity inversions are performed under the nonlinear balance condition. This allows one to determine the balanced flows associated with any individual perturbation of PV. By examining the balanced flows at the central position of the hurricane, one can identify which PV perturbation has the most influence on hurricane movement. We also define the hurricane advection flow as the balanced flow (in the center of the storm) associated with the whole PV in the troposphere, except for the PV anomaly of the hurricane itself.

The results from the observational study show that such a steering wind is a very good approximation to the real storm motion. This steering flow derived from the PV perspective is much more consistent and dynamically meaningful than the traditional steering stream, which is generally taken as the tropospheric annular mean flow. The results also show that hurricane movement is dominated by the balanced flows associated with the mean PV and perturbation PV in both the lower and upper troposphere. This form of PV diagnostics is conceptually simpler and much more useful in quantitatively understanding how individual portions of the large-scale dynamics interact with the hurricane.

Thesis supervisor: Dr. Kerry A. Emanuel
Title: Professor of Meteorology

ACKNOWLEDGMENTS

I wish to thank my advisor, Kerry A. Emanuel, for his guidance and support. His many stimulating ideas were invaluable in helping me to carry out my thesis work. I am also grateful to the other members of my thesis committee, Drs. Alan Plumb, Glenn Flierl, and John Marshall, for their helpful suggestions during the course of my study, and their careful reading of the thesis manuscript.

I have benefited considerably from scientific discussions with Drs. John Nielsen, Christopher Davis, Steve Meacham, Robert Black, and Nilton Renno, as well as Michael Morgan, Roger Atkinson, and Lars Schade. Steve Meacham provided the original two-layer contour dynamics code, Christopher Davis helped with the inversion code, and Robert Black commented very helpfully on part of the early thesis draft.

I have enjoyed both the academic and social interactions with many people in CMPO. In particular, I would like to acknowledge my friendships with Dan Reilly, Bob Conzemius, Dr. Dana Hartley, Dr. Volkmar Wirth, Ho-Chun Huang, Chris Forest, Francoise Robe, Marja Bister, and many other meteorology students. I also wish to thank Jane McNabb, Joel Sloman, Tracey Stanelun, Edward Nelson, and Debra Cochrane for their administrative assistance, and Diana Spiegel for her help on computer issues. Besides science, I have also learned many other interesting things from them.

Special thanks go to Dr. Julius Chang and Ms. Yi Chang for their extensive care and support of my wife and myself. In addition, I deeply thank both my parents and parents-in-law for their spiritual encouragement .

Finally, I wish to express my deepest appreciation to my wife, Li-Wen Chang, for her love and support. With great pleasure and pride, I would like to dedicate this thesis to her.

TABLE OF CONTENTS

LIST OF FIGURES

1. Introduction

a. Prelude

Previous studies of tropical cyclone motion have focused either on the phenomenon of steering by the mean flow (Chan and Gray 1982) or on the effect of uniform background potential vorticity gradients, that is, the evolution of barotropic vortices in a barotropic flow (Fiorino and Elsberry 1989). A combination of these two effects would suggest that tropical cyclones should follow the mean large-scale (steering) flow, but with a westward and poleward relative drift.

In reality tropical cyclones are strongly baroclinic, consisting of cyclones surmounted by anticyclones. The upper anticyclone, though weak in terms of wind velocity, can be spatially very extensive. Even slight displacements of the upper region of anticyclonic flow from the low-level cyclone could conceivably lead to large mutual propagation effects. Moreover, the background potential vorticity gradient may act on these two flow features in very different ways. Therefore, the propagation of a baroclinic hurricane, embedded in a nonuniform background potential vorticity gradient, could be very different from the traditional expectation, based on the so-called β effect.

In addition, it is not obvious how to best define the hurricane steering flow. There is no direct way to evaluate how a hurricane interacts with its environment and then how this interaction feeds backs onto hurricane movement. It is also desirable to understand more quantitatively how large-scale circulations and adjacent synoptic-scale features contribute to hurricane propagation.

In this thesis, two different approaches are used to study the problem: one employs a numerical model, and the other involves an observational study. The modelling work is a theoretical study that investigates a specific hypothesis within an idealized atmosphere. The observational work examines actual tropical disturbances and was originally intended to

prove or disprove the model results. However, the limitations inherent in the data made it somewhat difficult to compare with the theoretical model. Therefore, two portions of the body of work are in one sense connected to each other, but, each has its own aspects. The relationship will be discussed through out the thesis.

b. The numerical model

We design an idealized numerical model to explore a hypothesis about the effect of background vertical shear on tropical cyclone motion. Specifically, we hypothesize that in the absence of background PV gradients, Northern (Southern) Hemisphere (hereafter NH and SH) tropical cyclones should drift relative to the mean flow in a direction to the left (right) of the background vertical shear because of the flow induced by the upper anticyclone, which is displaced downshear from the center of the surface cyclone.

Our philosophy in investigating the hypothesis is to start with the simplest model possible such that the essential dynamical processes of hurricane motion can be easily understood. To explore the problem in a simple way, we employ a two-layer quasigeostrophic model, along with the method of contour dynamics and contour surgery. It is our belief that this is one of the simplest theoretical models that retains the fundamental physical mechanisms we are interested in studying. Among the specific questions to be addressed are:

- How does a hurricane diabatically generate negative PV anomalies aloft?
- How does the ambient vertical shear interact with a baroclinic hurricane vortex and influence vortex movement?
- Are these effects quantitatively as important as other effects, such as the traditional β effect?
- What is the behavior of the model with respect to the model's free parameters?

c. An observational study

In the observational study, we apply potential vorticity (PV) analyses in an attempt to understand hurricane steering. Three case studies have been used to apply PV diagnostics to hurricane movement. Piecewise potential vorticity inversions are performed under nonlinear balance conditions. This allows one to determine the balanced flow associated with individual PV perturbations. By examining the balanced flow near the central position of a hurricane, one can quantitatively study how each PV anomaly contributes to hurricane motion. The main objectives of the observational analyses are:

- To understand how a hurricane may influence its evolution by creating PV anomalies in the environment (such as the β effect and upper-level negative PV anomalies), that feed back to affect hurricane motion (to prove or disprove the relevance of the aforementioned modelling work).
- To provide a better definition of hurricane advection (steering) flow.
- To quantitatively understand how individual synoptic or larger-scale weather systems influence hurricane motion.

d. Outline of the thesis

The thesis is organized as follows. In chapter 2, the present understanding of tropical cyclone motion is reviewed, and the specific questions we wish to address are identified. A detailed formulation of the model is presented in chapter 3. The model results are described in chapter 4. The methodology to be used in the observational studies are discussed in chapter 5. Results from three case studies are presented in chapters 6 and 7. Finally, chapter 8 summarizes the primary results and principal conclusions of the thesis. Suggestions for future work are also presented.

2. Background and review

The dynamics of tropical cyclone motion are complex. As pointed out by Holland (1984), a complete description would require at least detailed knowledge of the interactions between the cyclone circulation, the environmental wind field, the underlying surface, and the distribution of moist convection. It has generally been proposed, however, that tropical cyclone motion is governed by the tropospheric average steering flow and a drift due to the presence of a background potential vorticity gradient. In this chapter, we first review the current understanding of these issues. Then we present our hypotheses and views, which comprise the essential foundation of this thesis work.

a. Review of general theories of hurricane motion

1) Hurricane steering

The steering concept is based on the assumption that tropical cyclones are barotropic vortices embedded in a background environment of larger-scale flow and thus move with a so-called "steering" flow, generally taken to be a pressure-weighted vertical average of the horizontal flow in the troposphere surrounding the hurricane (e.g., Chan and Gray 1982). The pressure level at which the speed and direction of the surrounding winds best correlate with the track of the storms is generally referred as the steering level. It is shown (Neumann 1979) that such a steering concept can account for about 80% of the variability in the 24 h tropical cyclone motion in the Atlantic.

Because the cyclone itself is part of the large-scale flow, defining an appropriate steering current is difficult. In fact, there is no unique way to determine the steering flow. For this reason, the uncertainty in the hurricane-steering relationship may arise not only from the inaccuracies inherent in determining the initial fields over the data-sparse oceanic

regions but also from the ambiguous definition of steering flow. It is not clear which level represents the best steering level, what is the best definition of the annular average (the band average flow surrounding hurricanes), and how definitions of steering flow should differ among tropical cyclones having differing characteristics, including storm intensity, size, location, and track directions, and track displacements. However, many studies have shown that the basic current at a middle tropospheric level or a deeper layer mean flow may represent the hurricane steering flow (Jordan 1952; Miller 1958; George and Gray 1976; Chan and Gray 1982; Chan 1985; Miller and Moore 1960; Neumann 1979; Brand et al. 1981; Dong and Neumann 1986).

Jordan is one of the pioneers in employing real data to affirm the steering concept. He showed that, on average, tropical storms move in the direction and with the speed of the steering current, defined as the pressure-weighted mean flow from the surface to 300 mb, extending over a 8^0 latitude band in width centered on the storm. Miller and Moore used a grid system to compute the geostrophic components around tropical cyclones at 700-, 500-, and 300-mb levels. They found that the 700- and 500-mb flows appear to be equally good in predicting the subsequent 24-hr hurricane motion. George and Gray composited 10 years of rawinsonde data for 30 stations in the western North Pacific. They showed that tropical cyclone motion is very well correlated with the surrounding lower troposphere flow fields averaged over a $1\text{-}7^0$ radial band. They also found that this general correlation of flow features applies equally well for different types of storms.

However, there are some inconsistencies in the findings of how hurricane motion is deflected from the steering current. For example, Miller (1958) found that most tropical storms moved to the right of the steering flows, whereas George and Gray's results show that for western North Pacific storms there is a leftward deviation from the middle tropospheric mean flow. Also, Brand et al. found that most western North Pacific storms moved to the left of the 500 mb flow at middle and higher latitudes, but to the right at lower

latitudes. Dong and Neumann suggested that these contradictions may be due to an improper stratification of cases.

A thorough composite observational study by Chan and Gray also supports the steering concept, though a systematic directional deviation between the steering flow and storm motion was generally found. Chan and Gray suggested that this consistent deviation is caused by some other factor or factors besides the steering flow. Chan and Gray show that the middle tropospheric (500-700 mb) 5^0-7^0 latitude-radius annular average wind has the best correlation with the cyclone motion. They found that tropical cyclones in the Northern Hemisphere move about 10-20^0 to the left of this steering flow and those in the Southern Hemisphere move about 10^0 to the right. They also found that tropical cyclones, in general, move about 1 ms^{-1} faster than the steering flow.

Dong and Neumann demonstrated that there is considerable uncertainty about which layer or level determines the steering flow. They suggested that a minimum forecast error would be realized by using the middle tropospheric levels or a deep-layer average in statistical prediction schemes, while the height of the best steering level or the depth of the best deep-layer steering increases in proportion to hurricane intensity. Similar results were found by Velden and Leslie (1991) in their study of cyclones in the Australian region.

An individual case study of Hurricane Josephine (1984) was conducted by Franklin (1990). He employed wind information measured from Omega dropwindsoundes during the "synoptic flow" experiments by the Hurricane Research Center. He showed that Hurricane Josephine generally moved in the direction of the 700-mb flow and with the speed of approximately the 500 mb flow. However, he pointed out that the 5-7^0 band average wind indicates a large vertical wind shear, and he demonstrated that in an environment with a mean vertical shear, the inappropriate initialization of the mean steering flow would result in serious errors in the barotropic storm track forecast.

Recent observational studies (Marks et al. 1992; Roux and Marks 1991) have employed airborne Doppler radar data to construct the 3-dimensional wind field near the

inner core of Hurricanes Norbert (1984) and Hugo (1989), individually. They found that each storm's motion is very close to the averaged flow over some small domain near the center. These findings reflect the original concept of steering flow, which regards the hurricane as a point vortex that it is advected by the mean environmental flow at its center. It should be mentioned that the reason why many studies have tended to construct an annular average to represent the hurricane steering flow is because of the paucity of meteorological observations in and around hurricanes. The band average is purely an empirical attempt to approximate the hurricane advection flow.

2) Hurricane propagation or drift

A hurricane is analogous to an eddy (or vortex) within a mean stream flow. In the case of a hurricane, a cyclonic eddy propagates (drifts) towards a region where the generation of a cyclonic vorticity is favored. In reality, this process is mainly dominated by the vorticity advection of the flow through the vortex center, identical to the steering concept. However, since such the terminology hurricane "propagation" (or hurricane "drift") has been used in the literature, we shall use similar terminology, and comment about the terminology at the end of this section.

(i) Analytical and numerical models

It is generally believed that some aspects of tropical cyclone motion can be described using initial value problems in simple barotropic models. Rossby (1948) indicated that a cyclonic vortex on a horizontal plane in the atmosphere is subject to a net force, directed poleward, because of the variation of the Coriolis force acting between the north and south side of the vortex. Adem (1956) derived an analytic series solution for the barotropic vorticity equation to describe self-propelled motion of atmospheric vortices. He

found that initially, the latitudinal variation of the Coriolis parameter induces a resultant poleward acceleration (as indicated by Rossby 1948 and 1949), and that the poleward translational motion combined with the rotational motion of the vortex produces an additional westward movement of the vortex (like a Rossby wave response, Rossby 1939). When the second order term (βt^2) in the series is considered, the westward displacement of the cyclone induces more poleward motion. A subsequent study by Adem and Lezama (1960) demonstrated that a cyclone initially embedded in a uniform flow would move with the velocity of the flow, but with a poleward and westward translation due to the variation of the Coriolis parameter. In some cases this translation represents a non-negligible percentage of the total displacement of a hurricane.

Numerical modelling studies by Anthes and Hoke (1975), Kitade (1980) and Holland (1983) demonstrated that tropical cyclones tend to move westward and poleward. In general, they considered the motion of an initially symmetric vortex in a barotropic flow and sought to understand the displacement of the vortex center. They proposed that differential advection of the earth's vorticity to the west and east of the cyclone would cause the storm to move initially westward. Then a secondary circulation is set up which advects the vortex poleward and westward.

Barotropic numerical studies of the evolution of hurricane-like vortices (in an initially quiescent environment) on a beta (β) plane by Chan and Williams (1987) have shown that variations of the Coriolis parameter across the tropical cyclone tend to induce a westward and poleward movement of tropical cyclones of about 2-3 ms^{-1}. This effect is generally referred as the "β effect" or "β drift " In particular, they argued that the main role of the linear β term is to induce a wavenumber one asymmetric circulation in the initially symmetric vortex. This east-west dipole vorticity tendency results in a weak (less that 0.5 ms^{-1}) Rossby-wave like propagation toward the west. However, what is more important is that this β effect (generated by advection of planetary vorticity) distorts the vortex and then induces an asymmetric flow that advects the storm poleward and westward. Modeling

work by Fiorino and Elsberry (1989), Shapiro and Ooyama (1990), and Smith et al. (1990) also showed similar storm drifts.

Fiorino and Elsberry decompose the total wind field into three components: a symmetric vortex, a larger-scale "steering" (environment) wind field and an asymmetric circulation (arising from an interaction between the symmetric circulation and the environment). By assuming no initial steering current and expanding the barotropic equation, they could determine the streamfunction tendency associated with the interaction between different components. Fiorino and Elsberry pointed out that the linear β term produces a large-scale asymmetric circulation dipole, with a significant magnitude, that is always oriented east-west relative to the (moving) storm center. An essential feature of these counterrotating gyres (sometimes referred as β gyres) is the near-uniform flow between the gyres that advects the vortex center. They also showed that the nonlinear term in the vorticity equation plays an important role in orienting the asymmetric gyres, modifying the direction of hurricane movement, and eventually establishing quasi-steady large-scale gyres that advect the vortex poleward and westward. They further demonstrated that the average velocity of the uniform flow is approximately equal to the translation speed of the vortex center.

The β effect has also been confirmed in several analytical studies. Sutyrin (1988) considered an initially circular vortex in a quasigeostrophic single-layer (shallow-water) model on a β plane. He also showed that the β effect is a result of wave drift and of secondary flows of dipole structure, which is essentially the azimuthal mode number one in his model. Sutyrin and Flierl (1991) studied the evolution of β gyres and corresponding vortex motion using a piecewise constant potential vorticity distribution (a contour dynamics model) in an initially axisymmetric vortex. Their results indicated that the β gyres are partly generated by advection of planetary vorticity and rotate differentially due to the symmetric vortex circulation. They are also partly induced by relative motion of the piecewise constant potential vorticity contours and correspond to the sum of normal modes

generated by the first part. The studies of Smith and Ulrich (1990) and Peng and Williams (1990), employing a nondivergent barotropic model, also predict gyre structures that resemble the numerical model solution.

Besides the planetary vorticity gradient, the environmental relative vorticity gradient also plays an important role in inducing similar vortex propagation effects. Kasahara (1957) has shown that the vortex moves with a speed close to that of the environmental current , but with a drift to the left of the direction of the absolute vorticity gradient of the basic flow. This drift speed is proportional to the vorticity gradient. By choosing different ways of partitioning the symmetric vortex and environment, Kasahara and Platzman (1963) were able to take into account the mutual interaction of the cyclone and the environmental flow. They inferred that, in addition to the vortex drift mentioned in Kasahara (1957), there is an additional component of vortex acceleration in the direction of the absolute vorticity gradient of the basic flow.

DeMaria (1985) solved the non-divergent barotropic equation using a spectral method with Fourier basis functions. He showed that, analogous to the poleward and westward motion of the β effect, the cyclone moves up and to the left of the absolute vorticity gradient. A series of barotropic modelling experiments were performed by Evans et al. (1991) to examine the interaction between the vortex and an idealized ridge. They demonstrated that the vortex propagation is very well correlated with the absolute vorticity gradient in the initial imposed environmental flow.

Very different points of views were proposed by Ulrich and Smith (1991). They studied vortex motion in zonal flows with three different latitudinal shears: a linear shear; a quadratic shear; and a sinusoidal shear. In the case of quadratic shear, three experiments were carried out having a common feature that the absolute vorticity gradient of the basic state is the same, but with the difference that relative contributions from the shear and β vary between the experiments. By comparing the results of these calculations, they were able to identify the role of non-uniform shear. They showed that the relative contributions

to the absolute vorticity gradient of the vorticity gradient associated with the shear and of β is a significant factor in determining vortex motion; not the absolute vorticity gradient alone. They concluded that the background shear flow has major impact on the vortex track, in part through its contribution to the absolute vorticity gradient and in part due to its distorting effects on vortex vorticity and vortex asymmetry. A subsequent paper (Smith and Ulrich 1993) also indicated that there is no clear correlation between the vortex motion and the basic-state absolute vorticity gradient.

The physical influence of the environmental shear on the vortex motion due to the relative vorticity gradient is at present not well understood. Nevertheless, most research to date assumes that barotropic drift due to the background potential vorticity gradient (or absolute vorticity gradient for the barotropic case) is the main mechanism that accounts for the deflection of tropical cyclone movement from the steering flow. A thorough review of the recent advances in understanding hurricane motion can be found in Elsberry and Abbey (1991).

It should be pointed out that most numerical studies of vortex motion in the atmosphere use barotropic models. Besides Kasahara (1960), Madala and Piacsek (1975), and Talbert (1987), very little work has been done using three-dimensional models to investigate tropical cyclone motion. The effect of vertical shear and vertical structure on hurricane motion has not been accounted for until very recently.

(ii) Observational studies

Carr and Elsberry (1990) performed a composite data analysis (using the same data as in Chan and Gray) to show evidence of drift relative to the environmental steering, defined as the middle tropospheric (surface-300 mb) 5^0-7^0 latitude radius average wind. They use the term "propagation" to refer to the observed deviation of storm motion from the environmental steering flow as defined. They found that most of the NH cyclones

propagate in a direction having components parallel and to the left of the large-scale climatological absolute vorticity gradient. Franklin (1990) also showed evidence of a relationship between the environmental absolute vorticity gradient of the asymmetric wind field and Hurricane Josephine's (1984) propagation at three analysis times. In particular, the strength of the propagation appeared to be proportional to the magnitude of the environmental absolute vorticity gradient while the orientation of the propagation vector was about $20\text{-}60^0$ to the left of the gradient vector. Kaplan and Franklin (1991) conducted a case study of Tropical Storm Florence (1988). Their results are in good agreement with Franklin (1990). Specifically, they showed a linear relationship between the environmental absolute vorticity gradient and the $5\text{-}7^0$ latitude annular average wind, in agreement with DeMaria (1985). They also showed that the $5\text{-}7^0$ latitude band average wind is always to the left of the environmental absolute vorticity gradient, consistent with the results of DeMaria (1985) and Evans et al. (1991) Feur and Franklin (1991) also found similar results. They showed that the difference between the storm motion and the middle tropospheric flow in Hurricane Gloria (1985) is toward the northwest at 2-3 ms^{-1}. However, they noted that the decision to evaluate the environmental absolute vorticity gradient and environmental steering flow over the $5\text{-}7^0$ radial band is questionable.

A recent field experiment in the west Pacific in 1990 (see Elsberry et al. 1990) was aimed at providing better data for understanding this problem. However, as Ulrich and Smith (1991) pointed out, there may be difficulty in observing the asymmetric vorticity gyres in nature. It is still debatable (Reeder et al. 1991; Holland 1991) whether it will be possible to use such data to accomplish this goal.

3) Other factors influencing hurricane motion

The previous section has focused on the effect of the absolute vorticity gradient on hurricane movement. Other factors that contribute to influence hurricane motion are discussed as follows:

(i) Divergence: Both divergent and non-divergent models have been used to study the β effect on vortex propagation. Using both divergent and non-divergent barotropic models on a β plane, Anthes and Hoke (1975) showed that the vortex in the non-divergent model drifted more toward the northwest at a much higher speed (about 30% greater than the divergent vortex). However, a study using a shallow water (primitive-equation) model by Shapiro and Ooyama (1990) found different results. Shapiro and Ooyama's results indicate that the divergence has a very small effect on the cyclone's motion.

(ii) Vortex structure: Much emphasis has been put on the influence of vortex structure on storm motion. The barotropic modelling study by DeMaria (1985) has found that the propagation effect is dependent on the outer vortex structure and has little to do with the initial wind speed. Fiorino and Elsberry (1989) show that both the direction and speed of vortex motion associated with the β effect depend strongly on the strength of the flow between 300 and 1000 km from the center, but weakly on the flow in the inner region.

(iii) Relative angular momentum: Rossby (1948) showed that the poleward drift of a cyclonic vortex can be attributed to a net northward Coriolis force proportional to the total relative angular momentum. Willoughby (1988) considered the linear motion of a shallow-water barotropic vortex. He demonstrated that a model vortex in a quiescent environment on a β plane moves westward and poleward too rapidly (about 100 ms^{-1}). This speed is proportional to the relative angular momentum integrated over the vortex.

However, Shapiro and Ooyama (1990) showed that vortex motion is not related to the total relative angular momentum in a simple way. They also found that the total relative angular momentum in the model decreases with time, eventually oscillating about zero. As indicated by Flierl et al. (1983), an isolated vortex with zero total relative angular momentum would remain isolated in the sense that no significant Rossby wave radiation occurs. The results of Shapiro and Ooyama suggest that an isolated symmetric vortex, with a vanishing total relative angular momentum, may be used to represent the hurricane vortex. This also minimizes the remote effect due to the Rossby wave adjustments.

(iv) Asymmetric convection : Willoughby (1988) and Willoughby (1990) argued that hurricanes experience cycloidal track oscillations induced by rotating asymmetric convection. Willoughby (1988; 1992) attempted to simulate the asymmetric convection by imposing rotating mass source and sinks distributed sinusoidally around a radial band outside the radius of maximum winds. The convective forcing induces a circular vortex motion. Combined with the translation of vortex due to the environmental current, the resulting motion is a cycloidal track similar to observations. However, unlike for a rotating source-sink pair, Willoughby's (1992) results show that a nonrotating convective forcing establishes quasi-stationary gyres that persistently advect the vortex center toward the region of enhanced convection. Also, this forcing may excite the normal modes (Willoughby 1990), leading to motion that persists after the forcing has been removed.

(v) Vortex interaction: Early laboratory experiments by Fujiwhara (1923) studied the mutual interaction of binary vortex systems. In addition to rotational effect, he also observed a tendency for an attraction between vortices having the same sense of rotation. A close meteorological analogy to these laboratory vortices occurs when two tropical cyclones are sufficiently close for mutual interaction. An analytical model by Gryanik (1983) used singular geostrophic vortices to represent localized vortical disturbances. The mutual rotation of interacting hurricanes was qualitatively demonstrated.

Observational evidence (Brand 1970) suggests that there is a relationship between the separation distance between two tropical cyclones and the angular rotation rate of the two storms. Brand also showed that the effect of such a binary interaction depends on differences in storm sizes and intensity, and to variations in the currents within which the tropical storm systems are imbedded.

4) Summary

From a diagnostic point of view, at any instant in time, hurricane motion is dominated by the instantaneous flow through its center. [As indicated by Roux and Marks (1991), each storm's motion is very close to its depth-averaged wind velocity in the inner core region]. How the "propagation" effect appears to affect hurricane motion depends exactly upon how the environmental (steering) flow is defined. We believe that the "propagation" effects described by the aforementioned models are essentially part of the net (total) steering (advection) process. The differences among those models may be interpreted as the differences in the way these models perturb the environmental (potential) vorticity fields in such a way to change the net steering current. For example, the β effect is a process where a hurricane vortex embedded in an background planetary vorticity gradient induces dipole vorticity gyres that change the steering (advection) of the vortex. The "propagation" concept may help to understand the interaction of a vortex and its environment, but strictly speaking should not be separated from the (steering) advection idea.

Though Elsberry (1988) has recommended the 850-300 mb pressure-weighted wind over a 5-7^0 latitude radius annulus to define a standardized steering flow, Elsberry (1991) has admitted that the calculation of a radial-band average may include some false steering that can distort a calculation of the propagation effect. We think that one must be careful in conducting an observational study trying to show evidence of a hurricane

"propagation" effect. It is possible that an inappropriate representation of the steering flow or the environmental flow across vortex core could result in a spurious inference of hurricane "propagation." We agree with Smith and Ulrich's (1993) suggestion that to avoid the misinterpretation of the dynamical processes implied, a neutral term such as "relative motion" may be more appropriate than "propagation."

b. Distribution of potential vorticity in the troposphere

It has been observed (Davis, personal communication) that the typical north-south isentropic gradient of potential vorticity (PV) within the middle-latitude troposphere during winter is much less than that associated with the planetary vorticity gradient (Fig. 2.1). In addition, the horizontal gradient of potential vorticity tends to be concentrated near the tropopause (Nielsen et al. 1991). Moreover, Morgan (personal communication) calculated the potential vorticity fields in a cross section perpendicular to composited (21 cases) winter-time polar jets. As indicated in Figure 2.2a and b, there is a region of strong horizontal PV gradients near the jet. The highest PV gradient is 2.6 PVU per 100 km at the jet center. The PV gradient in lower latitudes under the tropopause is much weaker.

To test whether this is also true in the summertime tropical troposphere, we calculate an approximate form of Ertel's potential vorticity (defined in chapter 5) from twice-daily National Meteorological Center Northern Hemisphere final analyses (on a $2.5^0 \times 2.5^0$ latitude-longitude grid). By interpolating the wind and pressure onto isentropic surfaces, Ertel's potential vorticity is computed using a centered finite-difference scheme. Potential vorticity distributions from 2.5^0 to 62.5^0N on the 315, 335 and 355 K isentropic surfaces at 1200 UTC 18 August 1992 [when the center of Hurricane Bob (hereafter, Bob) was located about 170 miles to the east-southeast of Charleston, South Carolina] are shown in Figure 2.3a, b and c, respectively. Figure 2.3d shows a "tropopause map," which indicates the distribution of potential temperature on the 1.5 PVU (potential vorticity unit,

10^{-6} m^2 s^{-1} K Kg^{-1}) potential vorticity surface (see Davis and Emanuel 1991; Nielsen et al. 1991). Similar to Bretherton's (1966) view, the tropopause potential temperature map serves as a concise way to view the dynamic information in the upper troposphere in the absence of appreciable interior potential vorticity gradients. Also, distributions of the magnitude of the PV gradient on the 315, 335 and 355 K isentropic surfaces are displayed in Figure 2.4. Figure 2.4 also indicates the location of the tropopause (1.5 PVU) on each surface.

On the 315 K surface (Fig. 2.3a), it is found that the PV distribution is quite uniform everywhere in the subtropical and tropical region. Bob appears as a local PV maximum with a PV value of 0.8 PVU. As indicated in Figure 2.4a, the PV gradient is mainly concentrated in eastern Canada, where the tropopause intersects this isentropic surface. In the subtropical troposphere, the magnitude of the PV gradient is very weak, except that there exists a region of PV gradient of about 0.1 PVU/100 km near Bob. On the 335 K surface (Figs. 2.3b and 2.4b), more PV contours appear in the subtropics; however, the horizontal PV gradient is most distinct, with a magnitude of larger than 1 PVU/100 km, along the tropopause, which extends farther south into the United States. Again, to the south of the dynamic tropopause on the 335 K surface, the magnitude of the PV gradient is much weaker. The high PV air associated with Bob still exists at this level, but this changes dramatically as we go to higher levels.

On the 355 K surface (Fig. 2.3c), a tongue of high potential vorticity air dips down to the Gulf of Mexico, acting as an intrusion of the stratospheric "reservoir" of high PV air. Relative low PV air shows up at the top of Bob, with a tail extending toward the downshear side. Figure 2.3d shows similar patterns as those in Figure 2.3c. The lens of low PV air at the top of Bob appears as a relative warm potential temperature region on the "dynamic tropopause." The magnitude of the horizontal gradient of potential vorticity (Fig. 2.4c) in the subtropics and tropics at this level is much higher than in the lower and middle troposphere. These findings cast some doubt on the applicability of traditional theory,

which relates hurricane motion to the drift of barotropic vortices embedded in a uniform background potential vorticity gradient.

c. Another theoretical consideration of the β effect

Xu and Emanuel (1989) showed that the tropical atmosphere always has a vertical virtual temperature profile close to a reference profile resembling a reversible adiabat. From this observation, it can be shown that absolute vorticity vectors are nearly parallel to the surface of constant saturated equivalent potential temperature, as adjusted by the slantwise moist convection. Therefore, in the tropical atmosphere, the saturated moist potential vorticity (SMPV), defined as

$$\alpha(f\mathbf{k} + \nabla \times \mathbf{v})\cdot\nabla\theta_e^*$$

(where α is the specific volume, and θ_e^* is the saturated equivalent potential temperature), is nearly zero. As a result, it can be shown (Emanuel, personal communication) that the geopotential distribution in the troposphere is uniquely determined by the horizontal distribution of subcloud-layer θ_e and the three-dimensional distribution of potential vorticity in the stratosphere. Therefore, in the tropical troposphere, the β effect is due to subcloud-layer anomalies and stratospheric PV anomalies. However, since the subcloud-layer θ_e anomalies are strongly damped by contact with the ocean, the β gyres (the asymmetric circulation induced by the β effect) are dominated by the stratosphere potential vorticity anomalies arising from the anticyclone at upper levels.

As indicated from observations (Jordan 1952; Frank 1977), real hurricanes are characterized by anticyclonic flow near the tropopause. Since this flow typically interacts with a potential vorticity gradient near the tropopause that is as strong or stronger than gradients located in the middle or lower troposphere, it is not obvious which component of the hurricane circulation has the dominant effect on the PV evolution. It is conceivable that the principal effect of the hurricane on tropical cyclone motion is that associated with the

anticyclonic outflow near the tropopause; this effect tends to move the upper anticyclone westward and equatorward.

d. Hypotheses

As noted above, hurricanes have anticyclonic circulations near the tropopause, except perhaps near their centers. The reason for this can be interpreted from a potential vorticity perspective. As stressed by both Thorpe and Emanuel (1985) and Hoskins et al. (1985), in the absence of diabatic heating and friction at the boundary, the mass-weighted volume integral of potential vorticity over a suitably defined domain is conserved. Interior diabatic heating cannot change the mass-integrated total potential vorticity around the tropical cyclone. It only plays a role in redistributing potential vorticity in the vertical (by potential vorticity generation in the lower troposphere and potential vorticity destruction in the upper troposphere). However, because surface friction acts to destroy potential vorticity, the total potential vorticity, integrated in a volume bounded by a surface around which there is a cyclonic circulation at the sea surface, should decrease with time. From this point of view, it would be expected that a region of low potential vorticity is generated in the upper troposphere above a tropical cyclone. This low PV region near the tropopause is seen in the numerical simulations of Rotunno and Emanuel (1987) and also from Figures 2.3c and d in this paper. This argument is also in agreement with results from Schubert and Alworth (1987), that latent heat release generates PV at lower levels, but destroys it at upper levels. Hence, in terms of potential vorticity, a "steady-state" mature hurricane can be viewed as a diabatically and frictionally maintained constant positive potential vorticity anomaly in the lower troposphere, with an expanding negative potential vorticity anomaly in the upper troposphere.

Using the concepts of vortex interaction, a tropical cyclone, which is structured like a vertically distributed pair of vortices of opposite sign, would experience a mutual

propagation if the vortex dipole is tilted. In particular, we hypothesize that there are two ways to cause this kind of interaction.

1) The existence of ambient vertical shear: The background vertical wind shear acts to tilt the vortex pair by blowing the upper potential vorticity anomaly downshear of the lower anomaly. Evidence of this phenomenon is found in Figures 2.3c and d, and also by Molinari (1992) in PV analyses of hurricanes. A simple picture of this idea is illustrated in Figure 2.5. As the members of the vortex pair are displaced horizontally, they begin to interact with each other. Their mutual interaction will move the pair at right angles to the axis connecting them. Specifically, an anticyclonic circulation associated with the upper vortex would extend downward to the lower troposphere and advect the lower vortex to the left of the shear. On this basis, we infer that NH (SH) tropical cyclones should drift with respect to the mean winds in a direction to the left (right) of the background vertical shear vector.

2) The "β effect" on the upper anticyclone: The upper anticyclone drifts equatorward and westward due to the effect of the background potential vorticity gradient. Therefore, we suppose that the upper anticyclone, experiencing such a drift, would interact with the lower layer vortex and lead to an eastward and equatorward motion of the cyclone.

The numerical modelling study (discussed in chapters 3 and 4 of this thesis) shall focus on the first effect. Our previous work used a quasigeostrophic point-vortex model to investigate this problem. Here we shall upgrade the previous studies by using a contour dynamics model.

It should be noted that, while this work was carried out, other modelling work with similar ideas were conducted by Flatau (1991), Wang and Li (1992) and Shapiro (1992). We will compare our results with these studies in chapter 4. Also, the main portion of the present modelling work can be found in Wu and Emanuel (1993).

e. Background of potential vorticity

The dynamic properties of potential vorticity were not extensively utilized in observational work until the thorough review by Hoskins et al. (1985). Ertel's potential vorticity is defined as

$$Q = \frac{\xi}{\rho} \cdot \nabla\theta,$$

where Q represents PV, ρ is the density, ξ is the absolute vorticity vector, and θ is the potential temperature. There are three significant quantities of importance in using PV.

1) The conservation principle, which states that PV is conserved following an adiabatic and frictionless motion.

2) The invertibility principle, which states that given a distribution of PV, a prescribed balance condition, and boundary conditions, a balanced mass and wind field can be recovered.

3) The superposition principle, which states that when two PV anomalies of the same (opposite) sign are brought closer to each other, the mass-integrated total perturbation energy will increase (decrease).

From the invertibility principle, all of the dynamic information can be recovered from a single field, PV, given an appropriate balance condition. Consequently, the dynamics in a fluid system is succinctly contained in the PV field. Since the atmosphere is generally observed to contain various pieces of features with signatures in the PV field, the quasi-conservation property of PV allows one to easily identify the movement and change in shape and structure of these features.

Combining the use of the aforementioned PV principles, one can examine the evolution of a PV field on surfaces of constant potential temperature (another conserved quantity) to identify the movement of parcels or patches of air containing the PV information and thus understand the evolution of the dynamics.

Following the motion of the air parcel, PV changes through diabatic and frictional effects (Hoskins et al. 1985), that is,

$$\frac{dQ}{dt} = (\frac{1}{\rho})\, \xi \cdot \nabla(\frac{d\theta}{dt}) + (\frac{1}{\rho})\, (\nabla \times F) \cdot \nabla\theta,$$

where **F** is the frictional force. Also, the change of the mass-integrated volume integral of PV over a suitably defined domain can be described as

$$\frac{d}{dt} (\iiint \rho Q \, d\tau) = \iint \{ \, [(\frac{d\theta}{d\tau}) \, \xi + \theta \, (\nabla \times F)] \cdot \mathbf{n} \, ds \, \},$$

where τ is the material volume and **n** is the unit vector normal to the surface s bounding the material volume. Therefore, the nonconservative effects (e.g., latent heating) can also be addressed within the PV framework.

Because of the nature of PV, "PV thinking" has been applied to a broad spectrum of meteorological work. These include understanding the concept of quasi-balanced flow and so-called "slow-manifold" dynamics (McIntyre and Norton 1991); studying vortex dynamics (Polvani et al. 1989), polar vortex breaking (Polvani and Plumb 1992), and horizontal tracer transport (Waugh and Plumb 1992; Atkinson, personal communication); investigating long-lived mesoscale convective systems (Raymond and Jiang 1990); and diagnosing extratropical cyclogenesis events (Davis and Emanuel 1991; Davis 1992a).

In particular, Davis and Emanuel (1991) diagnosed extratropical cyclogenesis from a PV perspective. They inverted PV using a nonlinear balance condition. Moreover, they derived a method for performing a piecewise PV inversion under a nonlinear balance condition. One important feature of their piecewise inversion scheme is that the equation is manipulated in such a way that the solution behaves almost "linearly." In other words, the summation of the balanced fields associated with each individual PV perturbation is the total balanced field. In this way, they were able to demonstrate how specific parts of the PV anomaly distribution interact with one another, in an attempt to gain a clearer and more

coherent picture of the development of cyclones. Their methodology has been adopted in this study.

Potential vorticity methods have proven useful in understanding synoptic- and large-scale midlatitude dynamics, and are becoming more widely applied to tropical motion systems. Schubert and Hack (1983), Thorpe (1985), and Schubert and Alworth (1987) all employed an axisymmetric balance model to understand the structure and evolution of tropical cyclone using PV as the principal variable. Schubert et al. (1991) used a zonally symmetric balance model to extend the general potential vorticity approach from midlatitude dynamics to the dynamics of Hadley circulation. Molinari (1992) showed that the intensity change of Hurricane Helen (1980) can be well related to the evolution of the upper PV anomaly. Reilly (1992) conducted an observational case study and found that upper-tropospheric PV advection plays an important role in tropical cyclone genesis. Montgomery and Farrell (1993) also investigated the influence of upper-level potential vorticity disturbances on tropical cyclone formation within the context of two simple nonlinear balance models that incorporate moist processes. Their results agree with the indication from observations that tropical cyclogenesis is essentially a slow manifold phenomenon, primarily driven by the balance response to slowly interacting upper- and lower-level PV fields.

Our approach presumes that hurricane motion is also closely connected to the interaction of the hurricane with the environmental PV fields, and may be better understood in the context of quasi-balance dynamics.

f. Potential vorticity view of the hurricane advection flow

Within a PV perspective, the hurricane appears as a strong and localized positive PV anomaly in the lower and middle troposphere. Since this PV patch is so localized, it can be regarded as a "point vortex." From this point of view, the movement of a hurricane

should be dominated by the instantaneous flow through its center. This argument has been made in the aforementioned observational studies (Marks et al. 1992; Roux and Marks 1991). Instead of using the terminology "steering flow", we shall refer to the flow through the hurricane center as the hurricane "advection flow."

In reality, it is very difficult to accurately derive the advection flow in the center of a hurricane partly because of the insufficient observations in the storm region and partly because this component of the wind can be masked by the strong azimuthal winds surrounding the hurricane. For example, there can be a strong bias in estimating the advection flow when the observational data cannot accurately locate the hurricane center. To avoid this problem, researchers have tended to construct the annular mean tropospheric flow to average out the azimuthal winds and thus find the steering flow, and it has been shown by Chan and Gray (1982) that the middle tropospheric (500-700 mb) 5^0-7^0 latitude radius average wind has the best correlation with the cyclone motion. Though there is generally good agreement between this mean flow and hurricane motion, the problem is that the process of performing the annular average wind is purely empirical and doesn't have any dynamic basis. Therefore, we believe it is necessary to define the advection flow in a more consistent and dynamically meaningful way.

Though hurricanes are very distinct isolated vortices, they are embedded within background flows that have a rich and variable structure. The environment will have a significant impact on the vortex motion. For example, as a hurricane moves, it presumably will interact with any large-scale circulation and adjacent synoptic-scale systems (typical examples are the subtropical high over the ocean and midlatitude upper-tropospheric waves). Thus, the orientation and strength of the hurricane steering current will change in response to the normal propagation and development of large-scale pressure ridges and troughs in the atmosphere. It is very important to understand how individual synoptic or large-scale features interact with the storm track. Since the nonlinear balance condition is a good approximation for synoptic and large-scale flows in the tropics (Haltiner and Williams

1980), the PV approach provides a convenient basis for diagnosing how synoptic and large-scale dynamical systems interact with a hurricane. By performing piecewise potential vorticity inversions under nonlinear balance conditions, we can determine the balanced flow associated with individual PV perturbations. Then, by examining the components of the balanced flow at the hurricane center, we can identify how each piece of PV anomaly influences hurricane movement.

The observational study (appearing in chapters 5, 6 and 7 of this thesis) is aimed at the application of the PV diagnostics in understanding the dynamics of hurricane movement.

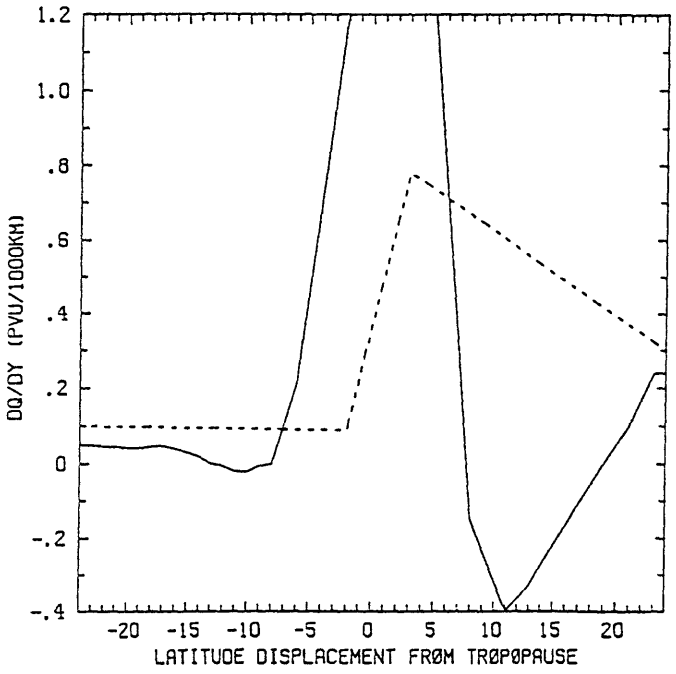

Figure 2.1 300 K mean Northern Hemispheric north-south gradient of Ertel's potential vorticity as a function of degrees latitude north from the tropopause, for winter 1978/79. The average was performed relative to the southernmost occurrence of the 1.5-PVU (potential vorticity unit, 10^{-6} m^2 s^{-1} K kg^{-1}) contour at each latitude (5^0 increments) for each analysis time. The dashed line corresponds to the gradient obtained by setting the vorticity equal to the planetary vorticity and the lapse rate equal to 0.05 K mb^{-1} in the troposphere and 0.5 K mb^{-1} in the stratosphere. The observed gradient (solid line) is less than half the "planetary gradient" (dashed line) between 8^0 and 24^0 south of the tropopause. (Davis, personal communication.)

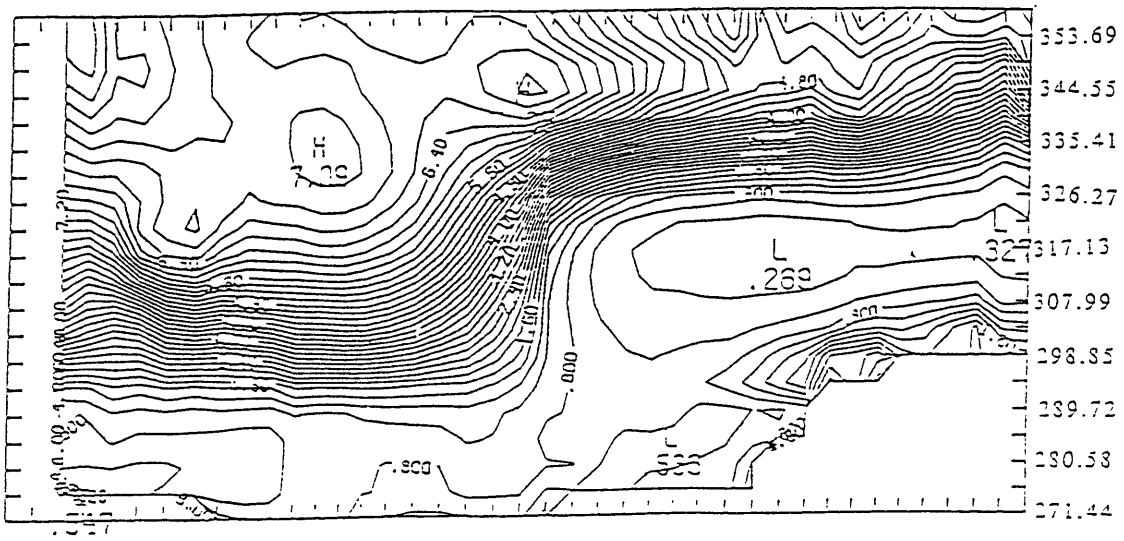

(a)

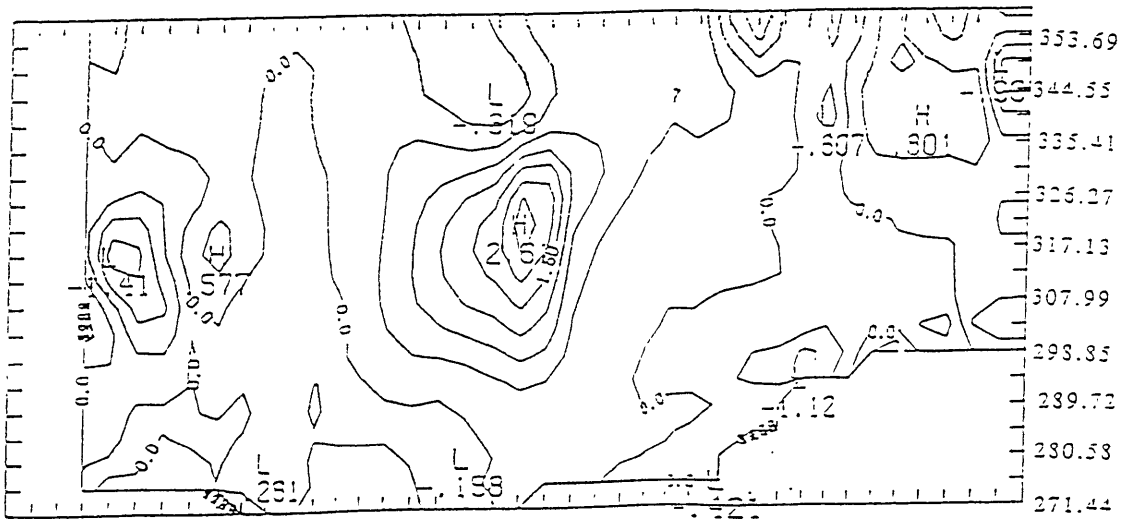

(b)

Figure 2.2 (a) Potential vorticity field in a cross section perpendicular to composited (21 cases) winter-time polar jets. The contour interval is 0.4 PVU. (b) as in (a) but for magnitude of the potential vorticity gradient. The contour interval is 1 PVU per 100 km. Each tick in the horizontal domain represents 100 km. (Morgan, personal communication.)

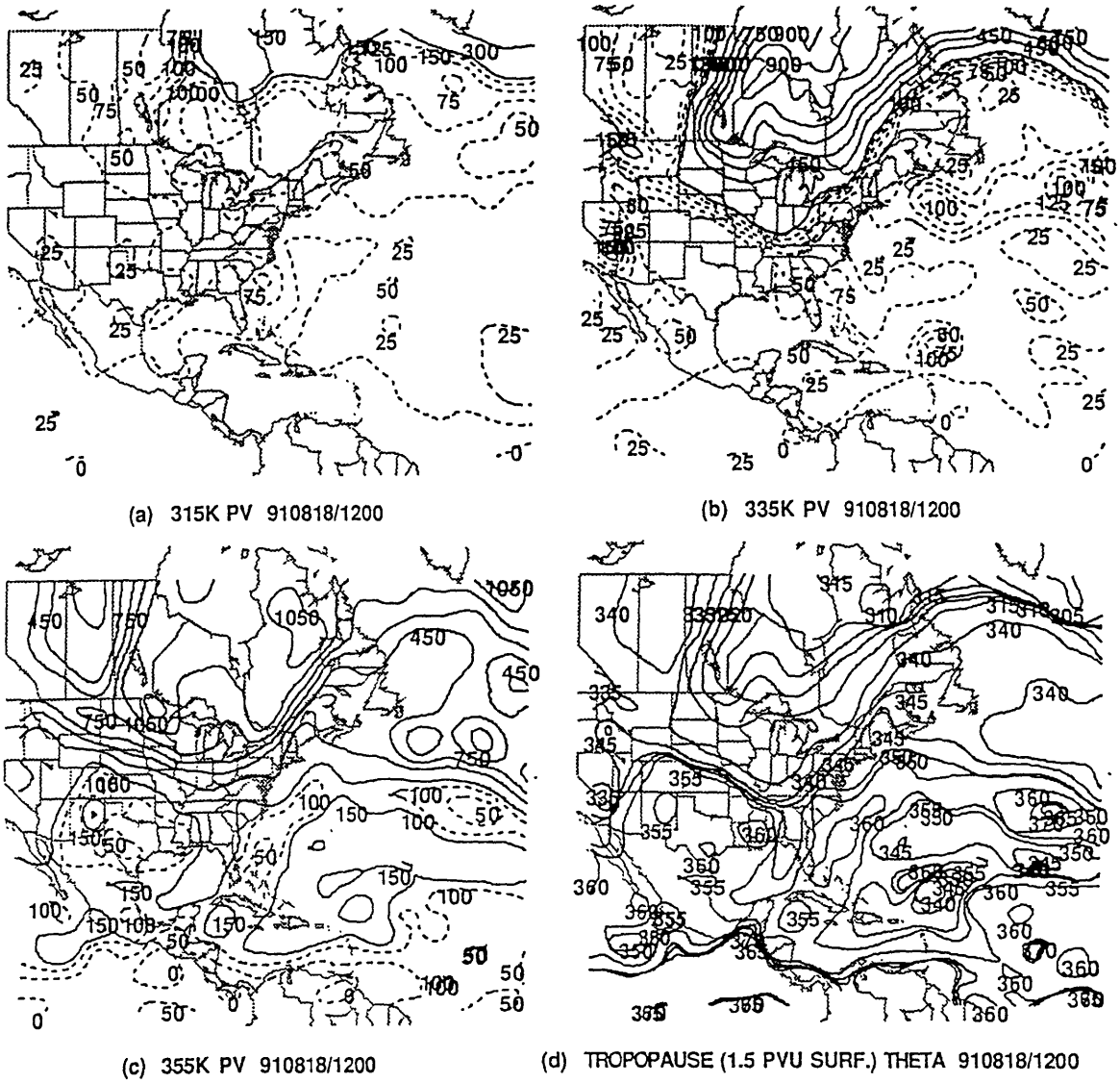

Figure 2.3 Ertel's potential vorticity and tropopause potential temperature fields at 1200 UTC 18 August 1991. (a) , (b), and (c) are the PV maps for the 315, 335, and 355 K isentropic surfaces, respectively. The unit is 0.01 PVU. Potential vorticity values smaller than (larger than or equal to) 1.5 PVU are shown as dashed lines (solid lines) with contour intervals of 0.25 PVU (1.5 PVU). (d) shows the tropopause potential temperature (on the 1.5 PVU surface). The contour interval is 5 K.

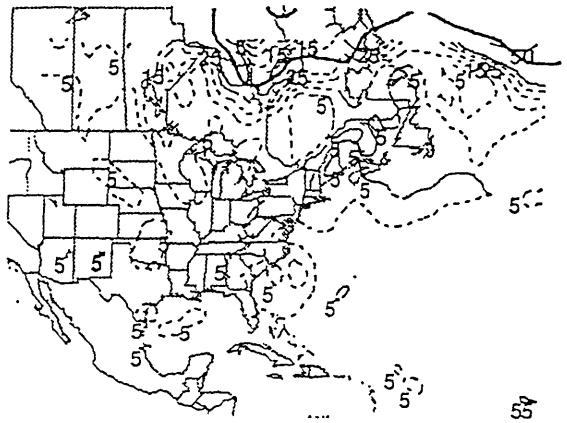

(a) 315 K MAG. OF PV GRADIENT 910818/1200

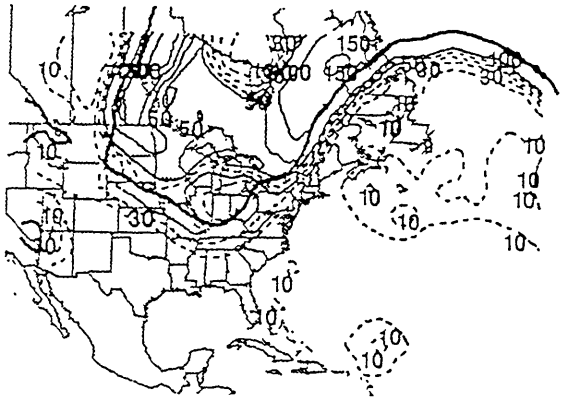

(b) 335 K MAG. OF PV GRADIENT 910818/1200

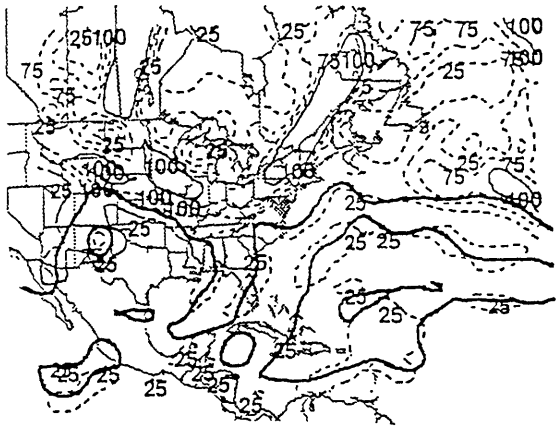

(c) 355 K MAG. OF PV GRADIENT 910818/1200

Figure 2.4 Magnitude of the Ertel's potential vorticity gradient (with unit in 0.01 PVU/100 km) at 1200 UTC 18 August 1991. (a) for the 315 isentropic surface: values smaller than or equal to (larger than) 0.25 PVU/100 km are shown as dashed lines (solid lines) with contour intervals of 0.05 PVU/100 km (0.25 PVU/100 km); (b) for the 335 isentropic surface: values smaller than or equal to (larger than) 0.5 PVU/100 km are shown as dashed lines (solid lines) with contour intervals of 0.1 PVU/100 km (0.5 PVU/100 km); and (c) for the 355 isentropic surface: values smaller than (larger than or equal to) 1 PVU/100 km are shown as dashed lines (solid lines) with contour intervals of 0.25 PVU/100 km (1 PVU/100 km). Heavy solid line indicates the 1.5 PVU contour at each isentropic surface.

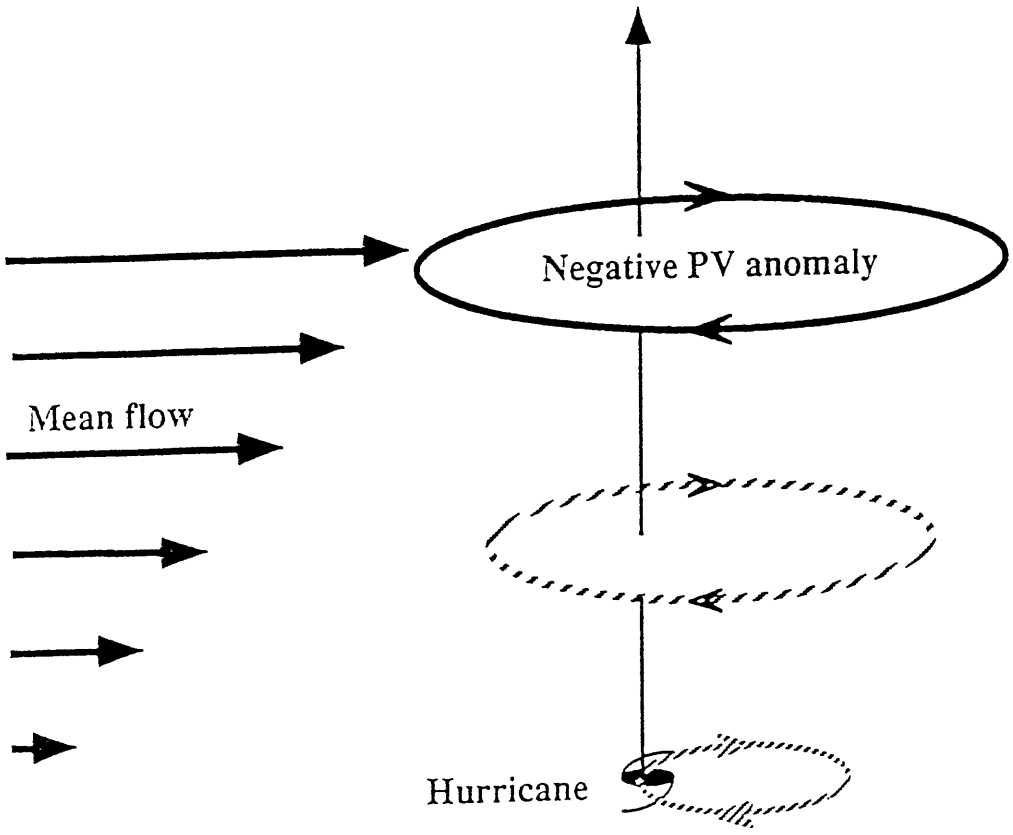

Figure 2.5 Illustration of the hypothesis I.

3. Description of the model

a. Background of the method of contour dynamics and contour surgery

Contour dynamics is a Lagrangian computational method used to integrate flows associated with patches of piecewise constant potential vorticity. This method leads to a closed dynamical system within which the evolution of the flow can be uniquely determined by the contours bounding the patches. (In practice, the contours are represented by a finite number of discrete nodes.) In other words, contour dynamics achieves its great numerical efficiency by integrating only on the contours instead of on the total potential vorticity field. To apply the contour dynamics technique, the Green's function associated with the differential operators of the fluid flow equations must be known. Because only certain fluid flows, such as barotropic, equivalent barotropic, or two-layer quasigeostrophic flows, have a simple enough mathematical form that their Green's functions can be analytically found, the contour dynamics technique is restricted mainly to applications on these flows. For example, using the method of contour dynamics, Polvani et al. (1989) performed an extensive study of geostrophic vortex dynamics in a two-layer quasigeostrophic model.

The method of contour surgery improves the resolution of the contour by adding nodes (called node adjustment) in regions of high curvature or smaller velocity. It is also more efficient and prevents unlimited enstrophy cascades to small scale by removing contour features (called contour adjustment) thinner than some prescribed tolerance. In this way, the contour dynamics may keep its computation at a manageable level while being able to produce very fine-scale and realistic structures. A detailed description of the methods of contour dynamics and contour surgery can be found in Dritschel (1989). The primary disadvantage of contour dynamic is that it prohibits the existence of background potential vorticity gradients except on contours where finite potential vorticity jumps occur.

Therefore, the contour dynamics approach inherently rules out the possibility of including a smooth planetary vorticity gradient. Although this makes the model somewhat unrealistic, it does allow us to isolate the effect of ambient vertical shear on tropical cyclone propagation. The other disadvantage of contour dynamics is that there is a time limit on the model integration, beyond which the number of nodes of the contour is too large to be integrated within a reasonable time.

b. Background of the models

A two-layer quasigeostrophic model is used to investigate the effect of background vertical shear. Since the two-layer model essentially assumes layers of constant density, diabatic effects cannot be explicitly included. For this reason, the forcing of potential vorticity from diabatic effects is specified. The approach we have taken is to simulate the interaction of a baroclinic vortex dipole with the background shear, using the methods of contour dynamics and contour surgery applied to a two-layer quasigeostrophic system.

We consider the simplest analog of a mature tropical cyclone to be a diabatically and frictionally maintained point vortex of constant strength in the lower layer and, in the upper layer, a patch of uniform, zero potential vorticity air surrounded by an infinite region of constant potential vorticity. The diabatic sink of potential vorticity in the upper layer is represented as the expansion of the area of the upper potential vorticity anomaly owing to a radial outward potential flow emanating from a point-mass source collocated with the lower vortex.

Physically, this representation mimics the action of moist convection near the hurricane center in creating a source of near-zero PV air in the upper troposphere, which is advected outward by the upper-level divergent hurricane outflow. The idealization of a patch of near-zero PV air in the upper troposphere is based both on the results from the numerical simulations of Rotunno and Emanuel (1987) and on the theoretical arguments (as

discussed in chapter 2c) that the saturated moist potential vorticity is close to zero in a state of slantwise moist neutrality (the upper-tropospheric air is so cold and dry that the potential vorticity is very nearly equivalent to the saturated moist potential vorticity). For a quasi-steady hurricane, the vertical mass flux is mainly controlled by the process of Ekman pumping in the boundary layer. Therefore, according to the principle of mass continuity, the upper divergent potential flow can be derived from the lower boundary frictionally driven mass influx. A simple picture of this model is illustrated in Figure 3.1.

To isolate the effect of the ambient vertical shear, we explore the case of a vanishing ambient potential vorticity gradient. Therefore, the upper vortex patch is advected by the rotational flows (associated with both the upper-layer contour itself and the lower-layer vortex), the divergent flow (associated with the mass source), and the mean shear flow. The evolution of the upper vortex patch is integrated by the method of contour dynamics and contour surgery. This formulation is an ideally simple model for exploring the effects of vertical shear in isolation. The quasigeostrophic aspect of the model is a poor representation of the vertical penetration of the effect of potential vorticity anomalies near the storm center, where the Rossby number is large, but should be adequate for describing the effect of the low-level cyclonic anomaly on the upper-level contour evolution at relatively large radius and for describing the downward penetration of the effect of the upper level anomaly, whose associated rotational flow is probably weak enough to satisfy quasigeostrophy at all radii. We emphasize that the present work is meant to describe the first-order effects of vertical shear given the approximations inherent in the model.

c. Formulation of the model equations

In a continuous quasigeostrophic flow, the meridional gradient of zonal mean pseudo potential vorticity is

$$\frac{\partial q}{\partial y} = \beta - \frac{\partial^2 U}{\partial y^2} - \frac{f_0^2}{N^2}\left[\frac{\partial^2 U}{\partial z^2} + \frac{1}{H}\frac{\partial U}{\partial z}\right], \tag{3.1}$$

where U is the zonal mean wind, f_0 is the Coriolis parameter evaluated in the middle of the domain, N is the Brunt-Väisälä frequency, and H is a scale height defined as

$$H = \left[-\frac{\rho}{N^2}\frac{\partial(N^2/\rho)}{\partial z}\right]^{-1},$$

where ρ is the mean density. N^2 and ρ may vary only with altitude.

The aforementioned observations suggest that, at least in the subtropics, the meridional gradient of mean pseudo-potential vorticity is much smaller than β. For this reason and in order to isolate the direct effect of vertical wind shear on storm propagation, we take

$$\frac{\partial q}{\partial y} = 0,$$

and

$$\frac{\partial U}{\partial y} = 0.$$

By equation (3.1), then, we are constrained to use a vertical profile of U that satisfies

$$\frac{d^2 U}{dz^2} + \frac{1}{H}\frac{dU}{dz} - \frac{N^2\beta}{f_0^2} = 0. \tag{3.2}$$

Taking N^2 to be approximately constant, the zonal wind profile that satisfies this is

$$U = U_0 + \left(U_T - U_0 - \frac{N^2H^2}{f_0^2}\beta\right)\left(\frac{e^{-z/H} - 1}{e^{-1} - 1}\right) + \left(\frac{N^2H^2}{f_0^2}\right)\beta\left(\frac{z}{H}\right),$$

where $U_T = U$ (at z=H) and $U_0 = U$ (at z=0). If it is further required that the surface meridional temperature vanishes [i.e., dU/dz (at z=0) = 0], as is approximately true in the tropics, then

$$U = U_0 + \frac{N^2H^2}{f_0^2}\beta\,(e^{-z/H} - 1 + \frac{z}{H}).$$

This profile has very little shear through most of the troposphere, with an increasing shear near the tropopause. For typical values of the parameters, this would give an increase of about 10 m s^{-1} between the mean surface zonal wind and the wind at the tropopause. (This mean shear could be reduced to zero if a weak easterly shear near the surface is assumed.)

In a two-layer representation, it is not possible to represent in a direct way the curvature of the mean wind profile, but the mean meridional gradient of potential vorticity can be canceled out by introducing upper and lower boundaries with gentle meridional slopes. When this is done, the conservation equations for pseudo-potential vorticity in each layer become

$$\frac{dq_1}{dt} = [\frac{\partial}{\partial t} + J(\Psi_1, *)]\, q_1 = H_1, \tag{3.3}$$

$$\frac{dq_2}{dt} = [\frac{\partial}{\partial t} + J(\Psi_2, *)]\, q_2 = H_2 + F_2, \tag{3.4}$$

where subscripts 1 and 2 denote the upper and lower layer, respectively, and

$$q_1 = \nabla^2\Psi_1 + \frac{\Psi_2 - \Psi_1}{L_R^2} + f_0 + \beta_1 y,$$

$$q_2 = \nabla^2\Psi_2 + \varepsilon\frac{\Psi_1 - \Psi_2}{L_R^2} + f_0 + \beta_2 y,$$

where Ψ_1 and Ψ_2 are the streamfunctions in the upper and lower layers, respectively; H_1 is the diabatic source of potential vorticity in the upper layer; H_2 is the diabatic source in the lower layer; F_2 is the frictional dissipation of potential vorticity at the lower boundary; L_R is the radius of deformation ($L_R = (gD_1\Delta\rho/\rho)^{1/2}/f_0$); D_1 is the depth of the upper layer; $\Delta\rho$ is the density difference between the two layers; f_0 is the local Coriolis parameter, and β_1 and β_2 are the mean potential vorticity gradients in the upper and lower layers, respectively. These are given by

$$\beta_1 \equiv \beta - \frac{f_0\alpha_1}{D_1}, \tag{3.5}$$

$$\beta_2 \equiv \beta + \frac{f_0\alpha_2}{D_2}, \tag{3.6}$$

where α_1 and α_2 are the slopes of the upper and lower boundaries, respectively.

The Jacobian and Laplacian operators are given by

$$J(A,B) \equiv \frac{\partial A}{\partial x}\frac{\partial B}{\partial y} - \frac{\partial A}{\partial y}\frac{\partial B}{\partial x},$$

$$\nabla^2 = \frac{\partial^2}{\partial x^2} + \frac{\partial^2}{\partial y^2},$$

and $\varepsilon = D_1/D_2$ is the ratio of the upper to lower layer thickness (when the fluid is at rest).

The flow is divided into two parts:

1). a mean zonal flow (denoted by overbars), which is taken here to be independent of y, and

2). vortical disturbances associated with the potential vorticity anomalies (denoted by primes), that is,

$$\psi_1 = \overline{\psi}_1 + \psi_1' = -\int U_1\, dy + \psi_1',$$

$$\psi_2 = \overline{\psi}_2 + \psi_2' = -\int U_2\, dy + \psi_2'.$$

Then (3.3) and (3.4) become

$$\left(\frac{\partial}{\partial t} + U_1\frac{\partial}{\partial x}\right) q_1' + J(\psi_1', \overline{q}_1 + q_1') = H_1, \tag{3.7}$$

$$\left(\frac{\partial}{\partial t} + U_2\frac{\partial}{\partial x}\right) q_2' + J(\psi_2', \overline{q}_2 + q_2') = H_2 + F_2, \tag{3.8}$$

where

$$\overline{q}_1 = f_0 + \left(\beta_1 + \frac{U_1 - U_2}{L_R^2}\right) y,$$

$$\overline{q}_2 = f_0 + \left(\beta_2 - \varepsilon\frac{U_1 - U_2}{L_R^2}\right) y,$$

and

$$q_1' = \nabla^2 \psi_1' + \frac{\psi_2' - \psi_1'}{L_R^2},$$

$$q_2' = \nabla^2 \psi_2' + \varepsilon \frac{\psi_1' - \psi_2'}{L_R^2}.$$

To be able to apply contour dynamics, we require that the mean potential vorticity gradient vanishes, that is,

$$\frac{\overline{dq_1}}{dy} = \frac{U_1 - U_2}{L_R^2} + \beta_1 = 0,$$

$$\frac{\overline{dq_2}}{dy} = \varepsilon \frac{U_2 - U_1}{L_R^2} + \beta_2 = 0.$$

Using (3.5) and (3.6), this determines the slopes of the two boundaries:

$$\alpha_1 = \frac{D_1}{f_0} \left(\beta + \frac{U_1 - U_2}{L_R^2} \right),$$

$$\alpha_2 = \frac{D_2}{f_0} \left(-\beta + \varepsilon \frac{U_1 - U_2}{L_R^2} \right).$$

Typical values of α_1 and α_2 are 1×10^{-3} and -1×10^{-3}, respectively. Thus, we are free to choose U_1 and U_2, the mean flow velocities in the upper and lower layers. This does not violate the spirit of our analysis, which constrains the flow to have no mean gradient of pseudo-potential vorticity. As seen earlier, this requirement determines the curvature of the flow profile and not its mean shear.

d. Model simplifications

1). As there is no mean gradient of potential vorticity, the system becomes Galilean-invariant, and we can further assume no mean wind in the lower layer, that is, $U_2 = 0$.

2). Real hurricanes contain highly concentrated potential vorticity anomalies at the center. This is idealized as a point potential vortex in the lower layer. Therefore, in the lower layer, we assume that a mature tropical cyclone is diabatically and frictionally maintained and represent it there as a point vortex of constant strength S_2, that is,

$$q_2' = S_2\,\delta(\mathbf{x} - \mathbf{x}_p(t)),$$

where $\mathbf{x}_p$ is the position of the point vortex, and

$$H_2 + F_2 = 0.$$

The last relation is based on the assumption that the destruction of potential vorticity by friction is balanced by its creation by diabatic heating. This representation makes the cyclone drift quite visible (i.e., the cyclone drift is simply the movement of the point vortex).

3). In the upper layer, the upward decrease of diabatic heating causes the potential vorticity associated with the anticyclone to decrease with time. We represent this by a patch of constant, negative potential vorticity anomaly, whose area expands owing to a radial outward potential flow, emanating from a point mass source collocated with the lower vortex. In other words, the forcing is represented as an advection of the potential vorticity by a potential flow $\mathbf{u}_p$. Therefore,

$$H_1 = -\,\mathbf{u}_p \cdot \nabla q_1',$$

$$q_1' = Q_1\,X_D(\mathbf{x}),$$

where Q_1 is the potential vorticity jump across the contour associated with a patch domain D, and X is a symbol for the generalized step function, that is,

$$X_D(\mathbf{x}) = 1, \text{ when } \mathbf{x} \in D,$$

$$X_D(\mathbf{x}) = 0, \text{ when } \mathbf{x} \notin D,$$

Then (3.7) and (3.8) can be rewritten (neglecting the prime symbol) as

$$(\frac{\partial}{\partial t} + U_1\frac{\partial}{\partial x} + \mathbf{u_p}\cdot\nabla)\, q_1 + J(\Psi_1, q_1) = 0, \tag{3.9}$$

$$\frac{\partial}{\partial t} q_2 + J(\Psi_2, q_2) = 0, \tag{3.10}$$

where

$$q_1 = \nabla^2\Psi_1 + \frac{\Psi_2 - \Psi_1}{L_R^2} = Q_1 X_D(\mathbf{x}),$$

$$q_2 = \nabla^2\Psi_2 + \varepsilon\frac{\Psi_1 - \Psi_2}{L_R^2} = S_2\,\delta(\mathbf{x} - \mathbf{x_p}(t)).$$

e. Estimation of the potential flow

In general, the transverse circulation of a mature hurricane consists of radial inflow within the frictional boundary layer, ascent within a narrow outward sloping eyewall, and radial outward flow in a thin layer at the top of the storm. From this point of view, the potential radial outward flow in our model can be approximated as a flow emanating from a mass source in the upper layer, whose mass flux is determined by the surface frictionally induced inflow. Considering an axisymmetric hurricane, the angular momentum M is defined as

$$M = rv + \frac{fr^2}{2},$$

where r is the distance from the storm center. The azimuthal component of the momentum equation in the surface inflow layer in cylindrical coordinates is

$$u\frac{\partial M}{\partial r} = -rg\frac{\partial \tau}{\partial p},$$

or

$$u\,[\,f_0 + \frac{1}{r}\frac{\partial(rv)}{\partial r}\,]\,r = -\,rg\frac{\partial\tau}{\partial p}\,, \tag{3.11}$$

where u and v are the radial and azimuthal components of the wind, respectively, f is approximated by the local Coriolis parameter f_0, and τ is the azimuthal component of frictional stress. We examine (3.11) at a particular radius r_c, where the relative vorticity ζ changes sign, that is,

$$\zeta = [\,\frac{1}{r}\frac{\partial(rv)}{\partial r}\,]_{\,r=r_c} = 0.$$

At this radius (3.11) becomes

$$u\,f_0\,r_c = -\,r_c\,g\frac{\partial\tau}{\partial p}\,.$$

Integrating vertically over the surface boundary layer, we get

$$\int u f_0 r_c \frac{dp}{g} = -\,r_c\,\tau_s,$$

where τ_s is the azimuthal component of surface frictional stress at radius r_c. By applying the bulk aerodynamic formula,

$$\tau_s = \rho_s\,c_D\,v_c\,|v_c|,$$

where c_D is the drag coefficient and v_c is the azimuthal surface wind at radius r_c, the total mass influx is

$$F_{in} = |\,2\pi r_c \int \rho u\,dz\,| = |\,2\pi r_c \int u\frac{dp}{g}\,| = \frac{2\pi\rho_s r_c c_D v_c^{\,2}}{f_0}\,, \tag{3.12}$$

where the hydrostatic equation is used. Also, the outward mass flux in the upper layer can be represented as

$$F_{out} = 2\pi\rho_1 u_p r_1 D_1, \tag{3.13}$$

where u_p is the outward radial wind at radius r_1 in the upper layer and ρ_1 is a mean density in the upper layer. By equating F_{in} and F_{out}, the potential flow

$$u_p = \frac{\rho_s r_c c_D v_c^{\,2}}{f_0 \rho_1 r_1 D_1}\,.$$

is obtained.

To get a feeling for how this potential flow changes the real PV in the upper layer, we approximate the PV destruction rate in this model as follows:

Supposing that the upper layer vortex patch covers an area A_1, the outward mass flux can also be represented as

$$F_{out} = \rho_1 D_1 \frac{dA_1}{dt}.$$

From (3.12) and (3.13), we derive

$$\frac{dA_1}{dt} = \frac{2\pi\rho_s r_c c_D v_c^2}{\rho_1 f_0 D_1}. \tag{3.14}$$

Because the divergent potential flow has no net effect on the absolute circulation bounding the upper-layer vortex patch, the upper-layer absolute circulation is conserved, that is,

$$\frac{dC_1}{dt} = \eta_1 \frac{dA_1}{dt} + A_1 \frac{d\eta_1}{dt} = 0, \tag{3.15}$$

where C_1 is the absolute circulation surrounding the upper-layer vortex patch, and η_1 and A_1 represent the absolute vorticity and the area of the upper patch, respectively. Then from (3.14) and (3.15), we obtain

$$\frac{d\eta_1}{dt} = -\frac{2\pi\rho_s r_c c_D v_c^2 \eta_1}{\rho_1 f_0 D_1 A_1}.$$

Therefore, if we assume that the vertical potential temperature lapse rate is constant in time, a simple estimation of the PV change rate due to the absolute vorticity change would be

$$\frac{d(PV)}{dt} \approx -g\frac{d\eta_1}{dt}\frac{\partial\theta}{\partial p} = g\frac{2\pi\rho_s r_c c_D v_c^2 \eta_1}{r_1 f_0 D_1 A_1}\frac{\partial\theta}{\partial p}. \tag{3.16}$$

Calculating (3.16) with typical values of the parameters in the model (as used in chapter 4), we can estimate the PV change rate to be at most -1 PVU day^{-1}. (The maximum is estimated by using the initial model information, when the PV patch area A_1 is smallest, and by representing η_1 by an extreme value, f_0) This result suggests that this model does not overestimate the PV destruction rate in the upper troposphere due to the heating.

f. Scaling of the model

We choose physical scaling parameters such that the normalized governing equations can be described by only a few nondimensional parameters. To do this, the following scales are chosen:

• horizontal length scale $L = r_c$, which is the radius where the surface relative vorticity of the storm changes sign (a typical value is 500 km);

• horizontal velocity scale $U = \rho_s c_D v_c^2 / (\rho_1 f_0 D_1)$, which is the frictionally induced potential flow speed in the upper layer at $r_1 = r_c$ (a typical value is 1 m s^{-1}).

Then, by using the advective time scale (a typical value of 5 days), (3.9) and (3.10) can be expressed in nondimensional form as

$$[\frac{\partial}{\partial t} + (\chi + \mu)\frac{\partial}{\partial x} + \nu \frac{\partial}{\partial y}] q_1 + J(\Psi_1, q_1) = 0, \tag{3.17}$$

$$\frac{\partial}{\partial t} q_2 + J(\Psi_2, q_2) = 0, \tag{3.18}$$

where

$$q_1 = \nabla^2 \Psi_1 + \gamma^2 (\Psi_2 - \Psi_1) = \Pi_1 X_D(\mathbf{x}),$$

$$q_2 = \nabla^2 \Psi_2 + \varepsilon \gamma^2 (\Psi_1 - \Psi_2) = \Pi_2 \delta(\mathbf{x} - \mathbf{x}_p(t)),$$

and

$\Pi_1 = Q_1 r_c \rho_1 f_0 D_1 / (\rho_s c_D v_c^2)$: the nondimensional upper-layer potential vorticity jump,

$\Pi_2 = S_2 \rho_1 f_0 D_1 / (\rho_s c_D v_c^2 r_c) = 2\pi \rho_1 f_0 D_1 / (\rho_s c_D v_c)$: the nondimensional lower-layer vortex strength, where we have approximated the strength of the lower-layer hurricane vortex as $S_2 = 2\pi v_c r_c$,

$\gamma = r_c / L_R$: the ratio of the horizontal length scale to the radius of deformation,

$\chi = U_1 \rho_1 f_0 D_1 / (\rho_s c_D v_c^2)$: the nondimensional upper layer mean wind,

$\mu = (x - x_p)/r_1(x)$: the nondimensional zonal component of the potential flow,

$\nu = (y-y_p)/r_1(\mathbf{x})$: the nondimensional meridional component of the potential flow, where

$\mathbf{x}=(x,y)$, $\mathbf{x_p}=(x_p,y_p)$ and $r_1(\mathbf{x})=[(x-x_p)^2+(y-y_p)^2]^{1/2}$.

Equations (3.17) and (3.18) are the final forms of the governing equations. The behavior of the model is governed by the following five dimensionless parameters:

$$\varepsilon = \frac{D_1}{D_2},$$

$$\gamma = \frac{r_c f_0}{(gD_1\Delta\rho/\rho)^{1/2}},$$

$$\chi = \frac{U_1\rho_1 f_0 D_1}{\rho_s c_D v_c^2},$$

$$\Pi_1 = \frac{Q_1 r_c \rho_1 f_0 D_1}{\rho_s c_D v_c^2},$$

$$\Pi_2 = \frac{2\pi\rho_1 f_0 D_1}{\rho_s c_D v_c}.$$

In summary, the dynamics of such a system is completely controlled by the vortical flows associated with the upper-layer vortex patch and the lower-layer point vortex, the upper-layer potential flow (μ,ν) emanating from a mass source, and the mean shear flow (χ). The algorithm of this two-layer contour dynamical model is identical to that of Polvani et al. (1989), except that at each time step, the potential flow (μ,ν) and mean shear (χ) has to be added to the calculation of the velocity of each contour node in the upper layer.

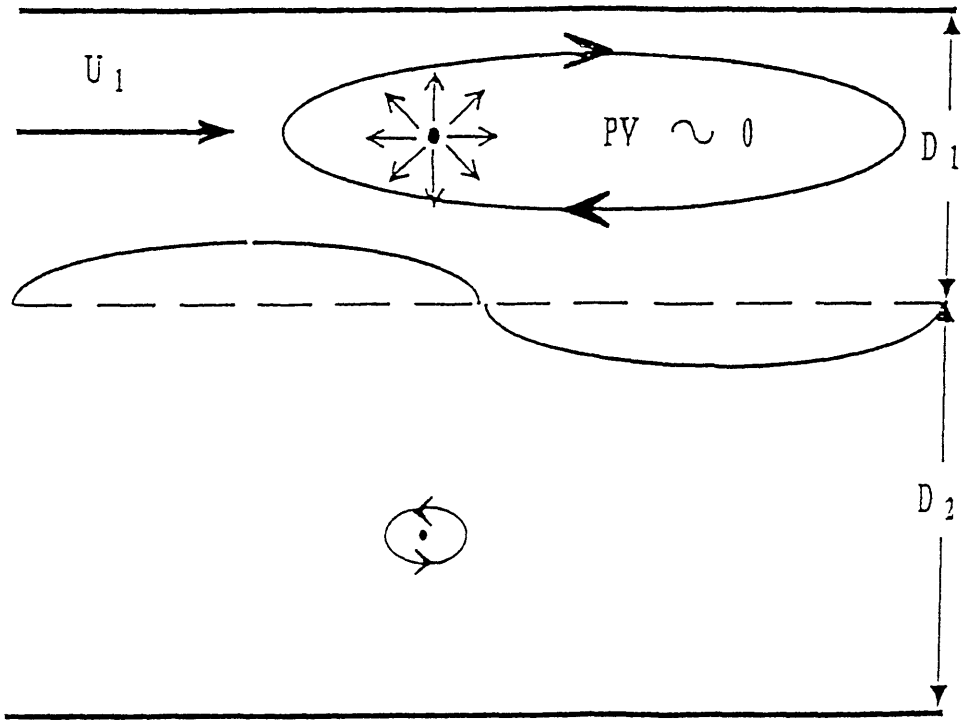

Figure 3.1 Illustration of the two-layer contour dynamic model.

4. Model results

a. Control experiments

We start our model integration by specifying the position of a point vortex in the lower layer, with a circular patch of zero potential vorticity in the upper layer, whose center is collocated with the surface vortex. The dimensionless radius of the initially circular contour of upper level potential vorticity patch is $r_n = r_i/r_c$. For convenience, only the NH case is studied.

The model is begun by specifying a lower point vortex whose strength, Π_2, is consistent with a vortex characterized by $r_c = 500$ km, $v_c = 10$ m s^{-1}, $D_1 = 2$ km, and an upper-layer vortex patch of radius $r_n = 0.3$ with a strength, Π_1, given by taking $Q_1 = -f_0$ (i.e., the anomaly has zero potential vorticity and the environment has potential vorticity f_0). We take the value of f_0 at 20^0 latitude, $c_D = 1\times10^{-3}$, and $\varepsilon = 0.25$. By choosing $\Delta\rho/\rho$ to be 0.05, which is equivalent to an atmosphere of the same vertical depth with uniform static stability $N^2 = 1\times10^{-4}$ s^{-2}, the value of γ is 0.79, and the corresponding values of Π_1 and Π_2 are 25 and 62.83.

The model starts with about 50 nodes equally distributed around the circular vortex. The number of these nodes increases with integration time, and may reach 2000 for complicated cases. There is one concern on the choice of the time step, that is, it is required that the position of the point vortex has to be always within the domain of the upper vortex patch. In other words, the advection of the mean shear on the uppershear side of the upper vortex patch can not be too fast, and has to be countered by the divergent potential flow. For efficiency, we choose the integration time step to be just small enough so that no numerical instability would occur. In general, a time step of 0.01 is found to be satisfactory, and is used in this study. Control experiments were performed by integrating the model to nondimensional time t = 4, with westerly vertical shear (χ) varying from 0 to

10. Beyond this time, the number of nodes sometimes become too large to be handled efficiently. In general, the vortex motion reaches a near quasi-steady or oscillatory state at about this time.

For the case with no vertical shear ($\chi = 0$), it is found, as expected, that the upper patch expands with time and remains circularly symmetric and that there is no lower vortex movement. The initial wind distributions in each layer are shown in Figure 4.1. It can be seen that the upper flow is anticyclonic and outward (with a maximum wind of about 3 m s^{-1}), and the lower-layer flow is cyclonic with a maximum wind of about 28 m s^{-1} at the grid closest to the point vortex's center. Figure 4.2 displays the evolution of the upper-layer flows in time. As the upper-layer vortex patch expands, the anticyclonic flow becomes stronger, and covers a larger area. At t = 4, the maximum anticyclonic flow has increased to nearly 17 ms^{-1}. The evolution of flows associated with the upper-layer vorticity patch in the lower layer (Fig. 4.3) indicates an weak, but strengthening anticyclonic flow symmetrically distributed surrounding the vortex center, so that no vortex drift is induced. The total flow field in the lower layer is similar to that shown in Figure 4.1b, though it has a slightly weaker intensity because of the projection of the anticyclonic flow from the upper layer vortex.

Next the case with weak shear is investigated, that is, $\chi = 1.25$ (this corresponds to an upper-layer mean wind of approximately 1.25 m s^{-1}). The evolution of the upper-level contour for this case is shown in Figure 4.4. It is found that the vortex patch expands and is advected downshear. Also, roll-up of the vortex patch occurs on the downshear side, essentially due to barotropic instability. The evolution of the vortex zonal and meridional drift velocity and total drift speed with time (Fig. 4.5a, b, and c) shows that the vortex drift is mainly meridional and increases with time. The induced zonal drift, though smaller in magnitude, is mainly associated with the roll-up of the vortex patch, which, after a certain integration time, is located eastward and southward of the lower vortex.

The time evolution of flow fields in the upper layer (a result of the sum of the mean shear, the divergent flow, and the flow associated with the upper-layer vorticity patch) is shown in Figure 4.6. The inclusion of mean shear breaks down the axisymmetry, and advects the vorticity patch to the east (downshear) side, thus inducing a southerly over the lower-layer vortex. An interesting question we may ask is that whether such vorticity and flow fields are realistic, or are they simply artifacts of the model? Comparing with the observations from Molinari (1992), it is clear that there exists an area of near-zero PV air above the downshear side of Hurricane Allen. A region of anticyclonic flow (Fig. 4.7) associated with that negative PV anomaly bears much resemblance to the flow field in our model (Figure 4.6). This suggests that our idealized model does represent some features in a real hurricane. The lower-layer flow fields associated with the upper vortex patch (Fig. 4.8) indicates how this flow advects the lower-layer vortex. For example, at the end of model integration (t=4), it contributes to a nearly 3 m s^{-1} northward movement of the lower vortex.

For cases with very little shear, for example, $\chi = 0.25$, the vortex patch simply rotates around the lower point vortex (Fig. 4.9). This can also be seen in the time evolution of the upper-layer flows (Fig. 4.10). The vortex drift velocity oscillates with time with an upper bound (Fig. 4.5a, b, and c), depending on the relative location of the vortex to the center of mass of the upper-layer vortex patch. The balanced flow in the lower layer associated with the upper vortex patch is indicated in Figure 4.11. It can be seen that near the end of the model integration, as the upper vortex patch bends itself to the south, more eastward vortex drift is found.

For cases with larger shear, for example, $\chi = 5$, the patch is rapidly advected downshear and becomes zonally elongated (Fig. 4.12). The low potential vorticity anomaly behaves more like a passive plume. Since the bulk of the upper vortex patch is far from the lower vortex, its influence on the lower vortex is limited, so that the induced vortex drift speed reaches a nearly quasi-steady value with increasing shear (Fig. 4.5a, b,

and c). In these cases, the elongation of the potential vorticity anomaly leads to barotropic instability and the filamentation in the middle of the contour strip. However, strong roll-up of the contour occurs at the downshear end of the anomaly. The upper-layer flow fields (Figure 4.13) indicates that an outflow jet exists to the northeast of the lower-layer vortex, and the main anticyclonic flow is advected to the downshear side. The evolution of the lower-layer flow field associated with the upper vortex (Fig. 4.14) demonstrates that the influence of the upper vortex on the point vortex is a consistent northeastward motion.

The trajectories of the lower vortex in the aforementioned three experiments are shown in Fig. 4.5d. In all cases, distinct northward vortex drifts associated with different magnitudes of the mean westerly shears are found, as expected. Also, the drift in the zonal direction is a function of the background shear, that is, more eastward drift is associated with weaker shear. Figure 4.15 displays the maximum total drift speed as a function of the ambient shear. The vortex drift initially increases as the shear increases, and there exists an optimal shear (about $\chi = 1.25$ for these parameter values) that maximizes the vortex drift. The maximum dimensional drift speed (approximately 3 m s^{-1}) in this case is comparable in magnitude with that associated with β drift (cf. Chan and Williams 1987). Above that optimal shear, the drift speed decreases with increasing shear and approaches a constant. This result clearly indicates that upper-tropospheric potential vorticity distributions, which are modified by the upper hurricane outflow, can be important in influencing storm motion.

b. Other sensitivity experiments

1) sensitivity to ε

We have performed two sets of experiments to determine the sensitivity of the vortex motion to the thickness ratio (ε) of the two layers. The first set of experiments was conducted by choosing ε to be 1, with χ varying from 0 to 10. Figure 4.16 show the

evolution with time of the zonal vortex drift velocity, the meridional vortex drift velocity, the total vortex drift speed, and the trajectories of the lower vortex for cases with χ = 1, 3 and 5. For relatively weak shear (χ=1), the induced drift speed oscillates with time. The vortex moves northeastward initially, then moves southeastward with a cycloid-like trajectory. For other cases, the result behaves like the control experiments, except that as more drift is induced, the "optimal shear" (see Fig. 4.18) is shifted to higher values, and the induced drift does not drop much when the ambient shear increases above the "optimal shear." The second set of experiments was performed by choosing ε to be 0.5. The results (Fig. 4.17) are consistent with the control experiments, with a moderate increase in vortex drift.

The variation of the maximum induced drift speed and its velocity vector with parameters χ and ε (Fig. 4.18) shows that both the maximum induced vortex speed and "optimal shear" increase with the value of ε. These results suggest that the drift induced by the interaction effect is quite sensitive to the thickness ratio of the two layers. What happens physically is that increases of ε strengthen the influence of the upper layer potential vorticity anomaly on the lower-layer vortex, and thus induce more vortex movement. In Figure 4.18b, there is a certain range of the parameters where the maximum induced vortex drift vector points southeastward. These parameters are mainly in the regimes in which the upper PV patch wavers around the point vortex, and causes an oscillatory drift.

2) Sensitivity to γ

Two other experiments are performed to test the model sensitivity to the ratio of the horizontal length scale to the radius of deformation (γ). We run the model with γ equal to 1 and 0.5, respectively, with varying values of χ. The evolution with time of the zonal vortex drift velocity, the meridional vortex drift velocity, the total vortex drift speed, and

the trajectories of the lower vortex for cases with χ = 0.25, 1.25 and 5 are shown in Figures 4.19 (for γ = 0.5) and 4.20 (for γ = 1). The results are very similar to those in the control experiments (Fig. 4.5). Also, the variations of the maximum induced drift speed and its velocity vector with the parameters χ and γ are shown in Figure 4.21. The result suggests that the maximum vortex drift is relatively insensitive to the parameter γ. Though the parameter γ reflects the degrees to which the upper and lower layers are coupled, its quantitative influence on vortex motion appears as a coefficient in the Modified Bessel Function of the second kind, of order one (K_1), whose value is quite insensitive to the choice of γ.

3) Sensitivity to Π_1, Π_2, and r_n

Final experiments were performed to test the sensitivity to the parameters Π_1 (nondimensional potential vorticity jump of the upper-layer vortex patch), Π_2 (nondimensional strength of the point vortex), and r_n (initial dimensionless radius of the upper patch).

The magnitude of lower vortex strength (Π_2) indirectly influences vortex motion through the feedback process of its effect on the evolution of the upper-layer vortex patch. For example, for smaller (larger) values of Π_2, a less (more) cyclonic flow is induced in the upper layer, and therefore the upper vortex patch tends to deform more toward the south (north). This effect is especially obvious for cases with weaker shear (smaller χ). The more the upper vortex patch bends toward the south, the more eastward drift the lower vortex would have. Experiments are conducted with Π_2 half of its value in the control experiments. The comparison of the evolution of the new vortex movement (Figure 4.22) with that (Fig. 4.5) in the control experiments suggests that the main effect of the initial vortex strength (Π_2) on the vortex displacement is mainly in the zonal direction, but not in

the meridional direction. However, as the mean shear is increased to a higher value (e.g., $\chi = 5$), the vortex movement becomes rather insensitive to the value of Π_2.

Experiments are also performed by doubling and halving the value of Π_1. The value of Π_1 influences vortex motion in two ways: first, it directly and linearly affects vortex motion through its strength; second, it affects the evolution of the upper patch that feeds back onto vortex drift. For example, as Π_1 is decreased, the upper patch becomes dynamically more passive, and its self-advection effect is weaker. Hence, the upper patch is mainly advected downshear, with less contour deformed toward the south side due to its own anticyclonic flow. Then, the vortex motion has less drift toward the east. This is shown in the vortex track positions in Figure 4.23d. In addition, it is also found (e.g., Fig. 4.23a, b, and c) that an initial upper vortex patch with smaller (higher) potential vorticity jump tends to have less (more) vortex drift. This relation is nearly linear. This result indicates, as one would expect, that a hurricane surmounted by a stronger(weaker) negative potential vorticity anomaly would experience more (less) such interaction effect.

Finally, we have also checked the sensitivity of the model results to r_n. Our results indicate that an upper vortex patch with different initial area has little influence on the eventual movement of the vortex. The only concern is that when r_n is very small, there may be a rather large initial potential flow advecting the nodes outward in the beginning; however, as long as the integration time step is small enough, it does not cause any problem.

c. Comparison with other baroclinic models

As this work was carried out, other baroclinic models with different idealized conditions were also conducted in order to understand the effects of vertical structure and vertical shear on hurricane motion (Flatau and Schubert 1991; Wang and Li 1992; Shapiro 1992). In this section, we shall review those works and compare our work with those.

Wang and Li constructed a ten-layer primitive equation model to study the influence of the vertical structure on the movement of an initially isolated symmetric vortex on a β plane. They found that the cyclonic vortex remains coherent in the lower and middle troposphere due to the secondary circulations between layers, and that the vortex moves poleward and westward, similar to the movement of a barotropic vortex on a β plane. However, the anticyclonic vortex moved equatorward and westward, and couldn't remain vertically coupled with the lower-level cyclonic portion. This finding reflects our second hypothesis about the "β" effect on the upper anticyclone, though Wang and Li argued that the weak anticyclonic circulation in the far-field outside the initial vortex circle has an insignificant effect on vortex movement. However, since Wang and Li used a dry model that does not take into account the diabatic heating in the hurricane center, this model poorly resembles a baroclinic hurricane.

Flatau and Schubert studied hurricane motion using a three-dimensional, semi-spectral, primitive equation model. The mechanisms they propose are identical to ours: when a vortex pair is tilted, interaction between upper and lower level vorticity anomalies lead to vortex propagation relative to the steering flow. In agreement with our findings, they showed that, in the vertically sheared environment on the f plane, propagation due to interaction between the vortex pair is comparable to motion caused by the β effect. However, their results of experiments on the β plane indicates that the baroclinic effects only slightly modify the vortex motion, and the baroclinic vortex moves poleward and westward as predicted by barotropic models. Comparing our model with Flatau and Schubert's, the main difference is on how the moist processes are represented. We think it is a drawback of their model that the heat source is arbitrarily specified rather than being diagnosed to maintain the lower cyclonic and upper anticyclonic structure vortex.

By including the convective heating and momentum fluxes, Shapiro (1992) conducted a three-layer model simulation to evaluate the asymmetric evolution of a hurricane and its interaction with the large-scale environment. He showed that the

advection of potential vorticity by the cyclonic vortex circulation in the middle layer tends to induce an asymmetric potential vorticity field that is similar to the formation of β gyres in a barotropic model. This asymmetric circulation advects the middle-layer vortex towards the northwest. The diabatic heating redistributes the potential vorticity anomalies in the vertical direction and the convective momentum flux deposits some positive vorticity in the upper layer near the hurricane center. The outer upper-layer anticyclonic flow creates other potential vorticity gyres in the opposite sense as those in the middle layer. However, the effect that the upper-layer gyres advect the vortex toward the south is much weaker.

When a mean westerly shear is included in the model, it introduces a reversed (southward) potential vorticity gradient in the middle layer. Consequently, the middle-layer vortex moves towards the southeast at an average speed of about 0.9 ms^{-1}. Shapiro also indicated that the existence of ambient westerly shear advects the upper-layer negative potential vorticity anomaly downshear and thus induces an anticyclonic anomaly that advects the middle-layer vortex northward. Shapiro concluded that this effect is secondary to the β effect. Our results, however, suggest that the background shear can be important in causing the hurricane movement, though we have excluded the influence of any background potential vorticity gradient.

The fact that our model is an idealized one does not mean it only represents an ad hoc simplification. Indeed we were motivated in part by the observation that the PV gradients in the subtropical troposphere are much weaker than one would expect based on β, and in part by the legitimate desire to examine the effects of vertical shear in isolation. Our philosophy differs from Shapiro in that we take the PV distribution to be fundamental and the wind distribution to be incidental. In particular, we do not see any evidence for reversed PV gradients of the kind used by Shapiro.

Shapiro has stressed the importance of an inner cyclone at upper levels by including the vertical momentum transport in the model. Both from first principles and from results of numerical modelling (e.g. Rotunno and Emanuel 1987) it is clear that the potential

vorticity is nearly zero throughout the upper portion of the storm. This is not at all inconsistent with the presence of a cyclonic vertical component of relative vorticity at upper levels, as is also observed in the same simulations. (The anticyclonic part enters because of the relatively large slopes of θ surfaces, aloft near the core of hurricanes.) From the standpoint of invertibility, it is the PV that counts. Also, we are suspicious of any result that depends on cumulus momentum transport when both observations and fundamental theory are undecided even as to the sign of the transport.

d. Summary

In this chapter, the results from our modelling work have been presented. This work is treated as an initial value problem. The model is integrated with an initially circular vortex patch in the upper layer, with a lower-layer point vortex at its center. The interaction between the two vortices in a sheared environment is studied in order to understand the effect of the background shear and the negative PV anomaly, diabatically generated by the hurricane, on storm movement. Experiments with different values of dimensionless parameters in the model are also performed.

Our result shows distinct northward vortex drifts under mean westerly shears. This support our hypothesis that the Northern Hemisphere tropical cyclones tend to drift relative to the mean flow is a direction to the left of the background shear. It is indicated that the existence of the ambient vertical shear (χ) plays an important role for the vortex interaction, and an optimum background shear that maximizes the vortex motion is found. It is also demonstrated that such a drift is as strong as the β effect predicted in barotropic numerical models. This simplified model can produce the hurricane outflow jet. This study also suggests that the modification of upper-tropospheric potential vorticity distributions by hurricane outflow may play an important role in the evolution of cyclone motion.

The sensitivity experiments show that the thickness ratio between the two layers (ε) and the intensity of the upper vortex (Π_1) are most important for the vortex drift. The effects of the ratio of the horizontal length scale to the radius of deformation (γ) and the point vortex strength (Π_2) are secondary.

Finally, we also make comparisons between our model and some other models (Flatau and Schubert 1991; Wang and Li 1992; Shapiro 1992), which examine similar problems. The differences between these models are also discussed. It is stressed that our model, though simple, does include all the essential physical mechanisms we wish to understand, and it clearly portrays a picture of our fundamental ideas.

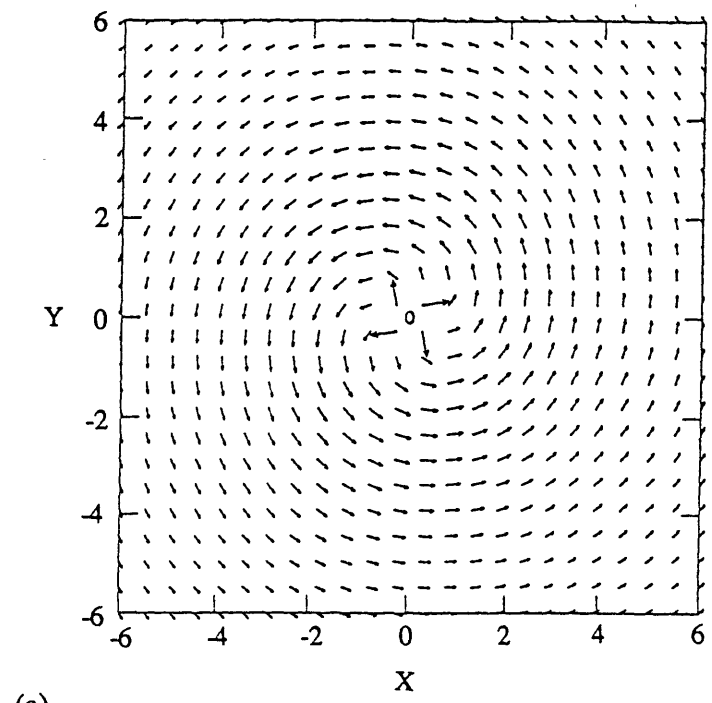

(a)

0.348E+01
MAXIMUM VECTOR

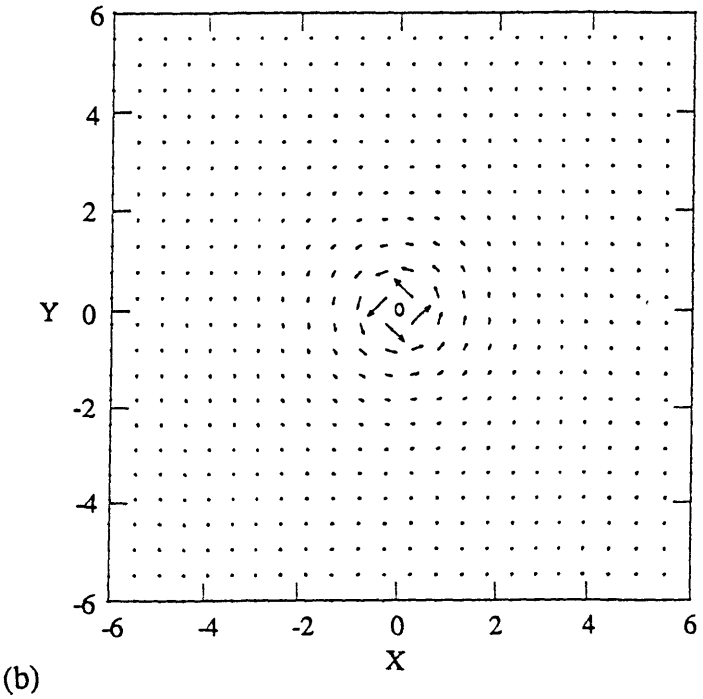

(b)

0.278E+02
MAXIMUM VECTOR

Figure 4.1 (a) Initial upper-layer wind fields, and (b) the initial lower-layer wind fields for ε=0.25, γ=0.79, and χ=0. The lower vortex is located in the center and is shown as "o." One unit length in the domain corresponds to 500 km.

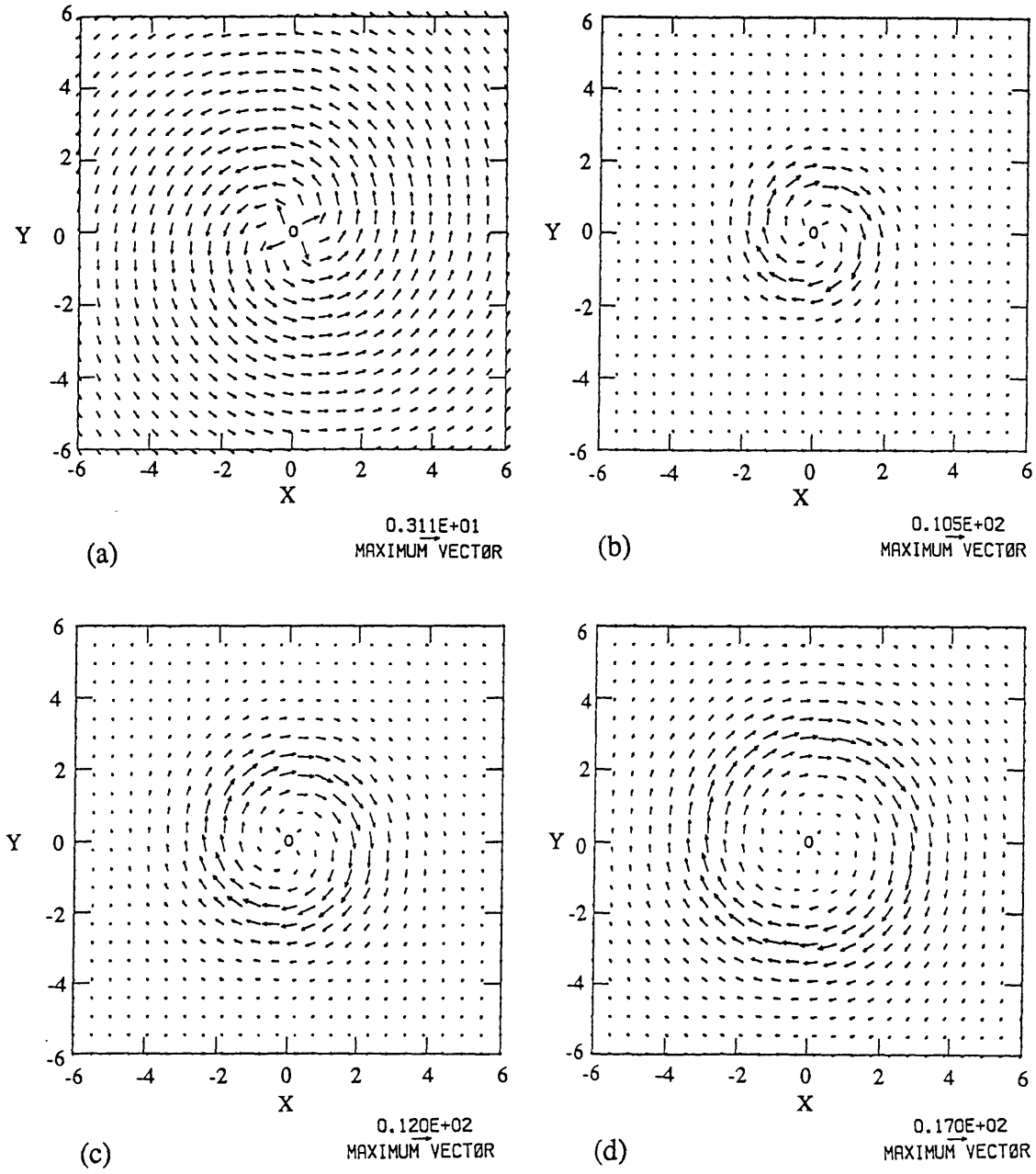

Figure 4.2 Time evolution of the upper-layer wind fields for ε=0.25, γ=0.79, and χ=0. (a) t=0, (b) t=1, (c) t=2, and (d) t=4. The lower vortex is located in the center and is shown as "o." One unit length in the domain corresponds to 500 km.

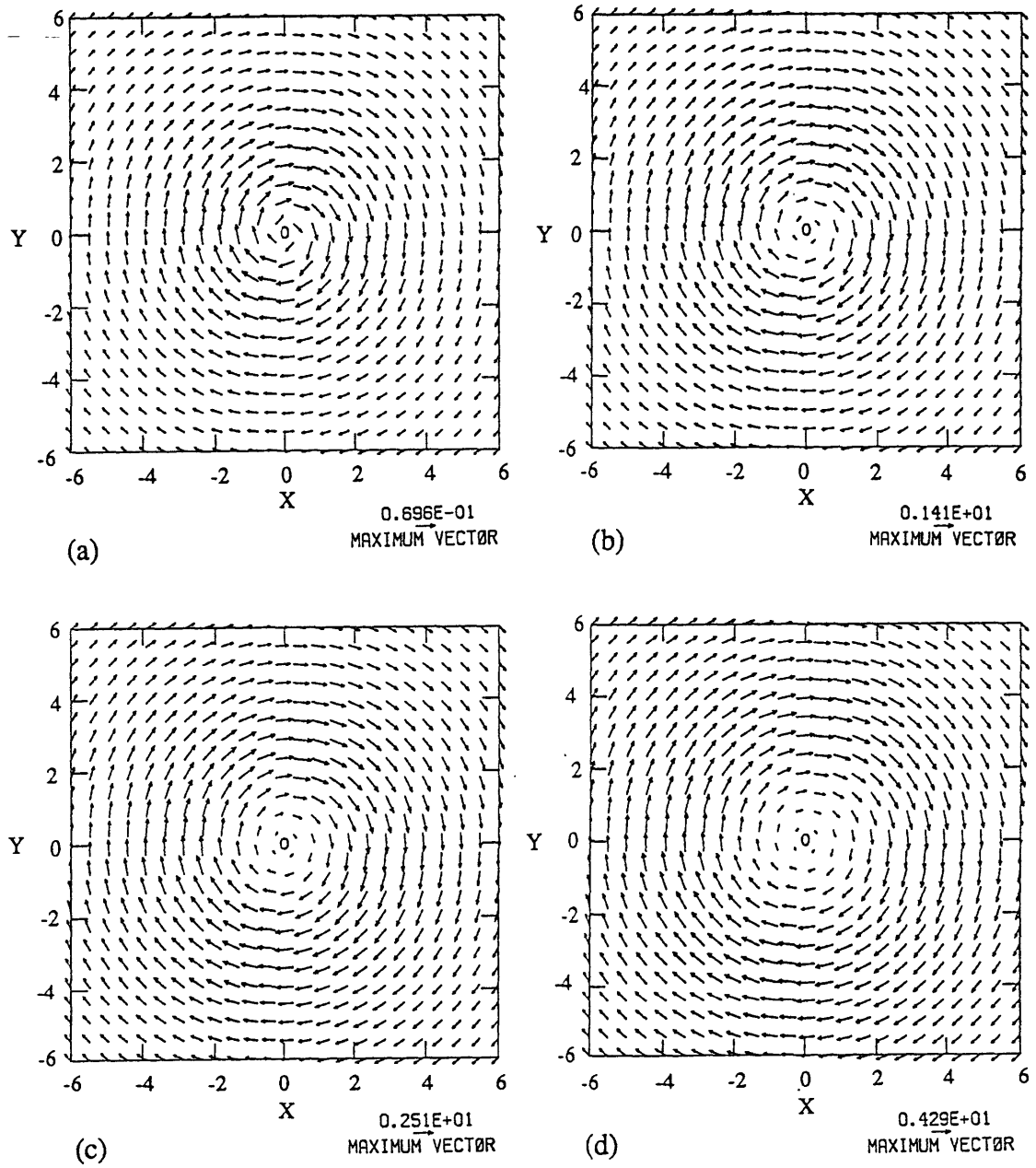

Figure 4.3 Time evolution of the lower-layer wind fields associated with the upper vortex patch for ε=0.25, γ=0.79, and χ=0. (a) t=0, (b) t=1, (c) t=2, and (d) t=4. The lower vortex is located in the center and is shown as "o." One unit length in the domain corresponds to 500 km.

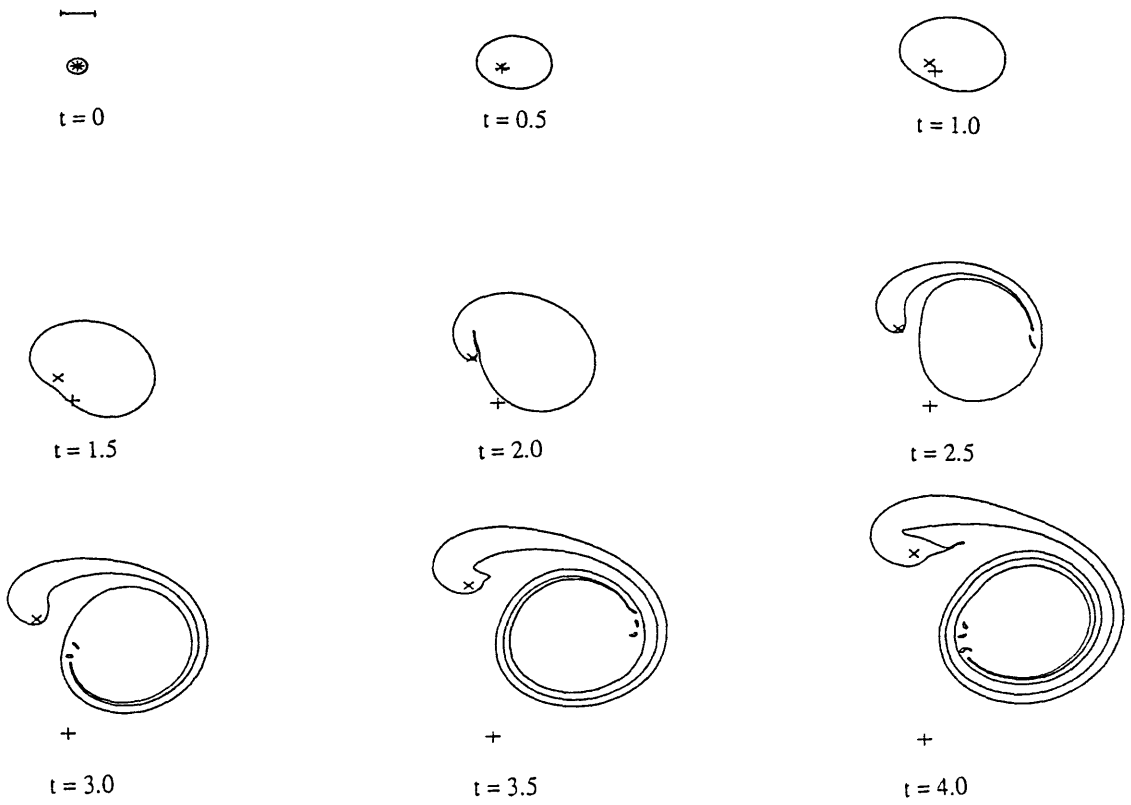

Figure 4.4 Time evolution of the upper-layer vortex patch for ε=0.25, γ=0.79, and χ=1.25. The lower-layer point vortex is shown as "x." The initial position of the point vortex is indicated as "+." The time interval between each plot is 0.5. The unit length scale (500 km) is shown in the upper left corner.

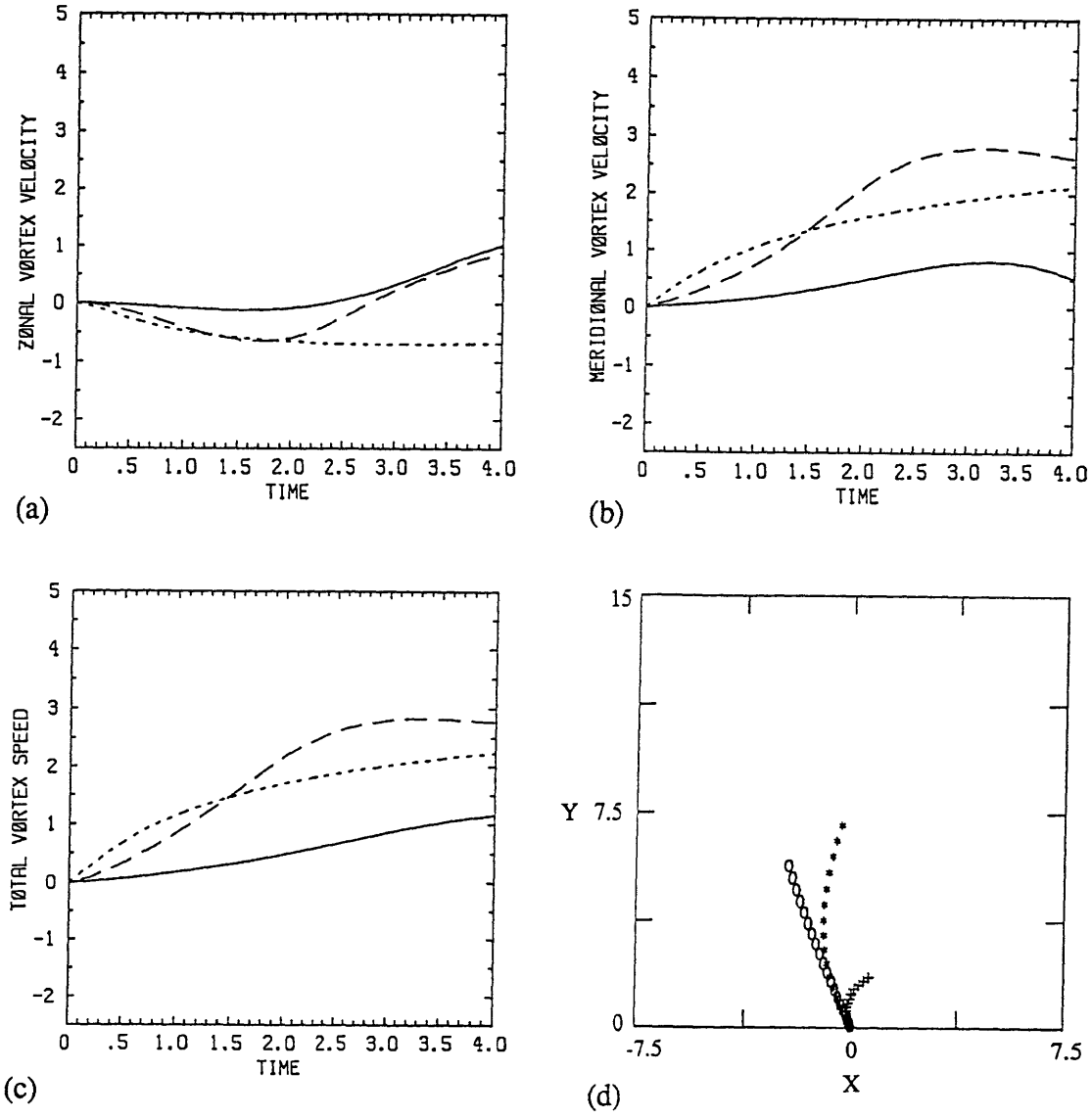

Figure 4.5 Time evolution of the induced lower-layer vortex (a) zonal velocity, (b) meridional velocity, and (c) total speed for ε=0.25, γ=0.79, and χ=0.25 (solid line); for χ=1.25 (long-dashed line); and for χ=5 (short-dashed line). (d) Trajectories (units of 500 km) of the lower-layer vortex for χ=0.25 (shown as "+") ; χ=1.25 (shown as "*"); and χ=5 (shown as "o").

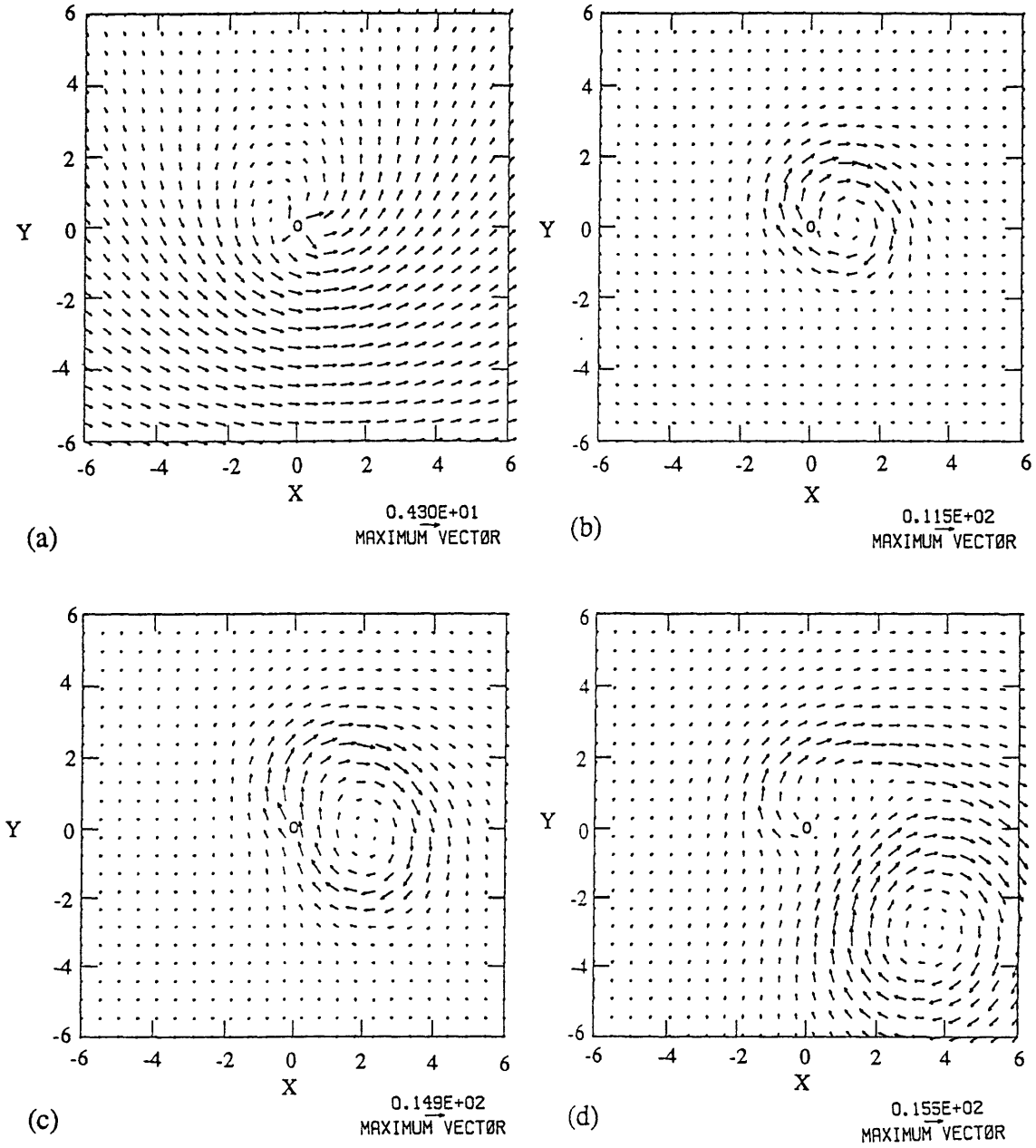

Figure 4.6 Time evolution of the upper-layer wind fields for ε=0.25, γ=0.79, and χ=1.25. (a) t=0, (b) t=1, (c) t=2, and (d) t=4. The lower vortex is located in the center and is shown as "o." One unit length in the domain corresponds to 500 km.

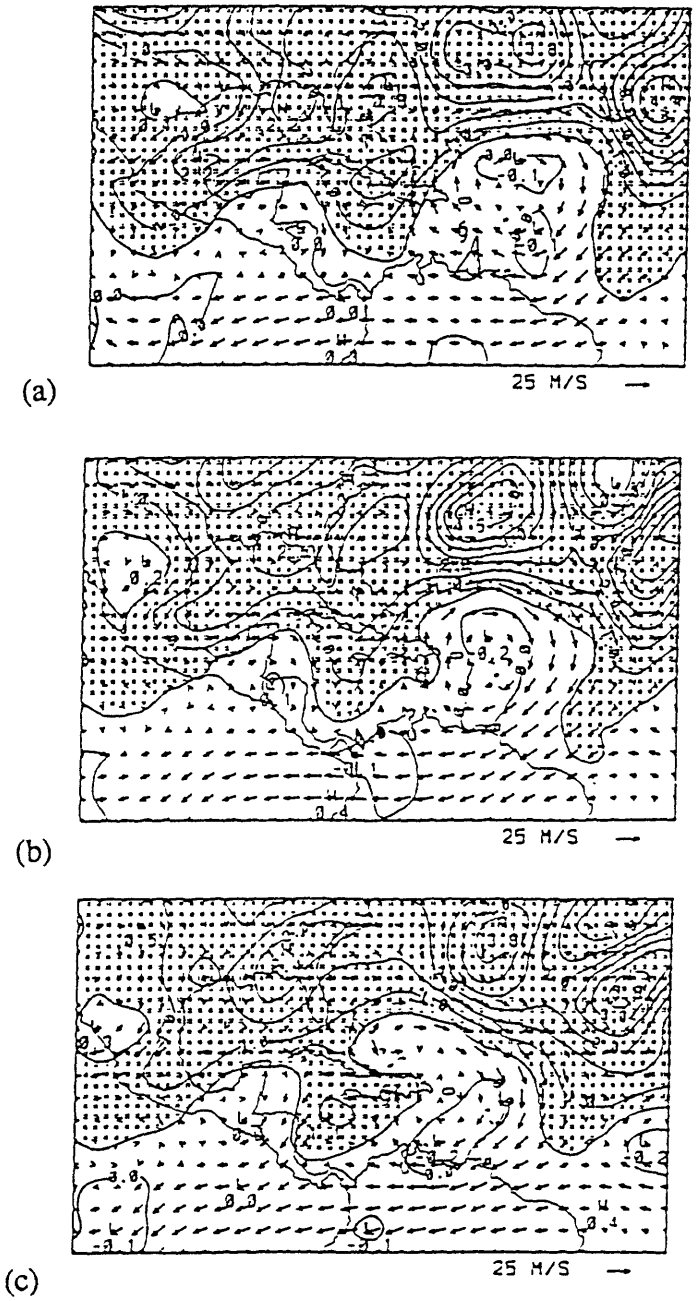

Figure 4.7 Isentropic potential vorticity at =350 K on (a) 0000 UTC 5 August, (b) 1200 UTC 5 August, and (c) 0000 UTC 6 August 1980. Values greater than 0.5 PVU units are shaded. Hurricane Allen is shown by the tropical storm symbol. (Molinari, 1992.)

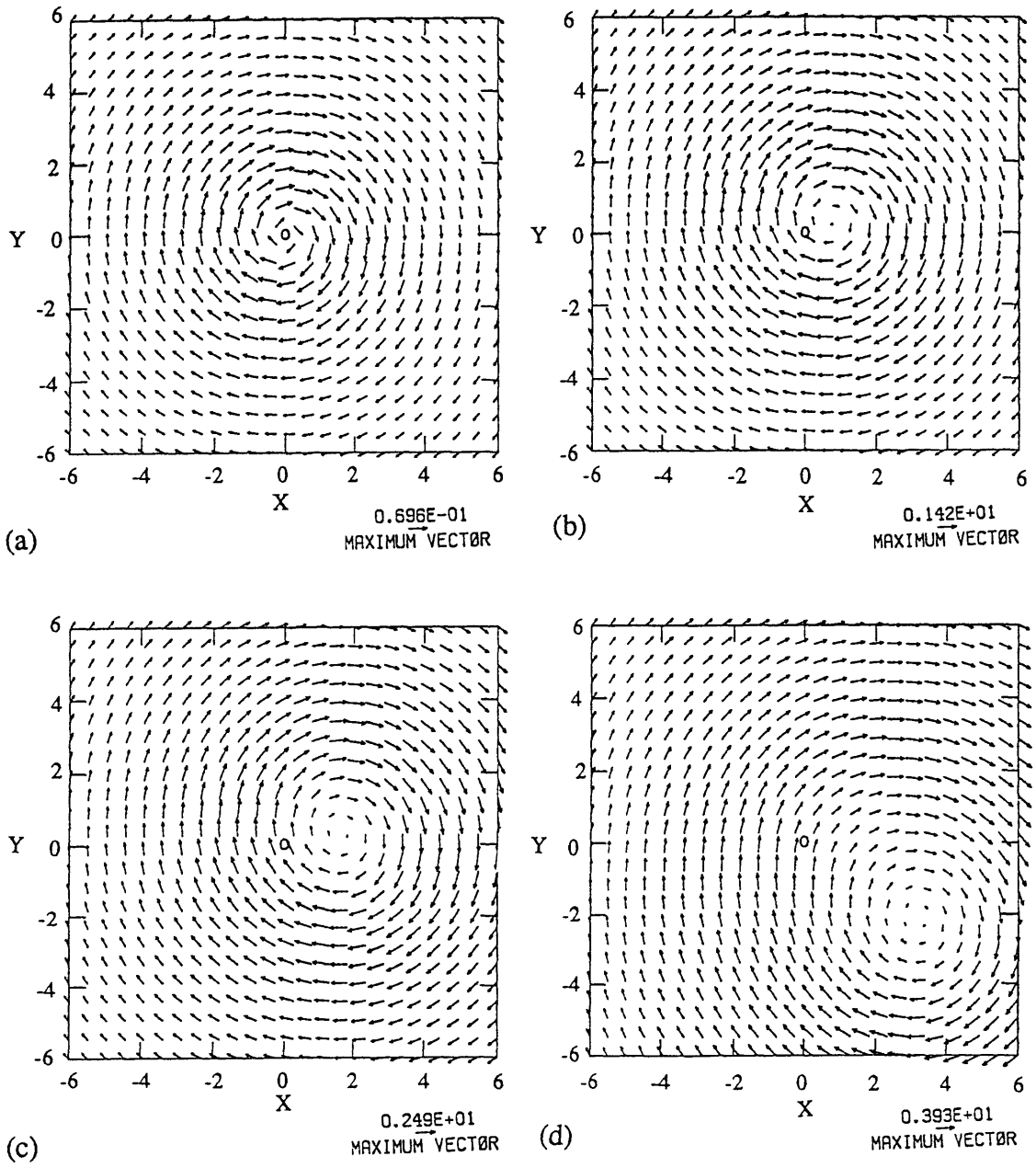

Figure 4.8 Time evolution of the lower-layer wind fields associated with the upper vortex patch for ε=0.25, γ=0.79, and χ=1.25. (a) t=0, (b) t=1, (c) t=2, and (d) t=4. The lower vortex is located in the center and is shown as "o." One unit length in the domain corresponds to 500 km.

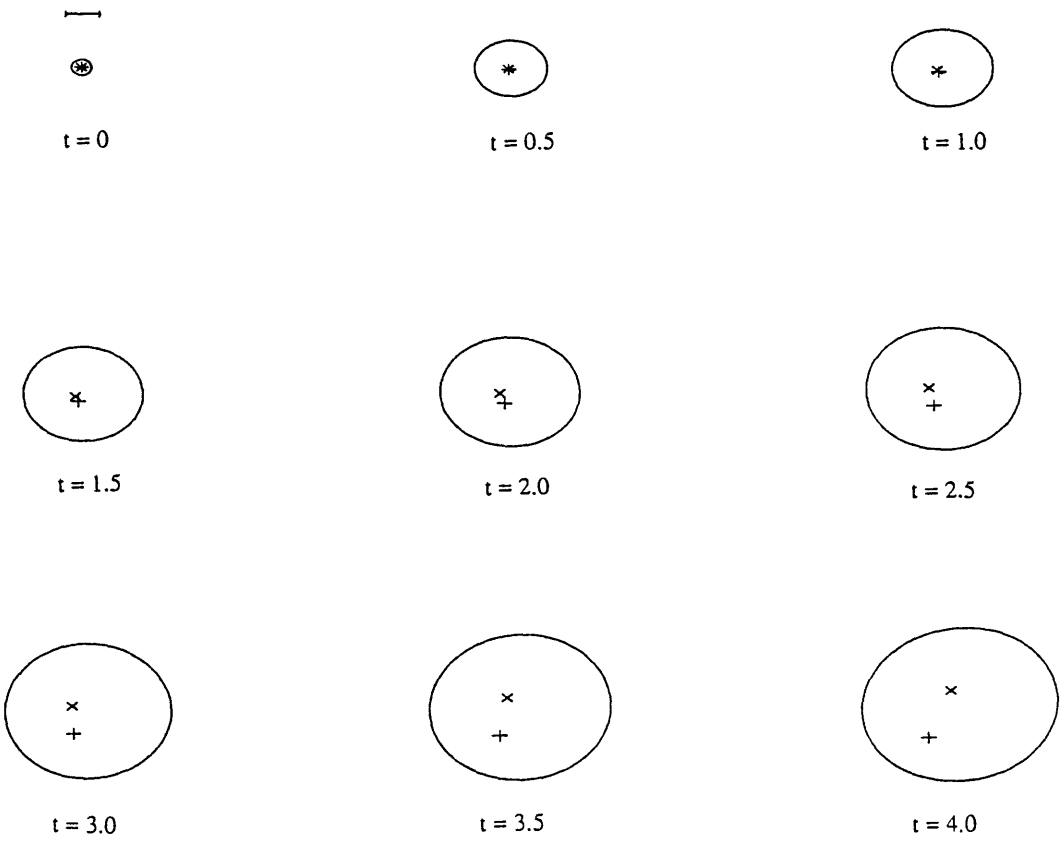

Figure 4.9 Time evolution of the upper-layer vortex patch for ε=0.25, γ=0.79, and χ=0.25. The lower-layer point vortex is shown as "×." The initial position of the point vortex is indicated as "+." The time interval between each plot is 0.5. The unit length scale (500 km) is shown in the upper left corner.

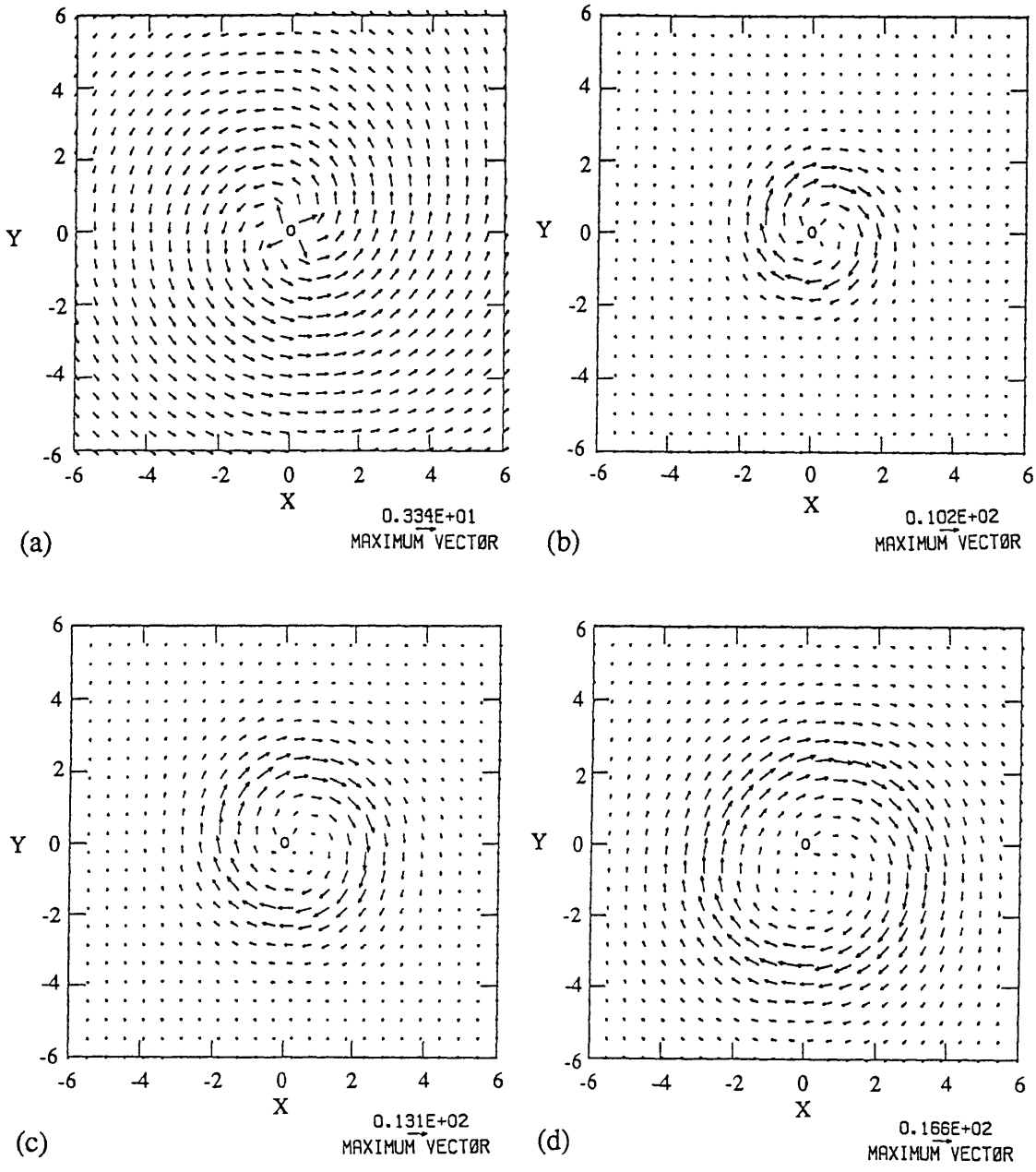

Figure 4.10 Time evolution of the upper-layer wind fields for ε=0.25, γ=0.79, and χ=0.25. (a) t=0, (b) t=1, (c) t=2, and (d) t=4. The lower vortex is located in the center and is shown as "o." One unit length in the domain corresponds to 500 km.

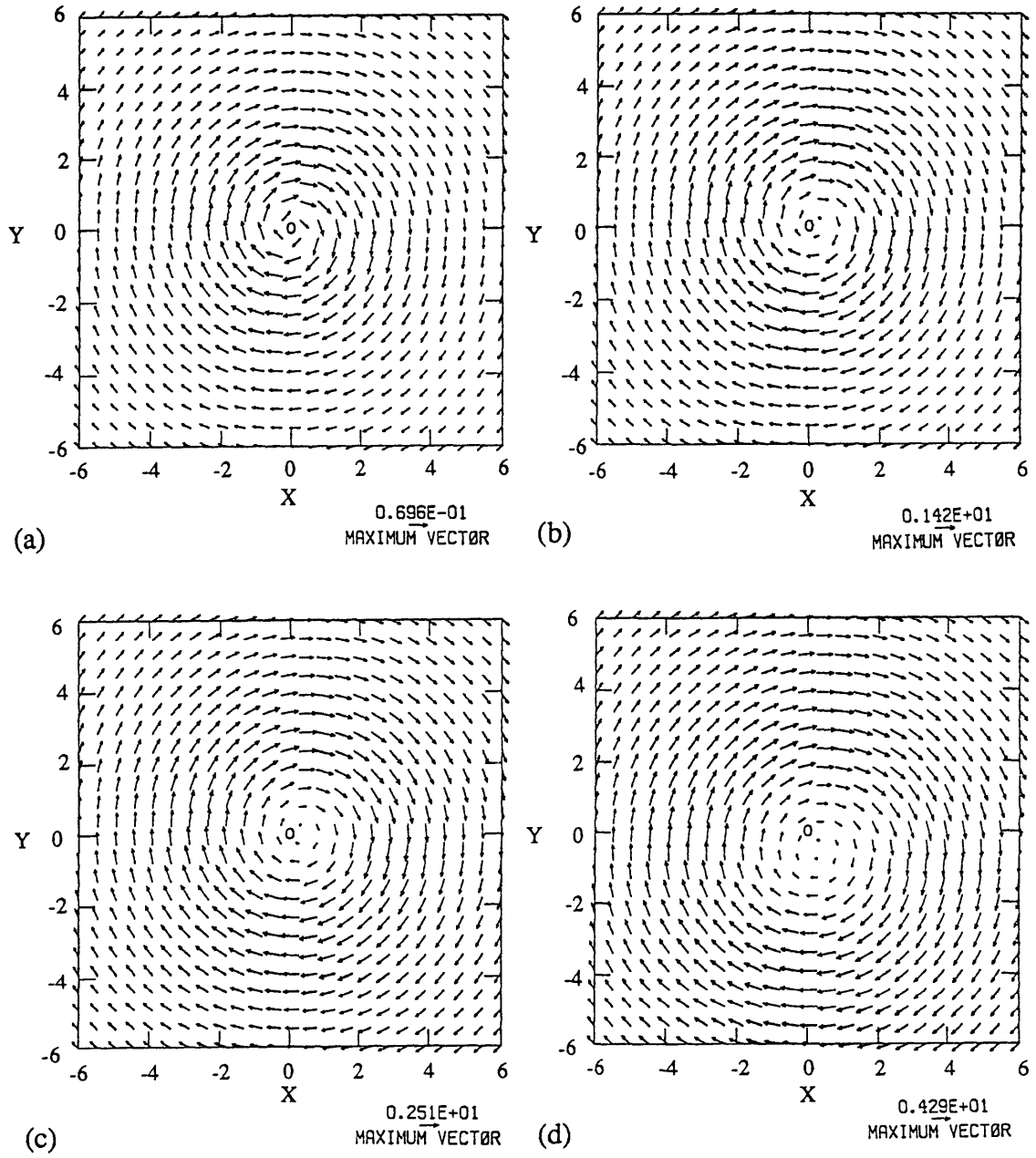

Figure 4.11 Time evolution of the lower-layer wind fields associated with the upper vortex patch for ε=0.25, γ=0.79, and χ=0.25. (a) t=0, (b) t=1, (c) t=2, and (d) t=4. The lower vortex is located in the center and is shown as "o." One unit length in the domain corresponds to 500 km.

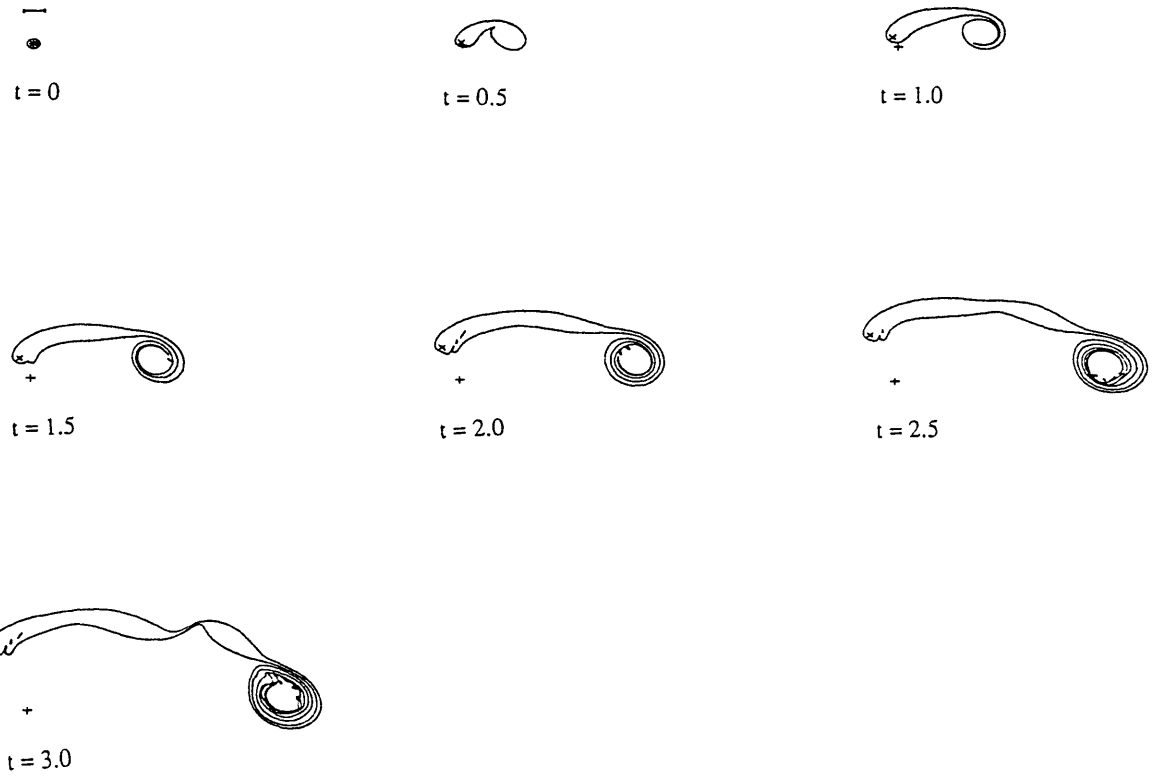

Figure 4.12 Time evolution of the upper-layer vortex patch for ε=0.25, γ=0.79, and χ=5. The lower-layer point vortex is shown as "×." The initial position of the point vortex is indicated as "+." The time interval between each plot is 0.5. The unit length scale (500 km) is shown in the upper left corner.

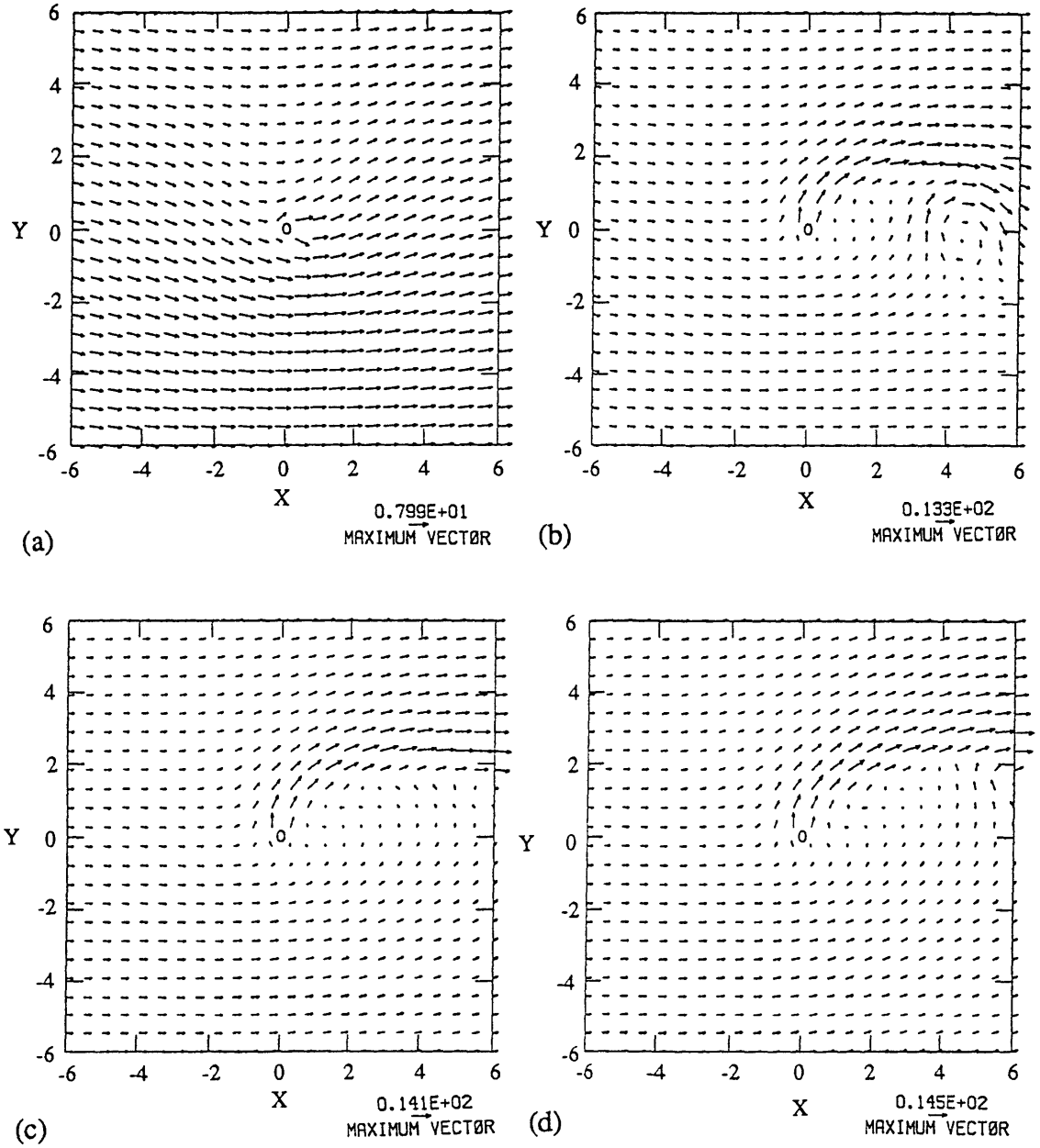

Figure 4.13 Time evolution of the upper-layer wind fields for ε=0.25, γ=0.79, and χ=5. (a) t=0, (b) t=1, (c) t=2, and (d) t=4. The lower vortex is located in the center and is shown as "o." One unit length in the domain corresponds to 500 km.

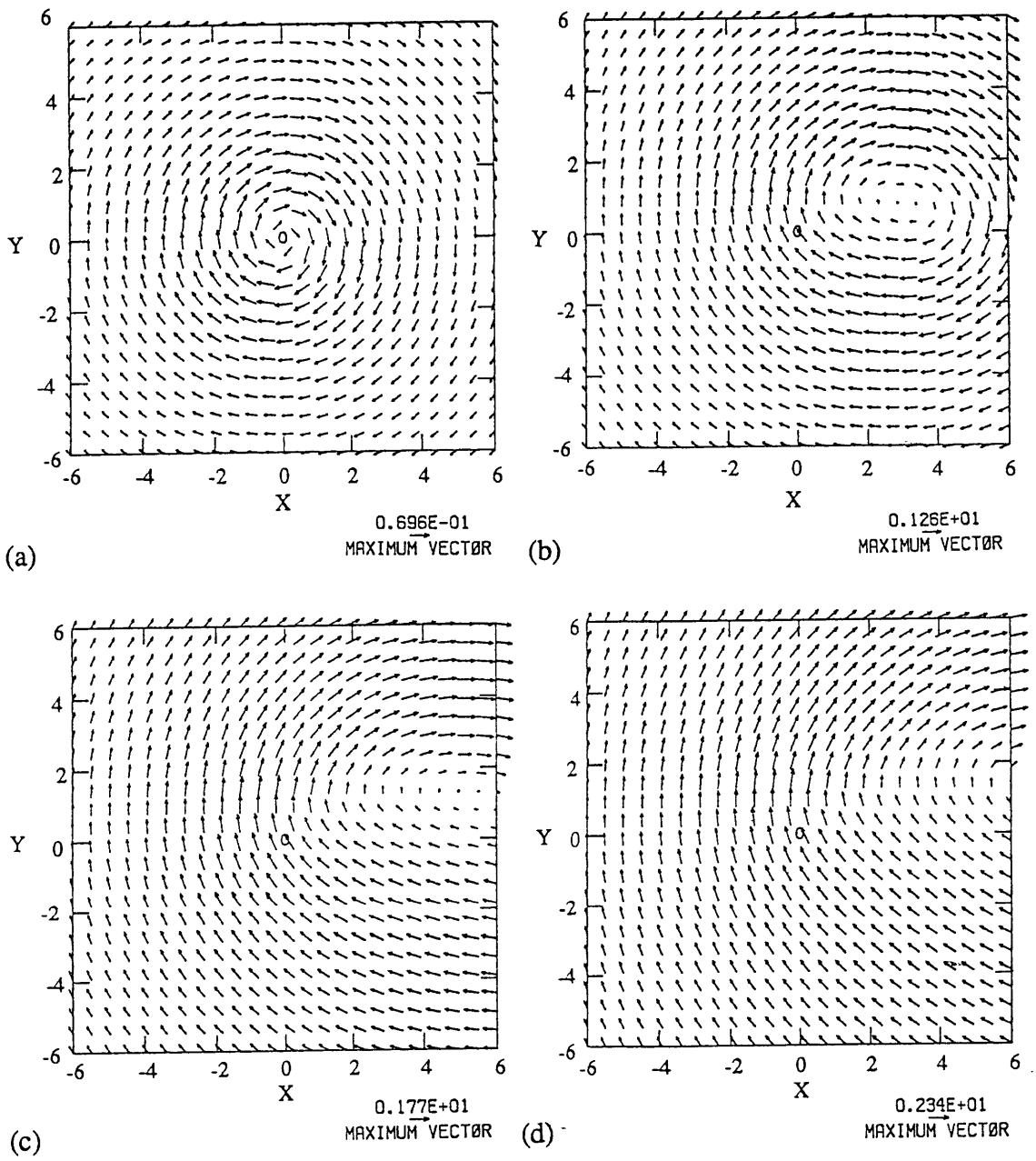

Figure 4.14 Time evolution of the lower-layer wind fields associated with the upper vortex patch for ε=0.25, γ=0.79, and χ=5. (a) t=0, (b) t=1, (c) t=2, and (d) t=4. The lower vortex is located in the center and is shown as "o." One unit length in the domain corresponds to 500 km.

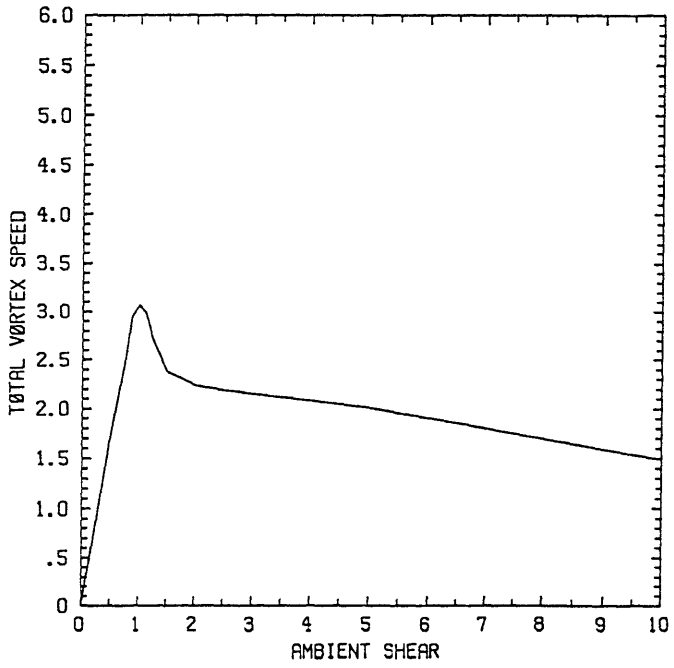

Figure 4.15 Relation between the maximum induced vortex speed and the magnitude of the vertical shears (χ) for ε=0.25 and γ=0.79.

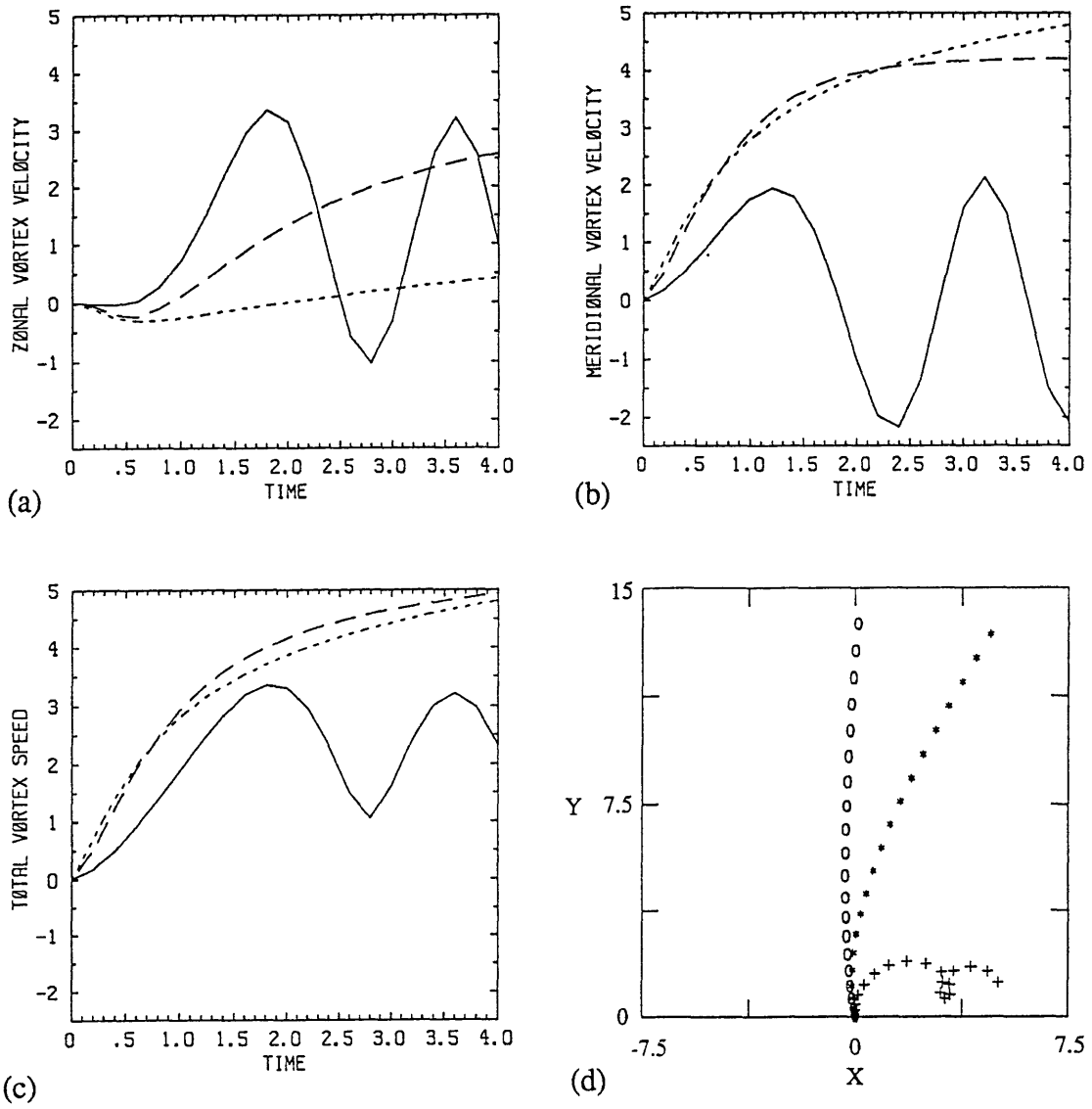

Figure 4.16 Time evolution of the induced lower-layer vortex (a) zonal velocity, (b) meridional velocity, and (c) total speed for ε=1, γ=0.79, and χ=1 (solid line); for χ=3 (long-dashed line); and for χ=5 (short-dashed line). (d) Trajectories (units of 500 km) of the lower-layer vortex for χ=1 (shown as "+") ; χ=3 (shown as "*"); and χ=5 (shown as "o").

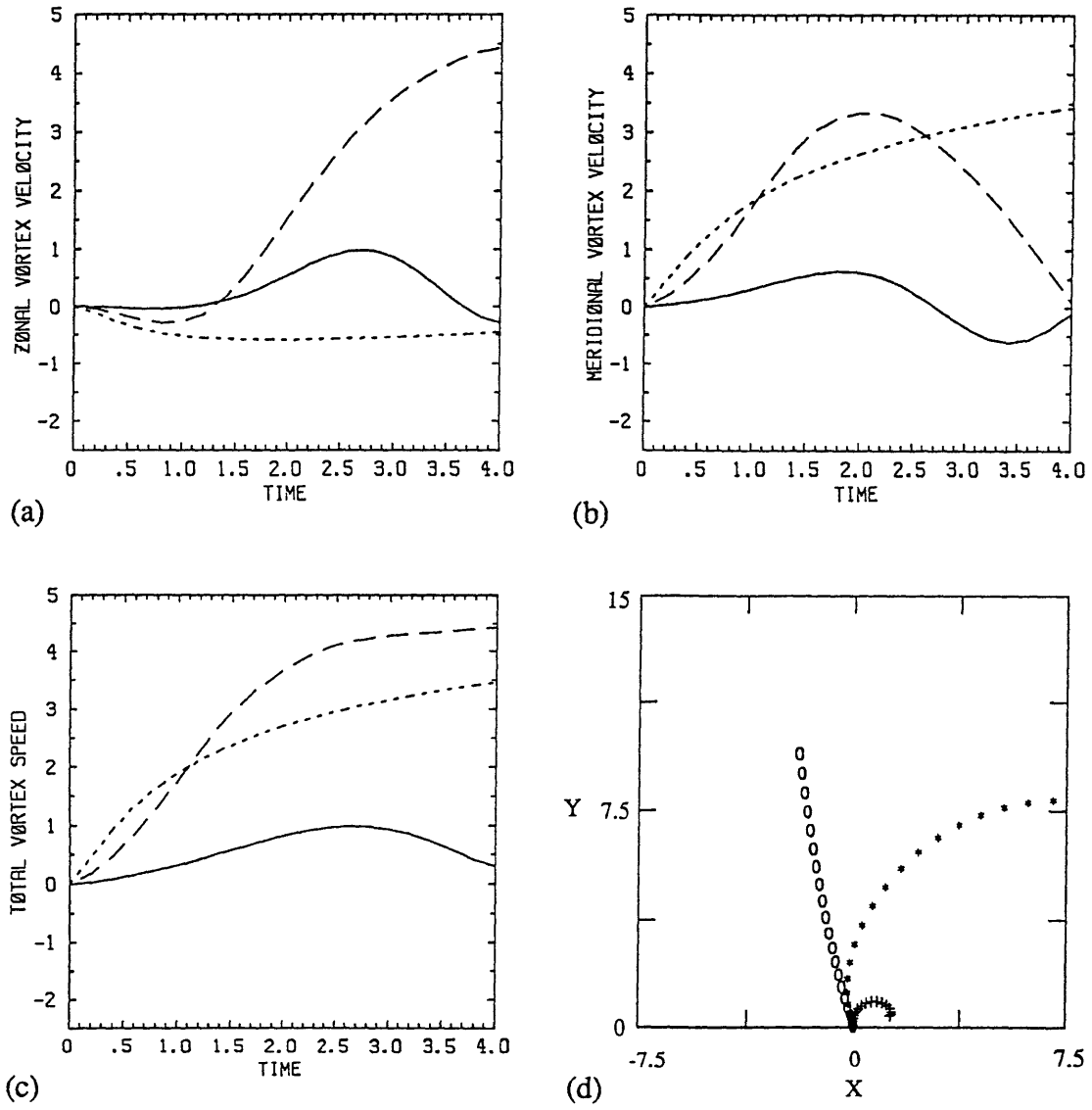

Figure 4.17 Time evolution of the induced lower-layer vortex (a) zonal velocity, (b) meridional velocity, and (c) total speed for ε=0.5, γ=0.79, and χ=0.25 (solid line); for χ=1.25 (long-dashed line); and for χ=5 (short-dashed line). (d) Trajectories (units of 500 km) of the lower-layer vortex for χ=0.25 (shown as "+") ; χ=1.25 (shown as "*"); and χ=5 (shown as "o").

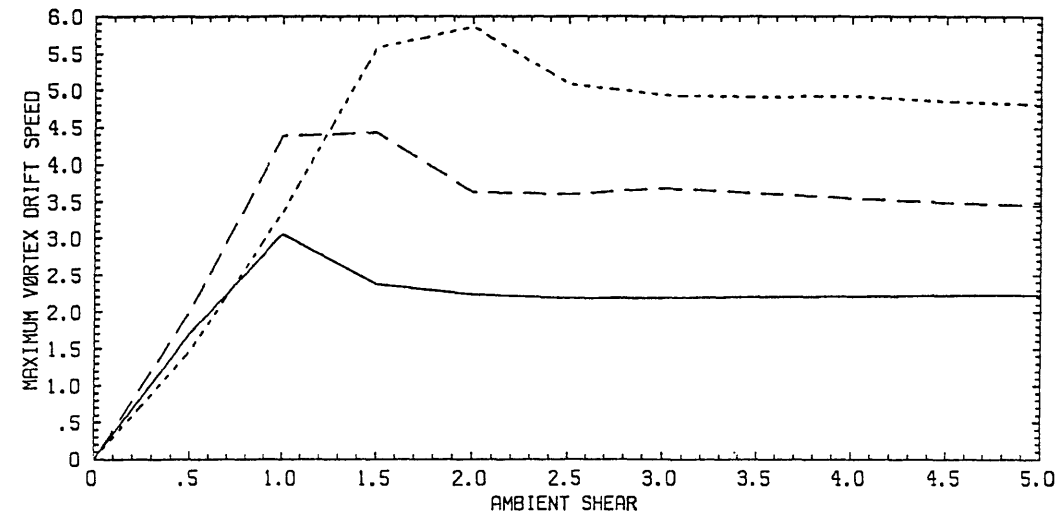

(a)

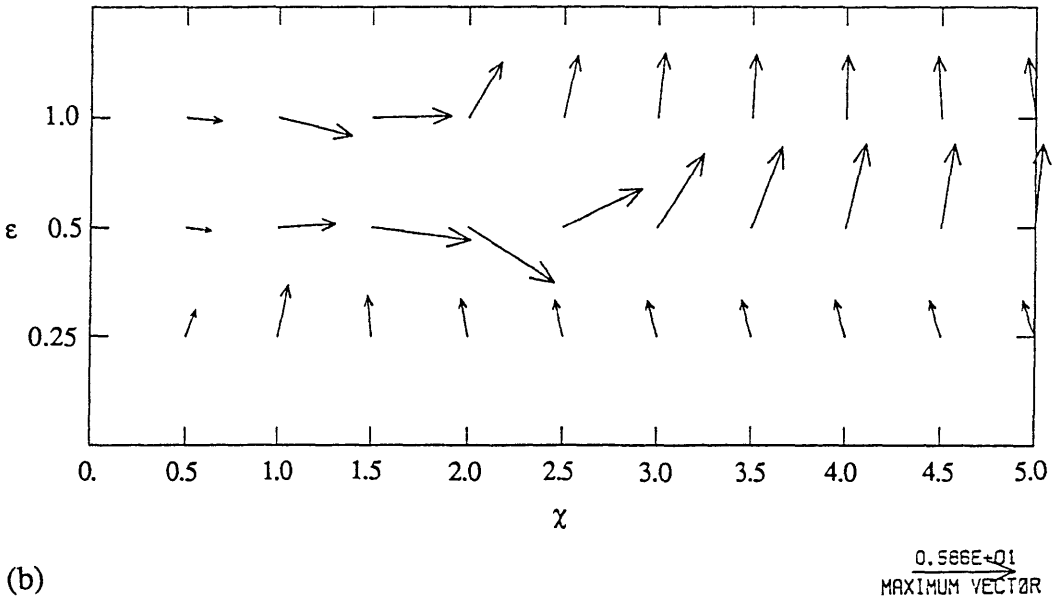

(b)

Figure 4.18 (a) Relation between the maximum induced vortex speed and the magnitude of the vertical shears (χ) for γ=0.79 and ε=0.25 (solid line); ε=0.5 (long-dashed); ε=1 (short-dashed). (b) Maximum induced vortex velocity vector as a function of the magnitude of χ and ε for γ=0.79.

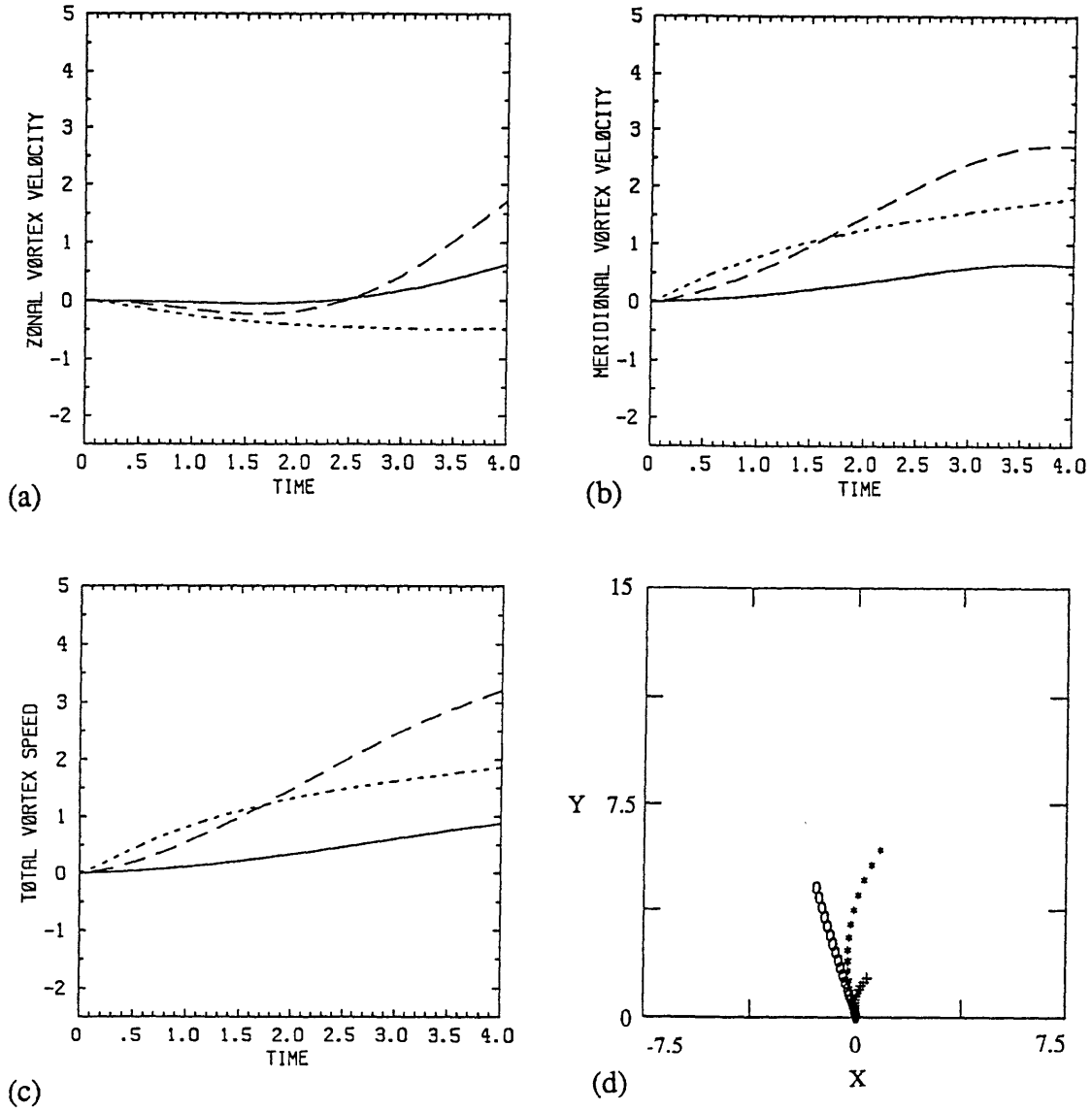

Figure 4.19 Time evolution of the induced lower-layer vortex (a) zonal velocity, (b) meridional velocity, and (c) total speed for ε=0.25, γ=0.5, and χ=0.25 (solid line); for χ=1.25 (long-dashed line); and for χ=5 (short-dashed line). (d) Trajectories (units of 500 km) of the lower-layer vortex for χ=0.25 (shown as "+") ; χ=1.25 (shown as "*"); and χ=5 (shown as "o").

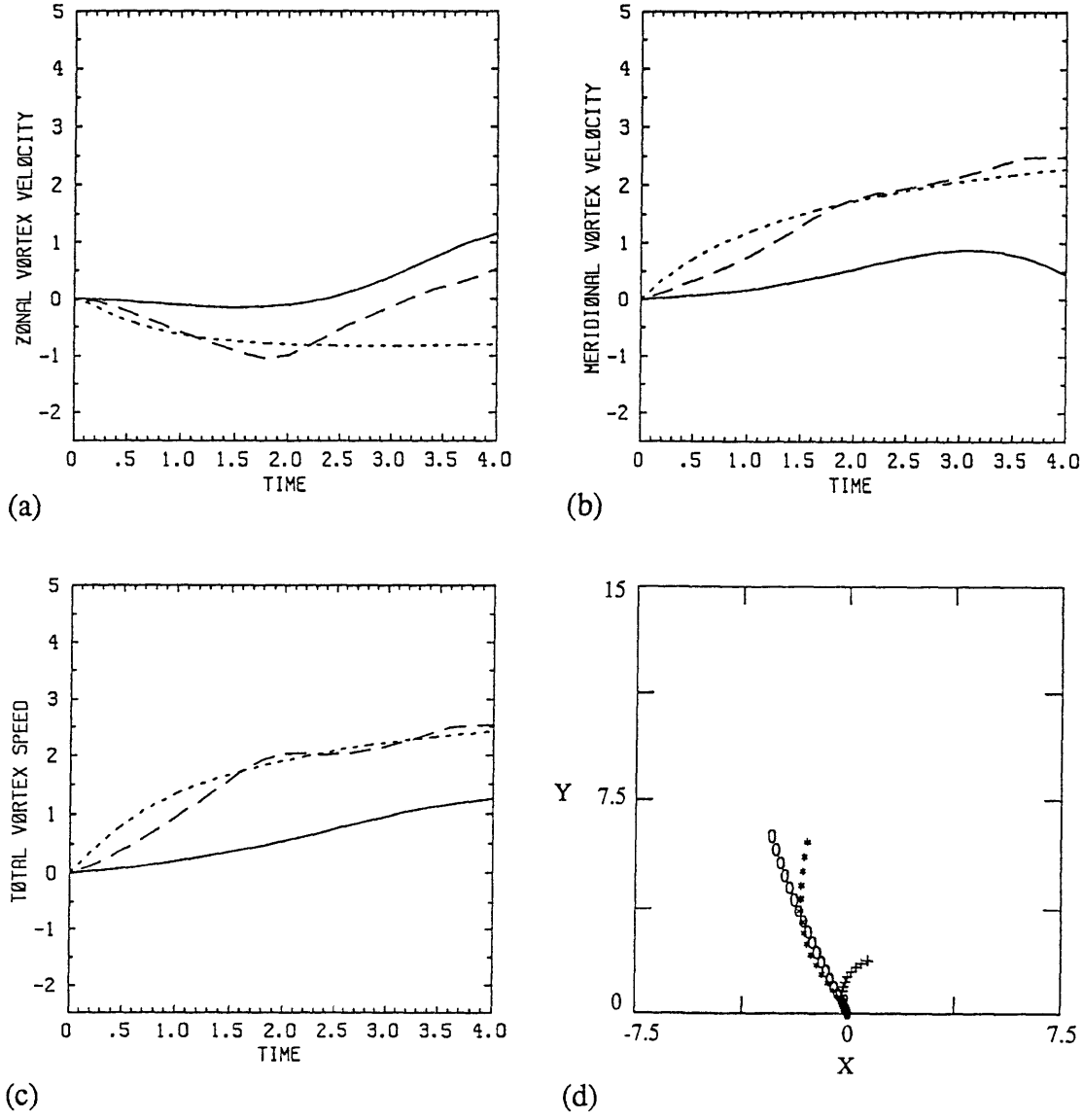

Figure 4.20 Same as Fig. 4.19 but γ=1.

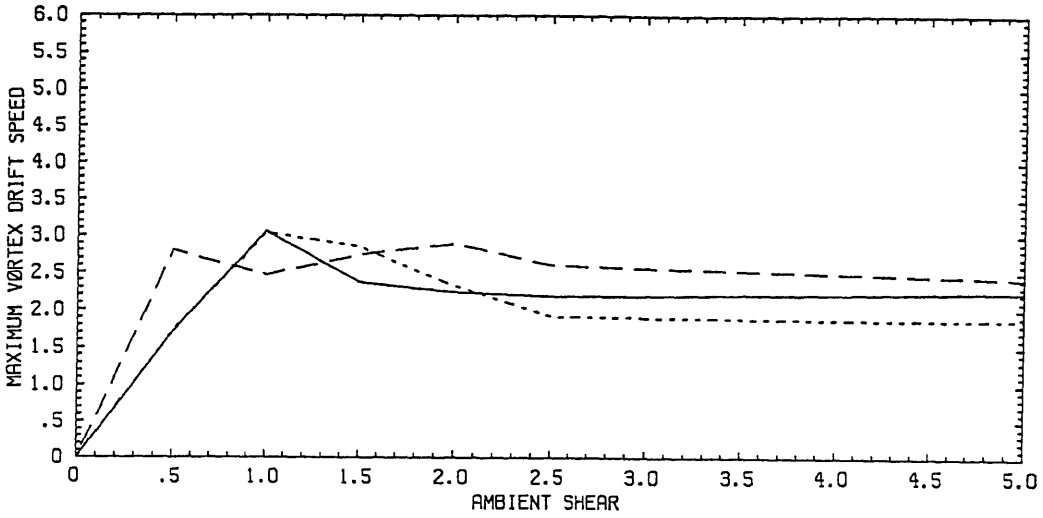

(a)

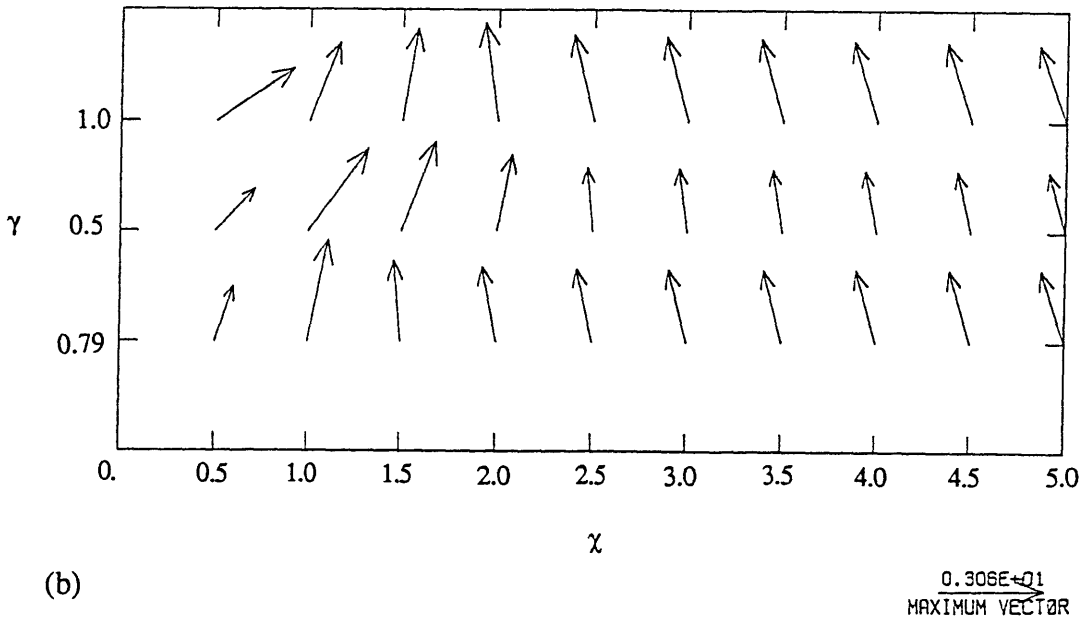

(b)

Figure 4.21 (a) Relation between the maximum induced vortex speed and the magnitude of the vertical shears (χ) for ε=0.25 and γ=0.79 (solid-line); γ=0.5 (long-dashed line); and γ=1 (short-dashed). (b) Maximum induced vortex velocity vector as a function of the magnitude of χ and γ for ε=0.25.

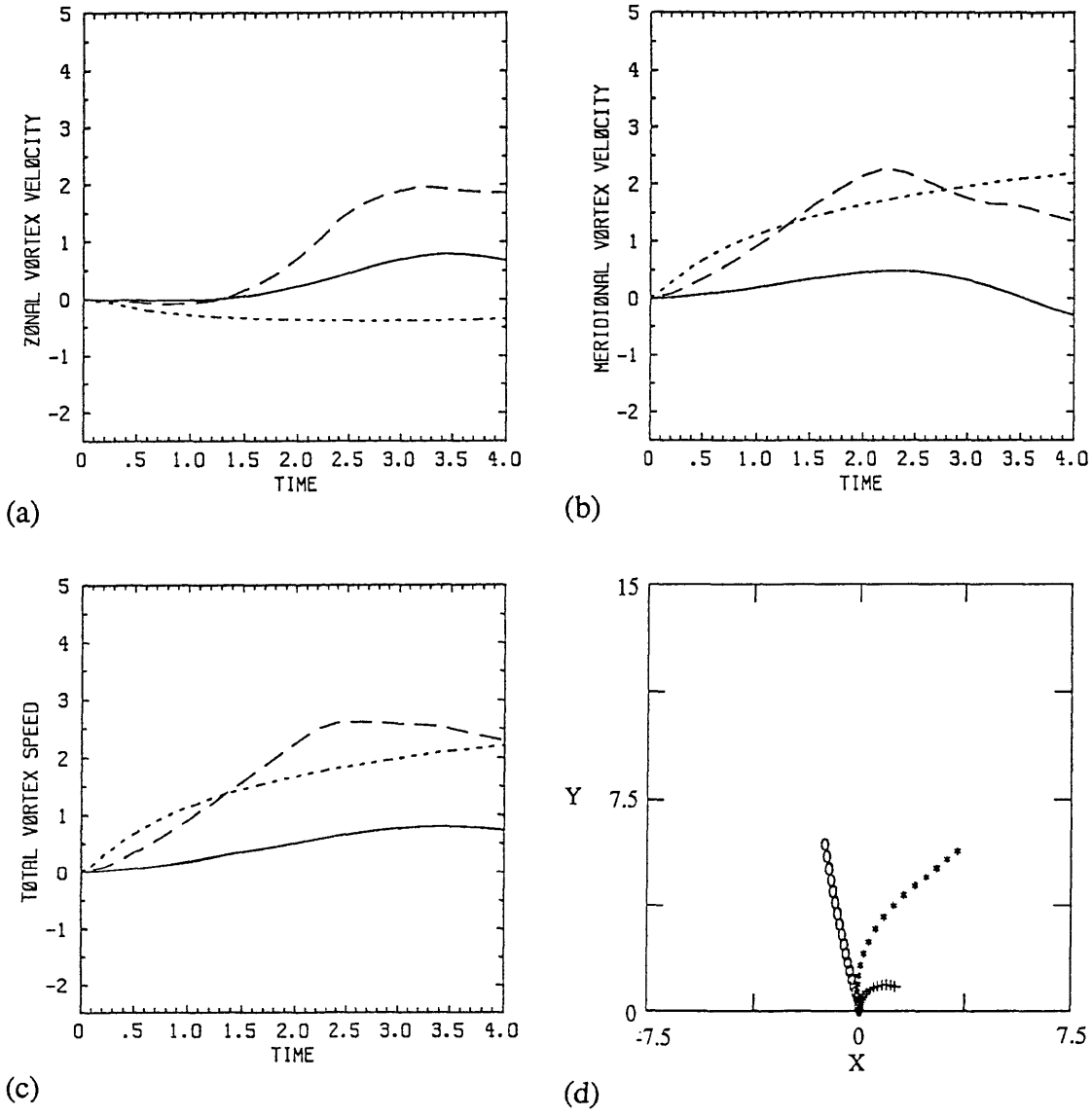

Figure 4.22 Same as Fig. 4.5 but Π_2 halved.

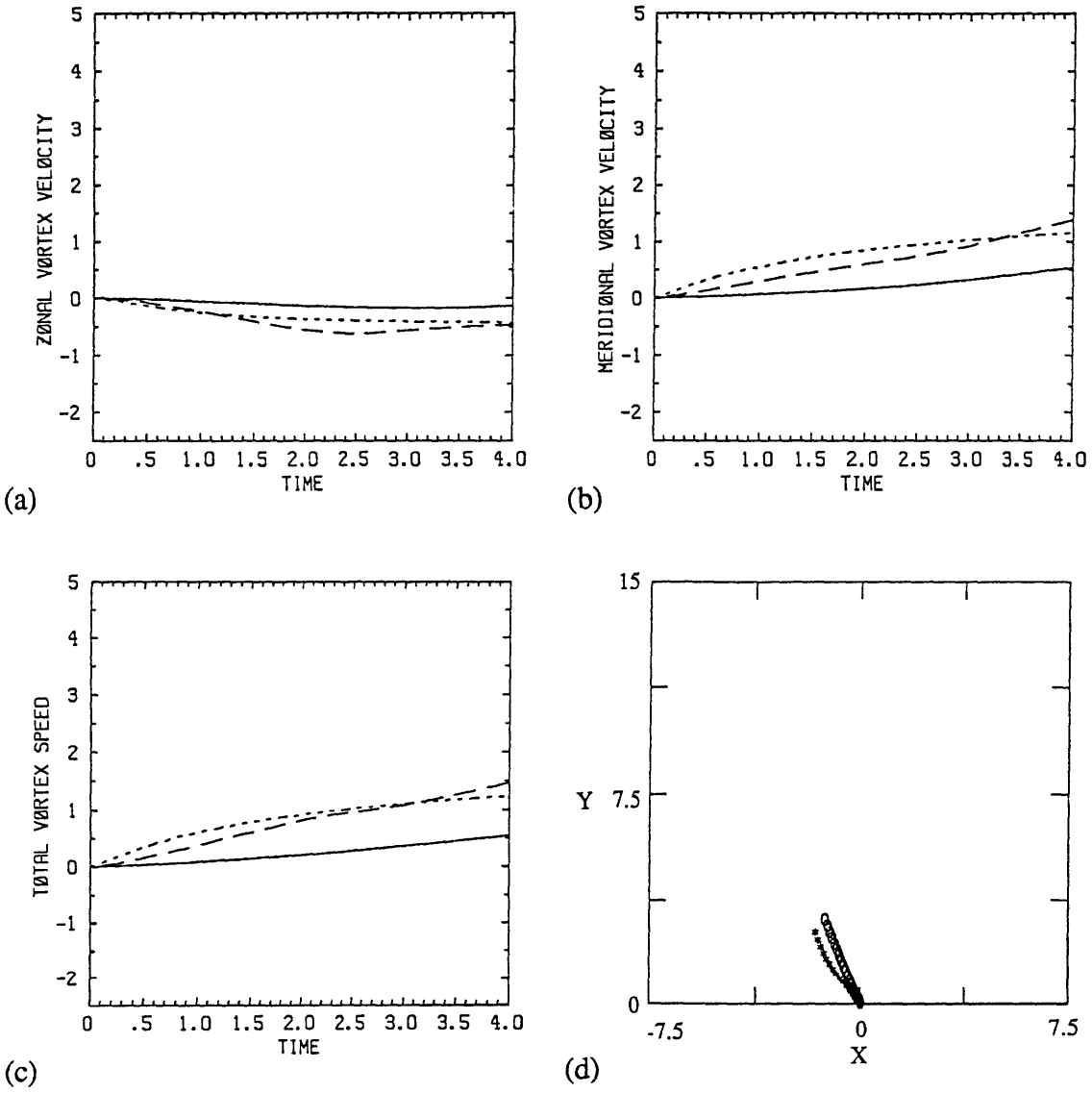

Figure 4.23 Same as Fig. 4.5 but Π_1 halved.

5. Methodology

a. Data

The data used are taken from the final global analyses of the National Meteorological Center (NMC) archived on a 2.5×2.5 latitude-longitude grid. Geopotential height, temperature, and horizontal winds are available at 0000 and 1200 UTC on 10 mandatory isobaric surfaces. Relative humidity is also available at the lowest six levels. The tracks and intensities of the hurricanes in this study are taken from the National Hurricane Center (NHC) post-season analyses for both the 1991 and 1992 seasons (1991 and 1992 Hurricane Preliminary Reports). These are considered the best available data. In this work, three Atlantic storms are studied. The domain we use extends from 2.5 to 62.5^0N and from 120 to 30^0W. The GEMPAK package is used for many of the analyses and plotting. Most of the maps we will show later are plotted using GEMPAK and Mercator projections.

The primary data source of NMC analyses (Dey, 1989) is the conventional surface and upper network (including radiosondes), with supplementary data supplied by pilot balloons, cloud-tracked winds, aircraft reports, and remotely-sensed temperature soundings. Using a spectral statistical interpolation technique (optimal interpolation before 1991), raw observations are used to correct the first-guess fields provided by a 6-hour forecast of the NMC global spectral model (Kanamitsu et al., 1991; Kanamitsu 1989) initialized using the previous analysis. Therefore, although NMC analyses cannot resolve all the small-scale features, such as the detailed structure of hurricanes, they presumably can accurately represent synoptic- and large-scale features that can be resolved by information in the database, and should also be able to retain these features for some time even after adequate resolution by observations has been lost, such as in oceanic areas. Although there are uncertainties in the NMC analysis of divergence over the tropical region

(Trenberth and Olson 1988), our study primarily focuses on the balanced part of the flow field which will not be affected. For these reasons, we believe that the NMC analyses are suitable for the purpose of studying how synoptic and large-scale flows interact with hurricane motion, without needing to know the small-scale structure of a hurricane.

It should be kept in mind that smaller-scale disturbances originating over data-sparse areas may not be captured by the NMC analyses. For example, an upper-level PV anomaly diabatically generated by a hurricane may not be well represented in the NMC analyses. Also, the strong moist convection surrounding the hurricane eyewall may not be captured in these datasets.

b. Potential vorticity diagnostics

1) Total PV inversion

Davis and Emanuel's (1991, hereafter DE) method for PV inversion is employed in this study. The balance equation, originally derived by Charney (1955), in spherical coordinates is

$$\nabla^2\Phi = \nabla\cdot(f\nabla\Psi) + \frac{2}{a^4\cos^2\varphi}\frac{\partial(\Psi_\lambda,\Psi_\varphi)}{\partial(\lambda,\varphi)}, \tag{5.1}$$

where Φ is the geopotential, Ψ is the streamfunction of the nondivergent flow, f is the Coriolis parameter, λ is longitude, φ is latitude, a is the radius of the earth, and the last operator on the right-hand side of (5.1) is the Jacobian. The approximate definition of Ertel's PV in π-coordinates is

$$q = -\frac{g\kappa\pi}{p}\left(\eta\frac{\partial\theta}{\partial\pi} - \frac{1}{a\cos\varphi}\frac{\partial v}{\partial\pi}\frac{\partial\theta}{\partial\lambda} + \frac{1}{a}\frac{\partial u}{\partial\pi}\frac{\partial\theta}{\partial\varphi}\right), \tag{5.2}$$

where $\kappa = R_d / C_p$, p is the pressure, η is the vertical component of absolute vorticity, θ is the potential temperature, and π is the Exner function:

$$\pi = C_p \left(\frac{p}{p_0}\right)^{\kappa}.$$

we use the hydrostatic approximation,

$$\theta = -\frac{\partial \Phi}{\partial \pi}.$$

Also, replacing the total wind by the nondivergent wind

$$\mathbf{V} = \mathbf{k} \times \nabla \Psi,$$

we can solve the system of two equations (5.1) and (5.2) for the two unknowns Φ and Ψ, given the distribution of q, θ on the upper and lower boundaries, and Φ and Ψ on the lateral boundaries. We use the analyzed geopotential height as the lateral boundary condition for Φ and integrate the analyzed horizontal wind field to obtain the lateral boundary condition for Ψ with a constraint that there is no net divergence out of the domain. The upper and lower boundary conditions are the analyzed potential temperature at 925 (1000-850-mb average) and 125 mb (150-100-mb average).

As indicated by Davis (1990), the calculation of PV from (5.2) has errors (induced from random wind and temperature errors) ranging from 0.2 PVU in the lower troposphere to about 1.2 PVU in the lower stratosphere. However, since these are random errors, they may cancel out in different grid volumes. Consequently, the balanced flow, which reflects the integral effect of the PV fields, is probably relatively unaffected by random, small-scale noise. In our calculation, we have chosen a threshold for convergence so that the balanced solution has a precision of 0.1 m in height and 0.1 m s^{-1} in wind speed.

It should be noted that, in our calculation, we find that the inversion scheme tends to break down when the southern boundary is at or south of 7.5 ^{0}N. This is probably due to relatively large errors in the analyzed height field near the equator. The imbalance between the mass and wind fields at the southern boundary makes it very difficult to obtain a convergent solution. We have tried different methods (e.g., using the wind field to replace the height field) to cope with this problem, however, we have not found a

numerical method that successfully inverts PV near the equator. In general, the inversion scheme works when we take 10^0N or 12.5^0N as the southern boundary.

The balanced flow calculated from (5.1) is a non-divergent flow. As indicated by DE, it is also possible to recover the irrotational horizontal winds (divergent winds) and vertical velocities using an iterative procedure to solve a set of prognostic equations. This method is also adopted in the present study.

2) Piecewise PV inversion

Piecewise PV inversion represents the process of recovering the balanced flow associated with specific PV perturbations. It is probably the most useful method in the application of PV diagnostics. If the inversion operator is linear, the solutions can be superposed. Piecewise inversion is then simply an application of the method of Green's function. However, when the balance condition is nonlinear, the solution and its interpretation become much more complicated. Indeed, it has shown that there is no unique solution for nonlinear piecewise inversion (Davis, 1992b). For these reasons, different methods have been explored/developed for solving nonlinear piecewise PV inversion. (A comparison of three different methods of piecewise PV inversion can be found in Davis 1992b.)

In this work, we employ DE's method of piecewise PV inversion . The idea behind this method is illustrated as follows:

Considering a simple quadratic (nonlinear) system $q = AB$, let $q = q_M + q'$, $A = A_M + A'$, and $B = B_M + B'$, where subscript, "M", represents a mean and prime, "'", indicates the perturbation from the mean. Expanding the system, and dividing q into its mean and perturbation components, we obtain

$$q_M = A_M B_M, \tag{5.3}$$

and

$$q' = A_M B' + B_M A' + A'B'. \tag{5.4}$$

(5.3) indicates that the inversion of mean PV is identical to the total PV inversion, except that all the fields (including PV itself) are replaced by their mean.

Then we partition all perturbation fields into N parts, that is, $q' = \Sigma_{i=1}^{N} (q_i)$, $A' = \Sigma_{i=1}^{N} (A_i)$, and $B' = \Sigma_{i=1}^{N} (B_i)$. Substitutions of these summations into (5.4), we get

$$\Sigma_{i=1}^{N} (q_i) = A_M \Sigma_{i=1}^{N} (B_i) + B_M \Sigma_{i=1}^{N} (A_i) + A_1B_1 + A_1B_2 + A_2B_1 + \cdots + A_NB_N. \quad (5.5)$$

There are infinite number of permutations of series of equation that can relate q_i to A_i and B_i from (5.5), that is,

$$q_i = [A_M + \alpha \Sigma_{i=1}^{N} (A_i)] B_i + [B_M + \beta \Sigma_{i=1}^{N} (B_i)] A_i, \quad (5.6)$$

where α and β are arbitrary numbers that satisfy $\alpha + \beta = 1$. As in DE, we use the solution that possesses the symmetry of invariance under an exchange of α and β (i.e., $\alpha = \beta = 0.5$). The sensitivity of the solution to the choice of α and β will be discussed in chapter 6.

One important feature of (5.6) is that the equation is now partitioned such that the summation of the balanced field associated with each individual PV perturbation equals the total balanced field. In practice, however, we must deal with the influence from the lateral boundary. Though inverting over the entire hemisphere would give us the best accuracy and not require lateral boundary conditions, it is not practical in terms of numerical efficiency. When the PV field is divided into separate of PV anomalies, we have no a priori knowledge of the solution at the lateral boundary associated with individual PV anomalies. For this reason, we shall generally use homogeneous lateral boundary conditions in solving the piecewise PV inversion problem (we do not have to worry about the top and bottom boundary conditions because potential temperature perturbations at both of the two boundaries are considered as part of the PV anomalies). For numerical efficiency, we wish to choose the domain to be as small as possible. But in the meantime, we need to ensure that the lateral boundary extends at least a few Rossby radii from the region of interest so that the influence of the imposed boundary conditions is minimal. As

a compromise, in this study, we choose the domain for inversions to be from 2.5 to 62.5^0N and from 120 to 30^0W.

c. Potential vorticity partitioning

1) Defining the mean and perturbation

Defining the mean flow (basic state) for piecewise PV inversion is somewhat arbitrary. It depends upon the purpose of the work. For example, in the study of extratropical cyclogenesis, DE defined a perturbation as the departure from a time average. They chose a typical synoptic-scale wave period (e.g., five days) as the time averaging period.

Hurricanes are very intense and isolated vortices with lifetimes much greater than typical synoptic time scales. The motion of tropical cyclones, however, is strongly influenced by their interaction with the nonuniform background flow associated having varied time and spatial scales. Thus, it is difficult to uniquely define a suitable time mean for the study of hurricane motion.

As a first approach, we will construct the 1991 July-to-September time average flow as our reference state and define deviations from that mean as perturbations. The advantage to this definition is that the mean represents a climatological reference state that permits easy comparisons between different case studies of hurricanes. The shortcoming is that the perturbation thus defined may have less direct relation to the hurricane itself.

To recover the mean (climatological) balanced flow field, we perform a PV inversion of the total mean PV, using climatological values of Φ, Ψ and θ as boundary conditions.

2) partitioning of the perturbation

Although partitioning the PV perturbations is also somewhat arbitrary, there are at least two classes of perturbations to be considered: one is perturbations that are spatially isolated, and the other is perturbations that are associated with a distinct PV gradient in the mean flow. We seek to divide the PV perturbations into the minimum number of pieces that can efficiently represent the different aspects of hurricane motion. Initially, we will partition the perturbation into two parts: a lower PV perturbation [300 mb and below (including potential temperature perturbation at 925 mb), denoted as L6], and an upper PV perturbation [250 mb and above (including potential temperature perturbation at 125 mb), denoted as U4]. There are two reasons for such a vertical partition. First, a hurricane generally has a coherent positive PV anomaly in the vertical, extending from the surface to about 300 mb. Second, because there is usually a distinct separation between horizontal PV gradients near the tropopause and PV gradients elsewhere, the upper troposphere is the one of the most "dynamically active" regions for perturbations. (The other region is near the lower boundary.) Thus, we are interested in examining the influence on hurricane movement by the upper-tropospheric disturbances, which generally exist between 250 mb and the tropopause. From the formulation of the inversion scheme, we know that the total balanced flow should be equal to the summation of the balanced flows associated with mean PV, L6 and U4. However, since some midlatitude upper disturbances often extend down to 300 mb or lower, it should be remembered that L6 can also contain dynamical features that have roots in the upper levels. To quantify these, we may also perform piecewise inversion on any significant PV anomaly which we are interested in understanding.

c. Defining the hurricane advection flow

Our aim is to use PV diagnostics to better define hurricane advection (steering) flow. Using the gridded datasets, we interpolate the balanced winds to the center of the hurricane. One significant problem is that when one calculates the balanced wind associated with L6, which has a very strong azimuthal wind associated with the PV anomaly of the hurricane itself, the resulting interpolated wind is highly sensitive to the exact choice of the hurricane center. To avoid such a problem, we further divide L6 into two anomalies: the lower PV of the tropical storm (the positive PV anomalies at 300 mb and below representing the hurricane, denoted L6S), and the remainder (the entire PV anomaly distribution at 300 mb and below, excluding the hurricane anomaly, denoted L6E).

The balanced flow associated with L6S is quite axisymmetric, as might be expected. Therefore, we assume this part of the flow cannot by itself advect the hurricane. We can then avoid the sensitivity problem by defining the hurricane advection flow to be the summation of the balanced flow (at the cyclone center) associated with mean PV, L6E and U4. The hurricane advection flow is thus defined as the balanced flow (at the storm center) associated with the whole PV in the troposphere, except for the PV anomaly of the hurricane itself. In addition, we can also find a center that makes the interpolation of the balanced flow associated with the hurricane PV anomaly (L6S) zero. This is one way to better characterize the hurricane center in the analysis. We will refer such a center (identified from the balanced flow associated with L6S) as the "balanced vortex center."

6. Results of the observational case studies

Three case studies (Tropical Storm Ana, Hurricane Bob of 1991, and Hurricane Andrew of 1992) are presented in this and the next chapters. The tracks of the three tropical cyclones are displayed in Figure 6.1. These storms are chosen for two main reasons: first, they are recent storms located close to the US continent and, thus, may have good representation within observational data networks, suggesting that the quality of NMC analyses for the storm might be also better; second, they represent storms with diverse characteristics in terms of intensity, size, location, track direction, and track speed.

Hurricane Bob was an intense hurricane that moved mainly to the north and north-northeast along the east coast of United States. By contrast, Ana was a relatively weak tropical storm, originating along the East Coast between Georgia and Florida, that moved east-northeastward. Hurricane Andrew was the strongest of the three cases. Andrew had a relatively small-sized circulation. Unlike Bob and Ana, Andrew spent most of its lifetime south of 30^0N, maintaining a more tropical character. Also, Andrew's motion was different from the other two. It moved generally westward, except turning northward before its final landfall along the south-central Louisiana coast. We shall use the same climatological mean to define the perturbation fields associated with these three cyclones. We will then employ potential vorticity diagnostics to understand the key dynamical processes contributing to the differing track directions and track speeds among the storms.

In this chapter, the results for Hurricane Bob are shown. In the following chapter, the study of Tropical Storm Ana and Hurricane Andrew will be presented, and the three different storms will be compared.

a. Climatology

We have constructed a climatology by taking an Eulerian time (July-to-September) mean of all dynamical fields [including the (geopotential) height, potential temperature, wind, and potential vorticity fields in 1991]. The isentropic PV distribution (Figure 6.2) shows that the PV field is mainly uniformly distributed in the zonal direction. The PV contours are much more concentrated in the upper troposphere than in the lower and middle troposphere. A local PV minimum is observed over southern Georgia in the upper troposphere. It is not clear what this feature represents in the climatology. Figure 6.3 shows the comparison between the mean height from NMC analyses (solid) and the mean balanced height (dashed). They agree very well in most regions, except in the upper troposphere. In the lower troposphere, a large-scale distinct high is present over the Atlantic Ocean. The intensity of this high decreases with altitude. In the upper troposphere, the mean height field is zonal.

A comparison between the mean wind and the mean balanced wind (Figure 6.4) shows that their difference has magnitudes less than 1 m s^{-1} at most places (except perhaps over southeast part of the domain over the North Atlantic Ocean) at 850 mb, and less than 2.5 m s^{-1} at 250 mb, except near the boundaries. These differences are within about 15% of the magnitude of the wind, and are less than one half of typical rawinsonde errors [about 3 m s^{-1} in the lower troposphere and 5 m s^{-1} in the upper troposphere (Bengtsson 1976)]. Therefore, the mean reference itself is very close to a state of nonlinear balance. The mean wind field (Figure 6.5) indicates that upper-level winds are dominated by westerlies. In the lower and middle troposphere, the winds are dominated by easterlies in the tropical region, and westerlies in middle latitudes. Also, as shown in both Figures 6.3 and 6.5, there is a broad anticyclonic circulation over the subtropical Atlantic ocean associated with the summertime "Bermuda High."

This is the background environment the hurricanes are embedded in. We shall use PV diagnostics to understand how individual PV perturbations from this mean state contribute to deflecting storm motion from the mean advection flow. It must be remembered that we use the July-to-September mean of 1991 as the reference state for studies of the three storms of 1991 and 1992. We have not calculated the climatological mean for 1992. We presume that this three-month average of 1991 can well represent the mean state of 1992.

b. Case I: Hurricane Bob

1) Synopsis of Bob

Our synopsis is primarily based on the Preliminary Report from the National Hurricane Center. Hurricane Bob originated from the remnants of a frontal trough just south and southeast of Bermuda on 12 August 1991. The disturbance moved southwestward, and became organized over the next few days, and was deemed a tropical depression at 0000 UTC on 16 August near the Bahamas. The depression was upgraded to Tropical Storm Bob later on the same day when it was located about 135 miles northeast of Nassau. The storm then moved northwestward and continued strengthening, reaching hurricane strength on the 17th about 225 miles east of Daytona Beach, Florida. Bob then accelerated, turning toward the north and then north-northeast. Bob continued intensifying and reached its maximum intensity characterized by 115-mph sustained winds and a 950-mb central pressure on the 19th when it was located 100 miles east-southeast of Norfolk, Virginia. The storm's intensity weakened while moving to the north-northeast over cooler waters off the mid-Atlantic coast. It made landfall at Newport, Rhode Island about 1800 UTC. Bob next moved across Rhode Island and Massachusetts, while continuing to weaken. The storm made final landfall as a tropical storm near Rockland, Maine at 0130

UTC on 20 August and eventually evolved into an extratropical cyclone over the Gulf of St. Lawrence.

2) An example: 1200 UTC 18 August, 1991

We examine nine different times during the life of Bob, from 1200 UTC 16 to 1200 UTC 20 August 1991. In this section, we choose one particular analysis time (1200 UTC 18 August 1991, when Bob was located about 170 miles east-southeast of Charleston, South Carolina) to demonstrate the general behavior of the storm from the NMC analyses.

(i) General findings

In the relative vorticity field (Figure 6.6) Bob appears as a local maximum with vorticity value near 1×10^{-4} s^{-1} at 850 mb. This local maximum decreases with height and changes sign above 300 mb. A region of negative relative vorticity with values of -4×10^{-5} s^{-1} is observed at 150 mb above Bob. These features are also indicated in the PV field (as shown in Figure 2.3). The distribution of relative vorticity in the lower troposphere is more uniform than that in the upper troposphere. Except for the strong vorticity values associated with Bob and another system over eastern Quebec, there are no other strong features at 850 mb. But, in the upper troposphere (e.g., at 300 mb), many features with large relative vorticity values exist.

Figure 6.7 indicates the comparison between the NMC analyzed height and the balanced height fields. They agree very well in most regions, except for some differences over the Atlantic Ocean. Bob is identified as a height minimum in the lower and middle troposphere. The synoptic environment includes a mid- to upper-level trough extending from the southeastern United States beyond the Great Lakes, a subtropical high over the Atlantic, and a strong upper-level ridge east of Canada.

A comparison between the analyzed and balanced (non-divergent) winds at 850 and 250 mb is presented in Figures 6.8 and 6.9. A cyclonic flow (Figs. 6.8a and 6.8b) surrounds Bob at 850 mb with a maximum wind speed of nearly 12 m s^{-1}. This is less than one third of Bob's actual maximum wind speed. The upper-level trough over the Great Lakes can be clearly seen at 250 mb (Fig. 6.9a). This feature is also evident at 850 mb. The difference between the analyzed wind and the balanced wind (Fig. 6.8c, 6.9c) at either level is quite small compared to the magnitude of the total wind speed in most places (except over certain areas in the Gulf of Mexico at 850 mb, and near the lateral boundary at 250 mb).

Figure 6.10 shows the analyzed irrotational winds at 850 and 250 mb and the vertical motion at 450 mb. The irrotational wind is very weak (less than 0.5 ms^{-1} at all places) at 850 mb and slightly stronger at 250 mb. The vertical motion is strong in a few regions, but not near Bob. In contrast to the results of Davis and Emanuel (1991), the comparison of Figure 6.10 with Figures 6.8 and 6.9 indicates that inclusion of the irrotational flow with the non-divergent flow does not help to explain the difference between the analyzed and balanced winds. Nevertheless, comparing the balanced heights and winds with the "real" (NMC analyzed) heights and winds, we find that the analyzed data is very close to a state of nonlinear balance. This example suggests that there is a close relationship between the analyzed and balanced winds in this region.

As shown above, the comparison of wind, height, and relative vorticity fields from the NMC gridded datasets all indicate that the analyses capture Bob's existence. They also locate Bob's position reasonably well. However, the analyses clearly underestimate Bob's intensity. This is partly due to the lack of observations, and partly because of the coarse resolution of the datasets causing Bob's intensity to be smeared out. We also find similar results for the other two cases, Tropical Storm Ana and Hurricane Andrew. Because of this drawback in the datasets, we may not be able to accomplish one of our objectives very well, that is, to understand how a hurricane changes its background environment flow and

how these change the subsequent hurricane motion. We are aware of this limitation of the datasets: these data can represent synoptic- and larger-scale dynamical features quite well, but can not capture the strength and detailed structure of hurricanes as well.

Since piecewise inversion is performed in a pressure-like coordinates (Exner function), instead of isentropic surfaces, we also plot PV perturbations (relative to the climatological mean) on isobaric surfaces in Figure 6.11. Bob appears as a positive PV anomaly in the lower and middle troposphere. At higher levels above Bob, however, an area of negative PV anomalies is found, with a tail extending from the upshear side towards the downshear side. This map is similar to the picture portrayed by our theoretical model. However, in the real atmosphere, we note that there are also many other distinct PV anomalies, which are neglected in our idealized model. Figure 6.12 shows a detailed map of the 700-mb PV anomaly field. Bob is characterized as a positive PV anomaly with a maximum value of 0.4 PVU. Besides Bob, there are some other weaker PV perturbations found in the midlatitudes at this level. A negative PV anomaly and a positive PV anomaly are present on the northeast and the southwest side of Bob, respectively, which look somewhat like the β gyres predicted by barotropic numerical models. However, this cannot be confirmed without studying the time evolution of the PV fields.

We indicated in chapter 2 (Fig. 2.4) that the magnitude of the horizontal gradient of potential vorticity in the upper troposphere is much higher than that in the lower and middle troposphere. Figure 6.11 demonstrates that the amplitude of PV perturbations is also much higher in the upper troposphere than that in the middle and lower troposphere, which is probably not a coincidence. At 150 mb, in addition to many small-scale PV anomalies, there are two distinct synoptic scale PV anomalies: one positive PV anomaly associated with the trough over the Great Lakes, and a negative PV anomaly associated with a ridge located near Newfoundland. Since these PV anomalies are strong and have a relatively large horizontal scale, they will be dynamically important when the invertibility principle is applied. These features can also be identified in the so-called "dynamic tropopause"

potential temperature map (shown in Figure 6.13). The negative PV anomaly above Bob shows up as a warm potential temperature anomaly, and the aforementioned synoptic-scale positive and negative PV anomalies are manifested by warm and cold potential temperature anomalies, respectively. Since this map concisely depicts the dynamic information in the upper troposphere, for simplicity, we shall use such maps to follow the time evolution of the upper-level systems in our study.

(ii) Sensitivity tests of piecewise inversion

Before applying the method of piecewise PV inversion in our study, we first need to know how the behavior of the solution responds to the choice of lateral boundary conditions and of α and β in equation (5.6).

As indicated in equation (5.6), by definition, as long as the numerical scheme for solving the balance relationship is well behaved, the summation of all balanced flows from piecewise inversion should recover the total balanced flow. To demonstrate this quantitatively, we divide the dynamical variables into two parts: one is the climatological mean; the other is the perturbation field. We define the following balanced fields (geopotential height and streamfunction):

- BT: the balanced fields derived from the total PV inversion.
- BM: the mean balanced fields calculated from total PV inversion of the mean PV using mean fields as the boundary condition.
- BPI: the balanced fields derived from the piecewise PV inversion of the total perturbation PV using perturbation fields (differences of geopotential and streamfunction between the analysis and mean) for the boundary conditions.
- BPH: same as BPI, except using homogeneous boundary conditions.

Figure 6.14 shows the comparison of the balanced (geopotential) height at four different levels; the solid line represents BT; the dashed line indicates the sum of BM and

BPI. As shown in Figure 6.14, The two lines closely match. The good relationship in Figure 6.14 verifies the accuracy of the numerical scheme. Because we are using the exact form of boundary condition for piecewise inversion, not surprisingly, this result shows what the theory predicts. However, when the perturbation is divided into more than one part, there is no obvious correct choice of lateral boundary condition to impose, thus the choice of boundary conditions may induce errors in the solution.

For comparison, we also show Figure 6.15, which is the same as Figure 6.14, except that the dashed line represents the sum of BM and BPH. Obviously, when homogeneous boundary conditions are applied for the inversion, because of the errors induced at the boundary, the total balanced flow is not recovered. Figure 6.16 shows the difference between the height fields of BPI and BPH. Most of the differences occur at the boundary, especially at high latitudes. However, away from the boundaries, these differences are very small (less than 5%). The difference in balanced winds between BPI and BPH (Fig. 6.17) reflect the errors induced by the use of homogeneous boundary conditions. In the lower and middle troposphere, where the hurricane vortex is located, the errors are much smaller than the difference between the balanced winds and NMC analyses (cf. Figs. 6.8 and 6.9). These results indicate that the solution of piecewise PV inversion near the storm location is not very sensitive to the lateral boundary conditions. Therefore, we believe that using homogeneous boundary conditions in performing piecewise PV inversions is adequate for our study, and we shall employ such boundary conditions in the remainder of our study.

As indicated in chapter 5, the method of piecewise inversion we use includes an infinite number of solution permutations; depending on how we choose the two parameters α and β in (5.6). For this work, we adopt the symmetrical solution (i.e., $\alpha = \beta = 0.5$) used in Davis and Emanuel (1991). However, we need to know the sensitivity of the results to the choice of α and β in piecewise inversion. As an example, we perform piecewise PV inversions of the perturbation flow in the upper four levels (U4), which

possesses most of the largest-amplitude PV anomalies. We compare the symmetric solution (use α=0.5 and β=0.5, referred to as U4) with two other extremes: one using α=1 and β=0 (U4A); the other using α=0 and β=1 (U4B).

Figures 6.18, 6.19, and 6.20 overlay the balanced height fields for U4 and U4A , U4 and U4B, and U4 and the arithmetic average of U4A and U4B, respectively. We find that each extreme case causes some differences in the balanced fields. However, if we calculate the effects of these differences on the advection of Bob, they are less than 5% of the effect of U4 (0.1 m s^{-1}). Also, Figure 6.20 indicates that the average of U4A and U4B recovers most of the features in U4. Therefore, we think the choices of α and β linearly perturb the solution, but its effect on our study of estimating the advection of hurricanes is negligible. We have also found similar results for other analysis times. Consequently, we believe the approach we have taken for piecewise inversions is adequate for our purposes.

(iii) Advection flow of Bob

Figure 6.21 shows the balanced wind field associated with U4 at four different pressure levels. In the upper troposphere, there are small-scale cyclonic or anticyclonic circulations in the subtropics, but the large-scale flow field is dominated by a strong circulation dipole in midlatitudes. In the lower and middle troposphere, the flow in the subtropics becomes uniformly easterly. The lower-tropospheric flow field is dominated by the dipole of gyres; a cyclonic circulation associated with a positive upper-level PV anomaly located northwest of Lake Superior and an anticyclonic circulation associated with a negative upper-level PV anomaly over Newfoundland. This result indicates that the projection of the upper-tropospheric disturbance on the lower troposphere is dominated by the large-amplitude synoptic-scale PV gyres.

In a linear PV inversion (e.g., quasigeostrophic inversion), the penetration depth is determined by an external parameter, fL/N. The aforementioned finding reflects that, as

shown in Davis (1992b), the vertical penetration depth of a disturbance depends not only on the horizontal scale but also on the amplitude of PV anomalies in a nonlinear PV inversion.

Looking at the vertical distribution of the PV anomalies at this time (Fig. 6.11), we find that the two midlatitude PV anomalies are mainly confined between 250 mb and the top of the domain. Next, we conduct a piecewise inversion of each anomaly separately: U4P represents the upper-level positive PV anomaly over Lake Superior; U4N represents the upper-level negative PV anomaly over Newfoundland. The balanced flow fields associated with U4P and U4N are shown in Figure 6.22a and 6.22b, respectively. We clearly see that the circulations associated with these two PV anomalies have a strong component at the subtropics in the lower troposphere. The balanced flow associated with U4P would advect Bob 4 m s^{-1} toward the north-northeast, and U4N would advect Bob 3 m s^{-1} toward the northwest. If we add these two balanced flows together (U4P + U4N), the sum (Fig. 6.22c) is very close to that associated with U4 (Fig. 6.22d), except that the former has a stronger circulation that extends further south (e.g., over the Caribbean). The two synoptic systems act to steer Bob northward relative to the climatological flow by about 3 m s^{-1}, which is about 20% higher than for the total U4.

We have also performed piecewise inversions of the upper-level anomalies located in the subtropics and the negative upper-level PV anomaly aloft on the downshear side of Bob. The projection of each of these balanced flows at 700 mb is very weak (less than 1 m s^{-1}). Also, there is considerable cancellation between the flow fields making their net contribution to the advection of Bob less significant (less than 1 m s^{-1}). We may conclude that, compared to the aforementioned synoptic-scale PV anomalies, these PV anomalies are dynamically less important as far as their interaction with Bob is concerned.

Figure 6.23b shows the balanced flow associated with L6. A cyclonic flow surrounds Bob. However, when we invert L6E (neglecting the positive PV anomaly near the center of Bob), as shown in Figure 6.23c, the cyclonic flow around Bob disappears.

We note other rotational flows outside Bob in Figures 6.23b and c. If we invert the negative PV anomaly found to the northeast of Bob (denoted as L6N), which appears related to a β gyre, we find a balanced flow (Fig. 6.24) that contributes a 2.9 m s^{-1} southeasterly wind through Bob's center. However, the inversion from other parts of L6E tends to counter this wind. Therefore, unlike the large-scale flow fields associated with U4 (Fig. 6.23a), there is some cancellation of the flows associated with individual PV features in the lower and middle troposphere that cause the net influence from L6E on Bob's movement to be very small (less than 0.5 m s^{-1}).

The procedure of how we remove the hurricane PV anomaly (L6S) is demonstrated here. Figure 6.25 shows the PV perturbation distribution at 700 mb. In this case, we remove L6S in the nine central grids (shown as the area enclosed by heavy lines in Fig. 6.25) surrounding Bob. The 700-mb PV fields before and after removing the hurricane PV anomaly (L6S) are shown in Figure 6.26.

The process of removing the cyclone's PV anomaly is somewhat subjective. Here, we assume that the advection of the hurricane associated with L6S can be neglected. Because any asymmetric features in the PV anomaly taken out may actually contribute to advect the storm itself, a better method is to remove the axisymmetric component of the hurricane's balanced flow. However, as indicated in the previous section, since the NMC datasets do not capture detailed flow structure near the hurricane center very well, it is not clear whether the asymmetric features in the hurricane center are realistic or not. For this reason, we believe that it is appropriate to remove the entire PV anomaly near the hurricane center. To estimate the possible errors induced by this procedure, we perform sensitivity experiments by varying the area containing the actual PV anomaly to be taken out. The results indicate that as long as we remove most of the positive PV anomaly surrounding the hurricane, the process of removing more (or fewer) grid values only affects the hurricane advection flow by a very small value.

We also invert L6S. The recovered balanced flow is shown in Figure 6.23d. The flow field is quite axisymmetrically distributed around Bob's center, with a maximum azimuthal wind speed of about 8 m s^{-1}. Indeed, it is possible that we can find a location at which this wind field is minimized (actually near zero). We regard such a location as the storm center, analyzed by the datasets. As indicated in chapter 5, this center is referred to as the "balanced vortex center." It should be pointed out that the summation of the balanced flows in Figure 6.23c and 6.23d is equal to that in Figure 6.23b.

Figure 6.23d also demonstrates that such operational analyses do not pick up Bob's intensity, as the balanced flow associated with L6S is much weaker than the real hurricane strength. If the data could represent hurricane's intensity, then it would be potentially very useful to study the balanced flow associated with L6S in order to understand how it interacts with the hurricane's environment. Also, if the hurricane exhibits a "wobbly" track, then the asymmetric component of L6S is probably important.

As discussed in chapter 5, to define the advection flow of Bob, we interpolate the balanced winds from grids points to the appropriate hurricane center. There are many ways to define the hurricane center, for example, the local maximum in relative vorticity; potential vorticity; or minimum streamfunction, etc. Two definitions are used here; one is the "best track center", that is the storm center analyzed from the National Hurricane Center's post-season analyses using all of the information available; the other is the "balanced vortex center" (described in chapter 5) that minimizes the 850-500-mb averaged balanced flow associated with L6S.

Figure 6.27 shows a comparison of the 850-500-mb pressure-average balanced flow (interpolated to the hurricane center) with the actual hurricane motion at 1200 UTC 18 August. In this example, Bob's best track position is at 31.5 ^{0}N, 76.6 ^{0}W, and the balanced vortex center is located at 31.62 ^{0}N, 77.48 ^{0}W. The two centers differs by about 1^0 longitude. After interpolation, the balanced flows associated with U4 and the climatological mean are about the same for either center. However, the balanced flow

associated with L6 is very different for the two centers. This is the sensitivity problem we mentioned in chapter 5. As we have neglected the wind field associated with hurricane PV, we get the balanced flow associated with L6E. Again, it is about the same for the two different centers (note that when we use balanced vortex center for interpolation, by definition, the balanced flows associated with L6 and L6E are identical).

When we sum the balanced flows associated with mean, U4, and L6E together, we recover the 850-500-mb pressure-averaged advection flow for Bob. Figure 6.27 indicates that the advection flows using the two different interpolation centers are about the same. Moreover, these advection flows give a good estimate of the direction of Bob's motion (6.6 m s^{-1} north-northeastward), though the magnitude is about 1 m s^{-1} less than Bob's displacement speed. It should be noted that the actual storm motion is estimated by averaging the previous and post six-hour mean motion, calculated using the six-hour best track positions. Given an error of 0.1^0 for the best track positions, the estimation of the cyclone motion has a potential error of about 1 m s^{-1} in displacement speed and 10^0 in direction of movement. Also, with the PV analyses, we are making a local (in time) estimate of advection speed. But the actual storm motion may vary in time.

It can also be seen that Bob's movement is not only due to the mean flow but there are significant contributions from the balanced flow associated with the upper-tropospheric PV perturbation (U4). Two points should be addressed. First, Bob's motion is being strongly influenced by the midlatitude systems. Second, disturbances in the upper troposphere play an important role in advecting Bob.

The Preliminary Report of Bob from the National Hurricane Center describes that, around this time, Bob began turning towards the north and then north-northeast at an increasing forward speed, and that its motion was mainly due to the combined effect of the subtropical high pressure ridge over the Atlantic and a mid- to upper-level trough over the southeastern U.S. Compared with our findings, the former flow feature appears to be an effect of the climatological mean balanced flow. We think the latter conjecture is not a

correct statement. To show this, we also inverted the upper-level PV anomaly associated with the trough over the southern U.S. Since it has a very narrow horizontal scale, its projection onto the flow of the lower troposphere is very weak, and is not a primary factor in Bob's movement. As discussed previously, the flow associated with the synoptic-scale upper-level trough and ridge over the Lake Superior and Newfoundland advected Bob. Thus, through this exercise, we are able to clearly distinguish which dynamical features are most important in advecting the cyclone.

Figure 6.28 indicates the hurricane advection flow (interpolated to the 850-500-mb averaged balanced vortex center) at each level. In general, the flows between 700 to 400 mb are all very close to the actual hurricane motion vector. Higher deviations occur at 1000 mb and above 400 mb. Figure 6.28 also demonstrates that there is a westerly vertical shear of about 5 m s^{-1} between 700 to 200 mb over Hurricane Bob. We also find (not shown here) that advection flows using a single level wind (e.g., 700 mb) or over a deeper part of the troposphere (850 to 300 mb) also approximate the storm movement fairly well. However, in this work, we will generally use the 850-500-mb pressure-averaged flow to represent the hurricane advection flow.

3) Time evolution of Bob

(i) Evolution of upper-level PV anomalies

As the previous example indicates, upper-level PV anomalies are very important in influencing Bob's motion. Therefore, to understand the dynamics of Bob's motion, we need to understand the evolution of the upper-level PV perturbations. For Bob, the most important upper-tropospheric PV anomalies are located above 300 mb.

To simplify visualization, we use the potential temperature (θ) perturbation fields on the dynamic tropopause (surface of 1.5 PVU) to represent disturbances in the upper

troposphere. Because of the quasi-conserved nature of both PV and θ, it is convenient to use such maps to trace important dynamic features which contain valuable dynamic information in the upper troposphere. It should be also restated that a warm (cold) θ anomaly on the dynamic tropopause is equivalent to a negative (positive) PV anomaly on an isentropic surface in the upper troposphere (unlike for the lower boundary). Figure 6.29 shows a time series of such potential temperature anomaly maps from August 17 to August 20. The 700-mb balanced flow field associated with the PV perturbations in the upper four levels (U4) are displayed in Figure 6.30.

At 0000 UTC August 17 (Fig. 6.29a), a cold θ anomaly (referred to as C1) is found over South Dakota. Another cold θ anomaly (C2) extends along the southeastern US. A warm θ anomaly (W1) is located over Lake Superior, and another warm θ anomaly (W2) is found over the northwestern Atlantic. The balanced flow associated with U4 at 700 mb (Fig. 6.30a) indicates that Bob is advected by a weak southeasterly wind with magnitude of 1.4 m s^{-1}, mainly associated with W2. The upper-level features, without much change in intensity, are advected eastward for the next 12 hours (Fig. 6.29b). The flow field (Fig. 6.30b) shows that Bob is advected by about the same amount of balanced flow associated with the same PV anomaly (W2).

By 0000 UTC 18 August (Fig. 6.29c), C1 moves further southeastward, and C2 weakens over the southeastern states. Also, W1 intensifies and expands over southeastern Canada, and W2 moves close to the eastern boundary in the domain while intensifying. At this time, A new warm anomaly (referred to as W3) is found near the east coast of North and South Carolina. Figure 6.30c indicates that Bob is advected northwestward at this time by a weak balanced flow of 1.3 m s^{-1}, which is partly associated with W1.

Twelve hours later (Fig. 6.29d), another cold anomaly is advected southward from Hudson's bay and merges with C1. The new C1 covers the central US and Canada, centered slightly north of Lake Superior, and connects with C2 having a small tail extending to the west of Florida. W1 continues to intensify, with its center located over the

southeast coast of Canada, while W3 is quasi-stationary. As indicated in the previous section, the balanced flow (Fig. 6.30d) that advects Bob at this time is mainly associated with the dipole gyres, C1 and W1, which combine to advect Bob northward with a speed of 2.3 m s^{-1}.

By 0000 UTC 19 August (Fig. 6.29e), C1 has strengthened and moved southward with its center over west Wisconsin. The southern part of C2 is sheared out, and the northern end of C2 merges with C1. W1 is at the same location with little increase in intensity. W3 has strengthened and is located to the southeast of Bob. Interestingly, another warm anomaly (referred to as W4) forms and is located downshear of Bob. The 700-mb balanced flow (Fig. 6.30e) exhibits a southerly flow of 2.5 m s^{-1} through Bob's center. This flow is mainly associated with C1, W1, and W4.

After another 12 hours (Fig. 6.29f), C1 has further intensified. It moves southeastward to near north Illinois. Meanwhile, most of W1 has moved out of the domain. However, the magnitude of W4 has increased dramatically to 25 K. It also covers a much larger area. W4 is centered over New Hampshire, and extends eastward. The associated flow field (Fig. 6.30f) indicates a dipole of very strong gyres associated with C1 and W4. This flow advects Bob northward at 5.5 m s^{-1}.

By 0000 UTC 20 August (Fig. 6.29g), C1 has moved slightly southeastward. W3 further strengthens and extends from southeast Quebec to the eastern boundary of the domain. At this time, the magnitude of the influence of U4 on Bob's motion reaches its peak. As indicated in Figure 6.30g, this flow advects Bob north-northwestward at 6.8 m s^{-1}. This flow field is clearly dominated by C1 and W4. Finally, at 1200 UTC (Fig. 6.29h), C1 and W4 both move to the east, and their intensities are unchanged. Figure 6.30h shows that the flow pattern is still mainly associated with C1 and W4, which advects Bob northward with a wind speed of 5.4 m s^{-1}.

(ii) Upper-level negative PV anomaly above Bob

To compare our findings with the hypothesis of our model discussed in chapter 2, we would like to discuss the evolution of the negative PV anomaly above Bob. As shown in Figure 6.29, at 0000 UTC 17 August, there is no obvious anomaly directly above the location of the storm. However, one day later, at 0000 UTC 18 August, a warm θ anomaly of 10 K (W3) forms above Bob and extends to the northeast side of Bob. It remains so for the next twelve hours. However, at 0000 UTC 19 August, as Bob is still intensifying and moving along the east coast of Virginia, W3 extends from the south to the east of Bob with a maximum amplitude of 15 K. Meanwhile, another warm θ anomaly (W4) forms over Massachusetts, having a maximum amplitude of 15 K, and extends eastward.

The proximity of the storm is quite atypical at this point. Bob is already headed towards mid-latitudes where it can readily induce upper-level PV anomalies through dynamical processes, as opposed to vertical transport by nonconservative processes. As Bob moves northward, this warm anomaly (W4) always "follows" Bob, while its amplitude increases from 15 K on August 19 to 30 K at 1200 UTC August 20, when Bob is located over eastern New Brunswick. This could be either a "phase-locking" of the upper-level and lower PV anomalies or the production of negative PV anomaly by Bob. Similar results are found by looking at negative PV anomalies on 355 K surface (not shown here).

It should be noted that these warm anomalies could intensify because they are moving towards a region having a colder mean θ. However, if we follow the actual θ field on the dynamic tropopause (not shown here), we observe that only θ of W3, but not W4, increases with time in a Lagrangian sense. This result suggests that the early phase of W3 is due to the diabatic process associated with Bob, where as the development to the north (W4) is caused by two dynamic processes: one is the advection of thermal gradients at the

tropopause by the flow associated with the lower-level positive PV anomaly of Bob, and the other is the downshear transport of the low PV air, diabatically generated above Bob, by the upper-level ambient flow. Because the NMC analyses underestimate Bob's intensity, we can not distinguish the two possible dynamic processes by advecting the PV fields using Bob's associated balanced flow .

Since during these few days, Bob was located near the coastal area, we think that the analysis of these PV anomalies is quite realistic. We could perform piecewise PV inversions to understand how these negative PV anomalies interact with Bob. However, to prove or disprove our hypothesis in the modelling work, we need to be able to identify which PV anomalies observed in the data are generated by diabatic processes near the hurricane center. The best we can do is to follow the evolution of the PV field and trace the change of the PV anomalies. It is difficult to clearly distinguish which part of the anomaly is generated by the hurricane and which parts are due to horizontal advection from other regions. Thus, we shall address this qualitatively:

A simple, preliminary analysis is performed by inverting the U4 negative PV anomaly (denoted as U4NA, which includes W3 and W4) found above and from the downshear location of Bob, which we believe may be a negative PV plume either diabatically or dynamically (through the horizontal advection) produced by Bob. Figure 6.31a and b display the 200-mb PV anomaly areas chosen for inversion at 1200 UTC 18 and 19 August, respectively. The inverted balanced flow fields at 700 mb are shown in Figure 6.32. On August 18th, the balanced flow through Bob's center is 0.9 m s^{-1} to the north. However, on 19th, it has increased to a northwestward flow at 4 m s^{-1}, in a direction to the left of the mean southwesterly vertical shear (will be shown later) as predicted by our theoretical model. Piecewise inversions of W3 and W4 at the 19th are also performed, separately. The result shows the advection flow of Bob is mainly associated with W4. The influence from W3 is relatively weak.

To summarize, we find that as the strength of the negative PV anomaly aloft intensifies with time, its effects on advecting Bob also becomes stronger. Though we are not sure how much of the upper-level PV anomalies are diabatically produced by Bob, by following the evolution of the PV field, we believe that the strengthening of the negative PV anomaly aloft is closely related to Bob. It is not clear, however, whether dynamic or diabatic processes are the main cause of W3 and W4. Thus, our preliminary analysis does not exhibit enough evidence to support our hypothesis of chapter 2. We believe that more detailed work needs to be done in order to evaluate this effect more quantitatively. We will discuss this in the final chapter of this thesis.

(iii) Evolution of lower- and mid-level PV anomalies

The evolution of the 700-mb relative vorticity field from August 17th through 20th is shown in Figure 6.33. At 0000 UTC 17 August, Bob's maximum relative vorticity is 4.8×10^{-5} s^{-1}. This increases with time, becoming 1×10^{-4} s^{-1}, 1.3×10^{-4} s^{-1}, and 2.2×10^{-4} s^{-1} at 1200 UTC 18, 0000 UTC 19, and 1200 UTC 19 August, respectively. It weakens to 1.6×10^{-4} s^{-1} during the last 24 hours. A comparison (Fig. 6.34) of the evolution of the maximum relative vorticity field (analyzed from the data) with the best track maximum sustained wind (from Preliminary Report) indicates that the NMC analyses roughly capture the tendency of Bob's intensity, though it presumably underestimates Bob's actual strength. Figure 6.35 displays the evolution of the 700-mb perturbation PV field from August 17th to 20th. The amplitude of the positive PV anomaly associated with Bob increases from 0.2 PVU at 0000 UTC 17 August, to 0.4 PVU on August 18, and 1.2 PVU at 1200 UTC 19 August.

The wind field associated with Bob in the NMC datasets can also be studied as the balanced flow field (Fig. 6.36) of the positive PV anomaly of Bob (L6S). It should be noted that during this case, Bob's positive PV anomaly always extends upward to 300 mb.

There is no clear warm surface (925 mb) θ anomaly associated with Bob, however. Therefore, L6S only includes Bob's positive PV anomalies between 850 and 300 mb, but without θ anomalies at the surface boundary. Figure 6.36 shows that the 700-mb balanced flow is axisymmetry around Bob. Its magnitude becomes stronger with time, though always considerably weaker than the actual wind speeds of Bob.

The evolution of 700-mb balanced flow associated with L6E is displayed in Figure 6.37. Unlike the balanced flow associated with U4 or L6S (Figs. 6.30 and 6.36), this flow field has more detailed small-scale features, and there may be some cancellation between the flows associated with different PV anomalies. Thus, it may not be clear what the dominant dynamic feature is that advects Bob. In general, these balanced flows have about the same magnitude (1 to 2 m s^{-1}) near Bob's center as those associated with U4. Interestingly, At 1200 UTC August 19, as Bob moves rapidly toward the east-northeast, the effect of U4 increases dramatically, advecting Bob northward by a wind speed of 5.5 m s^{-1}. Meanwhile, the advection by L6E increases to a 4.5 m s^{-1} northward flow.

To demonstrate how each component of the 700-mb balanced flow contributes to Bob's motion at 1200 UTC 19 August, we display hodographs of the advecting flow in Figure 6.38. The eastward component of Bob's movement at this time is mainly due to the climatological mean flow. The PV perturbations (U4 and L6E) in the upper and lower troposphere play about the same role in advecting Bob towards the north. The summed balanced flows is a very good approximation to Bob's actual motion at this particular time.

(iv) β effect

As shown in Figure 6.35, from August 18th on, a lower-level negative PV anomaly is consistently found to the east-northeast of Bob, which looks somewhat like the negative branch of β gyres. We invert those negative PV anomaly features, located between the surface and 300 mb, at two different times: 1200 UTC August 18th and 1200 UTC 19th.

The PV anomalies at 700 mb to be inverted are illustrated in Figure 6.39, and the balanced flows associated with these PV anomalies are shown in Figure 6.40. On August 18th, the associated flow tends to advect Bob towards the north-northwest at 2.9 m s^{-1}. However, because of the cancellation with the balanced flow associated with other lower-tropospheric PV anomalies, the net effect of L6E on Bob's motion is a northward speed of 0.5 m s^{-1}. On August 19th, the balanced flow acts to advect Bob northward at 3.5 m s^{-1}. Unlike on the 18th, this negative PV anomaly contributes about 80% of the net advecting flow associated with L6E.

One may ask how closely the negative PV anomalies are related to so-called β gyres. The location of the anomalies relative to the hurricane and its induced storm drift agree very well with the predictions of β-effect theory. However, observations do not show any sign of the additional counterpart in the β gyres, that is, the positive PV anomaly located to the southwest of the storm. Also, given that the data underestimates Bob's strength, it is not clear whether such a negative PV anomaly could be generated by the advection of the background PV gradient by the cyclonic circulation associated with Bob. A strong circulation might make this more likely.

To show this, we calculated the advection of the observed PV field by the balanced flow (as shown in Fig. 6.36) associated with Bob's PV anomaly (L6S) at August 18th and 19th. The analysis (Fig. 6.41) indicates that at 0000 UTC 18 August, the relatively weak flow associated with Bob results in negative PV advection to the east of Bob and positive advection to the west. The magnitude of these PV advections are very small, however, with a maximum rate of about 0.1 PVU per 12 hours. The PV advection magnitudes increase as Bob's associated winds get stronger. From 0000 to 1200 UTC 19 August, PV advection magnitudes increase from 0.15 PVU to 0.3 PVU per 12 hours. In particular, stronger positive PV advection is found to the west of the storm. Comparing the structure and magnitude of the PV advections with the evolution of the PV anomalies in Figure 6.38, however, we do not believe that these perturbations are related to the so-called β gyres.

Thus, we find little evidence of the so-called β effect in our analysis. But, in reality Bob's associated winds are likely to be much stronger, giving more potential for such an effect (though the horizontal PV gradients in the basic flow of the troposphere is relatively weak). Nevertheless, our observational analysis is unable to confirm whether such an effect occurs. More work needs to be carried out to further study this effect, and we will discuss this issue at chapter 8.

4) Advection flow of Bob

Figure 6.42 shows the vector differences between the 850-500-mb pressured averaged calculating advecting flow and hurricane motion for nine different times. These vector differences appear to be quite random in direction. When the 850-500-mb pressure-averaged balanced vortex center is used for interpolation, the statistics from the nine different time show that the average magnitude of speed difference is -0.2 m s^{-1} with a standard deviation of 1.2 m s^{-1}, and the average direction difference is 8^0 to the right of Bob's actual heading direction, with a standard deviation of 8^0. The results are similar when using a single-level (700 mb) advection flow (Fig. 6.43a), or a tropospheric averaged (850 to 300 mb) advection flow (Fig. 6.43b), except that there is a larger vector difference at 0000 UTC 20 August when using the latter. Overall, despite the inherent limitations of the datasets, the advection flow derived from the PV diagnostics is a fairly good approximation of Bob's real movement. The result indicates that such a PV approach can be very useful in understanding hurricane movement. The result also implicitly suggests that, at least for Bob, the primary hurricane circulation has little direct effect (via L6S) on its own motion. (If not, one would expect larger vector differences in Fig. 6.42a, due to deficiencies in the analyzed representation of L6S feeding back onto the hurricane motion.)

As indicated by Figure 6.28, there is a mean westerly vertical shear of about 5 m s^{-1} between 200 mb and 700 mb over Bob at 1200 UTC 18 August. The advection flow at each level at 0000 and 1200 UTC 19 August is illustrated in the hodograph in Figure 6.44. The vertical shear in the advection flow between 200 and 700 mb is a west-southwesterly at 4 m s^{-1} on 0000 UTC 19 August, and a southerly at 10 m s^{-1} on 1200 UTC 19 August.

To deduce how the NMC data would perform in estimating the hurricane steering wind using traditional methods, we use the same data to construct the annular average wind surrounding the hurricane similar to the $5\text{-}7^0$ band average wind. This is done by averaging the wind field over 28 grids surrounding the hurricane (illustrated in Fig. 6.45). When the storm center is not on a grid point, we perform the same procedure four times and use each of the four grids surrounding the storm center as the central grid for subsequent averaging. Then, we interpolate the four annular averages to the hurricane center. Although such a steering flow roughly estimates the real storm motion, a comparison with Figure 6.41 shows that vector errors (Fig. 6.46) between the traditional method and storm motion are much larger than for the PV approach.

Compared to the annular mean winds, we believe that our analysis provides a more consistent method of determining the advection flow through hurricane center. In addition, the PV framework we employ is conceptually more concise, and allows one to study the essential dynamical mechanism responsible for hurricane motion.

c. Summary

In this chapter, we have presented a diagnostic study of the motion of Hurricane Bob using potential vorticity methodology. An example of the diagnosis is illustrated for 1200 UTC 18 August. We find that the NMC analyses capture the time evolution of Bob fairly well, except that the gridded analyses typically underestimate Bob's intensity. We also demonstrate that the height and wind fields from the NMC analyses are very close to a

state of a nonlinear balance. We show that horizontal PV gradient are more concentrated near the tropopause, and that the magnitude of PV anomalies are typically much stronger in the upper troposphere than elsewhere. This is not only true in midlatitudes, but also in the subtropics, where the hurricanes originate.

Sensitivity experiments of the piecewise PV inversion technique are performed. We demonstrate that homogeneous boundary conditions and a symmetric balance solution ($\alpha = \beta = 0.5$) are adequate for our study. We shall use the same methods in the study of the two subsequent cases.

PV perturbations are separated into three pieces: one including the upper four pressure levels (U4), the other two comprising the lower six levels (L6E and L6S). Our analysis is able to demonstrate how each individual PV anomaly contributes to Bob's motion. For example, we are able to identify which PV features in U4 are most influential in advecting Bob. This case study demonstrates that Bob is a middle latitude hurricane that strongly interacts with midlatitude synoptic-scale upper-level waves.

By studying the time evolution of the PV field, we also investigate the validity of the hypothesis of our theoretical model and the so-called β effect. Our analyses show that an upper-level negative PV anomaly, located above and downstream side of Bob, strengthens as Bob evolves. Our preliminary analysis suggests that this negative PV anomaly helps to advect Bob in a significant manner, especially at later stages. However, we are not sure how this PV anomaly is generated. Whether this observational analysis supports our hypothesis, that the negative PV anomaly diabatically generated by the hurricane may influence storm motion, is contingent upon our ability of being able to "prove" that the negative PV anomaly aloft (W3 and/or W4) are indeed diabatically produced by Bob, itself. More work needs to be done, however, to distinguish which part of the negative PV anomaly (if any) is actually generated by the cyclone.

We also observe that a lower-level negative PV anomaly is always found to the east-northeast of Bob and this PV anomaly plays an important role in advecting Bob. However, we do not find enough evidence to conclude that the β effect is operative.

Finally, our results from nine different times indicate that the advection flow derived from our method approximates Bob's actual motion very well. We emphasize that an additional advantage of PV perspective is that it not only offers a consistent way to detect the flow through the hurricane center but it also is capable of helping to determine how individual dynamical features contribute to the advection of the cyclone.

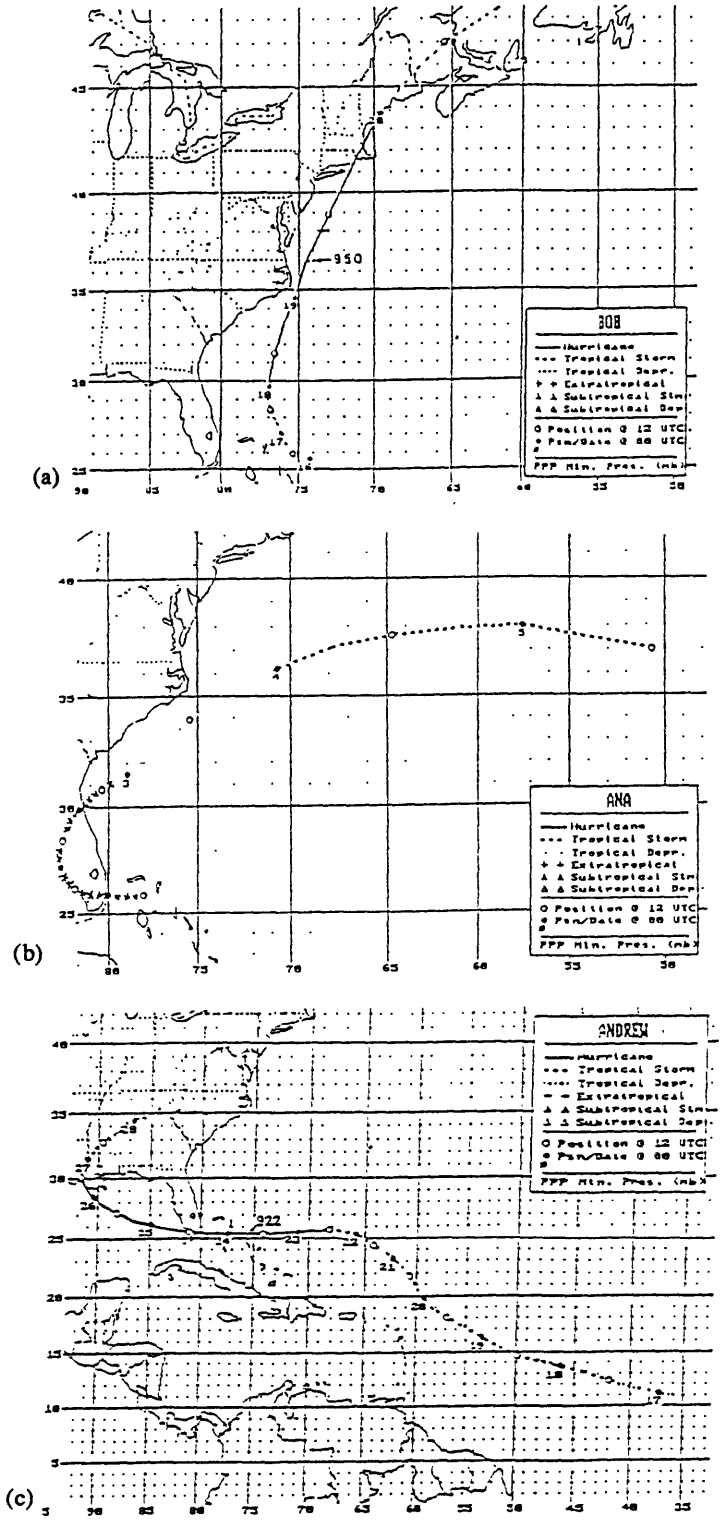

Figure 6.1 Best track positions for (a) Hurricane Bob of 1991, (b) Tropical Storm Ana of 1991, and (c) Hurricane Andrew of 1992. (From the Preliminary Report at the National Hurricane Center.)

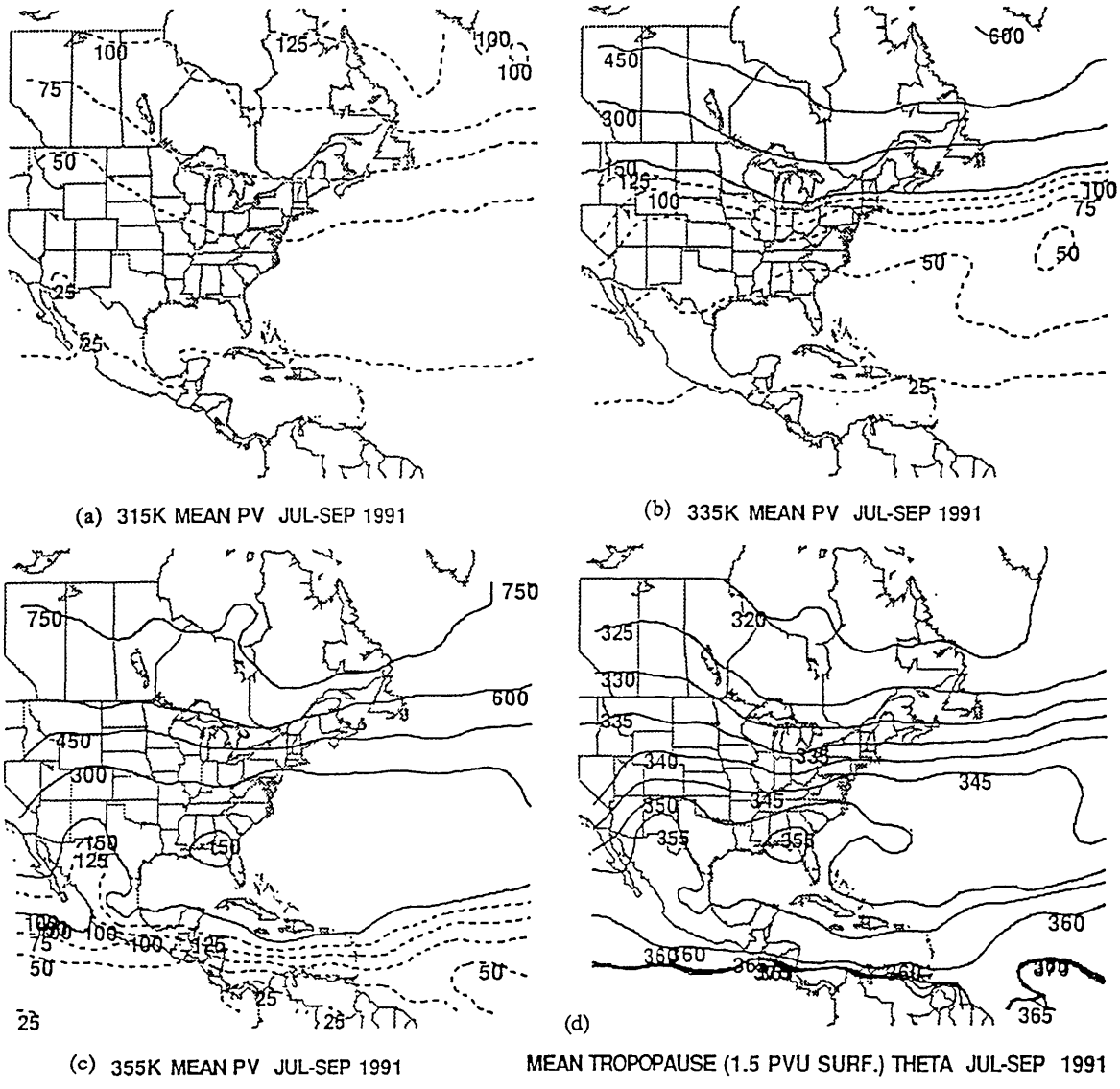

Figure 6.2 Mean (July-September 1991) Ertel's potential vorticity and mean tropopause potential temperature fields. (a), (b), and (c) are the PV maps for the 315, 335, and 355 K isentropic surfaces, respectively. The unit is 0.01 PVU. Potential vorticity values smaller than (larger than or equal to) 1.5 PVU are shown as dashed lines (solid lines) with contour intervals of 0.25 PVU (1.5 PVU). (d) shows the tropopause potential temperature (on the 1.5 PVU surface). The contour interval is 5 K.

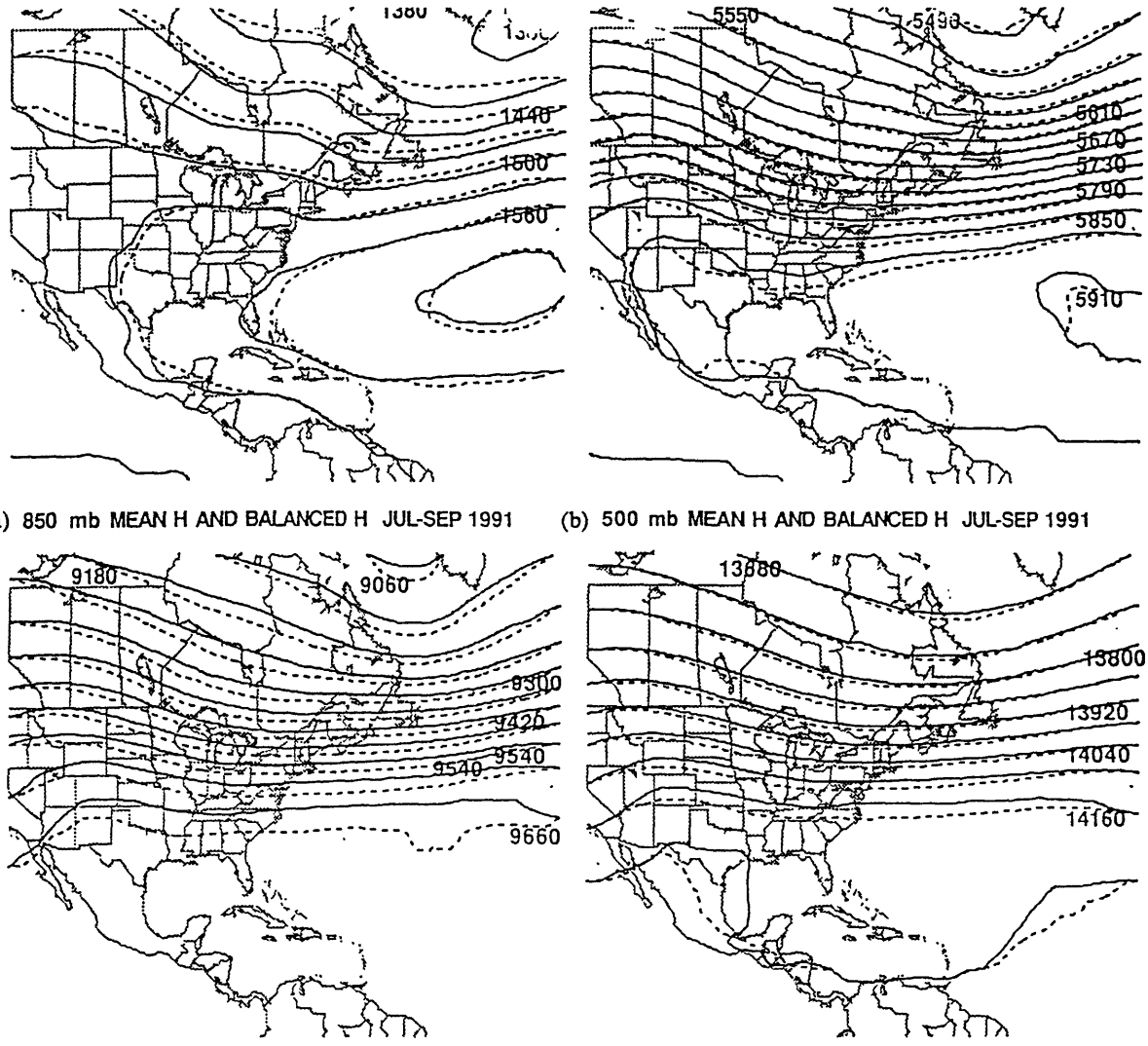

(a) 850 mb MEAN H AND BALANCED H JUL-SEP 1991

(b) 500 mb MEAN H AND BALANCED H JUL-SEP 1991

(c) 300 mb MEAN H AND BALANCED H JUL-SEP 1991

(d) 150 mb MEAN H AND BALANCED H JUL-SEP 1991

Figure 6.3 Mean NMC analyzed height field (solid) and mean balanced height field (dashed) at (a) 850 mb, (b) 500 mb, (c) 300 mb, and (d) 150 mb. Contour intervals are 30 m for (a) and (b), 60 m for (c) and (d).

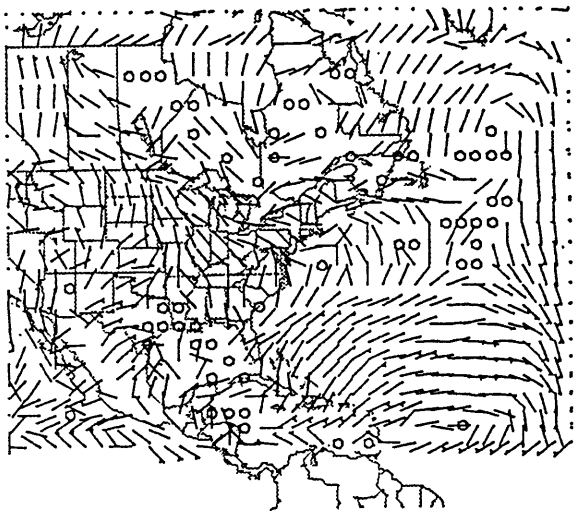

(a) 850 mb ANA. AND BAL. MEAN WIND DIFF. JUL-SEP

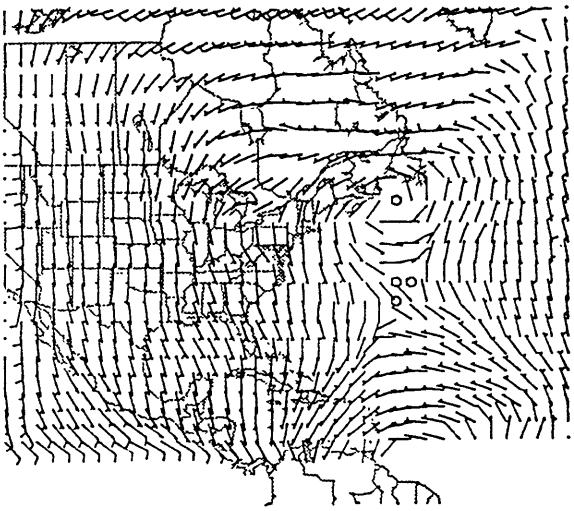

(b) 250 mb ANA. AND BAL. MEAN WIND DIFF. JUL-SEP

Figure 6.4 Difference between the mean NMC analyzed wind field and mean balanced wind field (barb with unit in knots) at (a) 850 mb, and (b) 250 mb. One long barb indicates 10 knots (8-12 knots); one short barb indicates 5 knots (3-7 knots); no barb indicates winds less than 3 knots; and "0" indicates no wind.

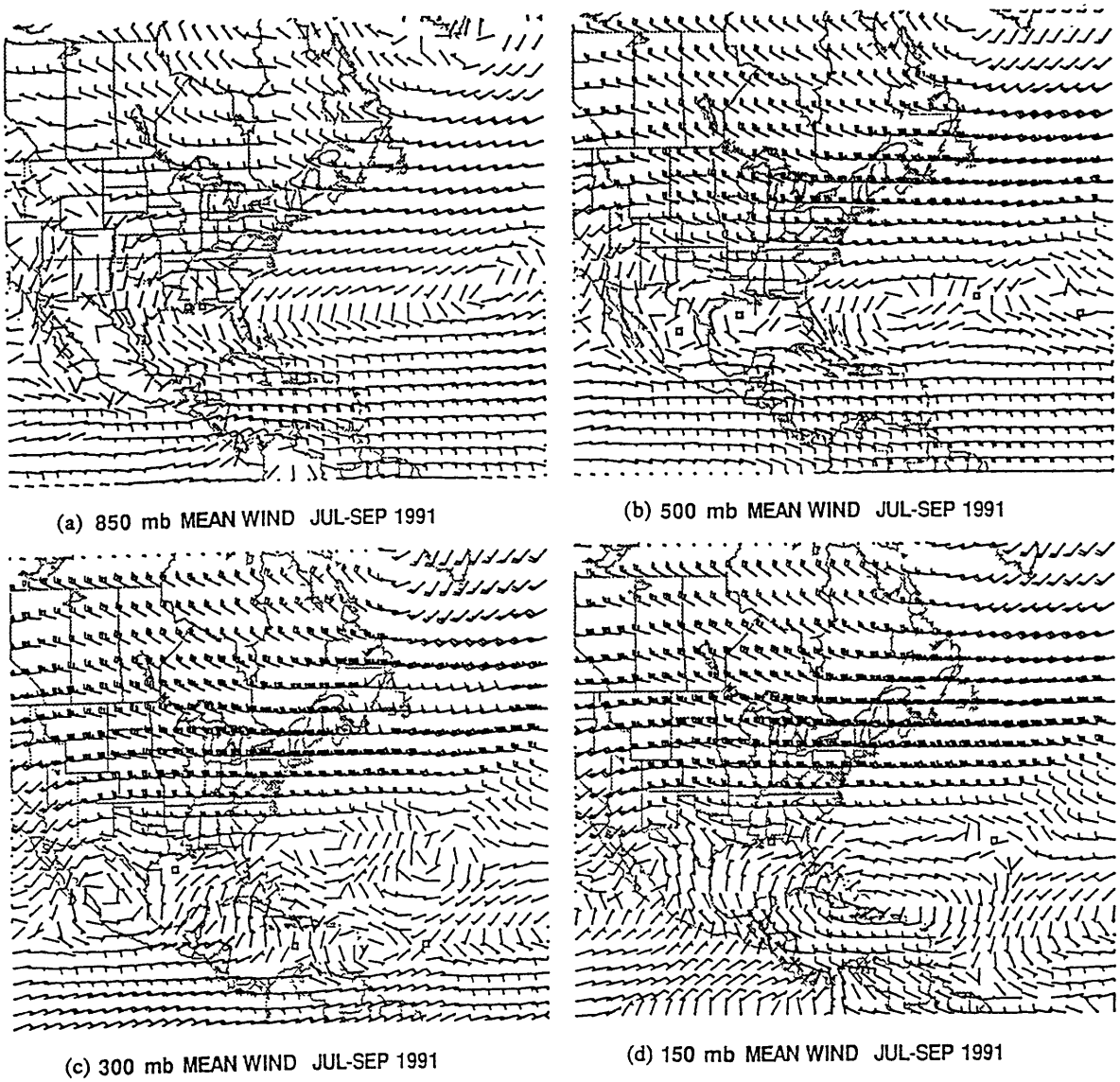

Figure 6.5 Mean NMC analyzed wind field (wind barb plotted as in Fig. 6.4) at (a) 850 mb, (b) 500 mb, (c) 300 mb, and (d) 150 mb.

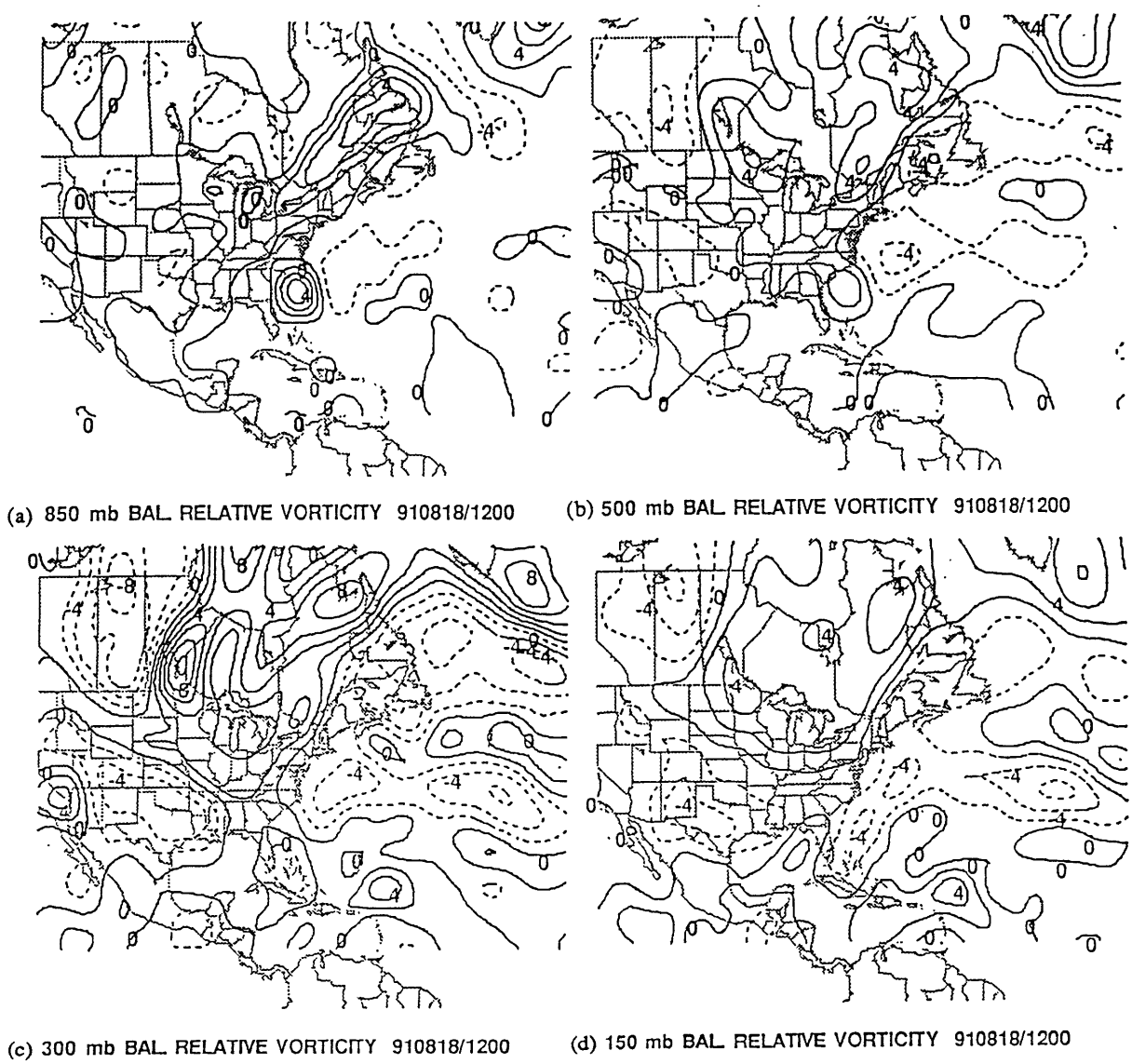

Figure 6.6 Relative vorticity field at 1200 UTC 18 August 1991 at (a) 850 mb, (b) 500 mb, (c) 300 mb, and (d) 150 mb. Solid (dashed) line indicates positive (negative) values. Contour interval is 2×10^{-5} s^{-1}.

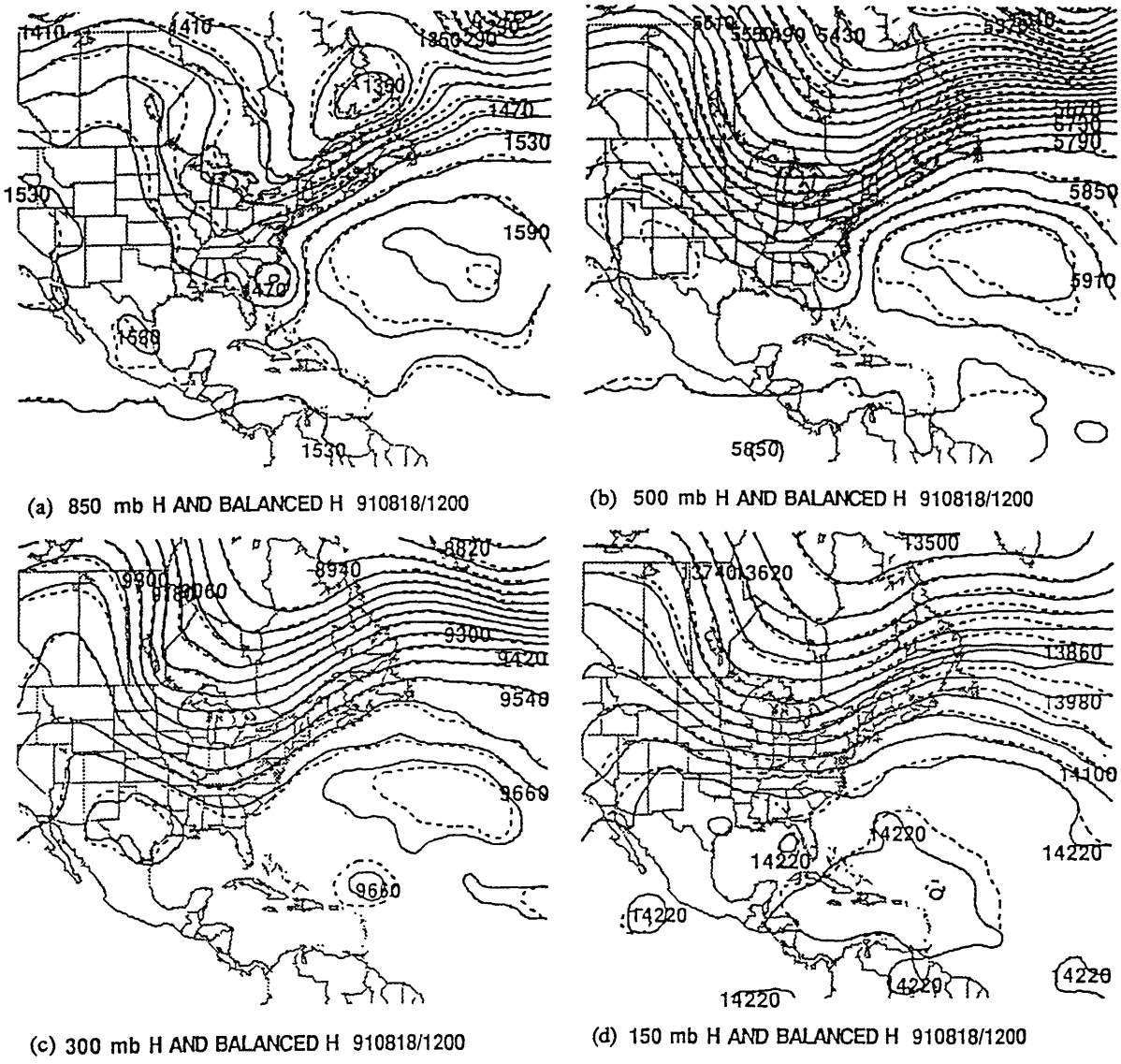

Figure 6.7 NMC analyzed height field (solid) and balanced height field (dashed) at 1200 UTC 18 August 1991 at (a) 850 mb, (b) 500 mb, (c) 300 mb, and (d) 150 mb. Contour intervals are 30 m for (a) and (b), 60 m for (c) and (d).

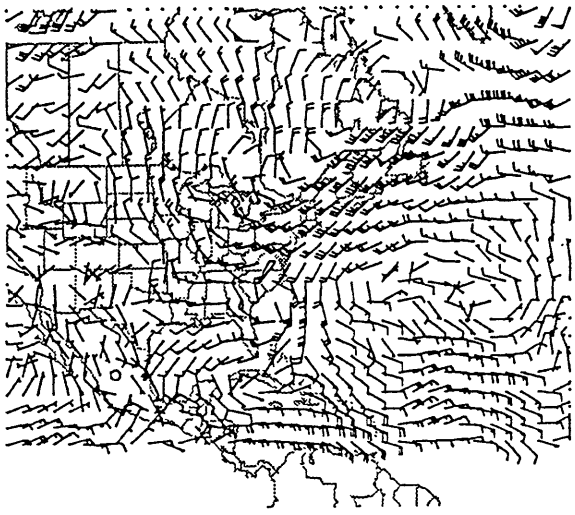

(a) 850 mb ANALYZED WIND 910818/1200

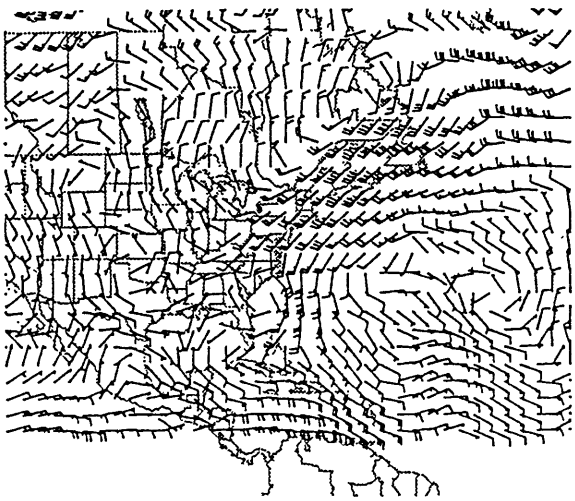

(b) 850 mb NON-DIVERGENT WIND 910818/1200

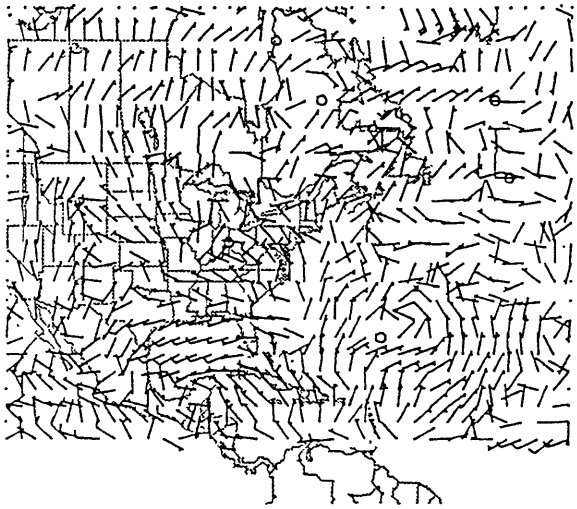

(c) 850 mb OBS. AND BAL. WIND DIFF. 910818/1200

Figure 6.8 NMC analyzed wind field and non-divergent wind field (wind barb plotted as in Fig. 6.4) at 1200 UTC 18 August 1991. (a), (b), and (c) are the 850-mb NMC analyzed wind field, non-divergent wind field, and the difference between the two, respectively.

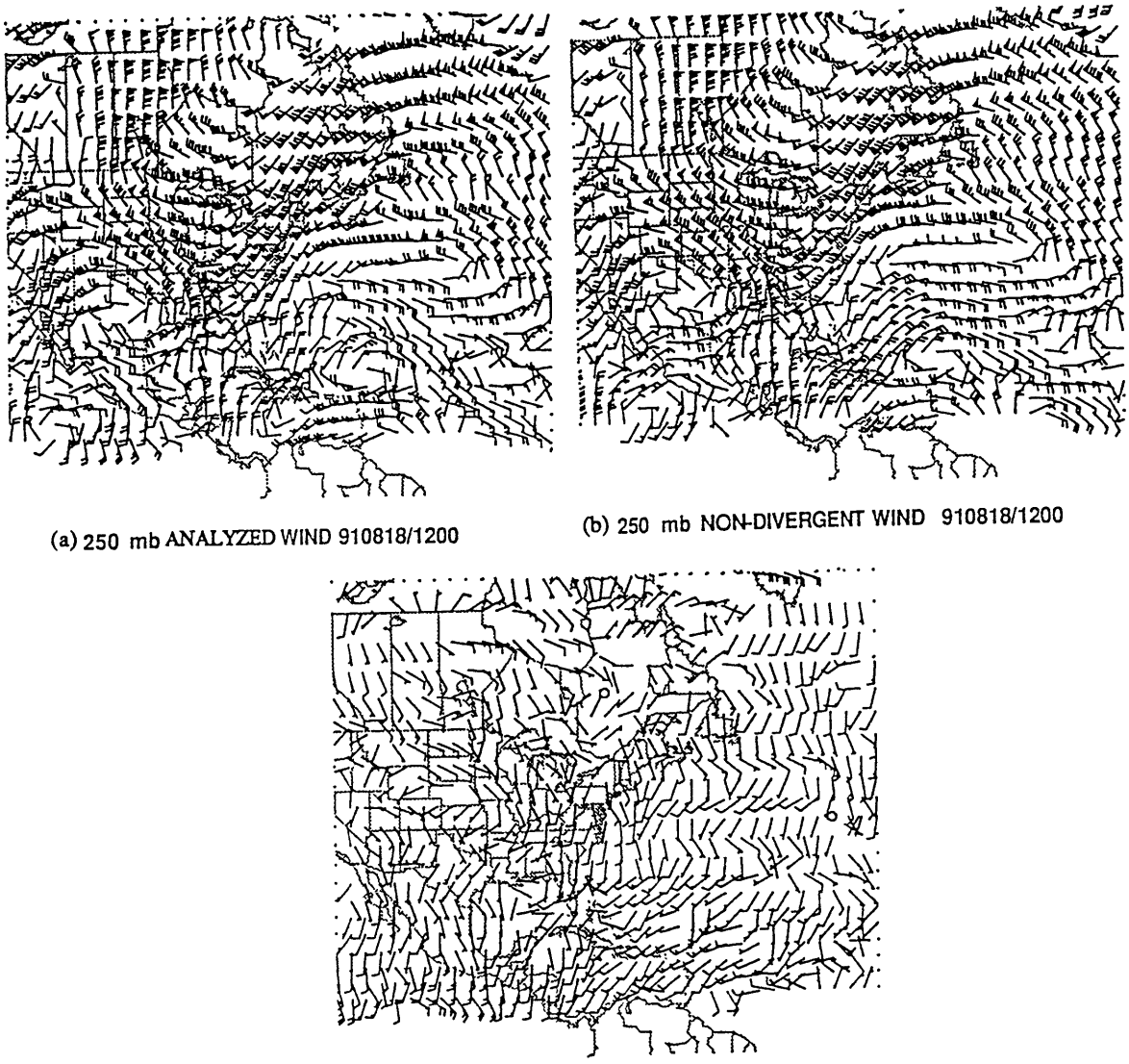

Figure 6.9 Same as Fig. 6.8, but at 250 mb.

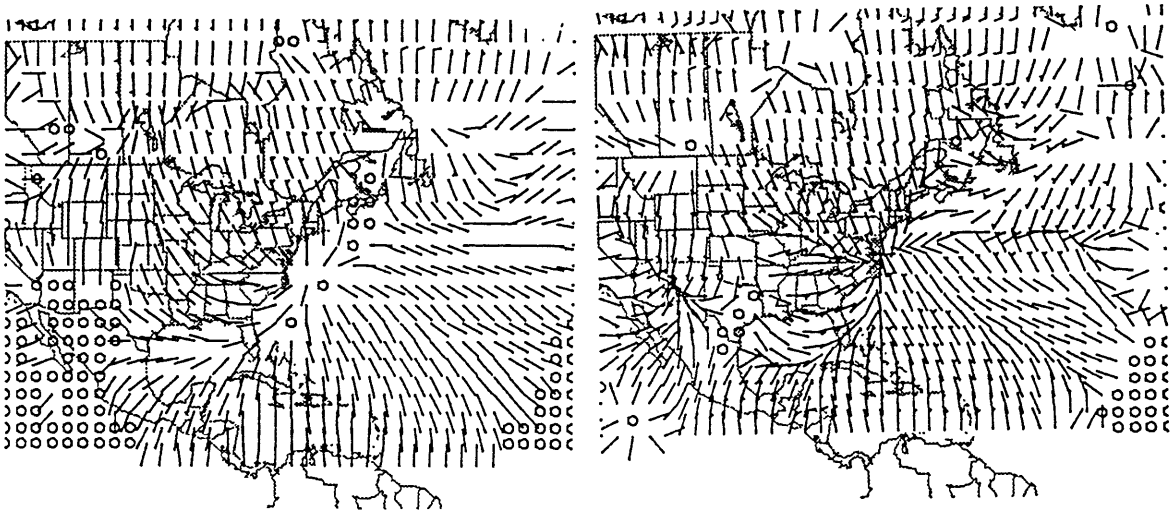

(a) 850 mb IRROTATIONAL WIND 910818/1200

(b) 250 mb IRROTATIONAL WIND 910818/1200

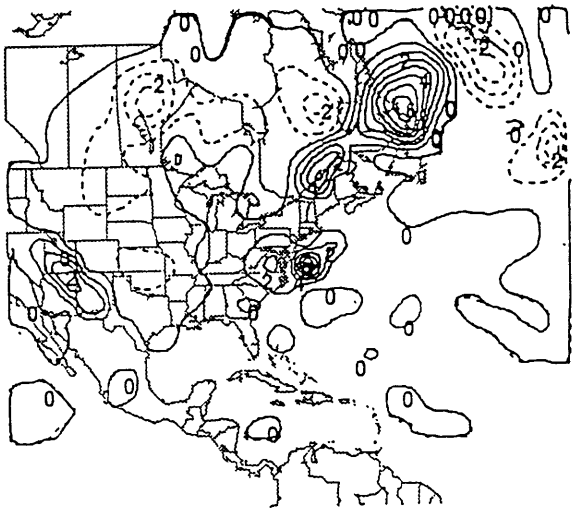

(c) 450 mb W 910818/1200

Figure 6.10 Irrotational wind field (wind barb plotted as in Fig. 6.4) at (a) 850 mb, and (b) 250 mb. (c) vertical velocity (interval of 1 cm s^{-1}) at 450 mb at 1200 UTC 18 August 1991.

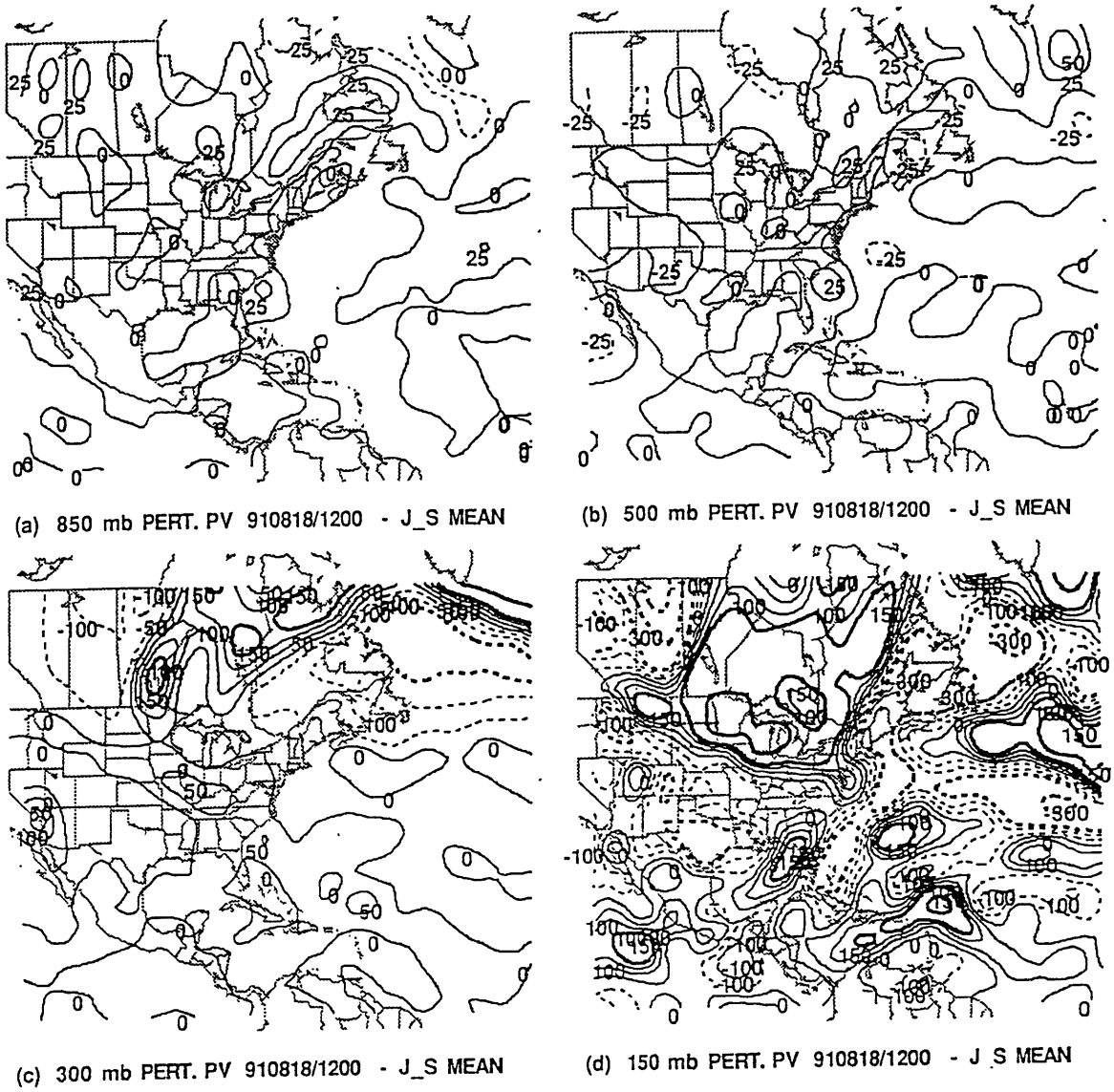

Figure 6.11 Ertel's potential vorticity perturbation field at 1200 UTC 18 August 1991. (a), (b), (c), and (d) are the perturbation PV maps for the 850, 500, 300, and 150 isobaric surfaces, respectively. The unit is 0.01 PVU. Potential vorticity values smaller than (larger than or equal to) 1.5 PVU are shown as thin lines (bold lines) with contour intervals of 0.25 PVU (1.5 PVU). Positive (negative) values are represented by solid (dashed) lines.

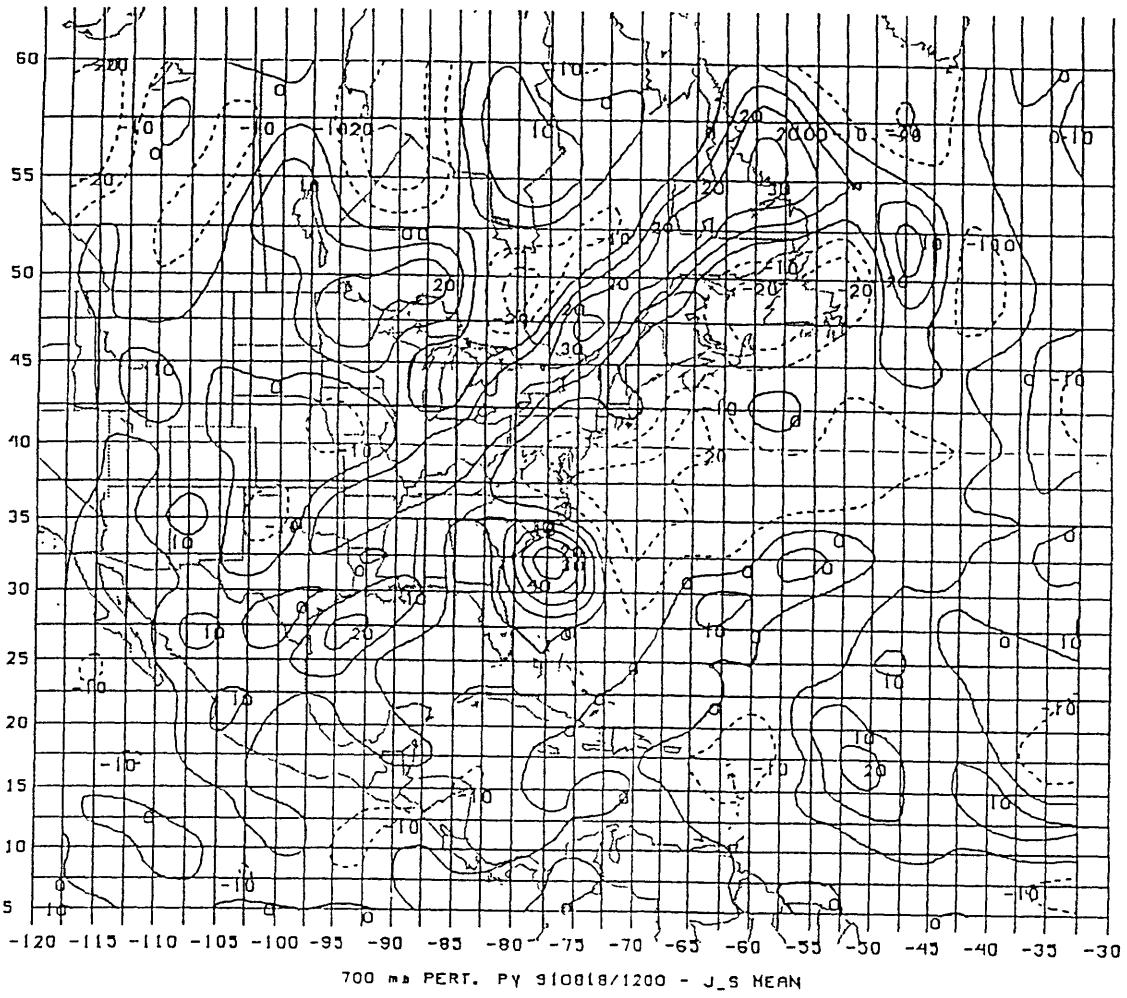

Figure 6.12 Ertel's potential vorticity perturbation field at 700 mb at 1200 UTC 18 August 1991. All positive (negative) values are represented by solid (dashed) lines. The unit is 0.01 PVU, and contour interval is 0.1 PVU.

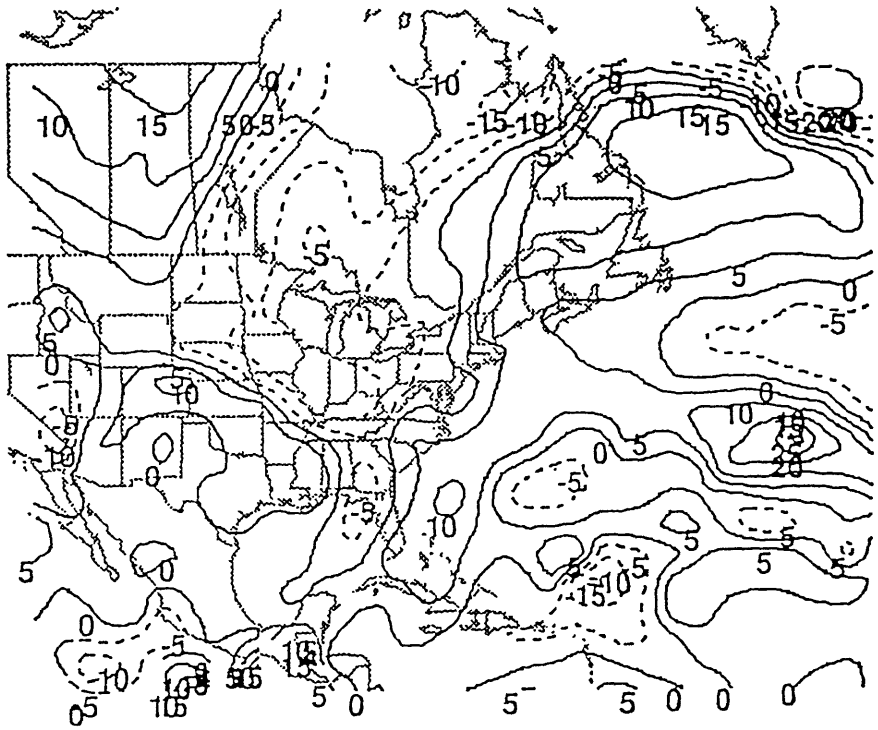

Figure 6.13 Tropopause potential temperature perturbation field (on the 1.5 PVU surface) at 1200 UTC 18 August 1991. Contour interval is 5 K. All positive (negative) values are represented by solid (dashed) lines.

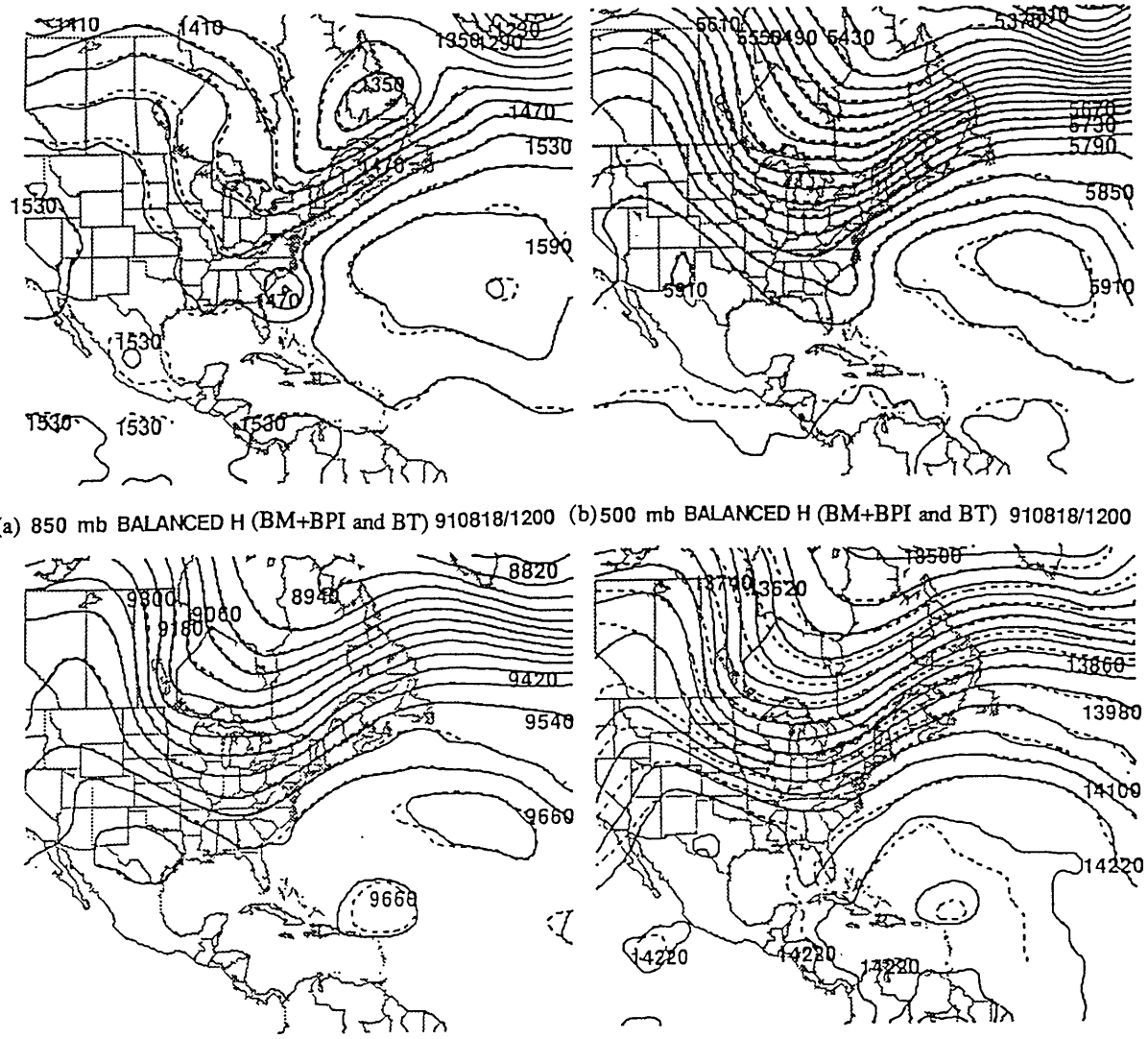

(a) 850 mb BALANCED H (BM+BPI and BT) 910818/1200 (b) 500 mb BALANCED H (BM+BPI and BT) 910818/1200

(c) 300 mb BALANCED H (BM+BPI and BT) 910818/1200 (d) 150 mb BALANCED H (BM+BPI and BT) 910818/1200

Figure 6.14 Balanced height fields associated with BT (dashed), and with BM+BPI (solid) at 1200 UTC 18 August 1991 at (a) 850 mb, (b) 500 mb, (c) 300 mb, and (d) 150 mb. Contour intervals are 30 m for (a) and (b), 60 m for (c) and (d).

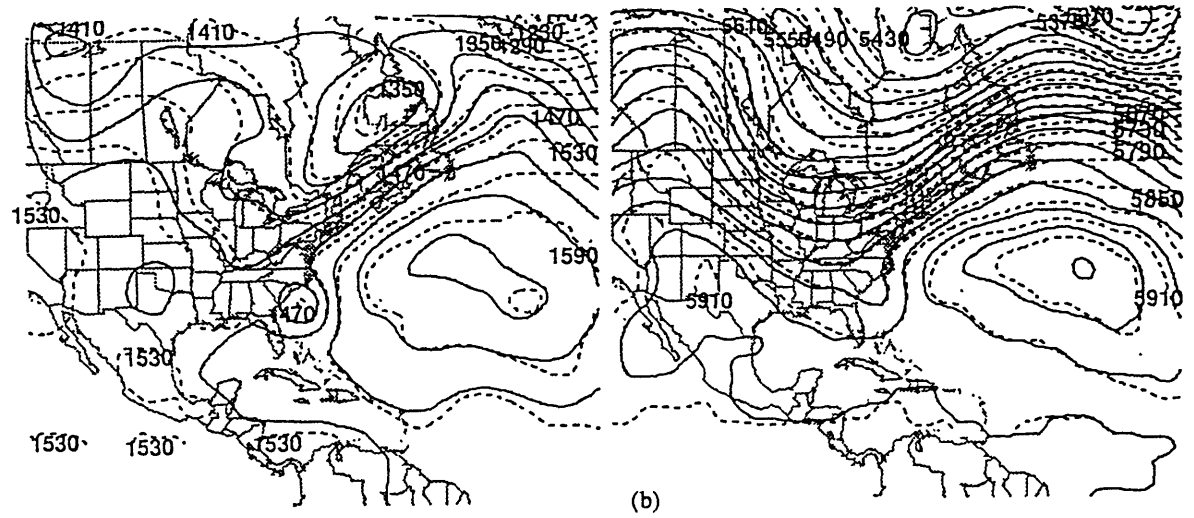

(a) 850 mb BALANCED H (BM+BPH and BT) 910818/1200

500 mb BALANCED H (BM+BPH and BT) 910818/1200

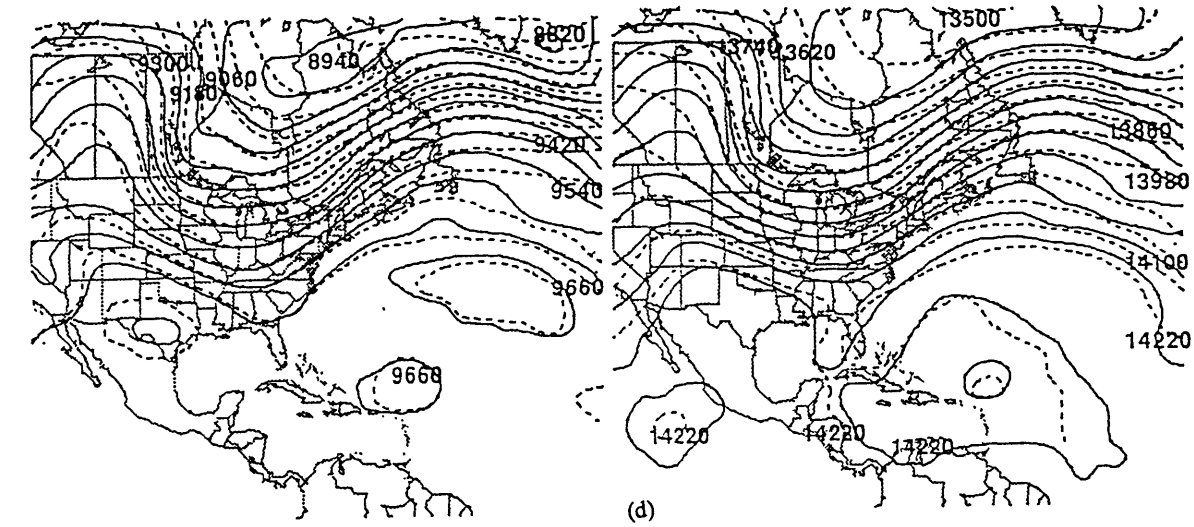

(c) 300 mb BALANCED H (BM+BPH and BT) 910818/1200

150 mb BALANCED H (BM+BPH and BT) 910818/1200

Figure 6.15 Balanced height fields associated with BT (dashed), and with BM+BPH (solid) at 1200 UTC 18 August 1991 at (a) 850 mb, (b) 500 mb, (c) 300 mb, and (d) 150 mb. Contour intervals are 30 m for (a) and (b), 60 m for (c) and (d).

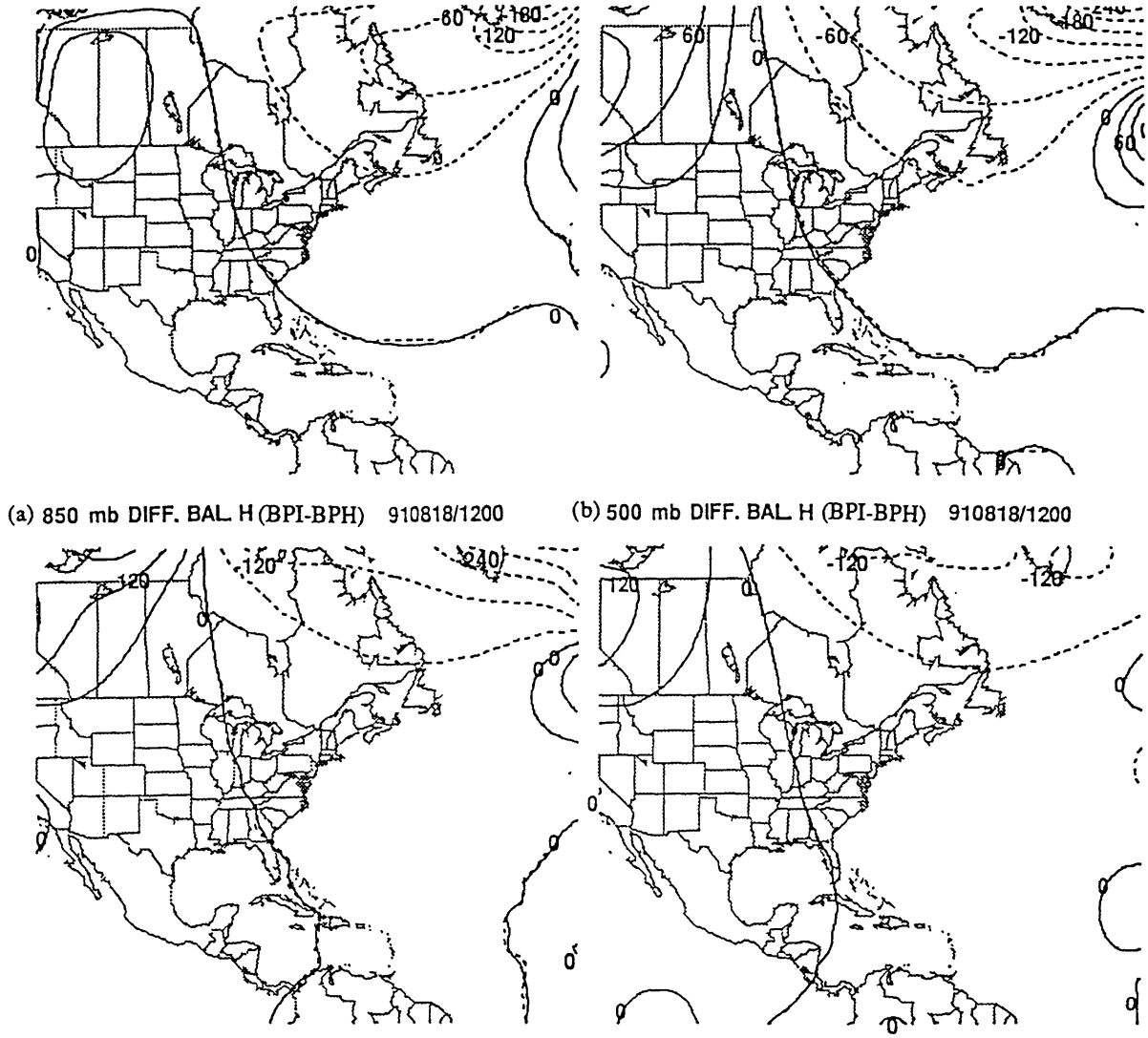

Figure 6.16 Differences between the balanced height fields associated with BPI and BPH at 1200 UTC 18 August 1991 at (a) 850 mb, (b) 500 mb, (c) 300 mb, and (d) 150 mb. Contour intervals are 30 m for (a) and (b), 60 m for (c) and (d). Solid (dashed) line indicates positive (negative) values.

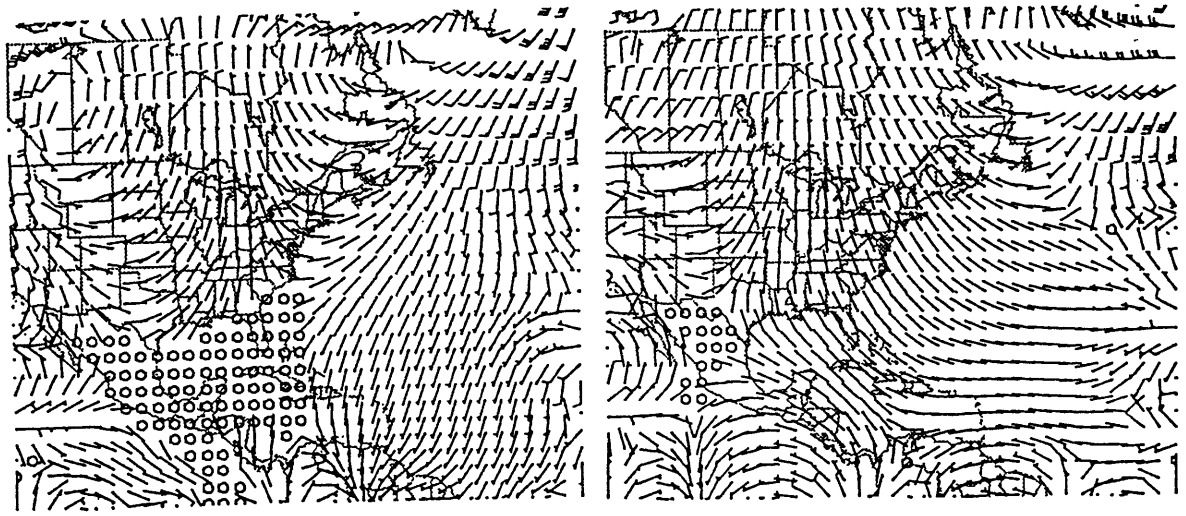

Figure 6.17 Differences between the balanced wind fields (wind barb plotted as in Fig. 6.4) associated with BPI and BPH at 1200 UTC 18 August 1991 at (a) 850 mb, (b) 500 mb, (c) 300 mb, and (d) 150 mb.

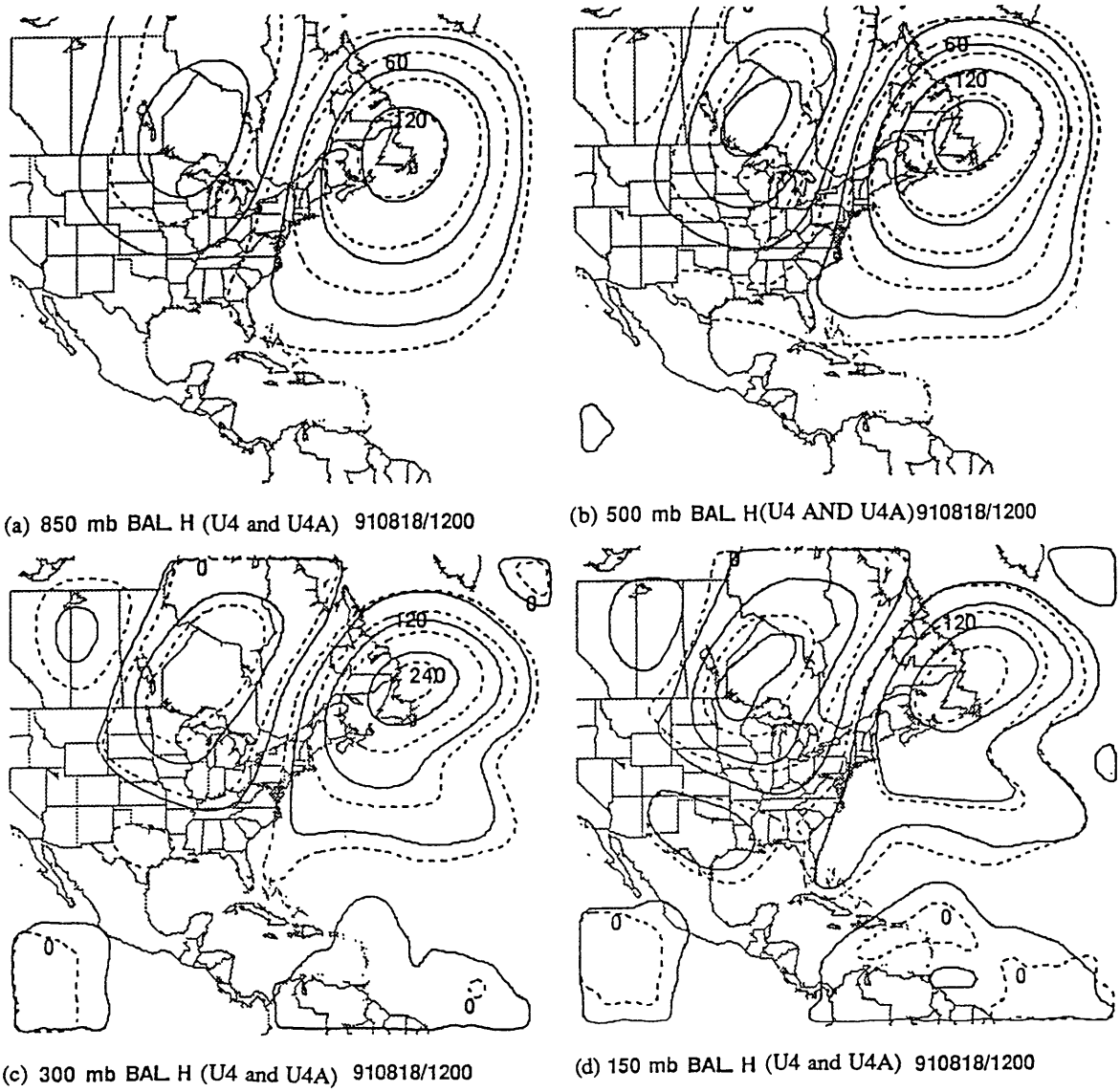

Figure 6.18 Balanced height fields associated with U4 (solid), and U4A (dashed) at 1200 UTC 18 August 1991 at (a) 850 mb, (b) 500 mb, (c) 300 mb, and (d) 150 mb. Contour intervals are 30 m for (a) and (b), 60 m for (c) and (d).

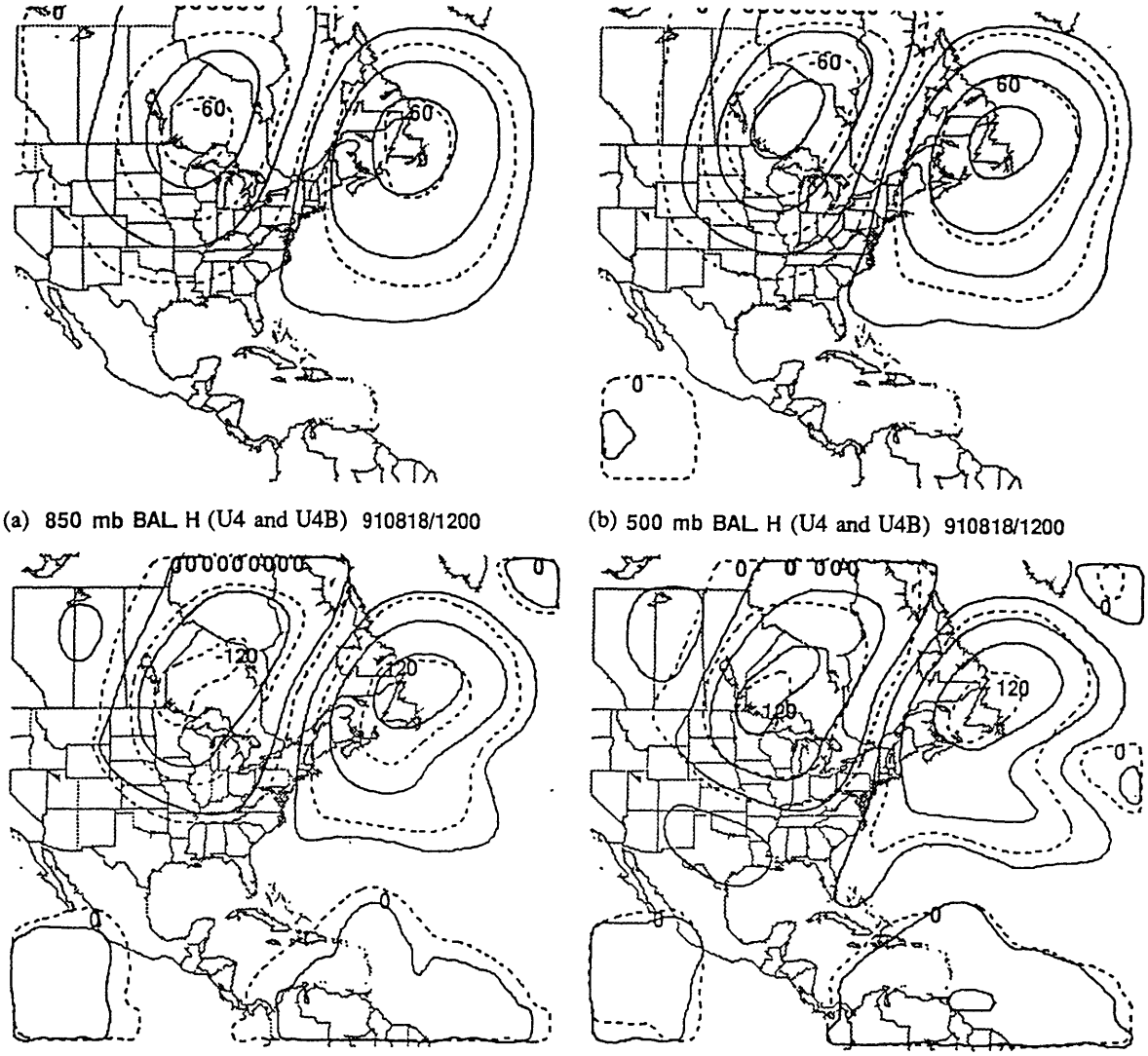

Figure 6.19 Balanced height fields associated with U4 (solid), and U4B (dashed) at 1200 UTC 18 August 1991 at (a) 850 mb, (b) 500 mb, (c) 300 mb, and (d) 150 mb. Contour intervals are 30 m for (a) and (b), 60 m for (c) and (d).

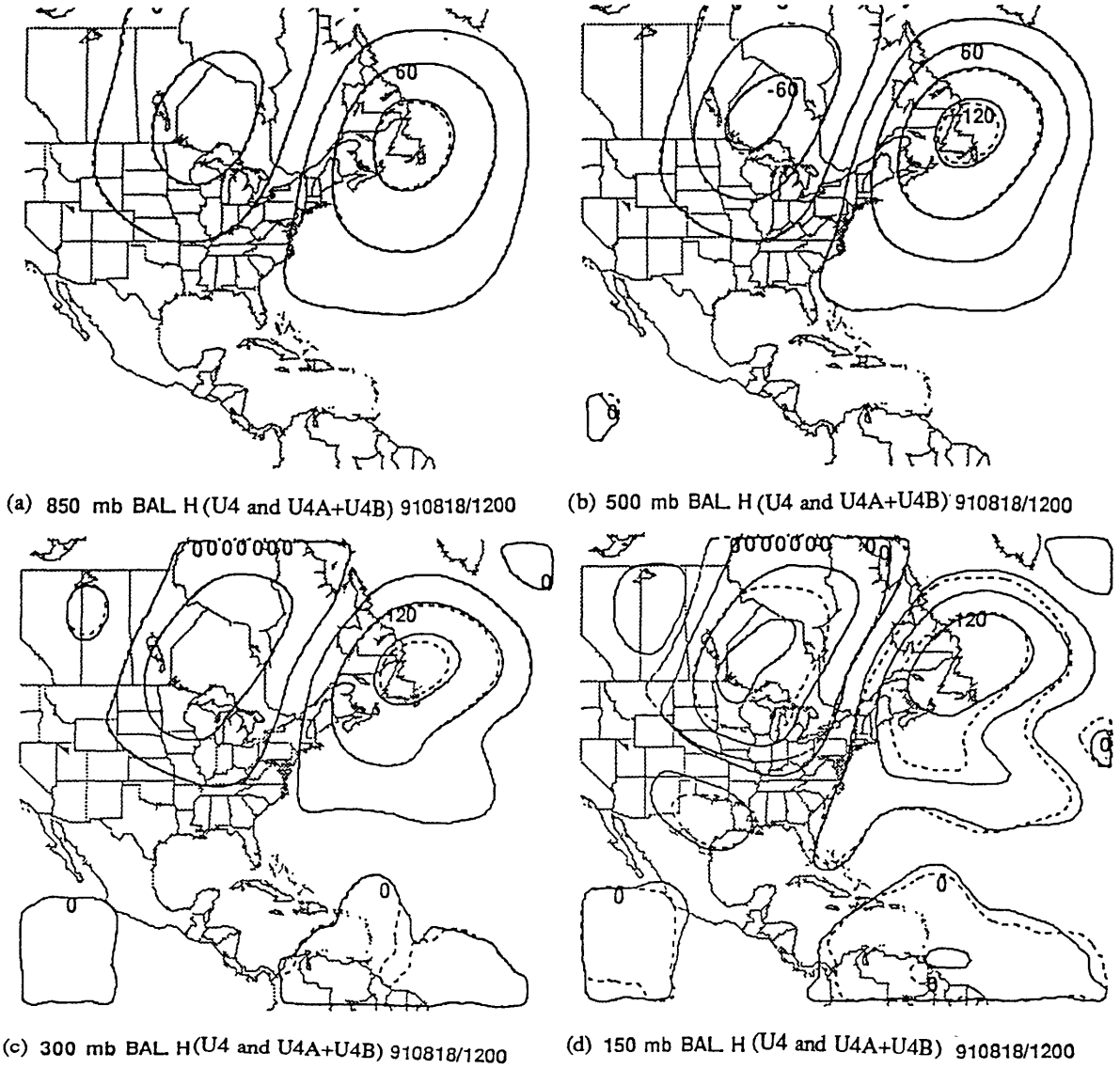

Figure 6.20 Balanced height fields associated with U4 (solid) and the average of U4A and U4B (dashed) at 1200 UTC 18 August 1991 at (a) 850 mb, (b) 500 mb, (c) 300 mb, and (d) 150 mb. Contour intervals are 30 m for (a) and (b), 60 m for (c) and (d).

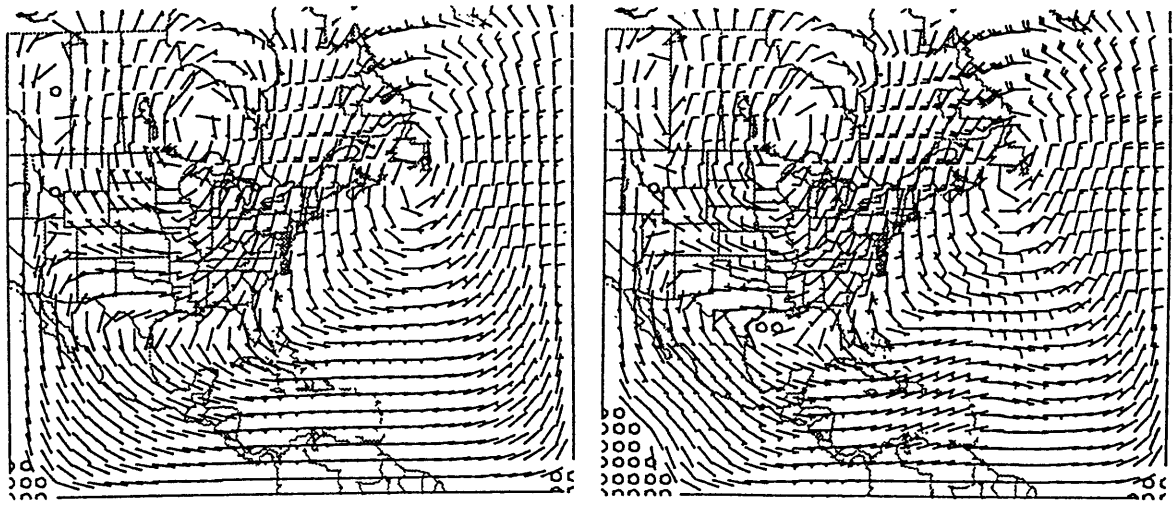

(a) 850 mb WIND (From U4 PERT. PV) 910818/1200 (b) 500 mb WIND (FROM U4 PERT. PV) 910818/1200

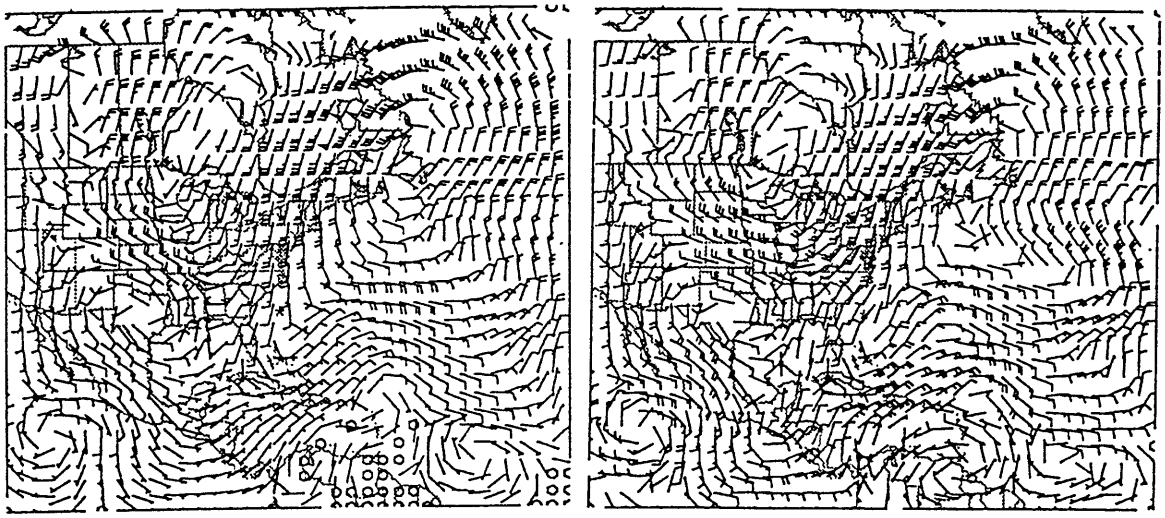

(c) 300 mb WIND (FROM U4 PERT. PV) 910818/1200 (d) 150 mb WIND (FROM U4 PERT. PV) 910818/1200

Figure 6.21 Balanced wind fields (wind barb plotted as in Fig. 6.4) associated with potential vorticity perturbation at and above 250 mb (U4) at 1200 UTC 18 August 1991 at (a) 850 mb, (b) 500 mb, (c) 300 mb, and (d) 150 mb. Hurricane Bob's best track positions are indicated by an asterisk (*).

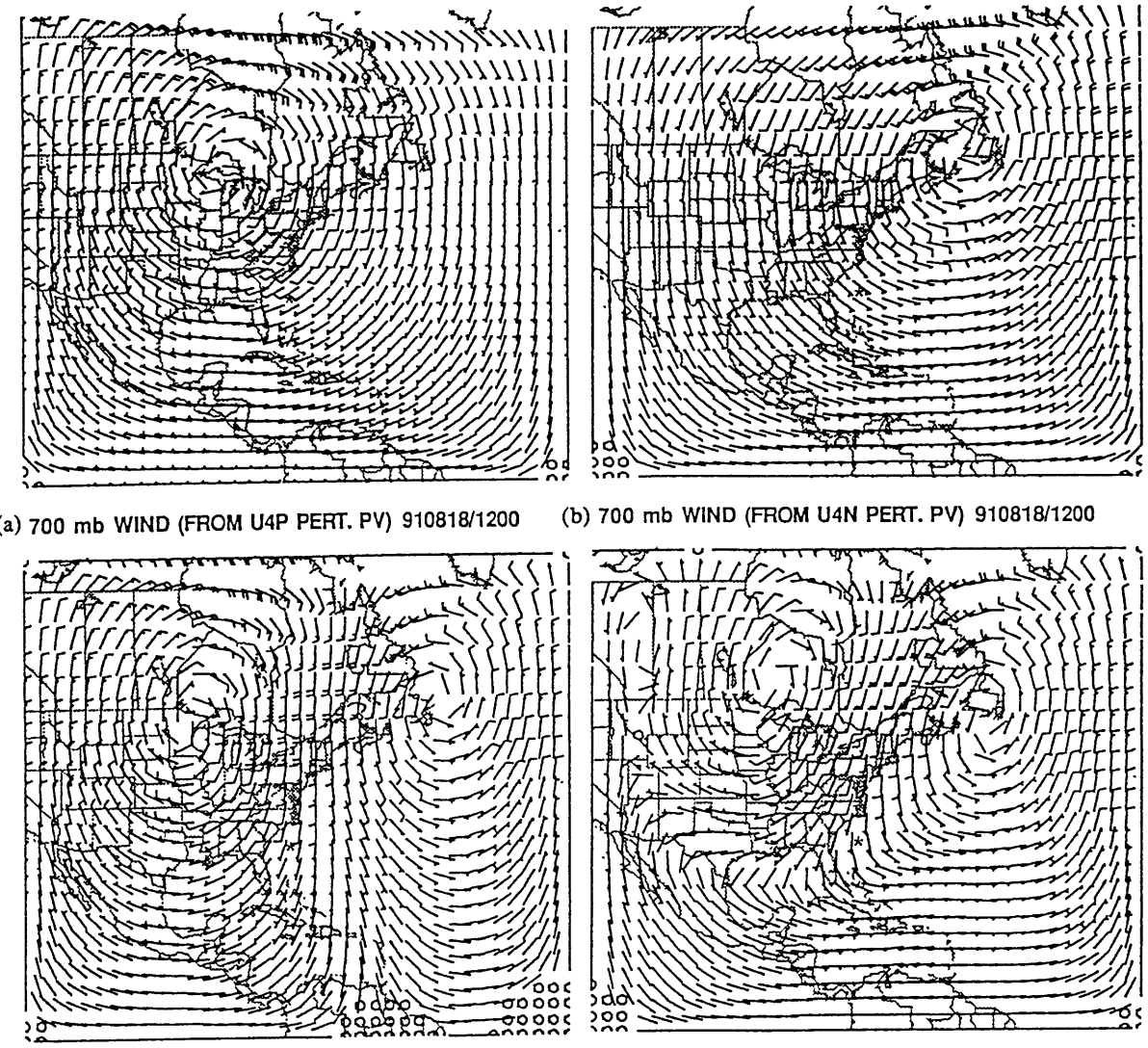

Figure 6.22 700-mb balanced wind fields (wind barb plotted as in Fig. 6.4) associated with (a) U4P, (b) U4N, (c) U4P+U4N, and (d) U4 at 1200 UTC 18 August 1991. Hurricane Bob's best track positions are indicated by an asterisk (*).

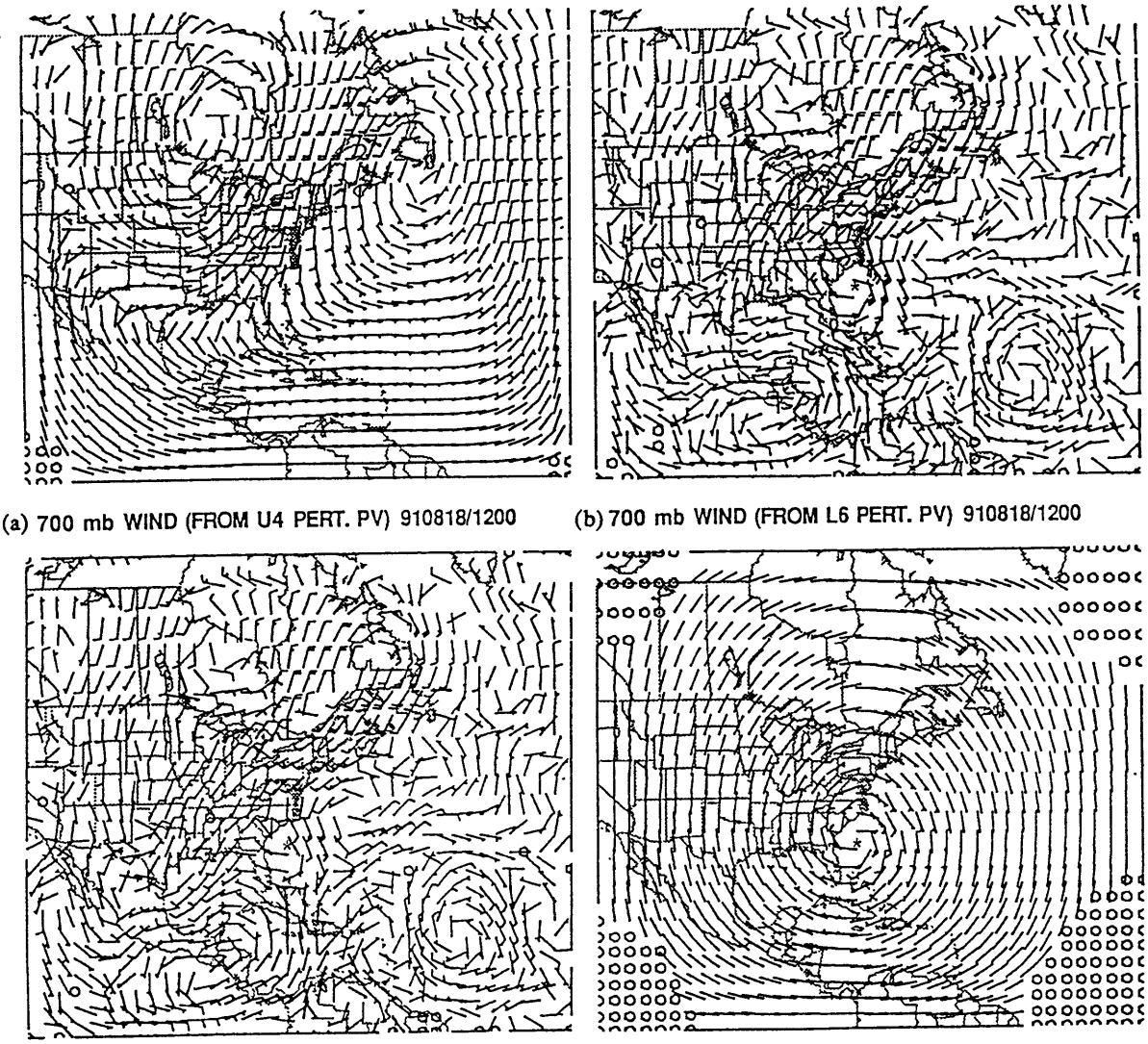

Figure 6.23 700-mb balanced wind fields (wind barb plotted as in Fig. 6.4) associated with (a) U4, (b) L6, (c) L6E, and (d) L6S at 1200 UTC 18 August 1991. Hurricane Bob's best track positions are indicated by an asterisk (*).

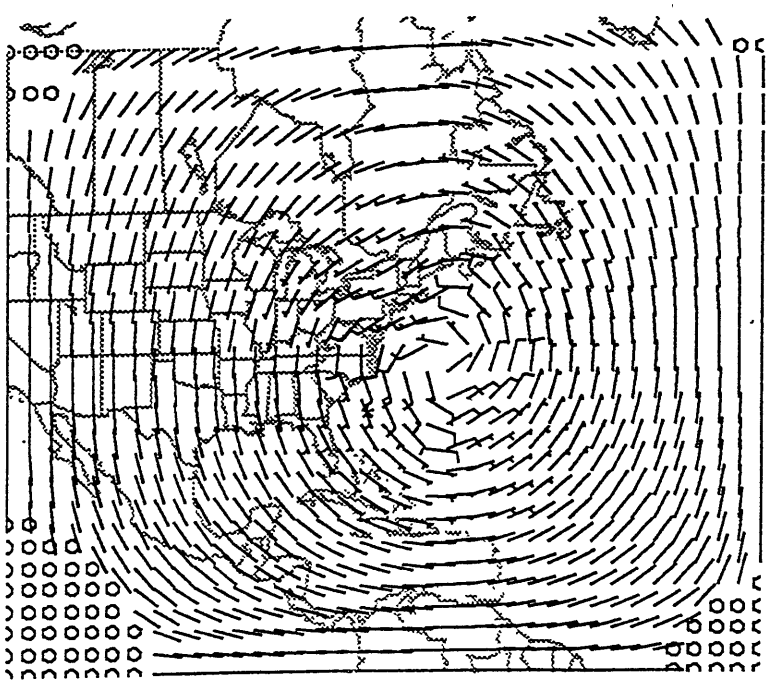

Figure 6.24 700-mb balanced wind fields (wind barb plotted as in Fig. 6.4) associated with L6N at 1200 UTC 18 August 1991. Hurricane Bob's best track positions are indicated by an asterisk (*).

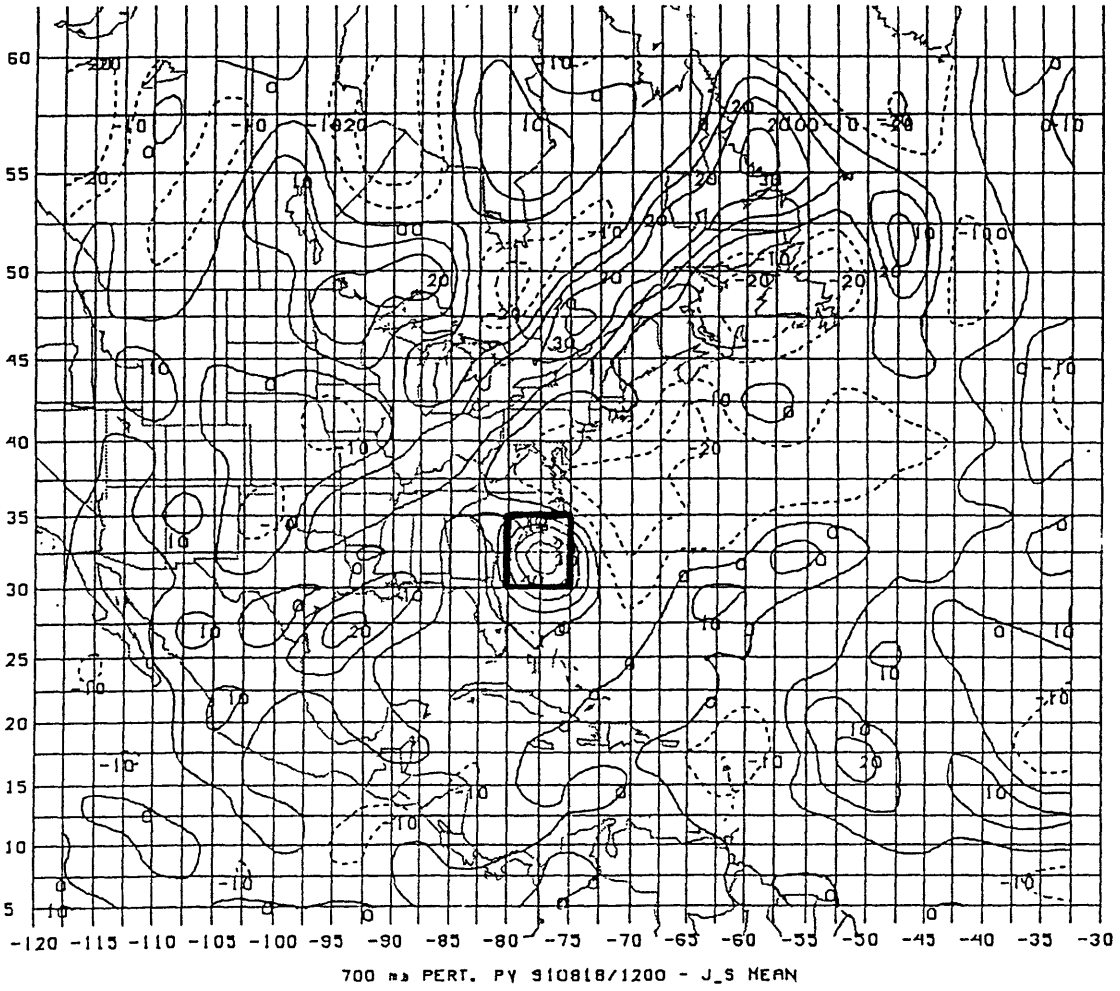

Figure 6.25 Ertel's potential vorticity perturbation field at 700 mb at 1200 UTC 18 August 1991. All positive (negative) values are represented by solid (dashed) lines. The unit is 0.01 PVU, and contour interval is 0.1 PVU. The area enclosed by heavy lines indicates the potential vorticity anomaly of Bob (L6S at 700 mb).

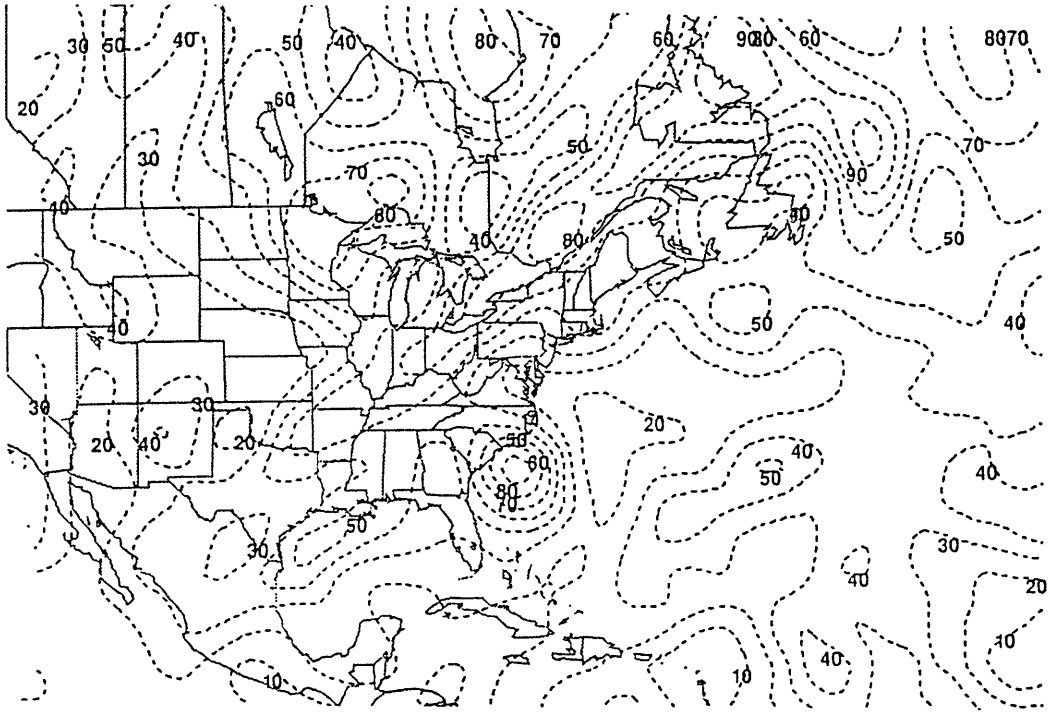

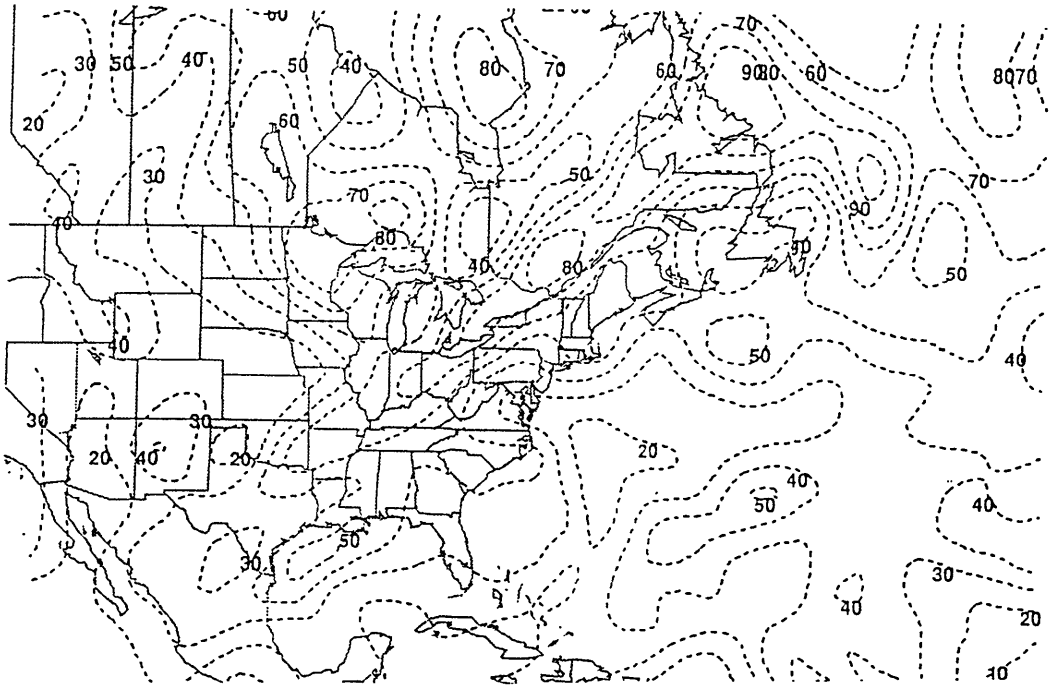

Figure 6.26 (a) Ertel's potential vorticity field at 700 mb at 1200 UTC 18 August 1991. (b) same as (a) but excluding L6S at 700 mb. The unit is 0.01 PVU, and contour interval is 0.1 PVU.

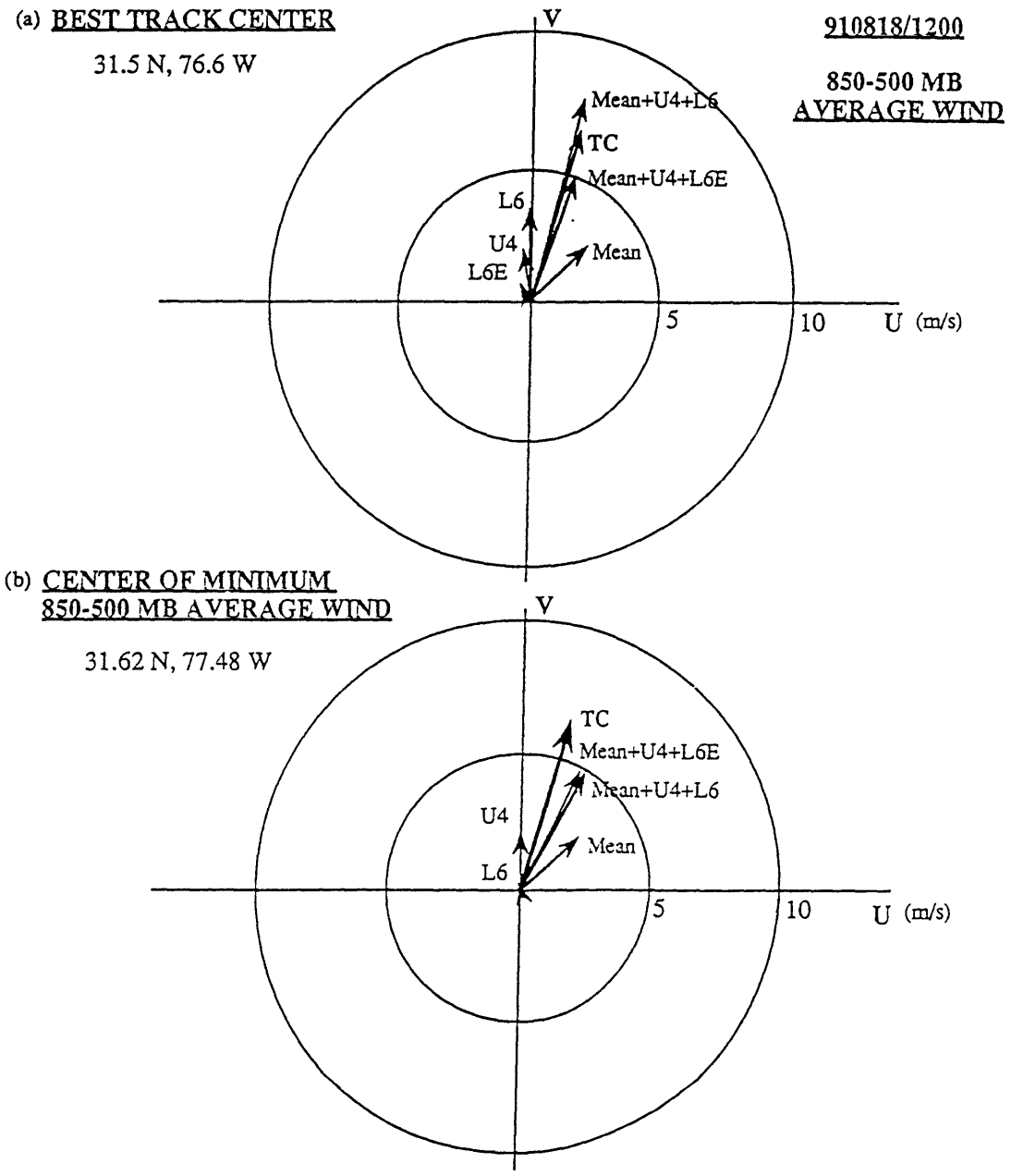

Figure 6.27 Velocity vectors of balanced flows and Hurricane Bob's motion at 1200 UTC 18 August 1991. Mean, U4, L6, and L6E represent the 850-500-mb pressure-averaged balanced flows associated with mean potential vorticity, potential vorticity perturbations of U4, L6, and L6E, respectively. Mean+U4+L6E represents the total hurricane advection flow. TC indicates Bob's motion estimated from every 6-hour best-track position. (a) Interpolation of the balanced wind fields at the best-track center; (b) at the 850-500-mb pressure-averaged balanced vortex center.

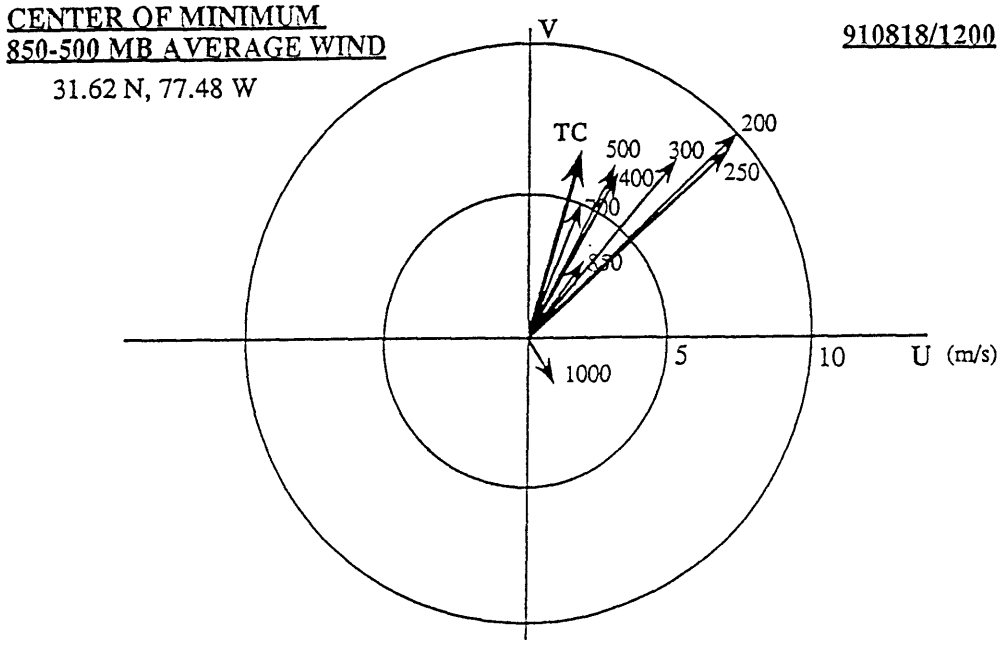

Figure 6.28 Velocity vectors of advection flow at each level and Hurricane Bob's motion at 1200 UTC 18 August 1991. The hurricane advection flow is defined as the interpolation of the balanced flows associated with mean, U4, and L6E at the 850-500-mb pressure-averaged balanced vortex center. TC indicates Bob's motion estimated from every 6-hour best-track position.

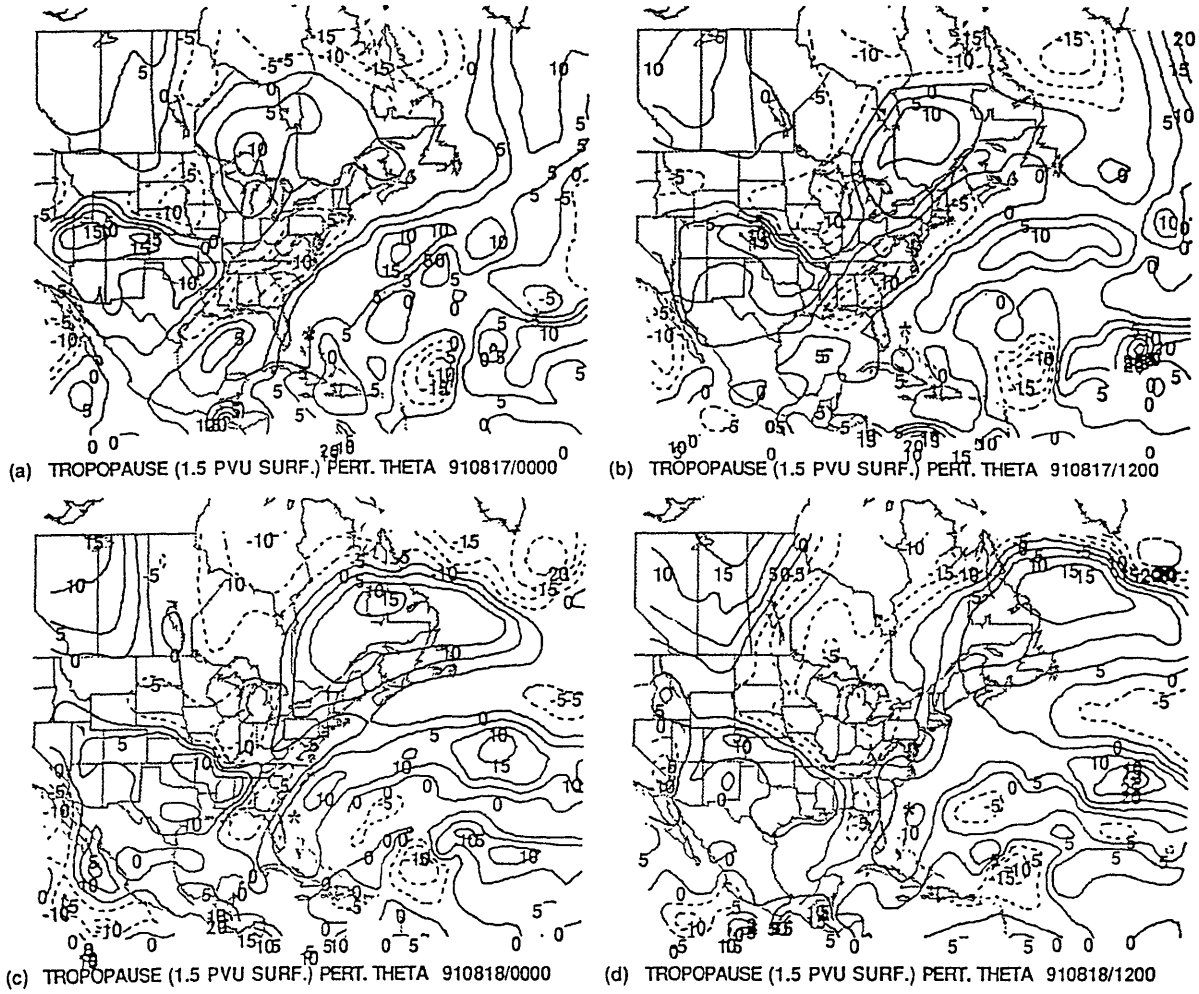

Figure 6.29 Time evolution of the tropopause potential temperature perturbation field (on the 1.5 PVU surface) from 0000 UTC 18 to 1200 UTC 20 August 1991. (a) 0000 UTC 17, (b) 1200 UTC 17, (c) 0000 UTC 18, (d) 1200 UTC 18, (e) 0000 UTC 19, (f) 1200 UTC 19, (g) 0000 UTC 20, and (h) 1200 UTC 20. The contour interval is 5 K. All positive (negative) values are represented by solid (dashed) lines. Hurricane Bob's best track positions are indicated by an asterisk (*).

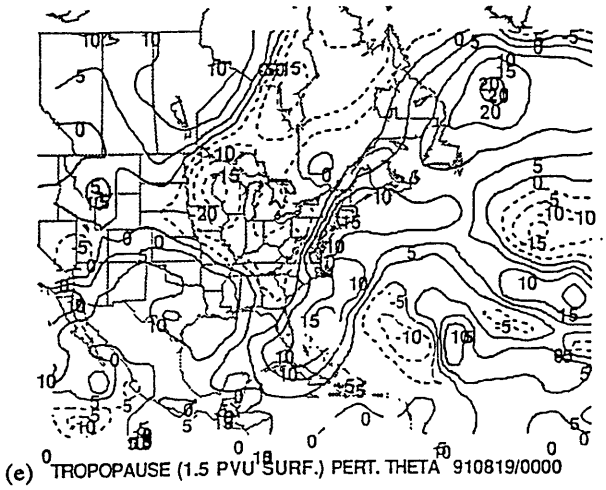

(e) TROPOPAUSE (1.5 PVU SURF.) PERT. THETA 910819/0000

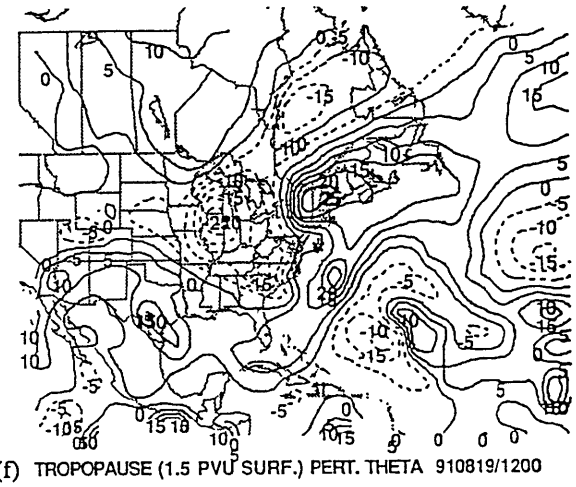

(f) TROPOPAUSE (1.5 PVU SURF.) PERT. THETA 910819/1200

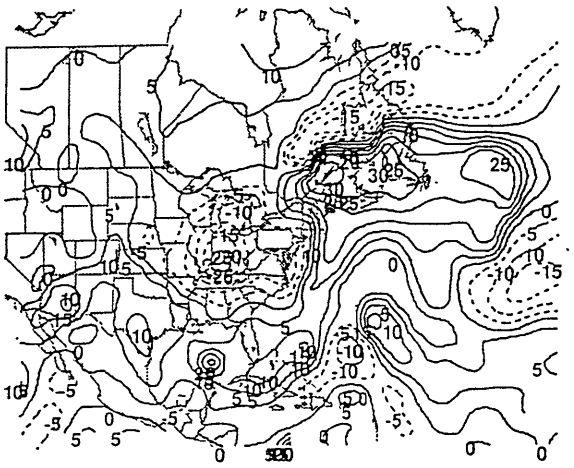

(g) TROPOPAUSE (1.5 PVU SURF.) PERT. THETA 910820/0000

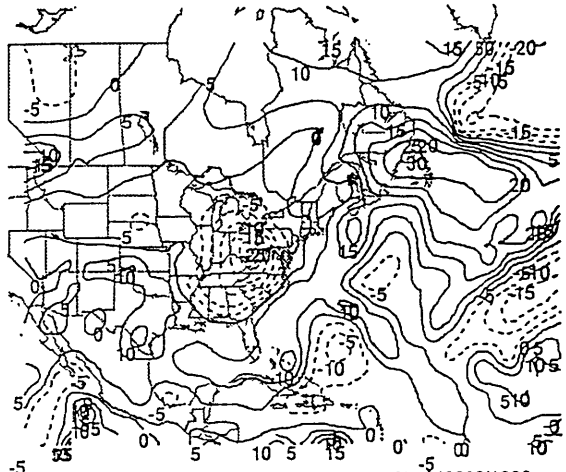

(h) TROPOPAUSE (1.5 PVU SURF.) PERT. THETA 910820/1200

Figure 6.29 (Continued)

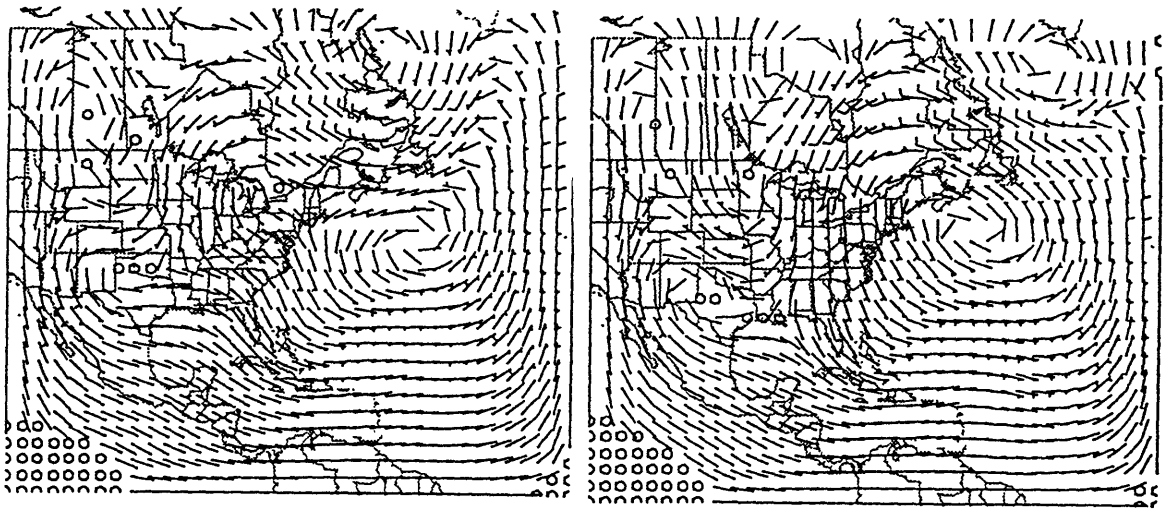

(a) 700 mb WIND (FROM U4 PERT. PV) 910817/0000

(b) 700 mb WIND (FROM U4 PERT. PV) 910817/1200

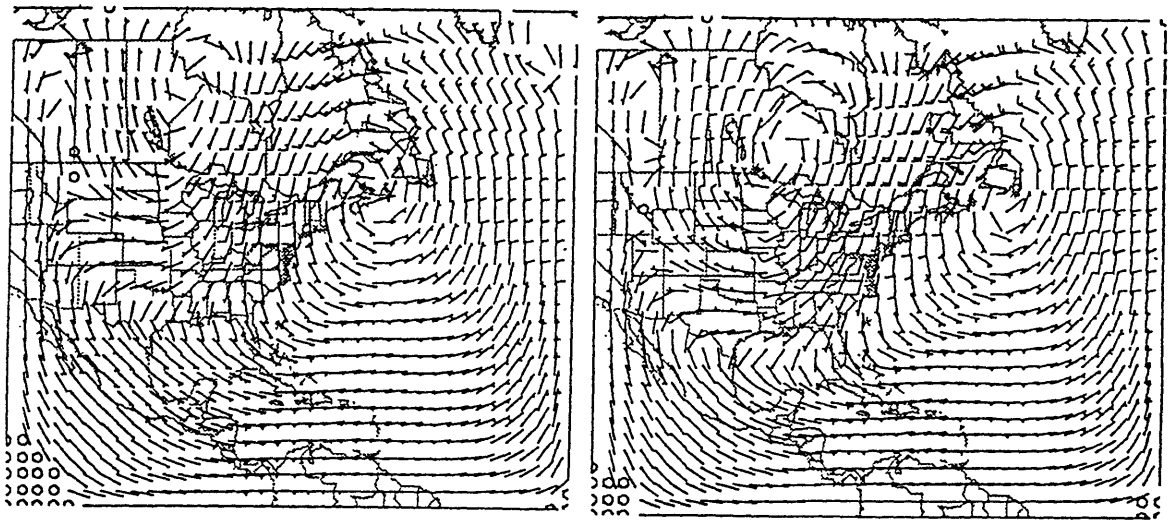

(c) 700 mb WIND (FROM U4 PERT. PV) 910818/0000

(d) 700 mb WIND (FROM U4 PERT. PV) 910818/1200

Figure 6.30 Time evolution of the 700-mb balanced wind field (wind barb plotted as in Fig. 6.4) associated with U4 from 0000 UTC 18 to 1200 UTC 20 August 1991. (a) 0000 UTC 17, (b) 1200 UTC 17, (c) 0000 UTC 18, (d) 1200 UTC 18, (e) 0000 UTC 19, (f) 1200 UTC 19, (g) 0000 UTC 20, and (h) 1200 UTC 20. Hurricane Bob's best track positions are indicated by an asterisk (*).

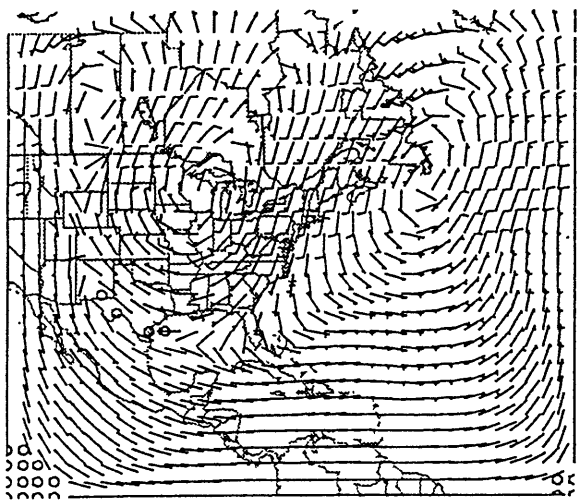

(e) 700 mb WIND (FROM U4 PERT. PV) 910819/0000

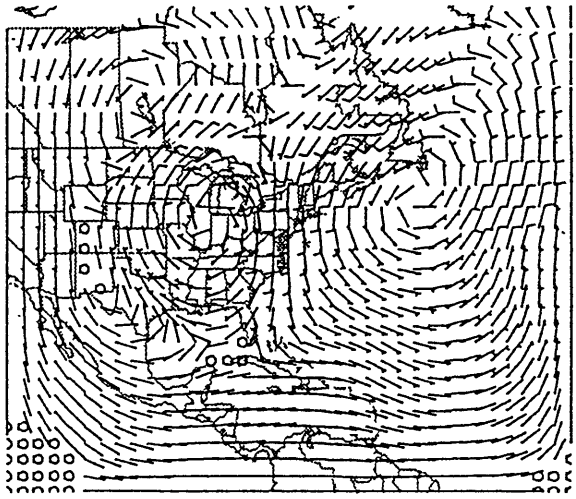

(f) 700 mb WIND (FROM U4 PERT. PV) 910819/1200

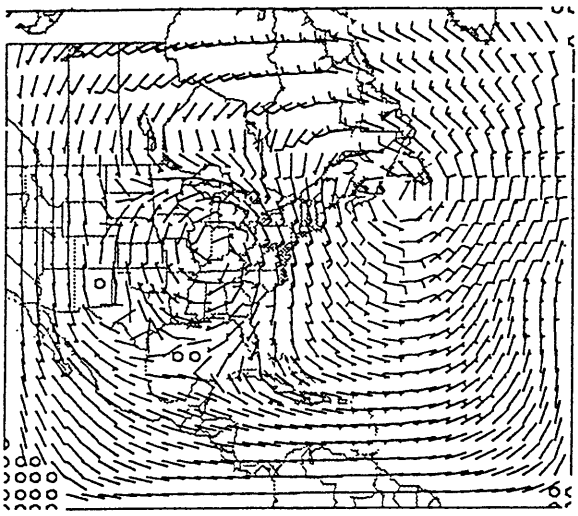

(g) 700 mb WIND (FROM U4 PERT. PV) 910820/0000

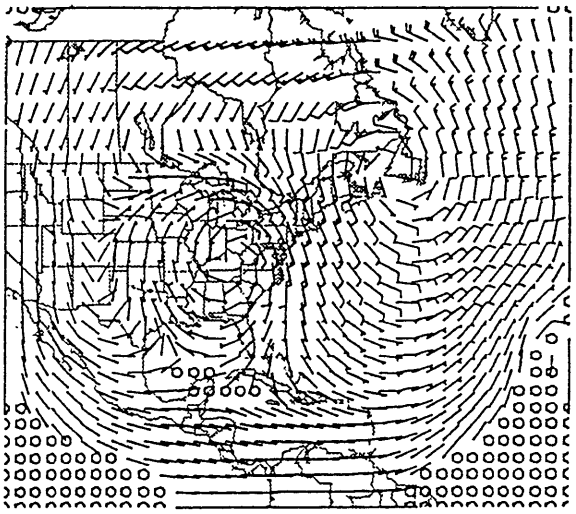

(h) 700 mb WIND (FROM U4 PERT. PV) 910820/1200

Figure 6.30 (Continued)

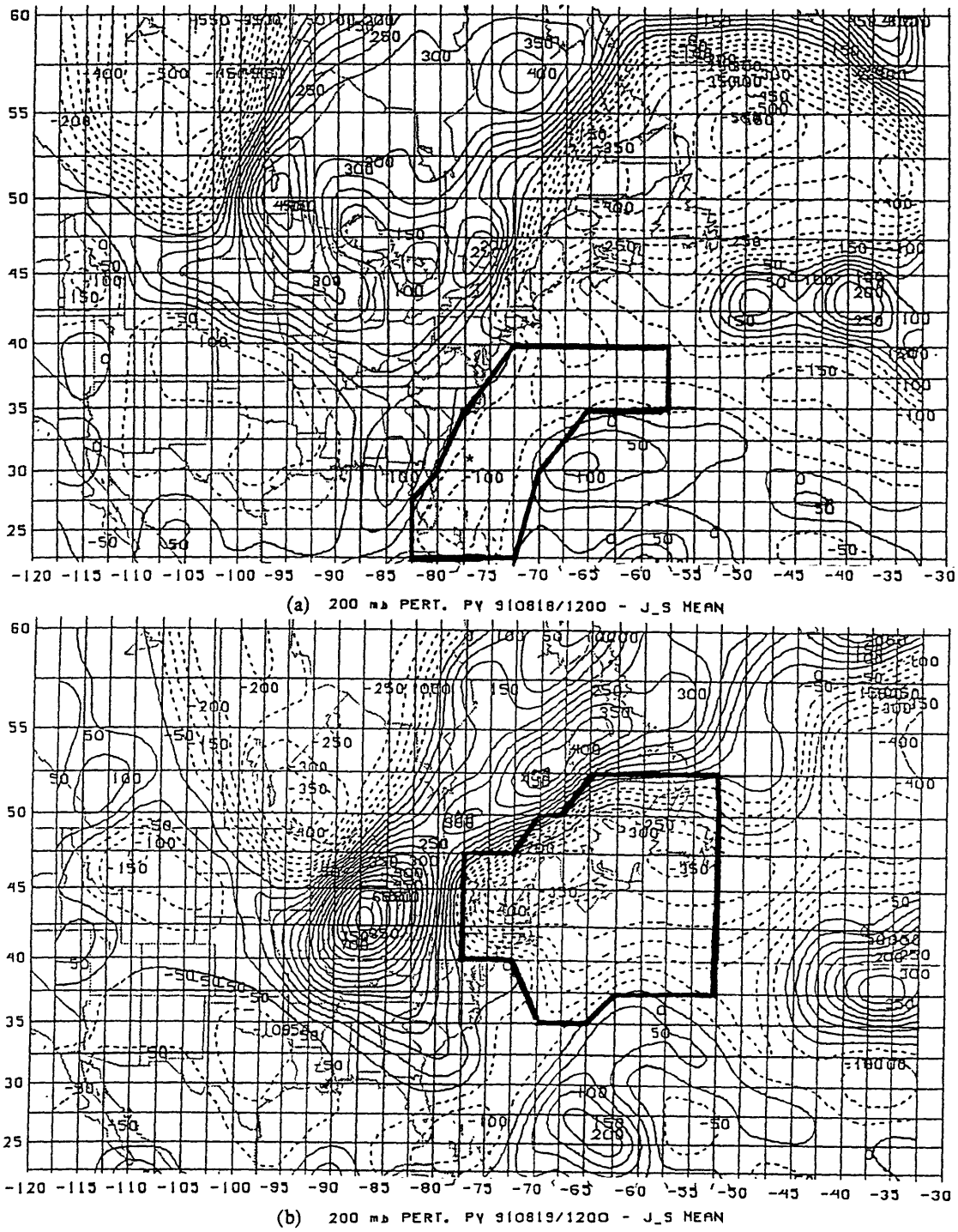

Figure 6.31 Ertel's potential vorticity perturbation field at 200 mb. (a) at 1200 UTC 18 August 1991, and (b) at 1200 UTC 19. The area enclosed by heavy lines indicates the potential vorticity anomaly (U4NA at 200 mb) to be inverted. The unit is 0.01 PVU, and contour interval is 0.5 PVU. All positive (negative) values are represented by solid (dashed) lines. Hurricane Bob's best track positions are indicated by an asterisk (*).

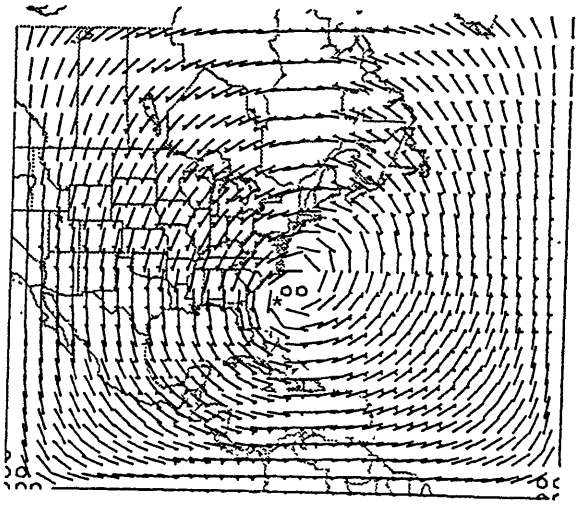

(a) 700 mb WIND (FROM U4NA) 910818/1200

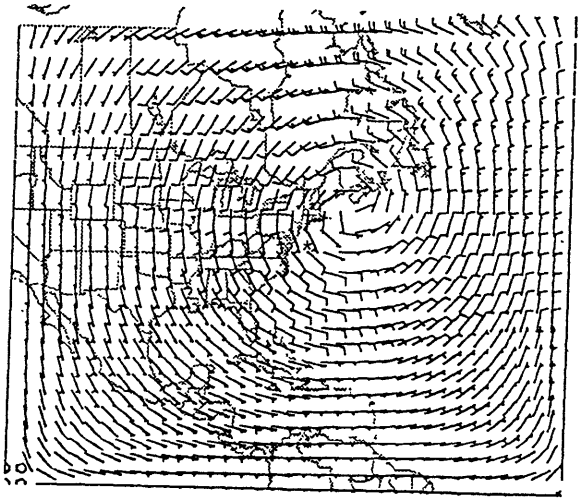

(b) 700 mb WIND (FROM U4NA) 910819/1200

Figure 6.32 700-mb balanced wind field (wind barb plotted as in Fig. 6.4) associated with U4NA. (a) at 1200 UTC 18 August 1991, and (b) at 1200 UTC 19. Hurricane Bob's best track positions are indicated by an asterisk (*).

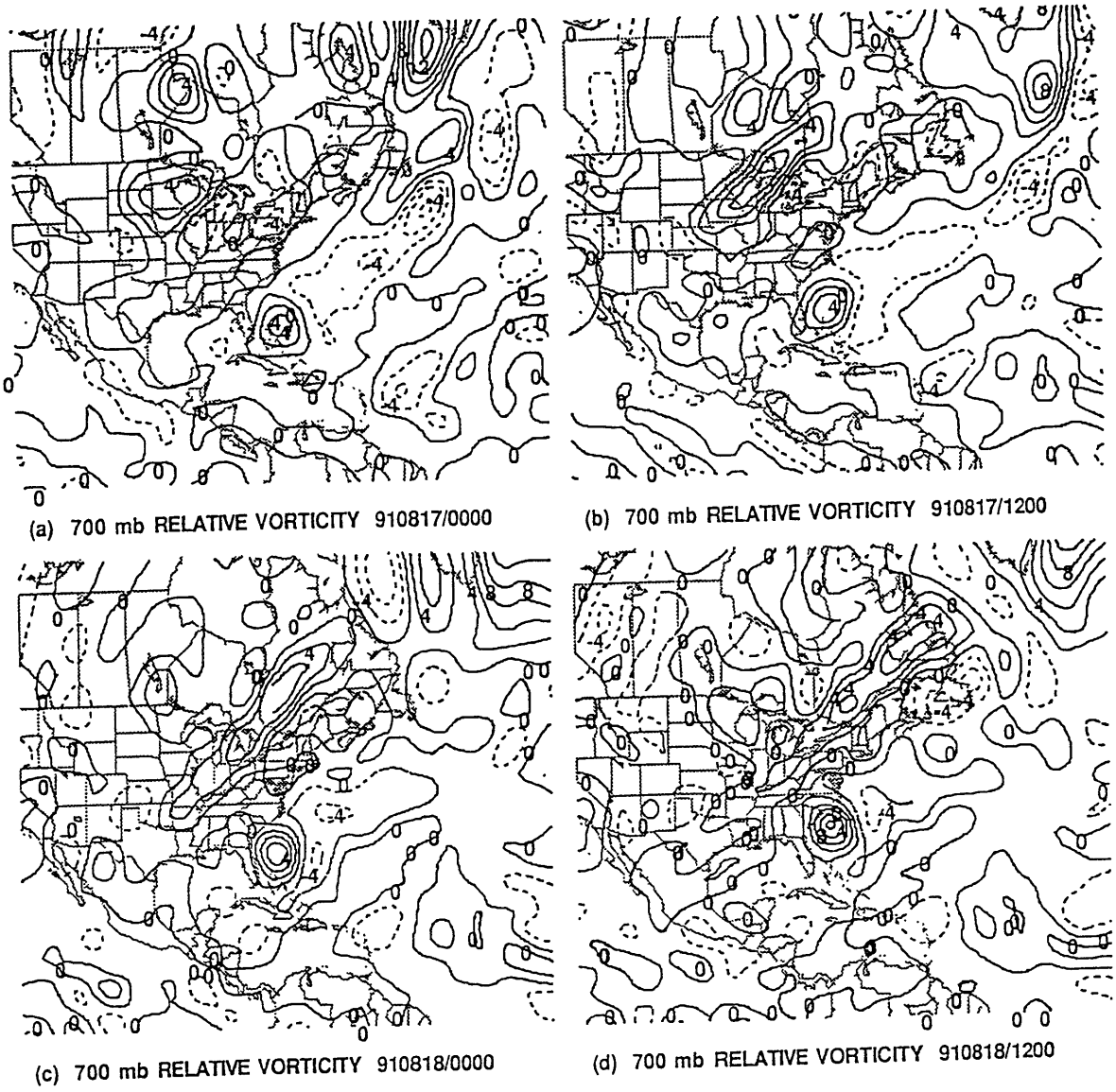

Figure 6.33 Time evolution of the relative vorticity field at 700 mb from 0000 UTC 18 to 1200 UTC 20 August 1991. (a) 0000 UTC 17, (b) 1200 UTC 17, (c) 0000 UTC 18, (d) 1200 UTC 18, (e) 0000 UTC 19, (f) 1200 UTC 19, (g) 0000 UTC 20, and (h) 1200 UTC 20. The contour intervals are 2×10^{-5} s^{-1} for (a), (b), (c) and (d), and 4×10^{-5} s^{-1} for (e), (f), (g) and (h).

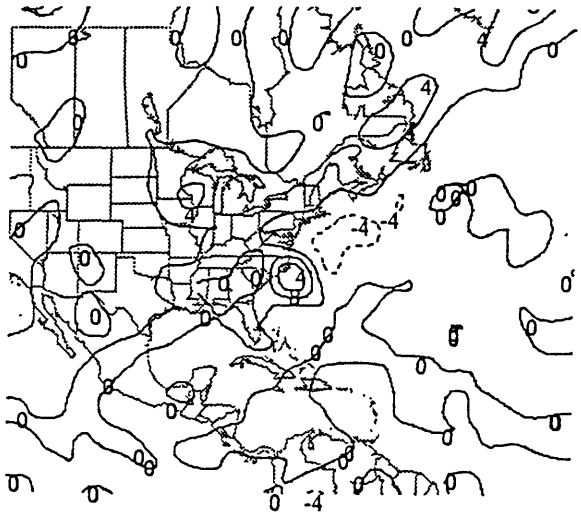

(e) 700 mb RELATIVE VORTICITY 910819/0000

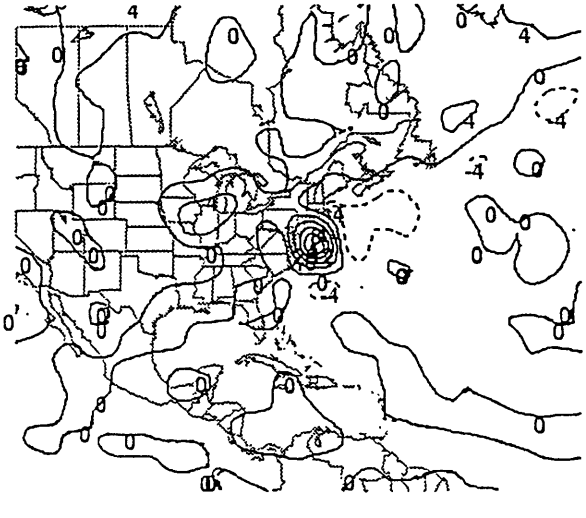

(f) 700 mb RELATIVE VORTICITY 910819/1200

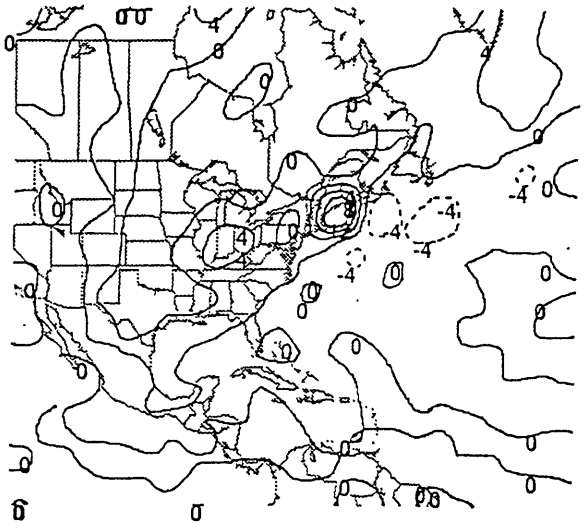

(g) 700 mb RELATIVE VORTICITY 910820/0000

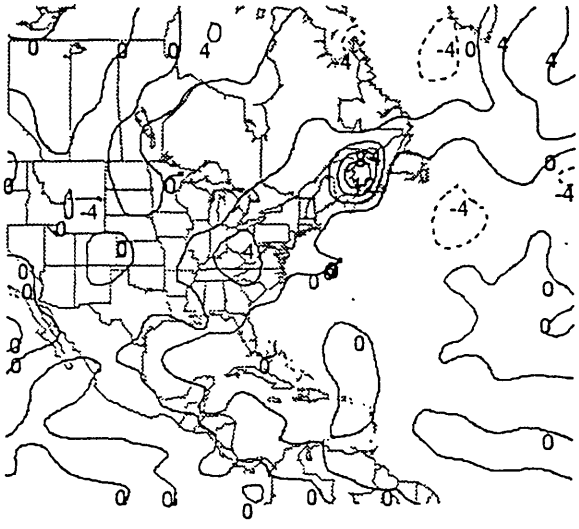

(h) 700 mb RELATIVE VORTICITY 910820/1200

Figure 6.33 (Continued)

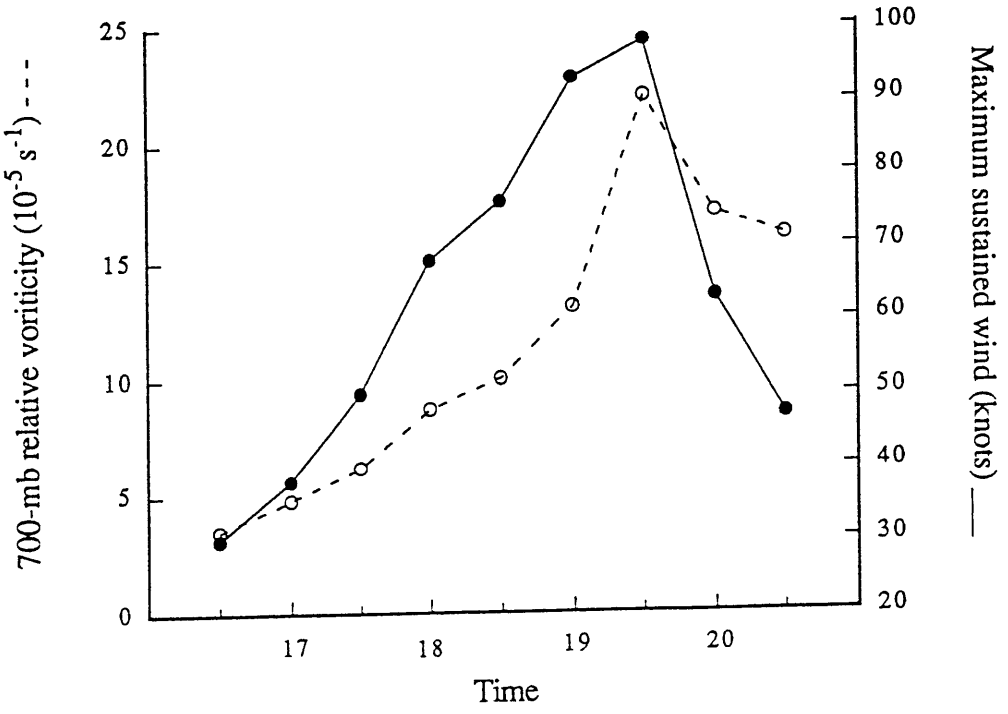

Figure 6.34 Analyzed maximum relative vorticity from NMC data (dashed) and best-track maximum sustained wind speed curve (solid, from Preliminary Report) for Hurricane Bob.

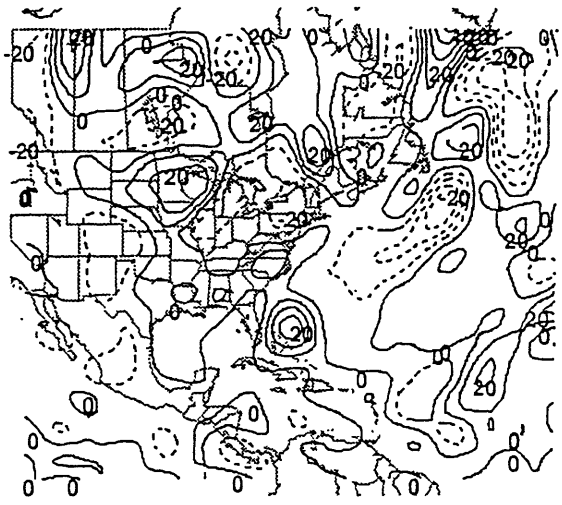

(a) 700 mb PERT. PV 910817/0000 - J_S MEAN

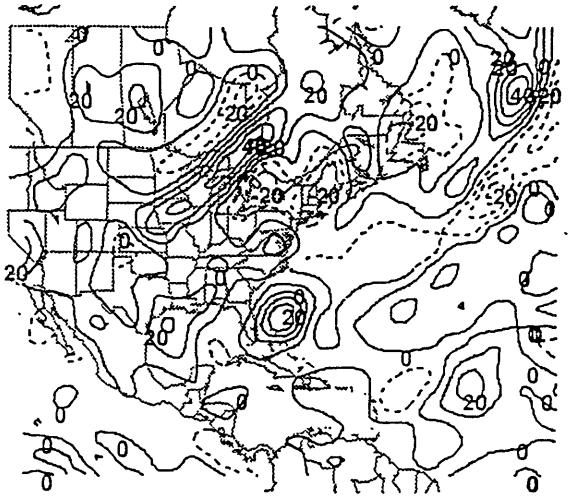

(b) 700 mb PERT. PV 910817/1200 - J_S MEAN

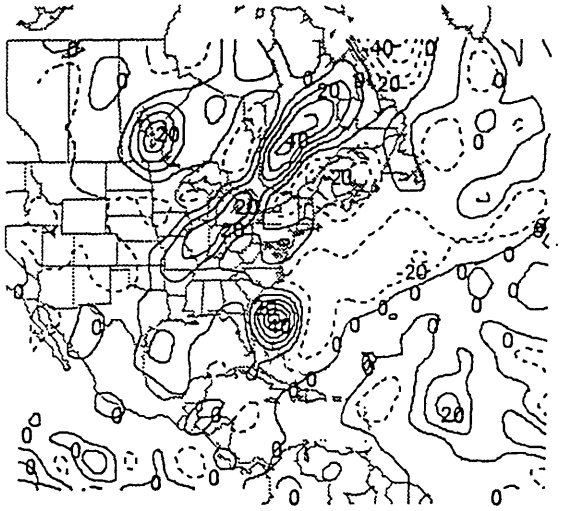

(c) 700 mb PERT. PV 910818/0000 - J_S MEAN

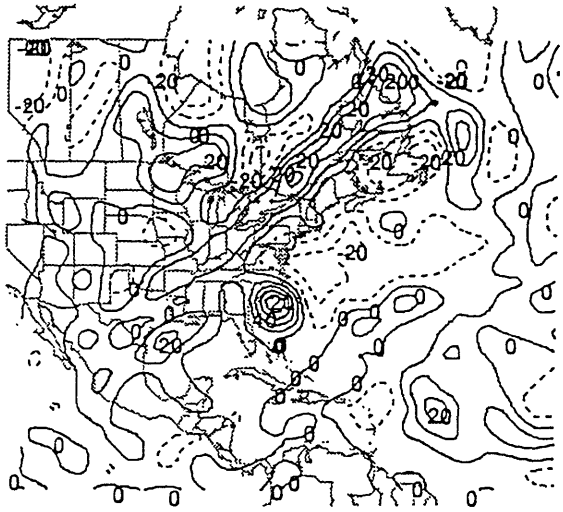

(d) 700 mb PERT. PV 910818/1200 - J_S MEAN

Figure 6.35 Time evolution of the Ertel's potential vorticity perturbation field at 700 mb from 0000 UTC 18 to 1200 UTC 20 August 1991. (a) 0000 UTC 17, (b) 1200 UTC 17, (c) 0000 UTC 18, (d) 1200 UTC 18, (e) 0000 UTC 19, (f) 1200 UTC 19, (g) 0000 UTC 20, and (h) 1200 UTC 20. The unit is 0.01 PVU, and contour intervals are 0.1 PVU for (a), (b), (c) and (d), and 0.2 PVU for (e), (f), (g) and (h). All positive (negative) values are represented by solid (dashed) lines.

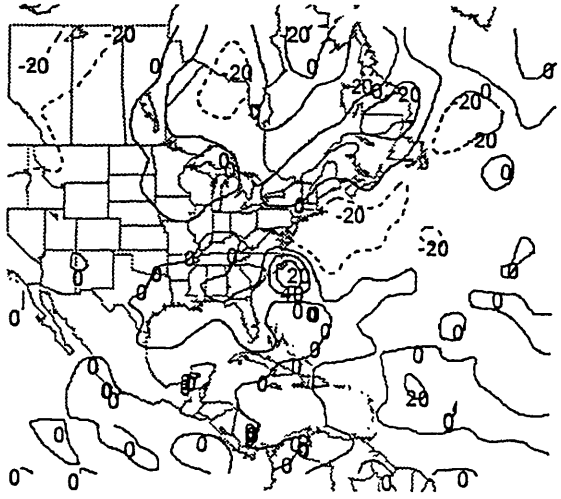

(e) 700 mb PERT. PV 910819/0000 - J_S MEAN

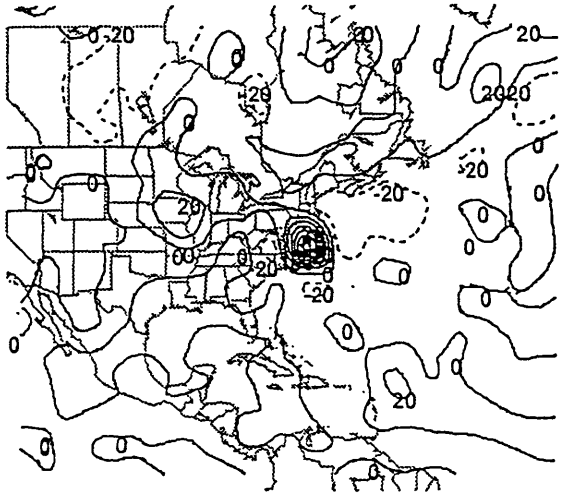

(f) 700 mb PERT. PV 910819/1200 - J_S MEAN

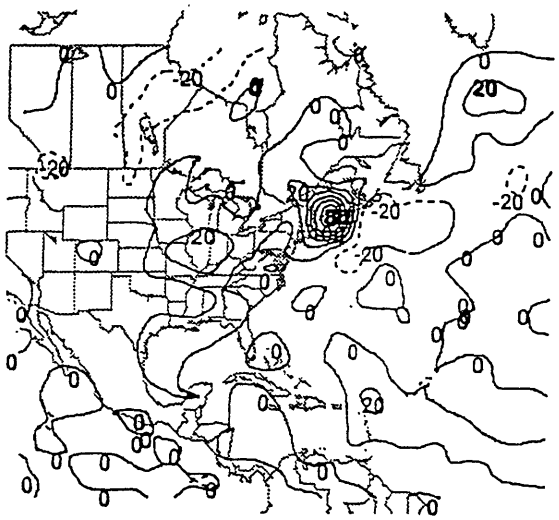

(g) 700 mb PERT. PV 910820/0000 - J_S MEAN

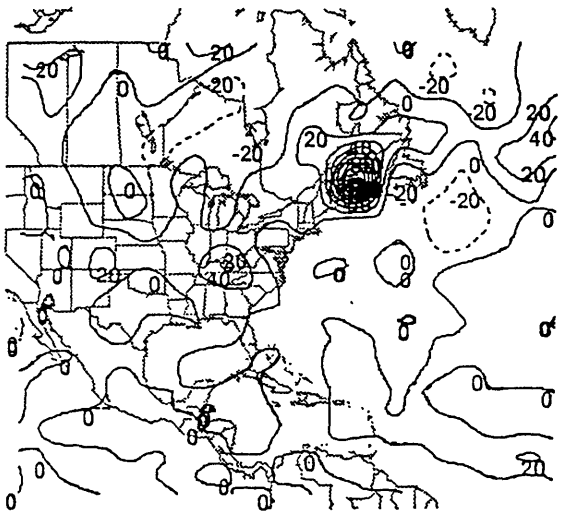

(h) 700 mb PERT. PV 910820/1200 - J_S MEAN

Figure 6.35 (Continued)

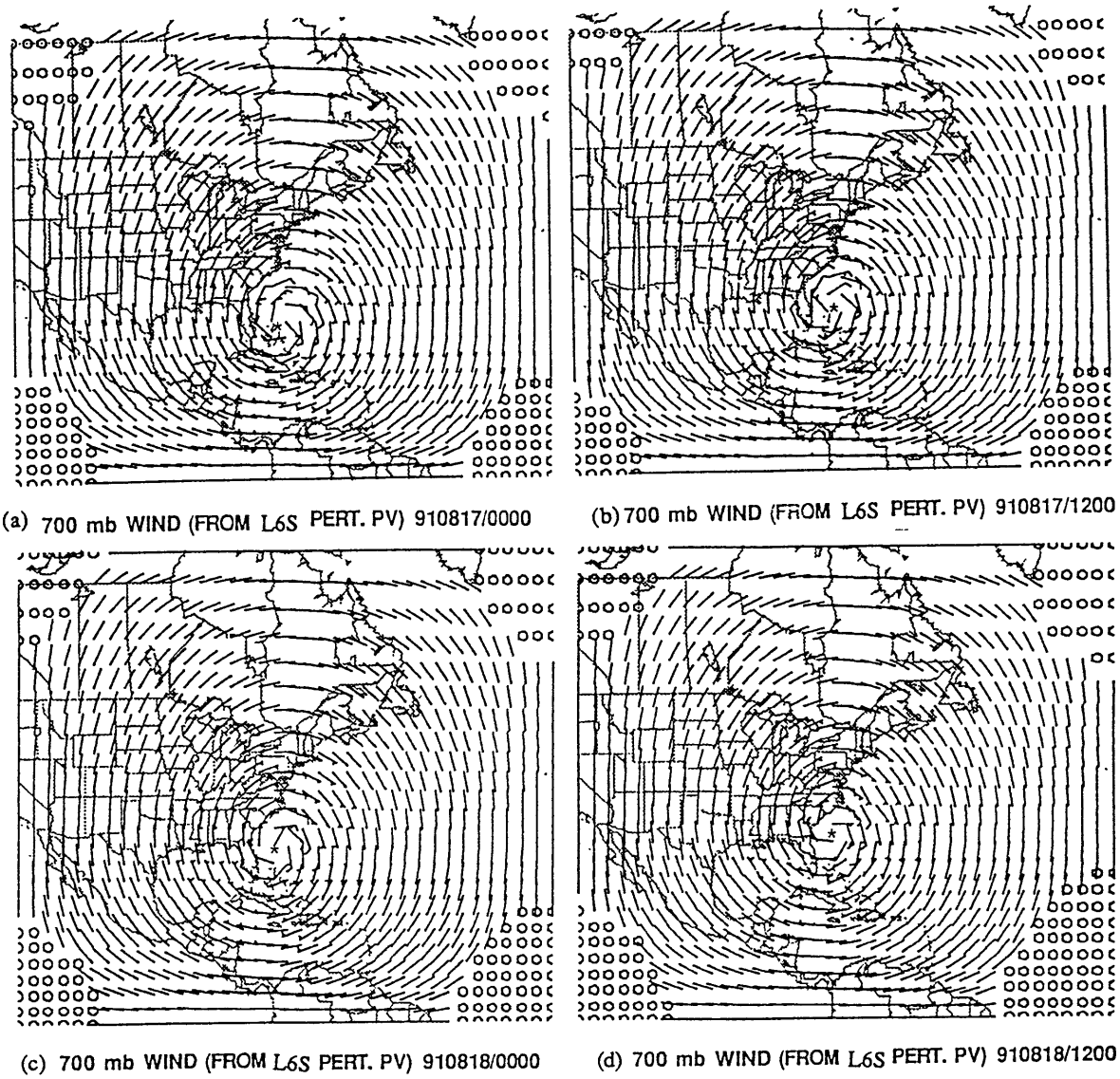

Figure 6.36 Time evolution of the 700-mb balanced wind field (wind barb plotted as in Fig. 6.4) associated with L6S from 0000 UTC 18 to 1200 UTC 20 August 1991. (a) 0000 UTC 17, (b) 1200 UTC 17, (c) 0000 UTC 18, (d) 1200 UTC 18, (e) 0000 UTC 19, (f) 1200 UTC 19, (g) 0000 UTC 20, and (h) 1200 UTC 20. Hurricane Bob's best track positions are indicated by an asterisk (*).

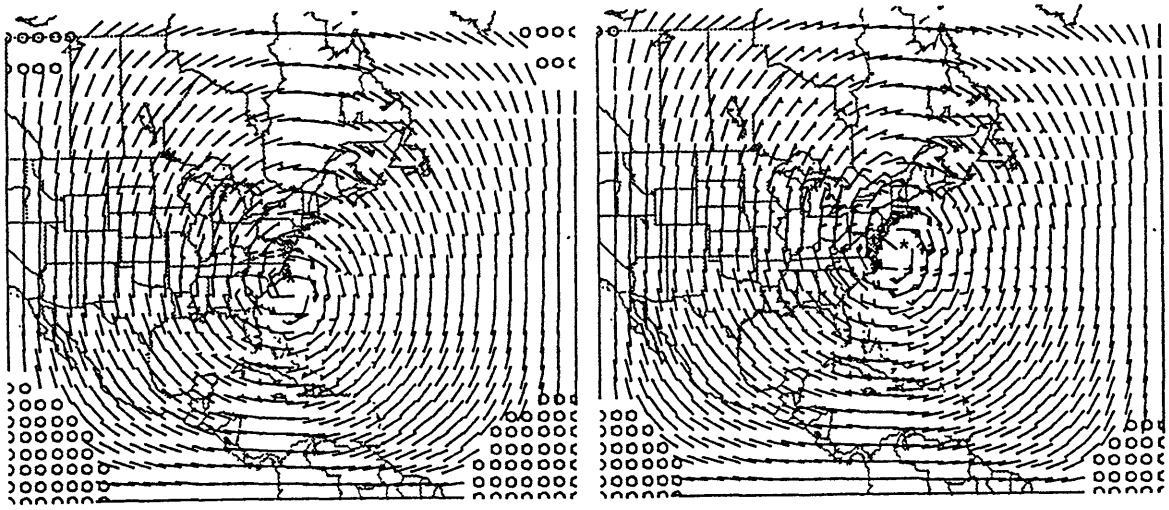

(e) 700 mb WIND (FROM L6S PERT. PV) 910819/0000 (f) 700 mb WIND (FROM L6S PERT. PV) 910819/1200

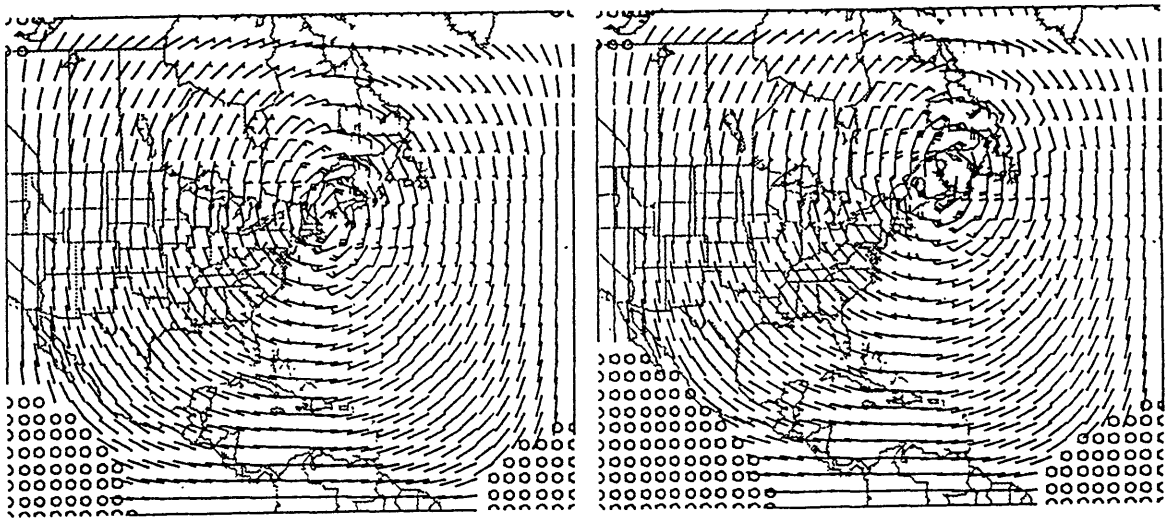

(g) 700 mb WIND (FROM L6S PERT. PV) 910820/0000 (h) 700 mb WIND (FROM L6S PERT. PV) 910820/1200

Figure 6.36 (Continued)

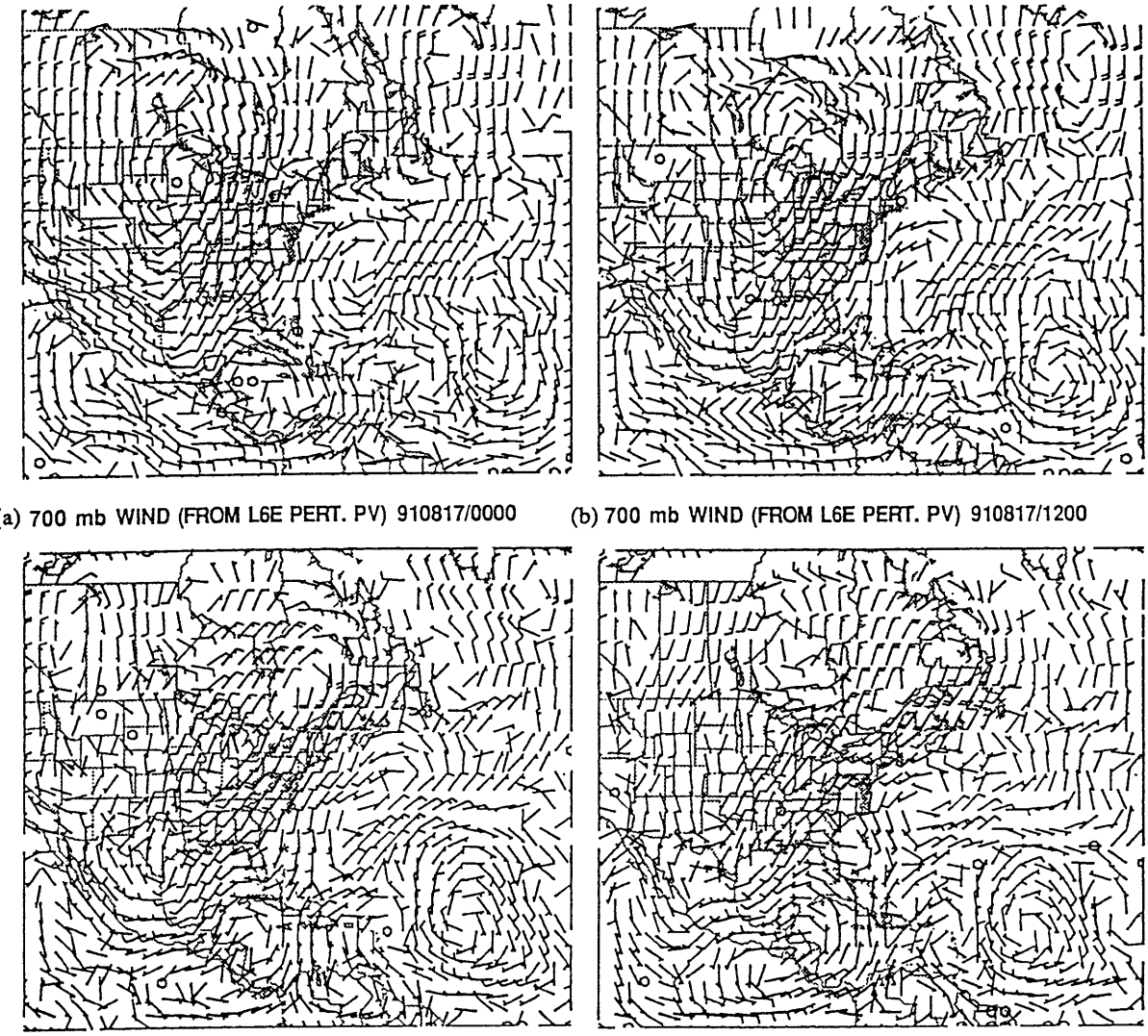

Figure 6.37 Time evolution of the 700-mb balanced wind field (wind barb plotted as in Fig. 6.4) associated with L6E from 0000 UTC 18 to 1200 UTC 20 August 1991. (a) 0000 UTC 17, (b) 1200 UTC 17, (c) 0000 UTC 18, (d) 1200 UTC 18, (e) 0000 UTC 19, (f) 1200 UTC 19, (g) 0000 UTC 20, and (h) 1200 UTC 20. Hurricane Bob's best track positions are indicated by an asterisk (*).

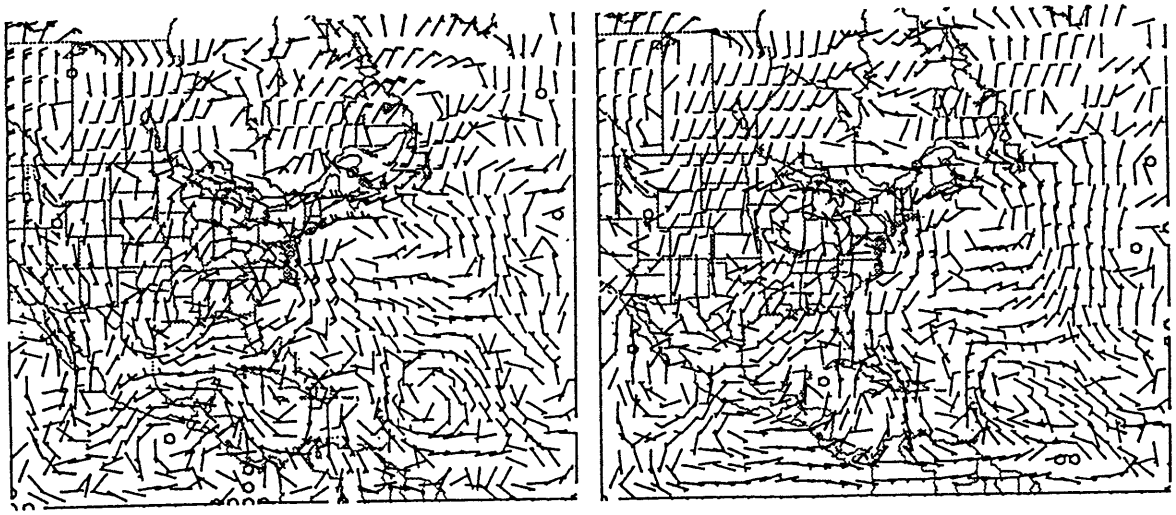

(e) 700 mb WIND (FROM L6E PERT. PV) 910819/0000 (f) 700 mb WIND (FROM L6E PERT. PV) 910819/1200

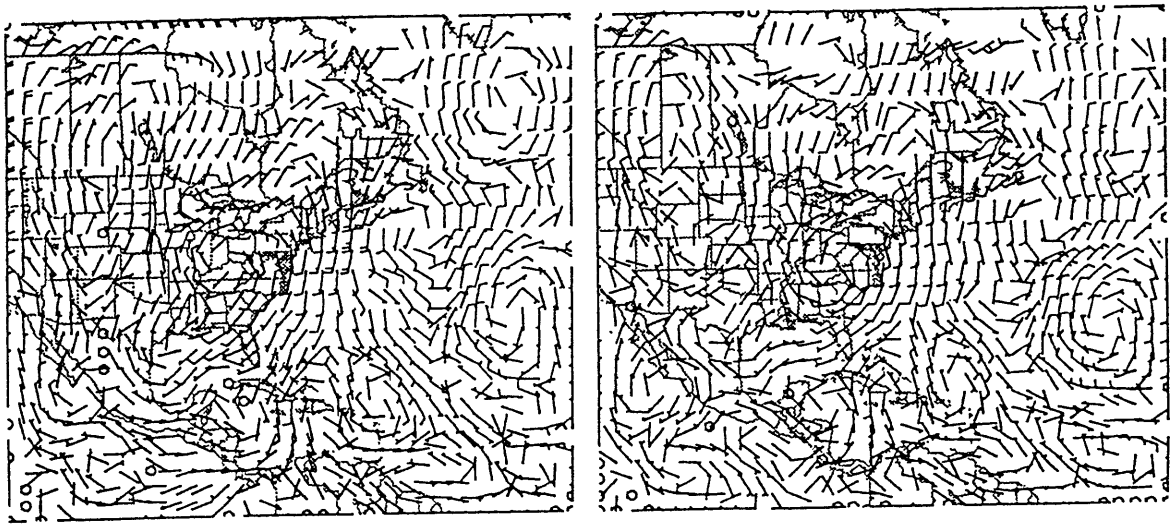

(g) 700 mb WIND (FROM L6E PERT. PV) 910820/0000 (h) 700 mb WIND (FROM L6E PERT. PV) 910820/1200

Figure 6.37 (Continued)

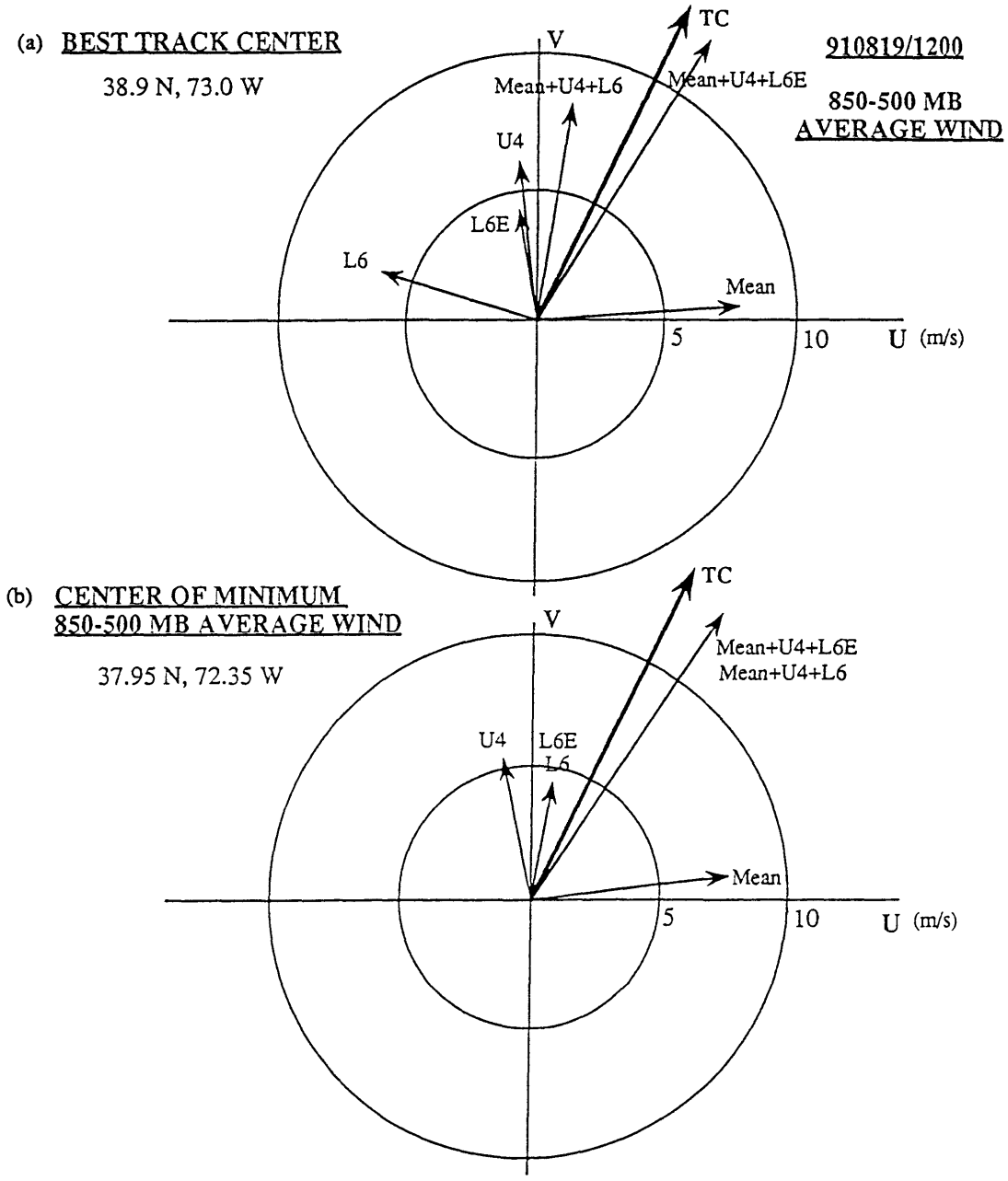

Figure 6.38 Velocity vectors of balanced flows and Hurricane Bob's motion at 1200 UTC 19 August 1991. Mean, U4, L6, and L6E represent the 850-500-mb averaged balanced flow associated with mean potential vorticity, potential vorticity perturbations of U4, L6, and L6E, respectively. Mean+U4+L6E represents the total hurricane advection flow. TC indicates Bob's motion estimated from every 6-hour best-track position. (a) Interpolation of the balanced wind fields at the best-track center; and (b) at the 850-500-mb pressure-averaged balanced vortex center.

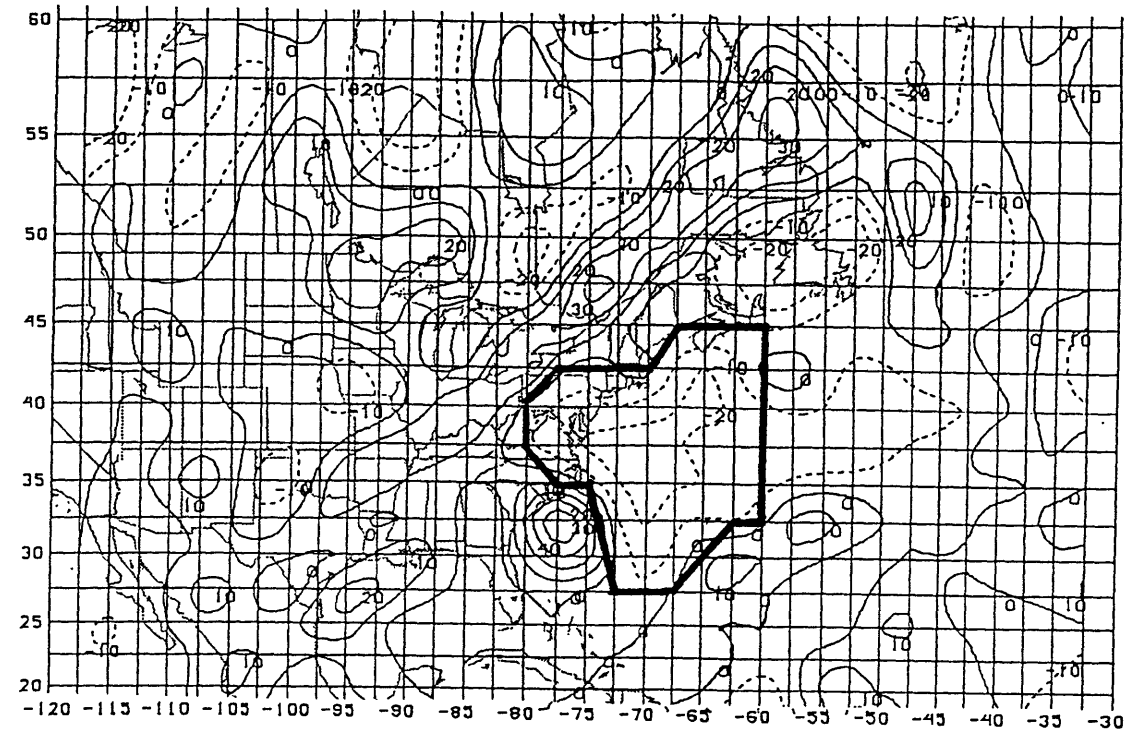

(a) 700 mb PERT. PV 910818/1200 - J_S MEAN

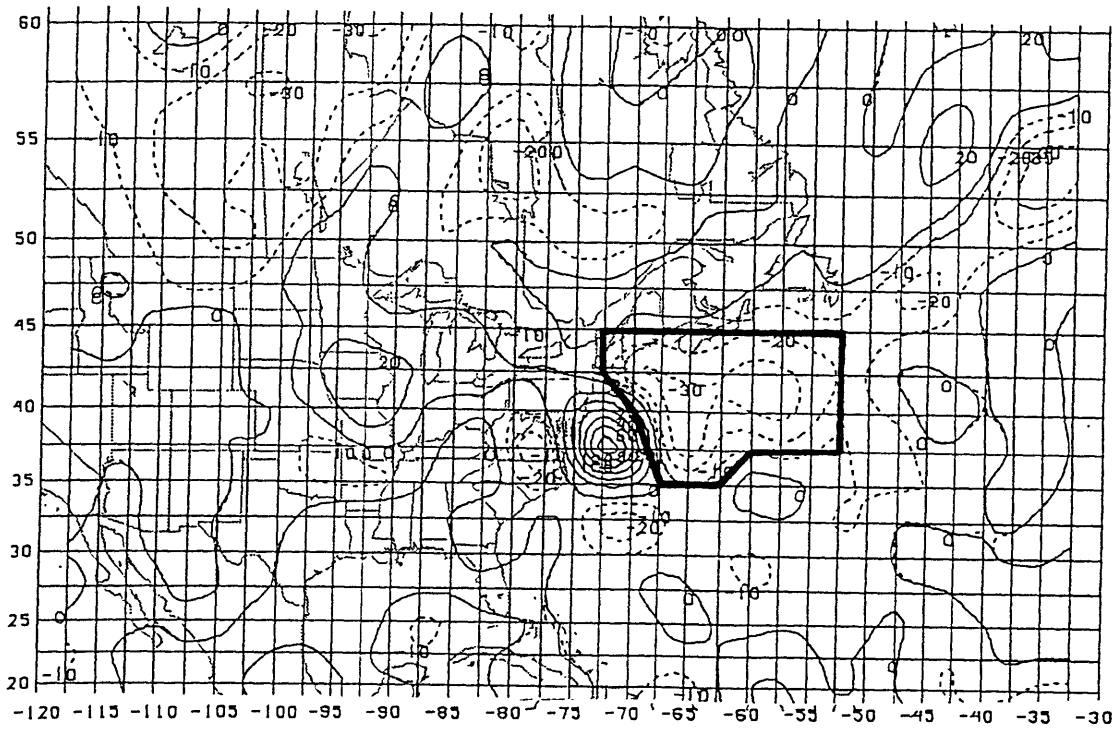

(b) 700 mb PERT. PV 910819/1200 - J_S MEAN

Figure 6.39 Ertel's potential vorticity perturbation field at 700 mb. (a) at 1200 UTC 18 August 1991, and (b) at 1200 UTC 19. The area enclosed by heavy lines indicates the potential vorticity anomaly (L6B) to be inverted. The unit is 0.01 PVU, and contour interval is 0.1 PVU. All positive (negative) values are represented by solid (dashed) lines.

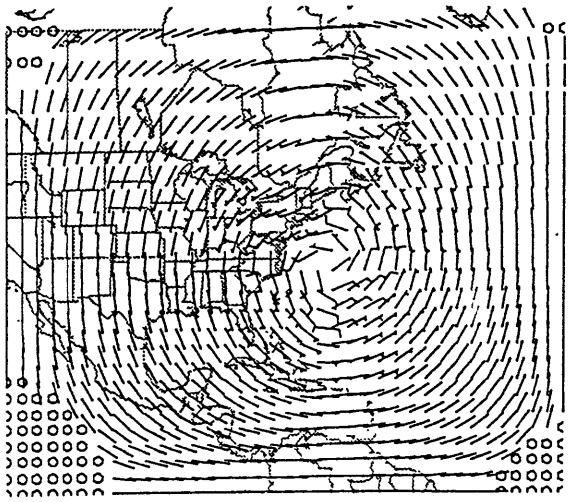

(a) 700 mb WIND (FROM L6B PERT. PV) 910818/120

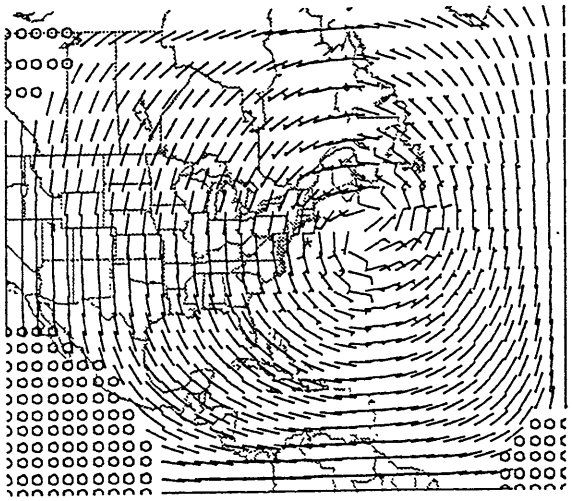

(b) 700 mb WIND (FROM L6B PERT. PV) 910819/120

Figure 6.40 700-mb balanced wind field (wind barb plotted as in Fig. 6.4) associated with L6B. (a) at 1200 UTC 18 August 1991, and (b) at 1200 UTC 19. Hurricane Bob's best track positions are indicated as "*."

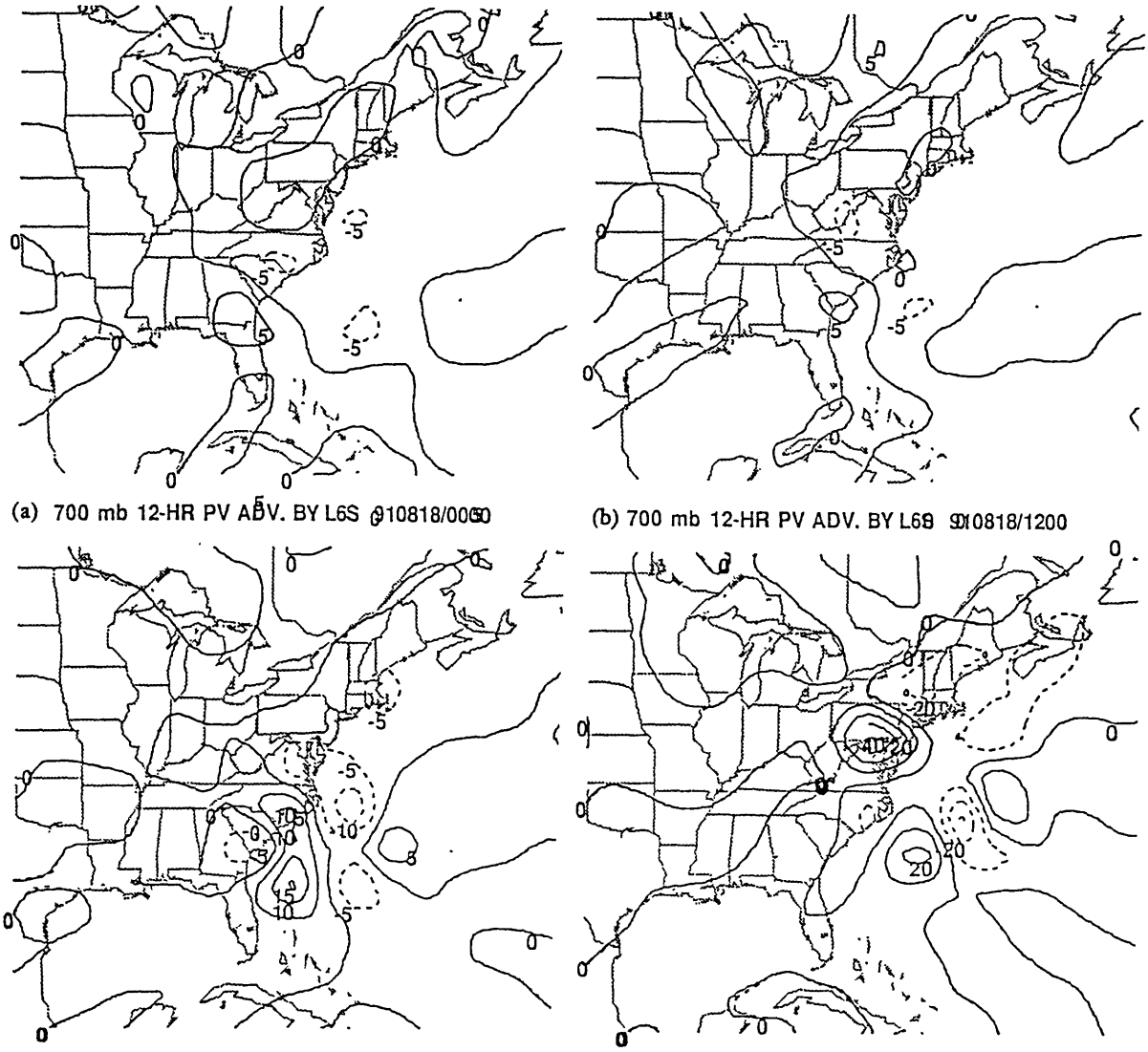

Figure 6.41 12-hr 700-mb Ertel's potential vorticity advection by the balanced flow associated with L6S. (a) at 0000 UTC 18 August 1991, (b) at 1200 UTC 18, (c) at 0000 UTC 19, and (d) at 1200 UTC 19. The unit is 0.01 PVU/12-hr, and contour intervals are 0.05 PVU/12-hr for (a), (b) and (c), and 0.2 PVU/12-hr for (d). All positive (negative) values are represented by solid (dashed) lines. Hurricane Bob's best track positions are indicated by an asterisk (*).

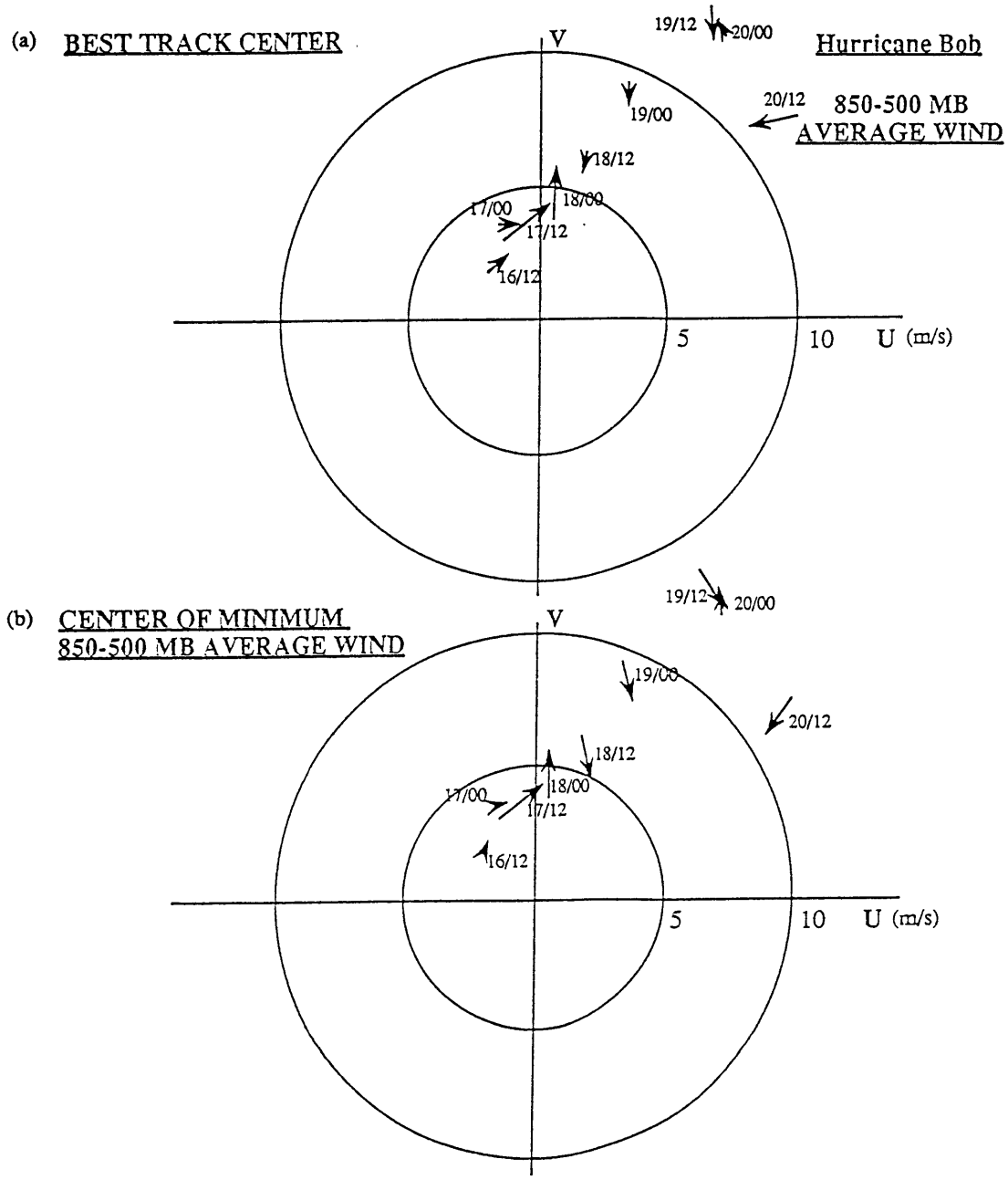

Figure 6.42 Velocity vector differences between the 850-500-mb pressure-averaged advection flow and Bob's motion from 1200 UTC 16 to 20 August 1991. (a) Interpolation of the balanced wind fields at the best-track center; and (b) at the 850-500-mb pressure-averaged balanced vortex center.

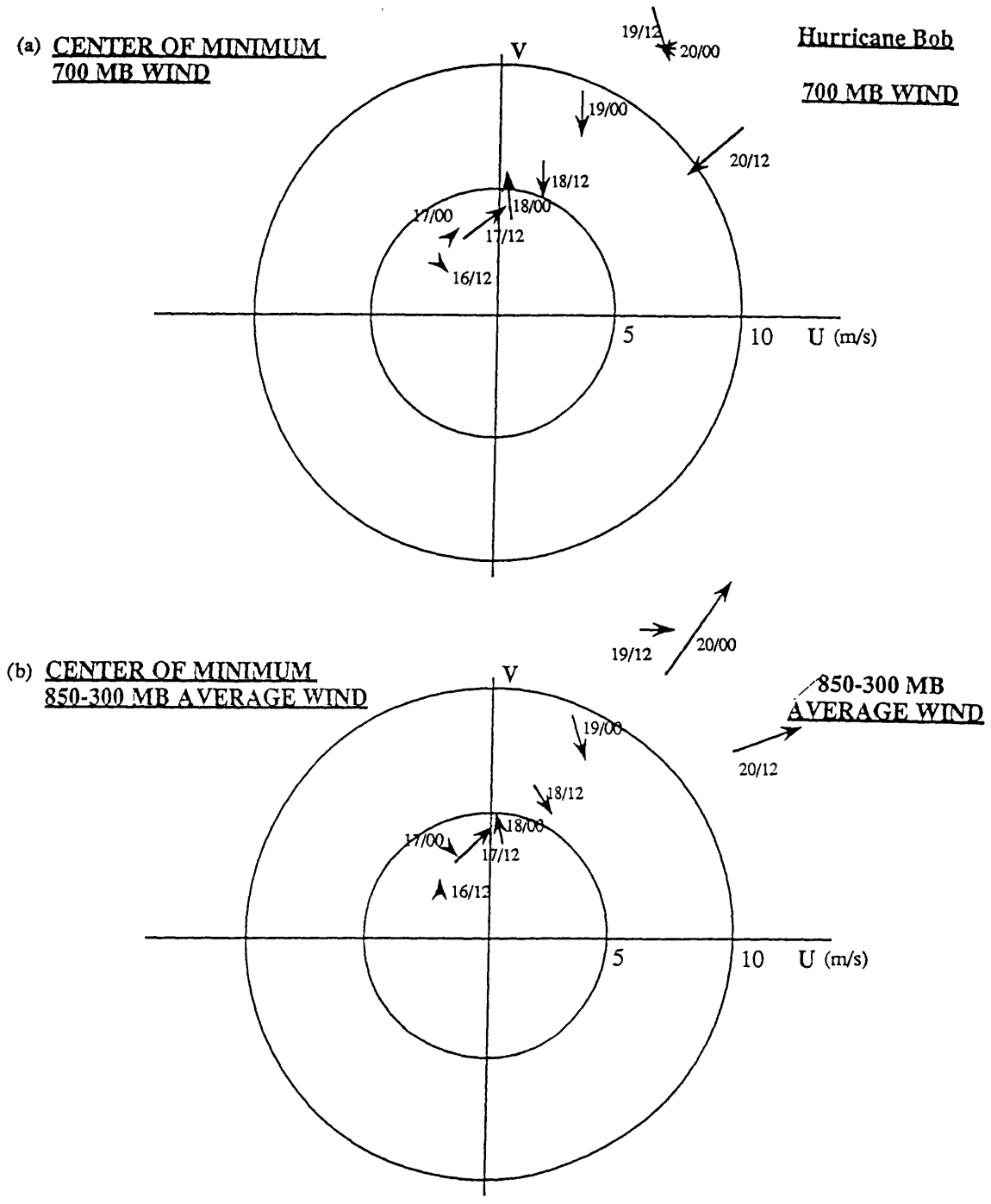

Figure 6.43 Velocity vector differences between the advection flow and Bob's motion from 1200 UTC 16 to 20 August 1991. (a) Interpolation of the 700-mb balanced wind fields at the 700-mb balanced vortex center. (b) Interpolation of the 850-300-mb pressure-averaged balanced wind fields at the 850-300-mb pressure-averaged balanced vortex center.

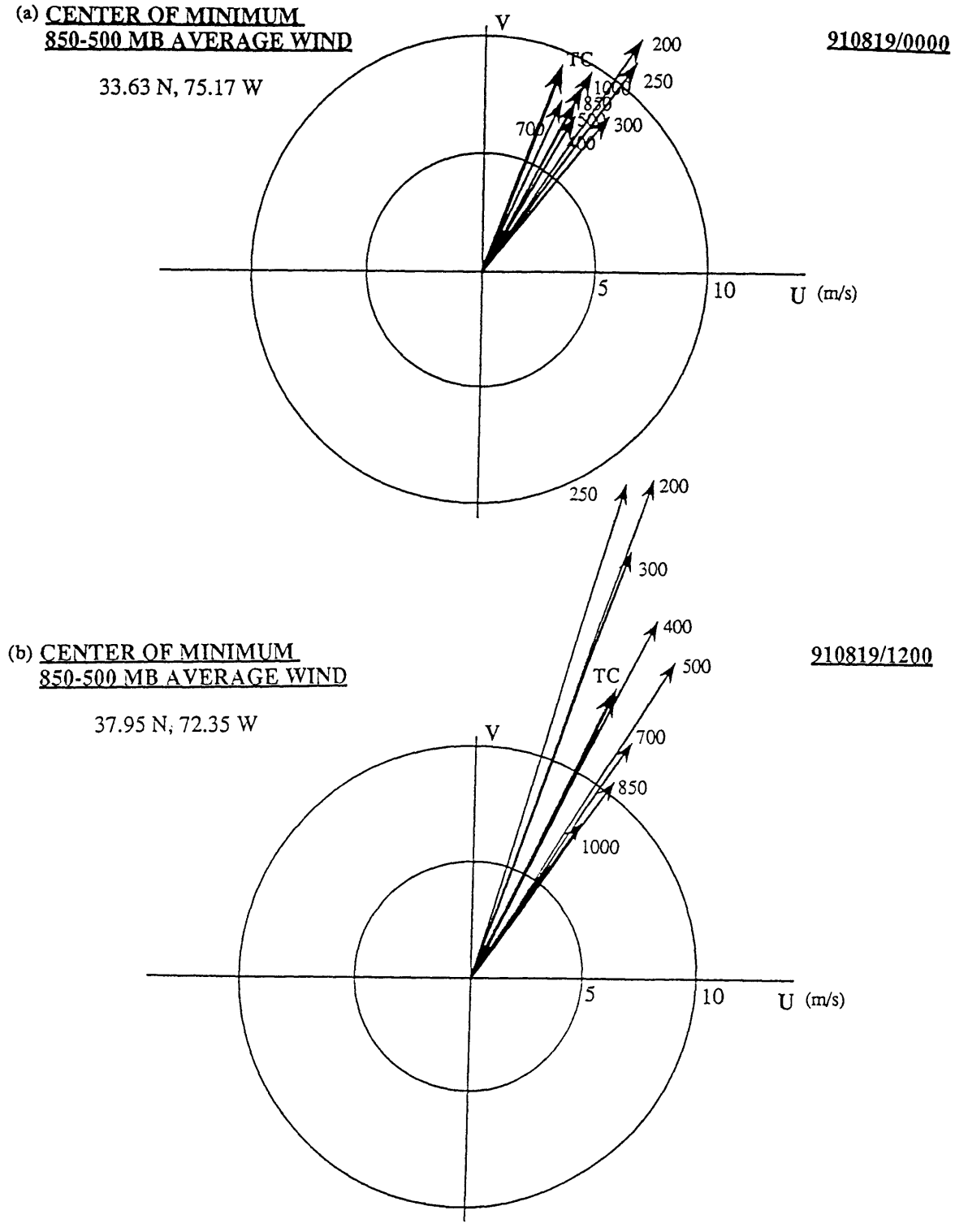

Figure 6.44 Velocity vectors of advection flow at each level and Hurricane Bob's motion at (a) 0000 UTC, and (b) 1200 UTC 19 August 1991. The hurricane advection flow is defined as the interpolation of the balanced flows associated with mean, U4, and L6E at the 850-500-mb pressure-averaged balanced vortex center. TC indicates Bob's motion estimated from every 6-hour best-track position.

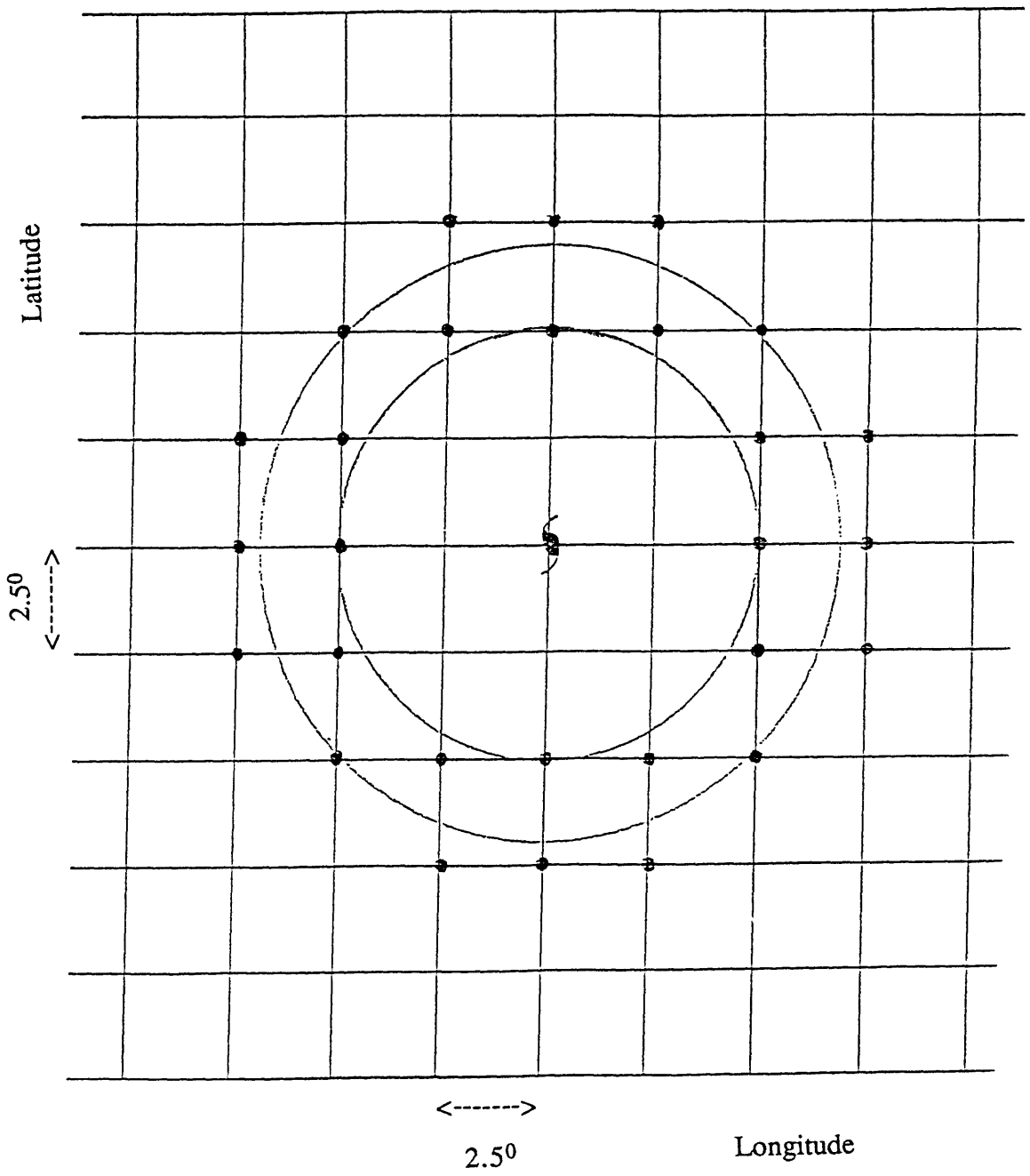

Figure 6.45 Illustration of the location of the 28 grids (•) used to mimic the 5-7^0 latitude annular average.

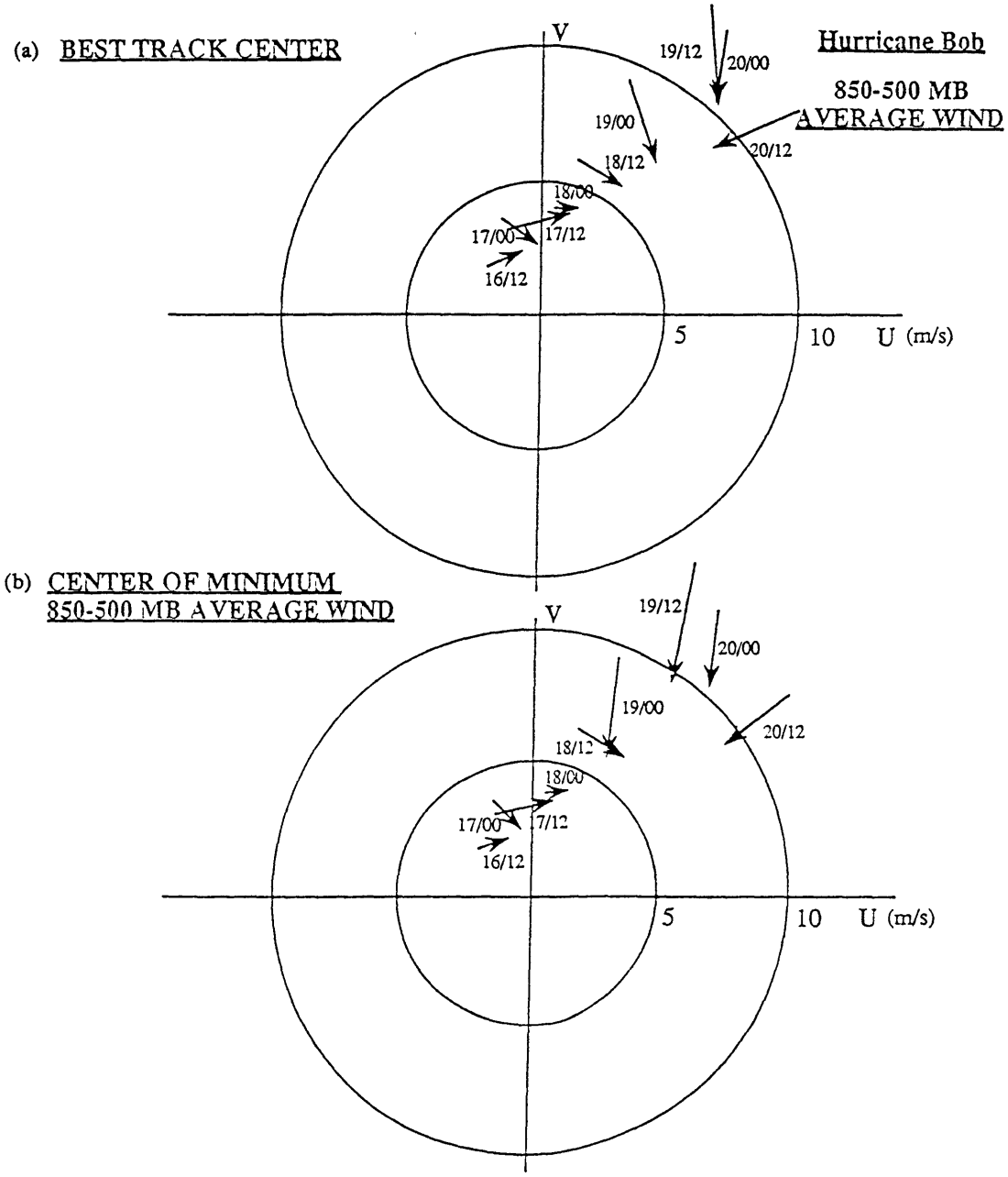

Figure 6.46 Velocity vector differences between the 850-500-mb pressure-averaged annular mean flow and Bob's motion from 1200 UTC 16 to 20 August 1991. (a) Interpolation of the wind fields at the best-track center; and (b) at the 850-500-mb averaged balanced vortex center.

7. More case studies

In this chapter, we discuss two more cases: Tropical Storm Ana and Hurricane Andrew. Finally, we shall compare all three cases.

a. Case II: Tropical Storm Ana

1) Synopsis of Ana

Ana was the first tropical storm of the 1991 hurricane season. Its best track positions are shown in Figure 6.1b. Ana originated from a low-pressure trough located about 300 miles east of Jacksonville, Florida on 25 June 1991. The system moved towards the northern Bahamas, and by 1200 UTC 27 June, a small surface low formed. In the next few days, this system moved across southern Florida, curved northward along the west coast of Florida, and then headed northeastward towards the St. Augustine area. At about 1800 UTC 2 July, Ana became a tropical depression about 100 miles south of Charleston, South Carolina.

Moving toward the northeast along the coast of South and North Carolina, Ana gradually intensified, and a weak circulation was found by an Air Force Research reconnaissance plane with 30 knot winds at the 1500-ft. flight level. At 2000 UTC 3 July, Ana was upgraded to a tropical storm by the National Hurricane Center.

Ana then moved east-northeastward, and at 0900 UTC 4 July, a maximum sustained wind of 45 knots was reported. Ana continued moving eastward and gradually lost its tropical characteristics by 1800 UTC on the 5th.

2) An example: 1200 UTC 3 July, 1991

Seven different times from 0000 UTC 2 July to 0000 UTC 5 July are used for this case study. Specifically, we choose 1200 UTC 3 July as an example for discussion.

Figure 7.1 displays the relative vorticity field at 1200 UTC July 3rd. Ana appears as a local relative vorticity maximum in the lower troposphere, with an amplitude of 4.5×10^{-5} s^{-1} at 700 mb. The amplitude of this vorticity maximum decreases upward, and vanishes above 300 mb. This can also be found in the PV field (Fig. 7.2). Ana has a PV maximum of 0.5 PVU at 850 mb, and increases to about 0.8 PVU at 700 mb and 500 mb. In the upper troposphere (e.g., at 150 mb), there is a large region of low PV air to the east of the storm over the western Atlantic. As already indicated in chapter 6, Figure 7.2 also shows that the PV distribution is quite uniform in the lower troposphere, and that the horizontal PV gradient is much higher in the upper troposphere.

Figure 7.3 shows the balanced height and NMC analyzed wind fields at 700 mb. An indication of Ana's circulation is observed. There exists a wave-like flow bending to the south of Ana, with a wind speed of about 10 m s^{-1}. Again, the NMC analyses cannot resolve the actual strength of Ana.

The PV perturbation field is shown in Figure 7.4. Ana is a positive PV anomaly in the lower and middle troposphere, with a maximum amplitude of 0.3 PVU. The PV perturbations in the upper troposphere have much higher amplitudes. The main features include a large-scale negative PV anomaly covering the southeast U.S. and west Atlantic (referred to N1), a negative PV anomaly over central Canada (N2), a positive PV anomaly over the northwest-central U.S. (P1), and a positive PV anomaly located to the south of Newfoundland (P2). Three anomalies, P1, P2 and N2 extended downward to 500 mb. Therefore, the simple partition of PV perturbations into U4 and L6 is not good in representing these PV anomalies. However, to be consistent with other cases, we conduct

piecewise inversion of some portions of these PV anomalies in the upper four levels and lower six levels, separately.

The 700-mb balanced flow fields associated with each PV perturbation are displayed in Figure 7.5. The balanced flow inverted from U4 (Fig. 7.5a) includes four main features: two cyclonic gyres associated with the synoptic-scale positive PV anomalies (P1 and P2), and two anticyclonic gyres associated with the large-scale negative PV anomalies (N1 and N2). The saddle point of the four circulations is located near Buffalo, New York. As indicated in Figure 7.5a, Ana is located near the center of the southern branch of the anticyclonic circulations, and it appears that Ana's motion is mainly under the influence of this clockwise flow.

To better understand the influence from each upper-level PV anomaly, we also conduct piecewise inversion of P1, P2, N1, and N2, individually, in the upper four levels. We find that the summed balanced flows associated with these four PV anomalies (Fig. 7.6) is very close to the balanced flows associated with the whole distribution of PV anomalies in U4. Indeed, each of these four PV anomalies contribute to a wind of 1 to 2 m s^{-1} through Ana's center. However, due to the cancellations between these flow fields, the total effect of U4 on Ana's motion is a weak westerly at 0.5 m s^{-1}.

Figure 7.5b shows the 700-mb balanced flow associated with L6. A weak circulation surrounding Ana is found. A southerly flow of more than 12 m s^{-1} exists to the east of Ana. The two cyclonic circulations near the central U.S. and south of Newfoundland are associated with the upper-tropospheric positive PV anomalies that extend down to the middle and lower troposphere. The balanced flow associated with L6E (excluded the positive PV anomaly associated with Ana) is displayed in Figure 7.5c. It is very similar to that shown in Figure 7.5b, except that a uniform southwesterly is found through Ana's center. This southwesterly flow extends consistently from the southwest of Florida to the east coast of North Carolina, and contributes to advecting Ana northeastward at 5 m s^{-1}. Our analysis from piecewise PV inversion of individual PV anomalies indicates

that this southwesterly flow is a result of the summation of the balanced flows associated with the two positive PV anomalies (extension of P1 and P2 between 700 and 300 mb), a positive PV anomaly near central Mexico, and a negative lower-level PV anomaly to the east and southeast of the storm. Finally, the 700-mb balanced flow (Fig. 7.5d) associated with Ana's positive PV anomaly (L6S) indicates a cyclonic circulation with a maximum wind of 6 m s^{-1}.

The 850-500-mb pressure-weighted average balanced flows associated with each PV perturbation are interpolated to the storm center to represent Ana's advection flow (Fig. 7.7). Again, we use both the best track center (33.9 ^{0}N, 75.4 ^{0}W) and the balanced vortex center (33.17 ^{0}N, 75.10 ^{0}W) for interpolation. In this example, these two centers are different by about 1^0 latitude. As discussed in the previous chapter, the balanced flows associated with mean and U4 are about the same when these different centers are used for interpolation, but the interpolation of the balanced flows of L6 differ by nearly 2 m s^{-1}. In this example, the advection of Ana is mainly associated with the climatology and L6. Unlike the case of Bob, due to the cancellation effects between the PV anomalies, the upper-tropospheric disturbances (U4) do not have a large effect on Ana's motion.

The summation of the balanced flows associated with the mean PV, U4, and L6E comprise Ana's advection flow. As shown in Figure 7.7, it is 1.7 m s^{-1} slower than Ana's actual motion, which is northeastward at 11 m s^{-1}. Also, the direction of the advection flow is 4.5^0 to the right of Ana's actual heading direction. The result demonstrates that our definition of advection flow is very close to the actual motion of Ana, and that the result is not sensitive to which interpolation center is used.

Figure 7.8 also shows the advection flow (interpolated to the 850-500-mb pressure-averaged balanced vortex center) at each level. In this example, it appears that the mean vertical shear above Ana is very weak. In other words, Ana is advected by a very uniform tropospheric flow at its center.

3) Time evolution of Ana

(i) Evolution of upper-level PV anomalies

Figures 7.9 shows the evolution of the tropopause potential temperature (θ) perturbation field, and Figure 7.10 displays the evolution of 700-mb balanced flow associated with the upper-four-level PV perturbations (U4). At 0000 UTC 2 July, as shown in Fig. 7.9a, there are three anomalies in the midlatitudes: one cold anomaly (referred to C1) is located over the west-central U.S., another warm anomaly (W1) over the Great Lakes, and a second cold anomaly (C2) centered over south Newfoundland. The balanced flow field at 700 mb (Figure 7.10a) shows a meridionally-elongated anticyclonic circulation squeezed between two cyclonic gyres. A west-southwestward flow of 2 m s^{-1} through Ana's center is found, and is mainly associated with W1, and partly with C2.

All the anomalies are advected eastward in time by the mean westerlies. Figure 7.9b shows that, twelve hours later, W1 is divided into two parts: the northern portion (W2) over central Canada, and the southern portion (W3) centered over New York. The 700-mb balanced flow field (Fig. 7.10b) is similar to those in Figure 7.10a, with a weaker advection flow (1.3 m s^{-1}) for Ana.

At 0000 UTC the 3rd, as indicated from Figure 7.9c, W3 weakens slightly, extends southeastward, and covers the southeast U.S. and the west Atlantic, but its center of maximum amplitude remains near New York and north Pennsylvania. C2 also remains at the same location, with a stronger amplitude than 12 hours ago. Figure 7.10c shows that the center of the anticyclonic circulation is farther south relative to W3's center. This is probably due to the "squeezing" effect by the two gyres of cyclonic flows associated with C1 and C2. At this time, Ana is located slightly to the south of the center of this anticyclonic circulation, and is advected by a northeasterly of 1.1 m s^{-1}.

Twelve hours later, as shown in Figure 7.9d, all systems move slightly towards the east; only C2's center remains at the same position with weaker intensity. As was discussed previously, the balanced flow field (Fig. 7.10d) is primarily composed of four circulations associated with C1, C2, W2, and W3. Also, there exists a rather weak westerly (0.5 m s^{-1}) that advects Ana, as Ana is located slightly to the north of the anticyclonic circulation center.

At 0000 UTC 4 July, as shown in Fig. 7.9e, W3 covers a broad area from the southeast U.S. to the west Atlantic. The 700-mb balanced flow (Fig. 7.10e) looks very similar to that 12 hours ago (Fig. 7.10d). The anticyclonic circulation to the southeast of North Carolina has an eastward advection effect (1.6 m s^{-1}) on Ana.

Twelve hours later, the potential temperature field (Fig. 7.9f) remains about the same as that in Figure 7.9e, except that the portion of W3 that covers the southeast U.S. shifted slightly northeastward. The inverted balanced flow at 700 mb (Fig. 7.10f) has an anticyclonic circulation more zonally elongated over the west Atlantic. It has a contribution of 2.7 m s^{-1} to Ana's eastward movement.

At 0000 UTC the 5th, as shown in Fig. 7.9g, W3 extends further to the east, and a region of high θ is found to the east of North Carolina. At this time, Ana is located between W3 and C2, and a stronger balanced flow (Fig. 7.10g) between these two PV anomalies advects Ana southeastward with a 4.5 m s^{-1} wind.

Overall, this case study indicates that how upper-level disturbances influence a storm's motion depends not only on the distribution and amplitude of these disturbances, but also, crucially, on the relative location of the storm to the upper features.

It should also be noted that following the evolution of the tropopause θ information in Figure 7.9, we do not observe any kind of warm θ anomaly (upper negative PV anomaly) related to Ana. In contrast to Bob's analyses, there is no clear signature of the generation of negative PV anomaly aloft of Ana, perhaps because Ana's intensity is too weak to be revealed in the data. For comparison, we also look at the evolution of the 200-

mb streamlines analyzed by the National Hurricane Center. It appears that there are only a few raw observations over the area near Ana, and no anticyclonic flow field is found over Ana.

(ii) Evolution of lower- and middle-level PV anomalies

Figure 7.11 shows the time evolution of the relative vorticity field. Ana has a relative vorticity of 3.6×10^{-5} s^{-1} at 0000 UTC on the 2nd. It increases to 4×10^{-5} s^{-1} 24 hours later, and 4.5×10^{-5} s^{-1} as it moves to the southeast of North Carolina at 1200 UTC 3 July. Then the intensity decreases to 3.6×10^{-5} s^{-1} on the 4th, but increases to 6×10^{-5} s^{-1} again at 0000 UTC on the 5th. The comparison between the analyzed relative vorticity field and the actual best track maximum sustained speed (Fig. 7.12) demonstrates that the NMC analyses do not correctly represent the actual evolution of Ana's strength.

Figure 7.13 displays the evolution of the 700-mb PV perturbation fields. Ana appears as a positive PV anomaly with an amplitude of 0.2 PVU at 0000 UTC on the 2nd. It increases to about 0.3 PVU at 1200 UTC 3 July. This PV anomaly weakens to 0.2 PVU on the 4th, but intensifies to 0.4 PVU at 0000 UTC on the 5th. Following the evolution of 700-mb PV fields, we do not see any evidence of β gyres near the storm.

The evolution of the 700-mb balanced flow associated with L6E is illustrated in Figure 7.14. At 0000 UTC 2 July, as indicated in Fig. 7.13a, there exists a strong positive PV anomaly (denoted as P1) over Saskatchewan and Manitoba, Canada, which is a extension of C1 from the upper troposphere downward to 700 mb. There is another intense positive PV anomaly (P2) over Gulf of St. Lawrence, which is the extension of C2. Two cyclonic circulations (Figure 7.14a) associated with P1 and P2 are very distinct. Meanwhile, there are a cyclonic circulation associated with the positive lower-level PV anomaly (P3) over north Mexico, and an anticyclonic circulation associated with a negative lower-level PV anomaly (N3) to the east of the Caribbean islands. A quite uniform

southwesterly extends from east of Gulf of Mexico through the east coast of Florida. This flow (associated L6E) advects Ana at a speed of 5.4 m s^{-1}.

Twelve hours later, as shown in Figure 7.13b, both P1 and P2 move slightly southeastward, P3 remains at the same location with stronger amplitude, and N3 also remains at the same region. The balanced wind fields (Fig. 7.14b) are similar to those in Figure 7.14a. The contribution of L6E to Ana's motion is a northeastward flow of 4.5 m s^{-1}.

At 0000 UTC on the 3rd, the main PV features (Fig. 7.13c) remain similar to those twelve hour ago. The balanced wind (Fig. 7.14c) shows a uniform southwesterly extending from northeastern Yucatan to the southeast coast of North Carolina, and a strong flow of 6.4 m s^{-1} at Ana's center. At 1200 UTC, P1 (Figure. 7.13d) moves southeastward and is centered over northern Minnesota. A negative PV anomaly (N2), which is a downward extension of W2, covers central Canada. As already discussed in the previous example, the balanced flow (Fig. 7.14d) advects Ana northeastward at a speed of 5 m s^{-1}.

At 0000 UTC 4 July, as seen in Figure 7.13e, all the main PV features, P1, P2, P3, N2 and N3 move somewhat eastward. Ana is advected north-northeastward (Figure 7.14e) at 3.9 m s^{-1}. Figure 7.13f shows that twelve hours later, N2 extends southeastward to the Gulf of St. Lawrence. Ana is located slightly to the south of the saddle point between the four circulations associated with P1, P2, N2 and N3 (Fig. 7.14f) . Only a weak southeasterly of 1 m s^{-1} is observed at Ana's center. Finally, at 1200 UTC 5th, as indicated in Figure 7.14g, Ana is advected east-northeastward at 2.5 m s^{-1}.

4) Advection flow of Ana

Figure 7.15 displays two hodographs that demonstrate the velocity vector differences between the 850-500-mb pressure-averaged advection flow and Ana's actual movement from 0000 UTC the 2nd to the 5th. The advection flow approximates Ana's

motion very well. In the seven different times, when the 850-500-mb averaged balanced vortex center is used for interpolation, the mean difference of the displacement speed is -0.2 m s^{-1}, with a standard deviation of 1.5 m s^{-1}, and the mean difference of the heading direction is -1^0, with a standard deviation of 3.1^0. Also these vectors appear to point randomly in any direction. This case study indicates that the advection flow derived from our PV diagnostics is particularly good in representing the direction of Ana's movement, though the advection speed is about 10 to 20% different from the real cyclone displacement velocity.

We also calculate the velocity differences (Fig. 7.16) between the annular mean flow, as defined in chapter 6, and the storm's actual motion. The differences are 5 times larger than those shown in Figure 7.15. This finding again shows that our method is capable of detecting the storm's advection current while, using the same NMC gridded datasets, the result of the approximate annular mean flow appears to be very noisy.

5) Summary

In this section, Tropical Storm Ana is studied. An example of the diagnosis is illustrated for 1200 UTC 3 July. We find that the NMC analyses underestimate Ana's intensity. Unlike the case for Bob, it does not capture the evolution of Ana's intensity. Our observations again indicates that the PV gradient is more concentrated near the tropopause, and also the magnitudes of the PV anomalies are much stronger in the upper troposphere.

Following the evolution of the PV fields, we are able to identify a few distinct PV features that are important in controlling the large-scale flow fields, and contribute to the advection of Ana. Our analyses also show that some upper-level disturbances extend downward to the middle and lower troposphere. However, due to the cancellation between the balanced flow field associated with these PV anomalies, and due to the relative location

of Ana with respect to these PV anomalies, it is not as clear as in the case of Bob which PV anomaly plays the most important role in advecting Ana. Also, we do not see any evidence of a negative PV anomaly generated by Ana, nor do we observe the so-called β gyres.

Finally, our results indicate that there is a very uniform tropospheric flow at Ana's center, and the advection flow derived from our potential vorticity diagnostics approximates Ana's motion very well, while annular mean flows do not.

b. Case III: Hurricane Andrew

1) Synopsis of Andrew

Andrew was the first and the strongest Atlantic tropical storm of the 1992 hurricane season. As seen from Andrew's best track positions (Figure. 6.1c), it had a long life time of nearly two weeks from August 16th to 28th, 1992. Andrew was a compact and ferocious hurricane which originated over the tropical North Atlantic Ocean, and then moved westward across the northwestern Bahamas and the southern Florida peninsula, and made its final landfall at the coast of south-central Louisiana. Because of Andrew's tremendous damage and destruction, it became the most expensive natural catastrophe in U.S. history.

Andrew formed from a tropical wave, which originally came from the west coast of Africa, over the tropical North Atlantic Ocean on 14 August . It became a tropical depression at around 1800 UTC 16 August. The depression became stronger as the environmental vertical wind shear diminished. At 1200 UTC 17 August, it was upgraded to Tropical Storm Andrew. Then Andrew moved northwestward with its central pressure slightly rising on the following three days.

Andrew intensified again on 21 August as it turned and accelerated towards the west, and became a hurricane on the morning of 22 August. In the meantime, Andrew's

eye formed. Andrew intensified dramatically in the next 36 hours, and reached its peak intensity at 1800 UTC 23 August, with a central pressure of 922 mb, and a maximum wind speed of 135 knots.

Andrew kept its westward movement, passed over northern Eleuthera Island late on the 23rd, and then over the southern Berry Islands early on the 24th. After crossing through the Straits of Florida, it made landfall near Homestead AFB at 0900 UTC 24 August, and then passed over the very southern portion of the Florida peninsula in about 4 hours.

As Andrew reached the Gulf of Mexico, it gradually turned towards the west-northwest and slowed down. Andrew made its final landfall near the south-central Louisiana coast at 0830 UTC 26 August, and weakened rapidly as it moved inland.

2) Examples: 1200 UTC 23 and 24 August, 1992

Eight different times from 1200 UTC 19 to 1200 UTC 26 August 1992 (only 1200 UTC are used) are studied for Andrew. We choose two particular times (1200 UTC 23 and 24 August) to show the general behavior of Andrew from the NMC datasets.

At 1200 UTC 23 August, a few hours before it reaches its maximum strength, Andrew is located about 400 miles east of Miami. The relative vorticity and potential vorticity fields are displayed in Figures 7.17 and 7.18, individually. Andrew shows up as a local relative (potential) vorticity maximum with an amplitude of 4.7×10^{-5} s^{-1} (0.5 PVU). This vorticity maximum extends from 850 to 300 mb. At 150 mb, a region of negative relative vorticity and local PV minimums are observed to the north-northeast of Andrew.

Figure 7.19a shows the balanced height and NMC analyzed wind fields at 700 mb. There exists a weak cyclonic circulation, with an azimuthal wind speed of about 6 m s^{-1}, surrounding Andrew. All the information indicates that, at this time, the NMC analyses, though it knows about Andrew's location, far underestimate Andrew's strength.

Compared to Bob, the NMC analyses are worse in capturing Andrew's intensity than Bob's. Figures 7.19b and c display the comparison of the balanced height and the NMC analyzed height fields at 850 and 150 mb. The differences appear to be larger than for Bob's case (cf. Fig. 6.7). This example suggests that the balanced flow may not represent the analyzed flow for the case of Andrew as well.

At 1200 UTC 24 August, Andrew is located at the very southwest portion of the Florida peninsula, with a much stronger intensity than 24 hours ago. Its relative vorticity and PV fields are displayed in Figures 7.20 and 7.21, respectively. At this time, Andrew has a local relative (potential) vorticity maximum of 9.4×10^{-5} s^{-1} (1.0 PVU). This vorticity maximum extends from 850 to 300 mb. At 150 mb, a strong local PV minimum was found to be above and to the east of Andrew.

The 700-mb balanced height and NMC analyzed wind fields are shown in Figure 7.22. At this time, Andrew appears to be a local height minimum, and the wind speed around Andrew increases to 14 m s^{-1}. However, other models, such as the NGM, show a wind maximum of about 30 m s^{-1} at about 850 mb at the same time. Again, the NMC analyses underestimate Andrew's strength. Comparing the NMC analyses at 1200 UTC the 23rd and the 24th, the NMC data analyze Andrew much better at the latter time, when Andrew is located in Florida rather than over the ocean.

Figure 7.23 displays the PV perturbation field at 1200 UTC 23 August. Andrew is a positive PV anomaly in the lower and middle troposphere, with an amplitude of 0.25 PVU, which is about the same strength as Tropical Storm Ana. At 150 mb, a negative PV anomaly of -1.5 PVU is found above and to the northeast of Andrew. In addition, a distinct positive PV anomaly (denoted as P6) exists over southeast Nova Scotia, and extends downward to about 500 mb. Also, a negative PV anomaly (referred to N6) exists over the north-central U.S. and central Canada, and is confined to above 400 mb. At 500 and 700 mb, a negative PV anomaly of -0.5 PVU is found over and to the north of the Gulf of St. Lawrence.

The 700-mb balanced flow fields associated with each PV perturbation are displayed in Figure 7.24. The balanced flow associated with U4 (Fig. 7.24a) is dominated by the dipole gyres associated with the two aforementioned distinct PV anomalies, P6 and N6. These circulations are nearly opposite to those indicated in Bob at 1200 UTC 18 August 1991. The flow advects Andrew towards the south-southwest at 2.1 m s^{-1}. The balanced flow associated with L6 (Fig. 7.24b) features a cyclonic circulation surrounding Andrew with a wind speed of about 10 m s^{-1}. However, as we invert L6E (excluding Andrew's PV anomaly), the 700-mb balanced flow field (Fig. 7.24c) shows a distinct anticyclonic circulation associated with the middle-tropospheric negative PV anomaly over the Gulf of St. Lawrence. This clockwise circulation extends southward into the subtropics, and combines with a uniform east-northeasterly that passes through Andrew's center with a speed of 4 m s^{-1}. Figure 7.24d shows the 700-mb balanced flow associated with Andrew's PV anomaly (L6S). The maximum wind speed associated with Andrew itself is only 5 m s^{-1} in this analysis.

Figure 7.25 shows the comparison of the advection flow (averaged between 850 and 500 mb) with Andrew's actuation motion at 1200 UTC 23 August. In this example, the balanced vortex center differs from the best track position by 0.7^0 latitude. The mean, U4, and L6 have about the same magnitude of contribution to Andrew's advection flow. The advection flow is about the same for both interpolation centers. The advection flow (using the balanced vortex center) is slightly (0.7 m s^{-1}) slower than Andrew's actual motion, which is 7.7 m s^{-1} westward. Also, the direction of the advection flow is about 12^0 to the left of Andrew's heading direction. The advection flow (interpolated to the balanced vortex center) at each level is also displayed in Figure 7.26. In this example, an east-northeasterly vertical wind shear of 8 m s^{-1} between 200 and 700 mb over Andrew is found.

Figure 7.27 shows the PV perturbation field at 1200 UTC 24 August. The positive PV anomaly of Andrew increases to 0.8 PVU at 700 mb, and 0.5 PVU at 500 and 300 mb,

which is two times the amplitude of Andrew's PV anomaly on the 23rd. At 150 mb, a negative PV anomaly of -1.5 PVU is found above Andrew. Also, at this time, P6 moves southeastward and stretches in a southwest-northeast orientation over the northwest Atlantic Ocean. N6 moves eastward with its PV maximum above central Canada. The middle-level negative PV anomaly, located near the Gulf of St. Lawrence on the 23rd, extends further south.

The 700-mb balanced flow fields associated with each PV perturbation are displayed in Figure 7.28. The balanced flow associated with U4 (Fig. 7.28a) is dominated by the dipole gyres associated with P4 and N4. Comparing with the balanced flow 24 hours ago, the dipole gyres seem to rotate each other in a clockwise direction and become stronger. A southwestward flow with a speed of 3.1 m s^{-1} is found at Andrew's center. The balanced flow associated with L6 (Fig. 7.28b) indicates a cyclonic circulation surrounding Andrew with a wind speed of about 13 m s^{-1}. However, as we invert L6E (excluding Andrew's PV anomaly), the balanced flow field at 700 mb (Fig. 7.28c) shows an easterly wind of 4.5 m s^{-1} through Andrew's center. Figure 7.28d shows the 700-mb balanced flow associated with Andrew's PV anomaly (L6S). The maximum wind speed associated with Andrew itself is 9 m s^{-1} in this analysis.

The comparison of the 850-500-mb pressure-averaged advection flow and Andrew's motion at 1200 UTC the 24th is displayed in Figure 7.29. Again, the advection flow is a good approximation to Andrew's movement, which is 8.9 m s^{-1} westward. The advection flow is slower than Andrew's propagation speed by 1 m s^{-1} , and 7^0 to the left of Andrew's displacement direction. The advection flow (interpolated to the balanced vortex center) at each level is also illustrated in Figure 7.30. In this example, an easterly vertical wind shear of 5 m s^{-1} between 200 and 700 mb is found over Andrew. The result also shows that the lower- and mid-tropospheric (1000 to 400 mb) advection flow has the best correlation with Andrew's actual motion.

3) Time evolution of Andrew

In this section, the evolution of the PV features in both the upper and lower-middle troposphere is discussed. The evolution of the balanced flow fields associated with these PV anomalies, and their impacts of Andrew's movement are also examined. Since Andrew has a relatively long life time, we choose a 24-hour interval for this evolution study. Specifically, the study of Andrew at 1200 UTC from the 19th to the 26th are presented here.

(i) Evolution of upper-level PV anomalies

Figure 7.31 shows the evolution of the potential temperature (θ) field on the dynamic tropopause (1.5 PVU surface) from 1200 UTC 19 to 26 August. Also, Figure 7.32 displays the evolution of the 700-mb balanced flow inverted from the upper-four-level PV perturbation (U4).

At 1200 UTC on the 19th, as shown in Figure 7.31a, a warm θ anomaly (referred to W4) is located to the east coast of Newfoundland. The central and east U.S. is covered by a broad cold θ anomaly (C4), with one maximum over the Great Lakes, and the other one near the border of Oklahoma and Texas. Above Andrew, we do not see any indication of a warm θ anomaly. The projection of the flow associated with U4 at 700 mb (Fig. 7.32a) is dominated by two dipole circulations associated with W4 and C4. A weak northward flow of 0.8 m s^{-1} through Andrew's center is found. One day later, both C4 and W4 move southeastward (Fig. 7.31b), and are still the main upper-level PV features that dominate the 700-mb flow field (Fig. 7.32b). The northward advection flow on Andrew associated with U4 increases slightly to a value of 1 m s^{-1}.

On the 21st, as shown in Fig. 7.31c, W4 moves to the eastern boundary of the domain, and C4 shifts eastward, extending from Louisiana to Newfoundland. Meanwhile,

a small-amplitude warm θ anomaly (W5) exists to the north-northeast of Caribbean Islands. Also, another warm anomaly (W6) enters the western boundary of the domain, and extends from the west coast of California to Utah. The balanced flow (Fig. 7.32c) that influences Andrew's motion is dominated by a southwesterly wind of 1.4 m s^{-1} between the two counterrotating circulations associated with C4 and W5.

Figure 7.31d indicates that on the 22nd, C4 breaks into two parts: one is a narrow band extending from Texas to Ohio (denoted as C5), and the other is located just south of Newfoundland (denoted as C6). W6 covers a broad area from California to Minnesota, and has an amplitude of 20 K. The balanced flow at 700 mb (Fig. 7.32d) is dominated by two gyres associated with W6 and C6. The circulation of C5 is countered by the flow associated with W6. At this time, the effect of U4 on Andrew's motion has changed: it advects Andrew southward by a weak flow of 0.7 m s^{-1}.

On the 23rd, as shown in Figure 7.31e, both W6 and C6 intensify, and are the most dominant dynamic feature in the upper troposphere. W6 extends from Arizona to Quebec, and C6 is located to the southeast of Newfoundland over the northwest Atlantic Ocean. C5 is still confined as a narrow band, centered over Louisiana, and another cold anomaly (C7) enters the western boundary of the domain. The projection of U4 at 700 mb is a pair of counter-rotating circulations (Fig. 7.32e) that advected Andrew southwestward at 2.1 m s^{-1}.

On the 23rd, a small-scale warm anomaly of 5 K is located above Andrew. However, just one day later, as displayed in Figure 7.31f, a very distinct warm anomaly of 20 K forms over Andrew. The timing of the occurrence of this θ (or PV) anomaly above Andrew matches very well with the time when the NMC analyses are able to better capture Andrew's strength. Therefore, this warm θ anomaly is a clear indication of the diabatic generation of the upper-level negative PV anomaly by Andrew, which is not resolved in the NMC data in Andrew's early stage.

Figure 7.31f also shows that on the 24th, the leading edge of W6 expands over Newfoundland, and C6 is stretched farther southward to the west Atlantic. The balanced flow (Fig. 7.32f) indicates a stronger wind between the two circulations that advects Andrew southwestward with a speed of 3.2 m s^{-1}.

On 25 August, Figure 7.31g displays a warm anomaly above Andrew, though its amplitude is 10 K weaker than one day earlier. Meanwhile, W6 moves slightly to the east, and C7 is centered over Montana. Also, C6 is divided into two pieces: one moves out of the eastern boundary of the domain, the other (C8) stays to the northeast of the Caribbean Islands. The 700-mb balanced flow (Fig. 7.32g) includes three primary circulations associated with P6, C7, and C8. Ana's motion due to the influence of upper PV perturbations is mainly contributed by the balanced flow associated with P6, which is an easterly wind of 3.5 m s^{-1}.

On the 26th, right after Andrew made landfall in south-central Louisiana, a warm anomaly (Fig. 7.31h) of 20 K is observed to the southeast and southwest of Andrew. At this time, C7 and P6 both shift slightly eastward. The balanced wind pattern at 700 mb (Fig. 7.32h) shows that U4 advects Andrew towards the north-northwest at 2.1 m s^{-1}.

Finally, to compare to our theoretical model, we need to invert the high θ (low PV) anomaly above Andrew. However, unlike in the case of Bob, as indicated in the previous discussion of the evolution of the PV field, the NMC analyses are not very consistent in representing Andrew's intensity and the generation of the low PV anomaly above Andrew. Therefore, we are not sure which part of the negative PV anomaly above Andrew is directly related to it. Also, we do not think the data are able to provide a reliable result that can be used to compare with our numerical model.

For comparison, we also look at the evolution of the 200-mb streamlines analyzed by the National Hurricane Center. They are very few raw observations available over the area near Andrew, and these analyses do not show any clear signature of upper anticyclonic flow over Andrew until it reaches the Gulf of Mexico. This result indicates that our

objective in examining the effect of upper negative PV anomalies may be limited by the lack of raw observations over the oceanic region.

(ii) Evolution of lower and middle-level PV anomalies

Figure 7.33 displays the evolution of the relative vorticity field, analyzed from the NMC datasets, from 1200 UTC 19 to 26 August. At 1200 UTC on the 19th, Andrew is a weak vortex, with a relative vorticity of 3.6×10^{-5} s^{-1}. One day later, this relative vorticity maximum increases to 4.1×10^{-5} s^{-1}. On the 21st, it reaches 7×10^{-5} s^{-1}. Then, it decreases to 5×10^{-5} s^{-1} on the 22nd, and remains so for another day. On the 24th, as Hurricane Andrew was located near Fort Myers, Florida, its relative vorticity doubles to 9.4×10^{-5} s^{-1}. It weakens to a value of 7.3×10^{-5} s^{-1} on the 25th, but intensifies again to its highest value of 1.2×10^{-4} s^{-1} on the 26th, the time after its final landfall. Comparing the evolution of Andrew's analyzed maximum relative vorticity with its best track maximum wind speed (Fig. 7.34), we find that the NMC analyses do not capture the tendency of Andrew's intensity change. Also, it appears that NMC analyses tend to pick up the storm's intensity better while the storm is over land. Thus, the NMC analyses of Andrew are clearly influenced by how close the storm is to an observation point.

The time evolution of the PV perturbation fields at 700 mb is shown in Figure 7.35, and the evolution of the 700-mb balanced flow associated with L6E is displayed in Figure 7.36. On the 19th (Fig. 35a), Andrew shows up as a positive PV anomaly of 0.2 PVU. The wind pattern of the 700-mb balanced flow (Fig. 7.36a) corresponds very well to the 700-mb PV anomaly field (Fig. 7.35a). There is a negative PV anomaly to the northeast and further north of Andrew that induces an anticyclonic circulation (Fig. 7.36a), and advects Andrew northward with a wind of 2 m s^{-1}.

On the 20th, the positive PV anomaly of Andrew (Fig. 7.35b) remains at the same strength of 0.2 PVU. Andrew is advected by an easterly flow of 2 m s^{-1} (Fig. 7.36b) which is a result of the local PV anomaly near Andrew.

One day later, Andrew's PV anomaly (Fig. 7.35c) intensifies to a value of 0.4 PVU. The balanced flow (Fig. 7.36c) in the eastern half of the domain is dominated by three main circulations associated with a positive PV anomaly over New England and the southeast portion of Canada, a negative PV anomaly to the northeast of Andrew, and another positive PV anomaly to the east of Andrew. The balanced flow of L6E at Andrew's center is an east-northeasterly wind of 2.3 m s^{-1}.

On the 22nd, as displayed in Figure 7.35d, Andrew's PV anomaly increases to 0.3 PVU. A broad area of negative PV anomaly (Fig. 7.36d) extends from the Great Lakes to Quebec. A large-scale anticyclonic circulation associated with this negative PV anomaly is present over the west Atlantic, and contributes in advecting Andrew west-southwestward at 4 m s^{-1}.

On the 23rd, Andrew is still seen as a positive PV anomaly (Fig. 7.34e) of 0.3 PVU. But one day later, its amplitude (Fig. 7.34f) increases to 0.5 PVU. The balanced flow field and the advection flow on Andrew are mainly associated with the aforementioned negative PV anomaly, as was discussed in the examples.

On 25 August, the PV anomaly of Andrew stays at 0.5 PVU, and a negative PV anomaly (Fig. 7.35g) covers the southeast U.S. As shown in Figure 7.36g, an anticyclonic circulation exists to the east coast of Georgia, and a northeasterly of 3.8 m s^{-1} passes through Andrew's center.

Finally, on the 26th (Fig. 7.35h), Andrew becomes a positive PV anomaly of 0.6 PVU. The contribution to Andrew's advection flow from L6E (Fig. 7.35h) is a northeasterly wind of 2 m s^{-1}, which is mainly associated with the broad negative PV anomaly over the southeast U.S.

Also, following the evolution of PV anomalies in Figure 7.35, the NMC data, as in the previous case, do not show any signature of β gyres near Andrew.

4) Advection flow of Andrew

Figure 7.37 shows two hodographs that demonstrate the velocity vector differences between the 850-500 pressure-averaged advection flow and Andrew's actual movement from 1200 UTC 19 to 26 August. In general, the advection flow approximates Andrew's motion pretty well, though a consistent southward component in vector differences is found. At the eight different times, when the 850-500-mb averaged balanced vortex center is used for interpolation, the mean difference of the displacement speed is -0.8 ms^{-1}, with a standard deviation of 0.5 ms^{-1}, and the mean difference of the heading direction is -17^0, with a standard deviation of 10^0. This case study indicates that the advection flow derived from our PV diagnostics is capable of capturing some of Andrew's movement, though the advection flow appears to be consistently biased towards the south.

We are not sure what causes this kind of systematic southward bias of the advection flow, which is not observed in the other two cases. We speculate that there are three possible reasons: first, Andrew is located close to the tropics where the analyzed winds may have been biased towards one particular direction; second, the southern boundary condition affects the meridional component of the balanced flow; third, there are some important PV features, which are not resolved by the NMC analyses, which would have advected Andrew northward.

We also calculate the velocity vector differences (Fig. 7.38) between the annular mean flow (as defined in chapter 6) and Andrew's actual motion. The magnitudes of these differences are about two times of those shown in Figure 7.37, and also have a consistent southward bias. This result also rules out the possibility of the second speculation in the previous paragraph.

5) Summary

In this section, our study of Hurricane Andrew is presented. Two examples of the diagnosis at 1200 UTC 23 and 24 August are illustrated. We find that the NMC analyses underestimate Andrew's intensity. Unlike in the case of Bob, the evolution of Andrew's intensity, indicated from the NMC data, is substantially underestimated.

Following the evolution of the PV field, we are able to a identify few distinct PV features that dominate the large-scale flow fields, and contribute to the advection of Andrew. Through this case study, we find that the flow fields that contribute to the steering of Andrew are clearly associated with some distinct PV anomalies in both the upper or lower and midtroposphere. Though at the later stage we observed a negative PV anomaly generated above Andrew, we are not able to perform any analysis in proving or disproving the model's results due to the inconsistency in the evolution of this PV feature. We do not find the so-called β gyres from the datasets either.

Finally, our results also indicate that there is a mean easterly vertical shear flow over Andrew. The advection flow derived from our potential diagnostics approximates Andrew's motion very well, though a consistent southward deflection is found.

c. Comparison and Summary

In this observational study, we use the NMC gridded datasets to examine three cases of storms by applying PV diagnostics. Our goal is to understand how the large-scale flow and the hurricane interact with each other, and also to investigate the different mechanisms responsible for the storm movement which are described in the traditional theory or in our model. The three storms studied are Hurricane Bob, Tropical storm Ana, and Hurricane Andrew.

The three storms have very different characteristics. Bob was a strong hurricane which spent most of its life time moving northwestward, then northward, and eventually northeastward along the east coast of U.S. Ana was a weak tropical storm, which originated near Florida. After curving in a clockwise direction from the southern portion to the northern portion of Florida, it moved northeastward off the eat coast of Florida, eventually moving towards the east in the Atlantic Ocean. Andrew was the strongest storm of the three, though its size is relatively small. Andrew was also the only storm among the three that originated from a tropical easterly wave. It had a relatively long life time, moving northwestward in the early stage, then westward through the Bahamas and southern Florida along 25^0 latitude, eventually turning northwestward over the Gulf of Mexico and northward before it made its final landfall in south-central Louisiana.

In general, the NMC analyses recognize the storms' locations pretty well. However, they tend to underestimates the storms' intensity, especially in the case of Andrew. The evolution of Bob's intensity change is pretty well analyzed. However, the evolution of Ana and Andrew is not well captured. Specifically, the data does not capture Andrew's strength until it landed in Florida.

We use July-to-September (1991) climatology as the basic mean state for the definition of the perturbation fields for all three storms. We divide the perturbation fields into two parts: an upper-four-level PV perturbation (U4) and a lower-six-level PV perturbation (L6). Also, L6 consists of two portions: one is the positive PV anomaly of the storm in the lower-six-levels (L6S), the other is the same as L6, but excluding L6S (i.e., L6E). Piecewise PV inversion is conducted to recover the balanced flows associated with each PV perturbation. By inverting L6S, we recover the balanced flow of the Hurricane vortex. The balanced vortex center is defined as the center of this cyclonic balanced circulation.

In both the cases of Bob and Andrew, the upper-level disturbances are observed to be mainly located above 300 mb. Therefore, U4 is a very good representation of these PV

features. However, in Ana's case, the mid-latitude disturbances project down to the middle troposphere. In all three cases, our analysis shows that the lower and middle tropospheric balanced flow field associated with U4 is very simple, and is mainly dominated by the large-scale and large-amplitude PV anomalies in the upper troposphere. It is not difficult to understand which individual PV feature is the primary contributor to the storm's motion.

This study shows that the upper-level PV anomalies can play important roles in the advection of the storm. However, their quantitative effect on the storm's motion highly depends on the relative location of the storm and the upper PV features. For example, at the nine different times in Bob's case, Bob is consistently advected by a northward flow between a pair of cyclonic and anticyclonic circulations, which are induced by two upper PV anomalies in the middle latitudes. But in Ana's case, there are many cancellations between the balanced flows associated with four main upper PV anomalies. Therefore, the effect of U4 on Ana's motion highly depends upon Ana's location. Finally, in Andrew's case, during the eight days, as the upper PV disturbances evolve and change, and as Andrew moves from the central Atlantic to the Gulf of Mexico, at each instant in time, Andrew's motion contributed by U4 depends on the position of the upper PV anomalies at that time.

The balanced flow pattern associated with L6E is more complicated than that associated with U4. In Bob's case, due to the many cancellations of the balanced flows associated with many PV features, it is not clear which are the dominant lower- or middle-level disturbances that advect Bob. However, Ana is advected by a uniform flow, which is the result of the summation of the balanced flows associated with some lower-level PV anomalies, and some middle tropospheric PV anomalies, which is the downward extension of the upper-level disturbances. Finally, in Andrew's case, we find that it is the PV anomalies near Andrew that play important roles in advecting Andrew.

In this observational study, we also examine the effect the negative PV anomaly above the storm as a proof or disproof of our model results. Bob is the only case that we

find evidence of the generation of negative PV anomaly above and to the downshear (northeastward) of the storm. Also, this negative PV anomaly becomes stronger in time as Bob intensifies. Our preliminary analysis shows that this PV anomaly contributes to the advection of Bob by a northward flow of 4 m s^{-1}. However, we are not sure whether this PV anomaly is indeed diabatically generated by Bob. Thus the result from our analysis is not enough to support or disprove the mechanism described in our model.

In the case of Ana, the data does not show any signature of a negative PV above the storm. In Andrew's case, the NMC analyses capture the negative PV anomaly above Andrew at a later stage after Andrew made landfall in Florida. However, the negative PV anomaly looks very localized and incoherent in time. Our efforts in investigating the effect of negative PV anomalies appear to be impeded by the lack of raw observations over the ocean.

To investigate the existence of the β effect, we also follow the time evolution of the PV perturbation fields in the lower and middle troposphere. Though in the case of Bob, a negative PV anomaly to the northeast of the storm is generally found, we do not see any other evidence that supports the β effect. For Ana's and Andrew's cases, we also do not observe any kind of β effect in the NMC data.

Finally, we also calculate the storm's advection flow as the summation of the balanced flows (interpolated to the storm's center) associated with the mean, U4 and L6E PV perturbations. Two centers are used for interpolation in this study: one is the best track position, the other is the balanced vortex center. In general, the lower-to-middle (850-500) tropospheric advection flow is a very good approximation to the actual storm motions for all the three different storms. The vector differences between our definition of advection flow and the actual storm motion are randomly oriented, except for the case of Andrew, where a constant southward bias exists.

The vertical structures of these storms' advection flows are different. For Bob, there is a mean westerly vertical shear over its center in the early stage, which gradually

shifts to a southerly shear. But for Andrew, a mean easterly shear is observed. In Ana's case, we find that the advection flow is very uniformly distributed in the troposphere.

We also compare our definition of advection flow with the annular mean flow. The results indicate that in all three cases (especially for the cases of Bob and Ana), the advection flow approximates the actual storm movement much better. It is emphasized that the advection flow we define is dynamically meaningful, since it is consistent with the concept that hurricanes, at the first-order approximation, are steered by the flow at its center. The essence of this work is that using PV diagnostics, we can get a clear picture of how the large-scale flow interacts with the storm.

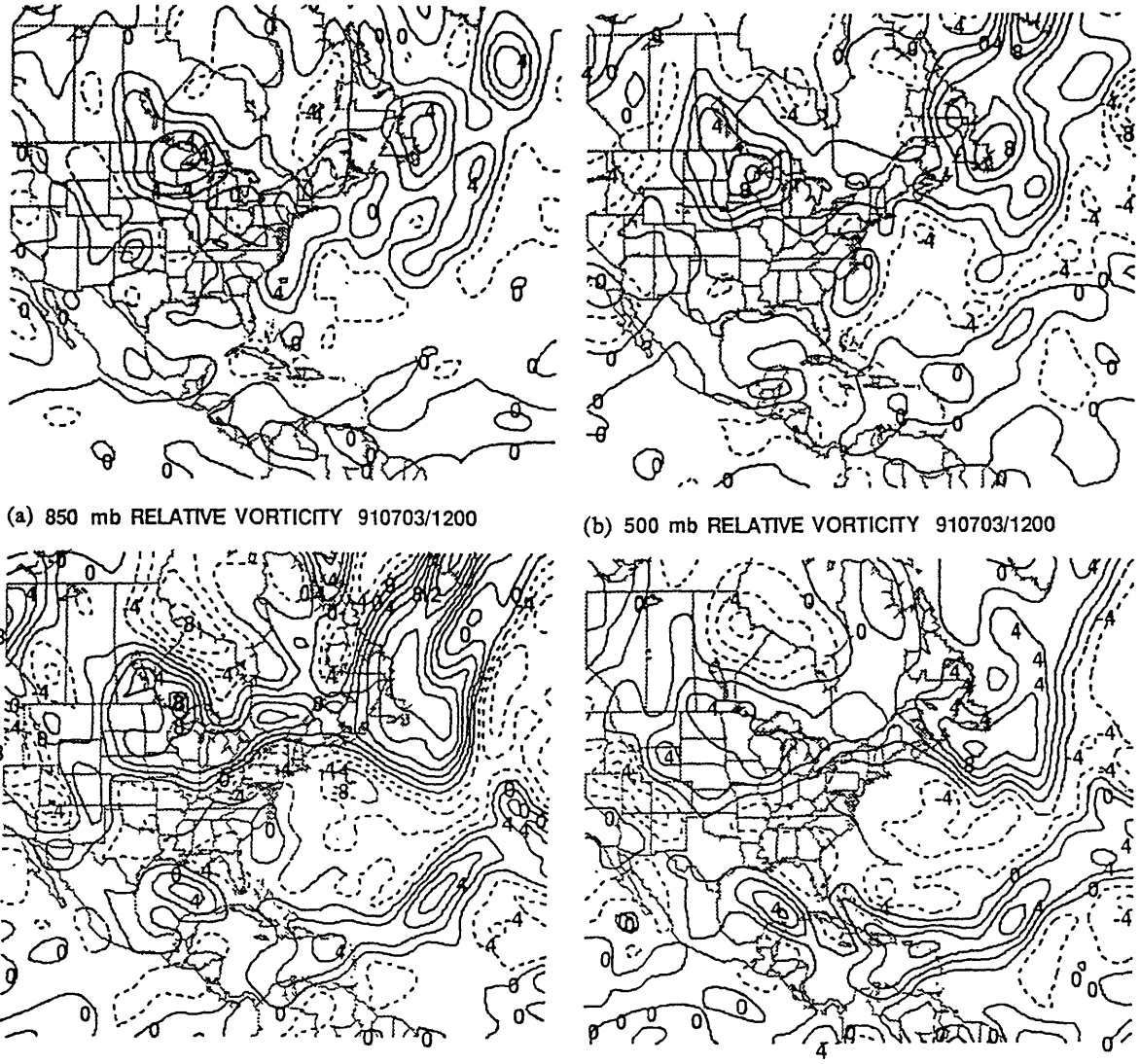

Figure 7.1 Relative vorticity field at 1200 UTC 3 July 1991 at (a) 850 mb, (b) 500 mb, (c) 300 mb, and (d) 150 mb. Solid (dashed) line indicates positive (negative) values. Contour interval is 2×10^{-5} s^{-1}.

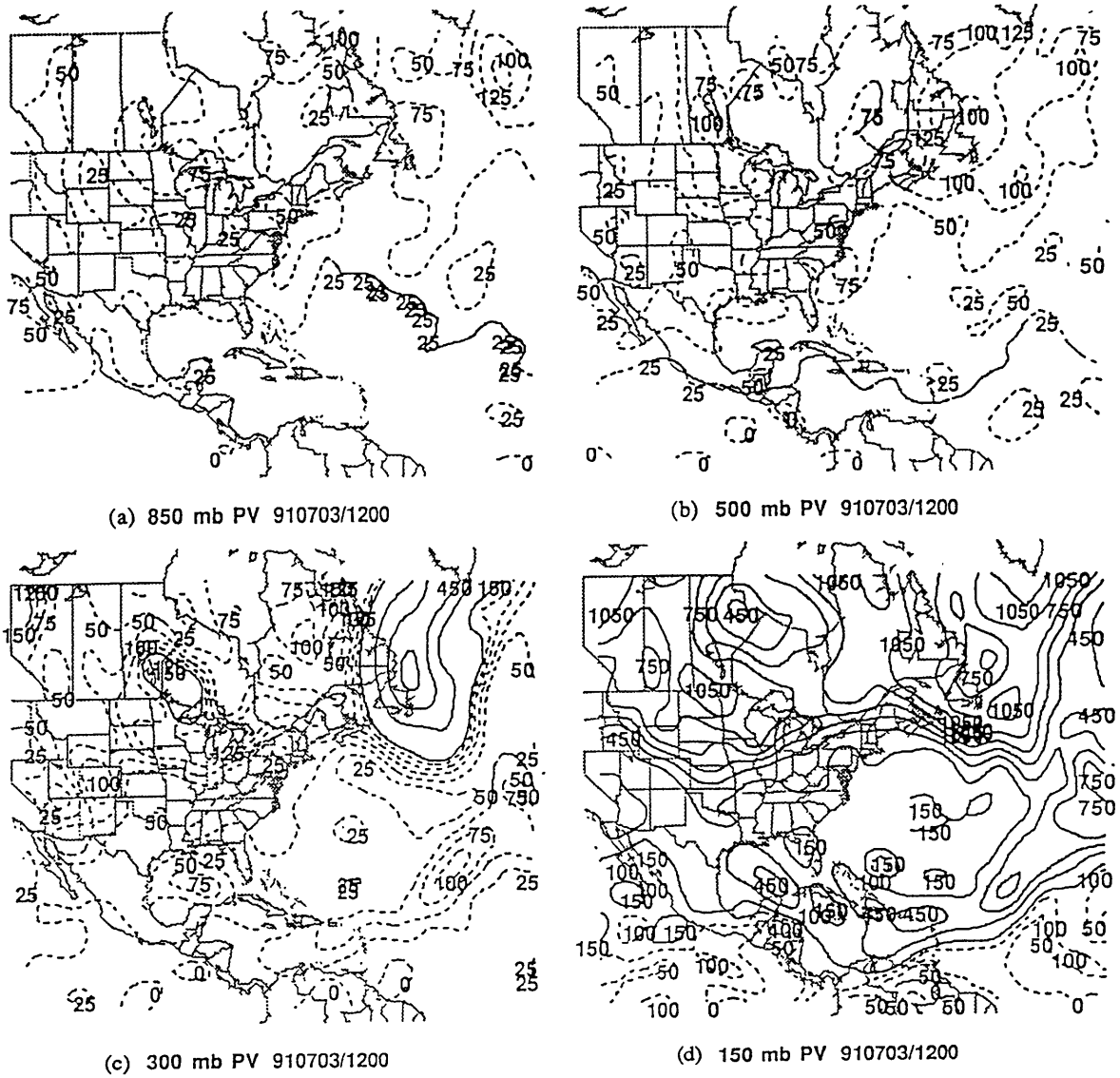

(a) 850 mb PV 910703/1200

(b) 500 mb PV 910703/1200

(c) 300 mb PV 910703/1200

(d) 150 mb PV 910703/1200

Figure 7.2 Ertel's potential vorticity field at 1200 UTC 3 July 1991. (a), (b), (c), and (d) are the perturbation PV maps for the 850, 500, 300 and 150 isobaric surfaces, respectively. The unit is 0.01 PVU. Potential vorticity values smaller than (larger than or equal to) 1.5 PVU are shown as solid (dashed) lines with contour intervals of 0.25 PVU (1.5 PVU).

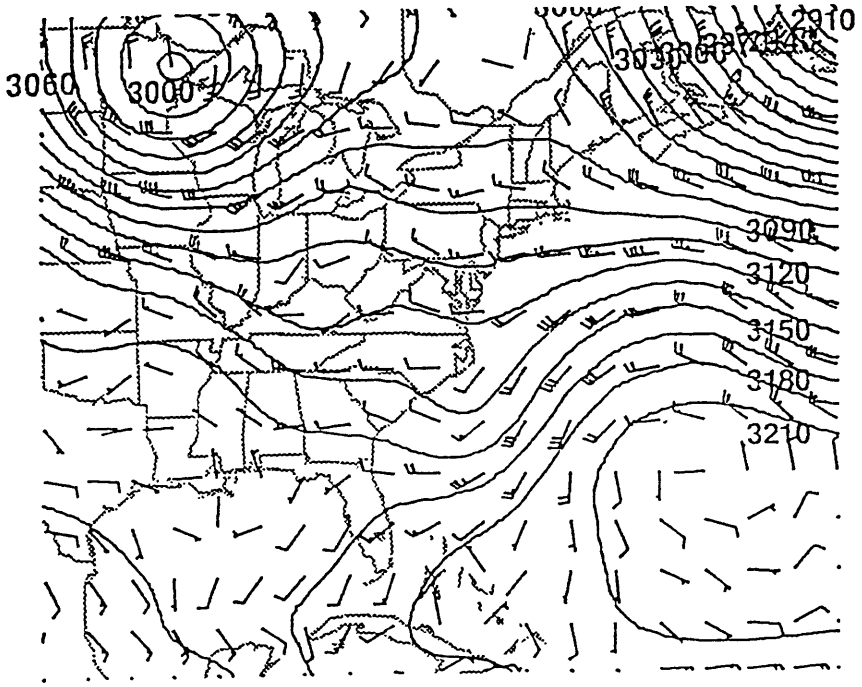

Figure 7.3 Balanced height field (contour interval of 15 m) and NMC analyzed wind field (wind barb plotted as in Fig. 6.4) at 700 mb at 1200 UTC 3 July 1991.

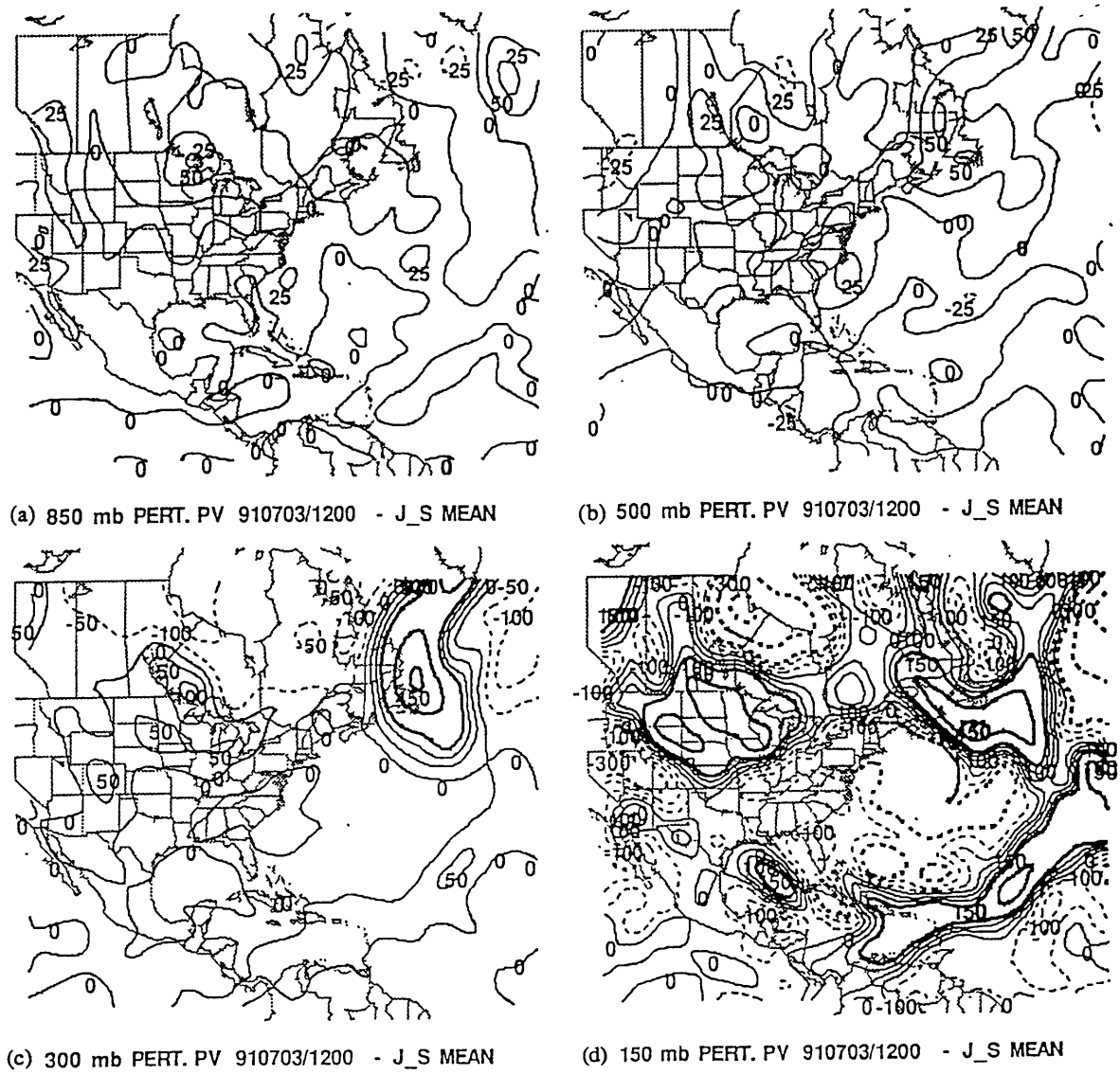

(a) 850 mb PERT. PV 910703/1200 - J_S MEAN

(b) 500 mb PERT. PV 910703/1200 - J_S MEAN

(c) 300 mb PERT. PV 910703/1200 - J_S MEAN

(d) 150 mb PERT. PV 910703/1200 - J_S MEAN

Figure 7.4 Ertel's potential vorticity perturbation field at 1200 UTC 3 July 1991. (a), (b), (c), and (d) are the perturbation PV maps for the 850, 500, 300 and 150 isobaric surfaces, respectively. The unit is 0.01 PVU. Potential vorticity values smaller than (larger than or equal to) 1.5 PVU are shown as thin lines (bold lines) with contour intervals of 0.25 PVU (1.5 PVU). Positive (negative) values are represented by solid (dashed) lines.

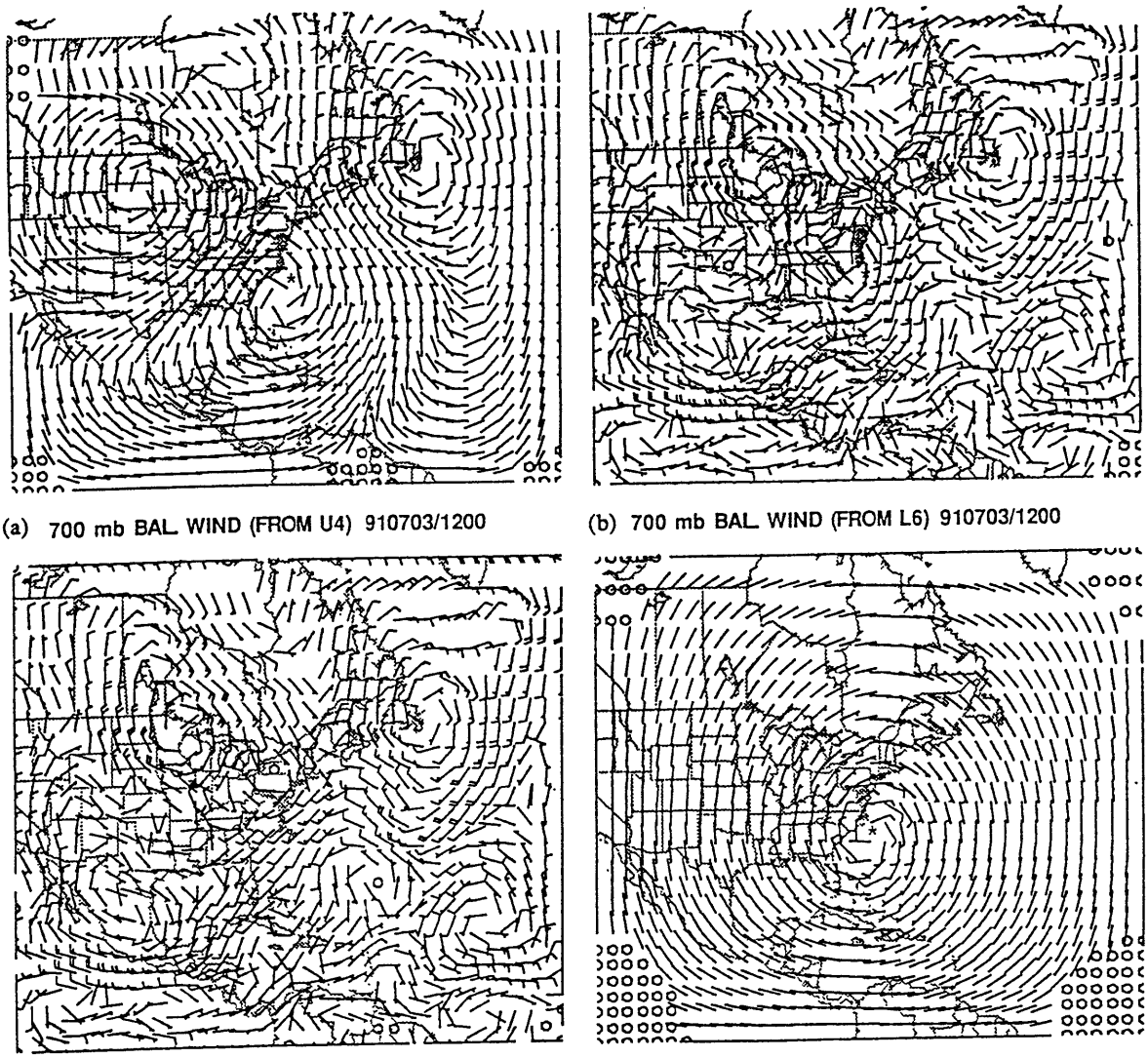

Figure 7.5 700-mb balanced wind fields (wind barb plotted as in Fig. 6.4) associated with (a) U4, (b) L6, (c) L6E, and (d) L6S at 1200 UTC 3 July 1991. Tropical Storm Ana's best track positions are indicated by an asterisk (*).

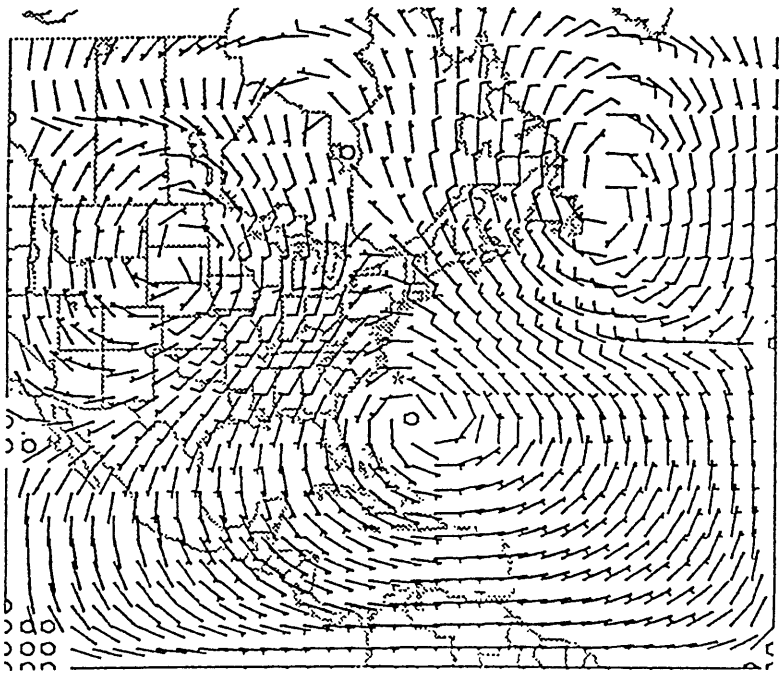

Figure 7.6 700-mb balanced wind field (wind barb plotted as in Fig. 6.4) associated with P1+P2+N1+N2 at 1200 UTC 3 July 1991. Tropical Storm Ana's best track positions are indicated by an asterisk (*).

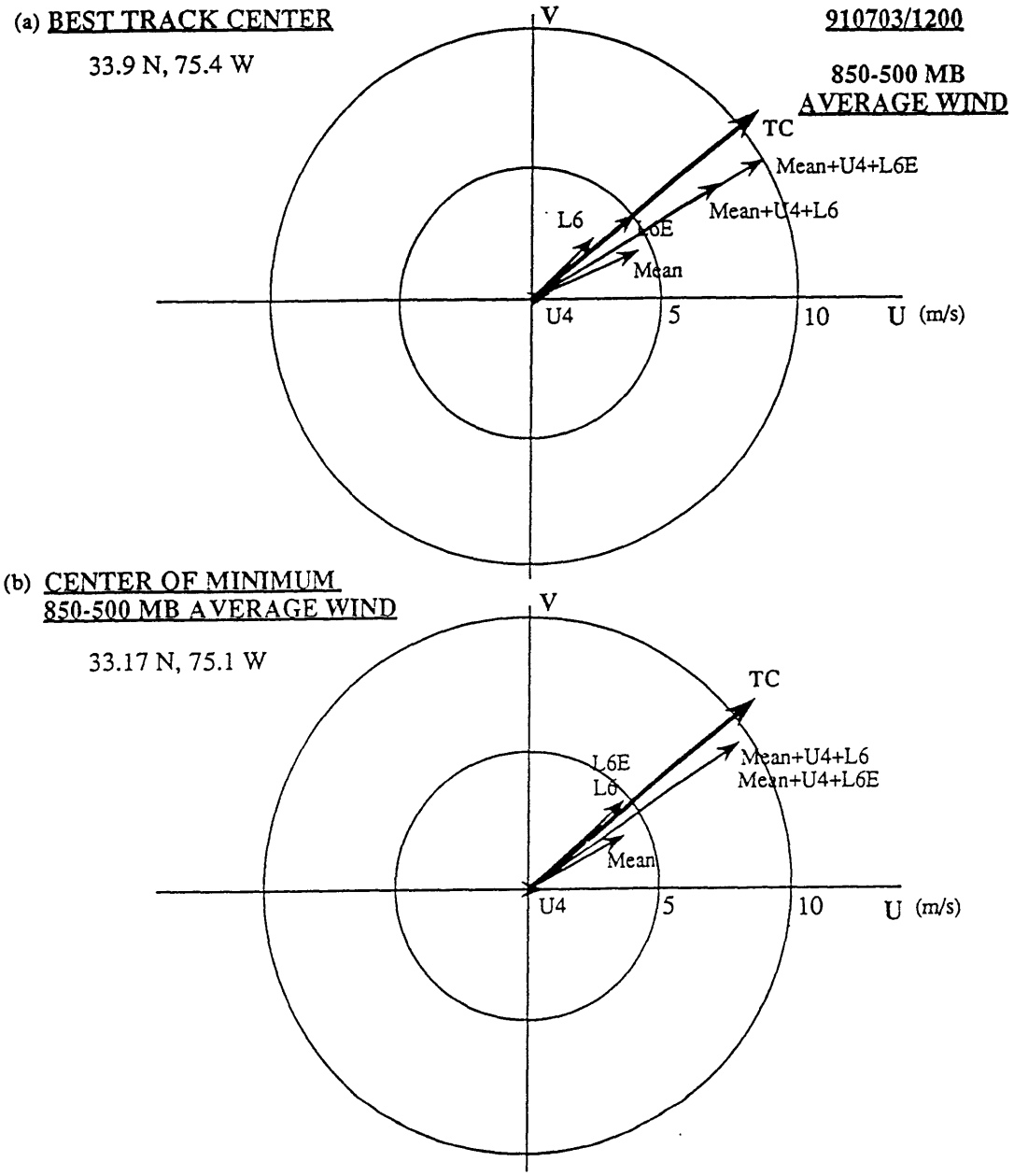

Figure 7.7 Velocity vectors of balanced flows and Tropical Storm Ana's motion at 1200 UTC 3 July 1991. Mean, U4, L6, and L6E represent the 850-500-mb pressure-averaged balanced flows associated with mean potential vorticity, and potential vorticity perturbation of U4, L6, and L6E, respectively. Mean+U4+L6E represents the total hurricane advection flow. TC indicates Ana's motion estimated from every 6-hour best-track position. (a) Interpolation of the balanced wind fields at the best-track center; and (b) at the 850-500-mb pressure-averaged balanced vortex center.

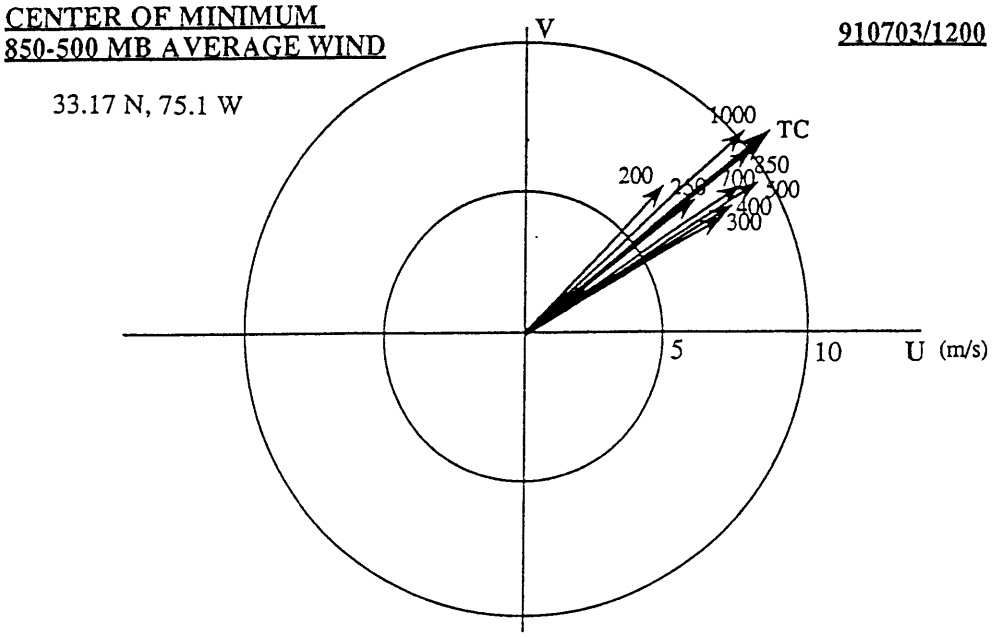

Figure 7.8 Velocity vectors of advection flow at each level and Tropical Storm Ana's motion at 1200 UTC 3 July 1991. The hurricane advection flow is defined as the interpolation of the balanced flows associated with mean, U4, and L6E at the 850-500-mb pressure-averaged balanced vortex center. TC indicates Ana's motion estimated from every 6-hour best-track position.

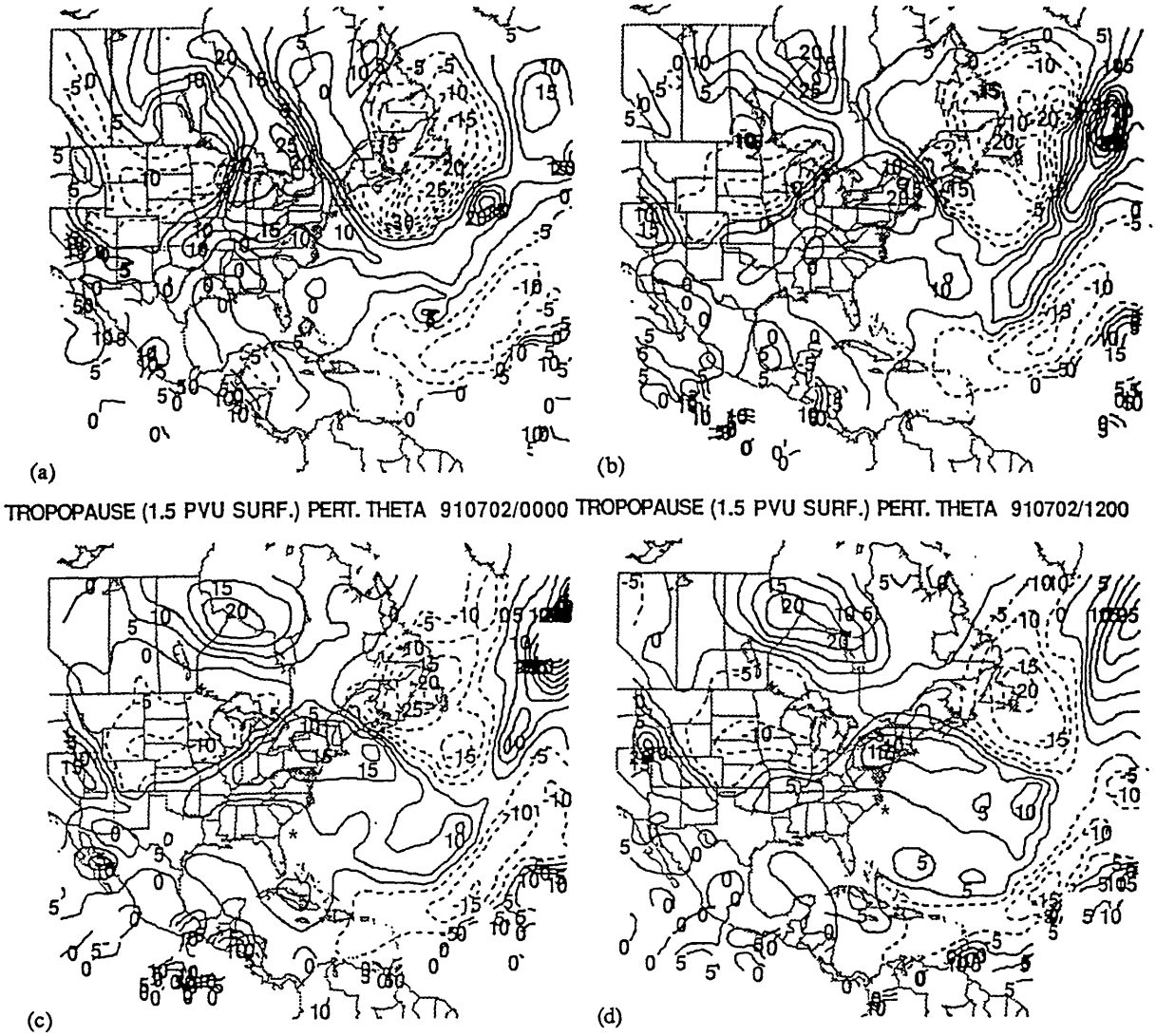

Figure 7.9 Time evolution of the tropopause potential temperature perturbation field (on the 1.5 PVU surface) from 0000 UTC 2 to 0000 UTC 5 July 1991. (a) 0000 UTC 2, (b) 1200 UTC 2, (c) 0000 UTC 3, (d) 1200 UTC 3, (e) 0000 UTC 4, (f) 1200 UTC 4, and (g) 0000 UTC 5. The contour interval is 5 K. All positive (negative) values are represented by solid (dashed) lines. Tropical Storm Ana's best track positions are indicated by an asterisk (*).

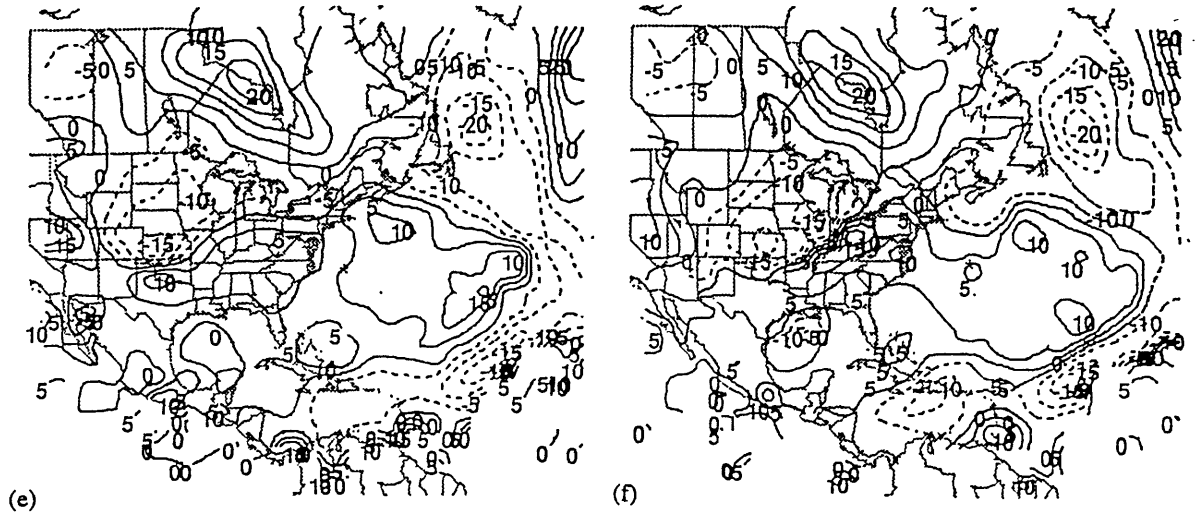

(e) TROPOPAUSE (1.5 PVU SURF.) PERT. THETA 910704/0000

(f) TROPOPAUSE (1.5 PVU SURF.) PERT. THETA 910704/1200

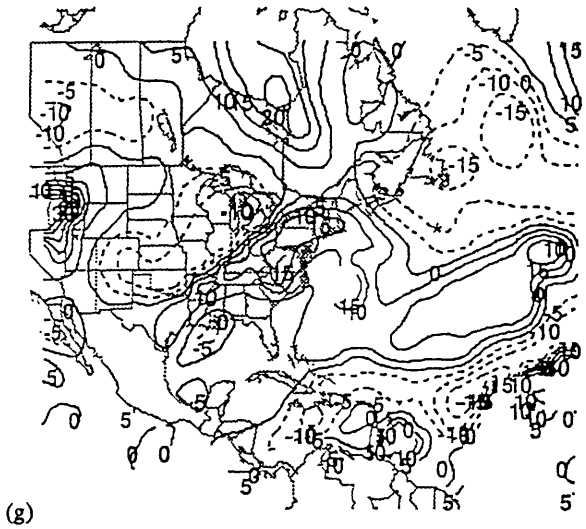

(g) TROPOPAUSE (1.5 PVU SURF.) PERT. THETA 910705/0000

Figure 7.9 (Continued)

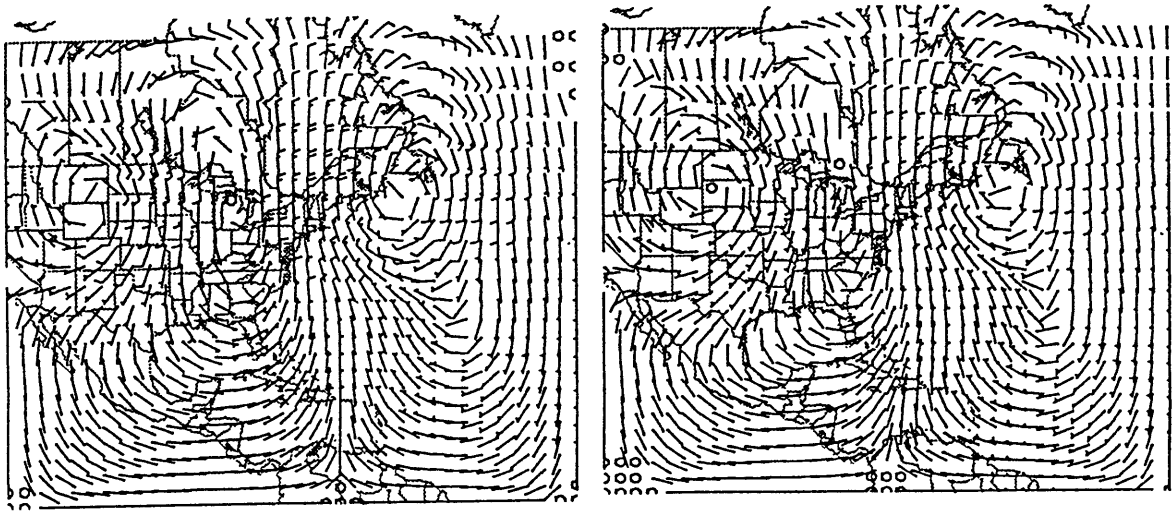

(a) 700 mb WIND (FROM U4 PERT. PV) 910702/0000

(b) 700 mb WIND (FROM U4 PERT. PV) 910702/1200

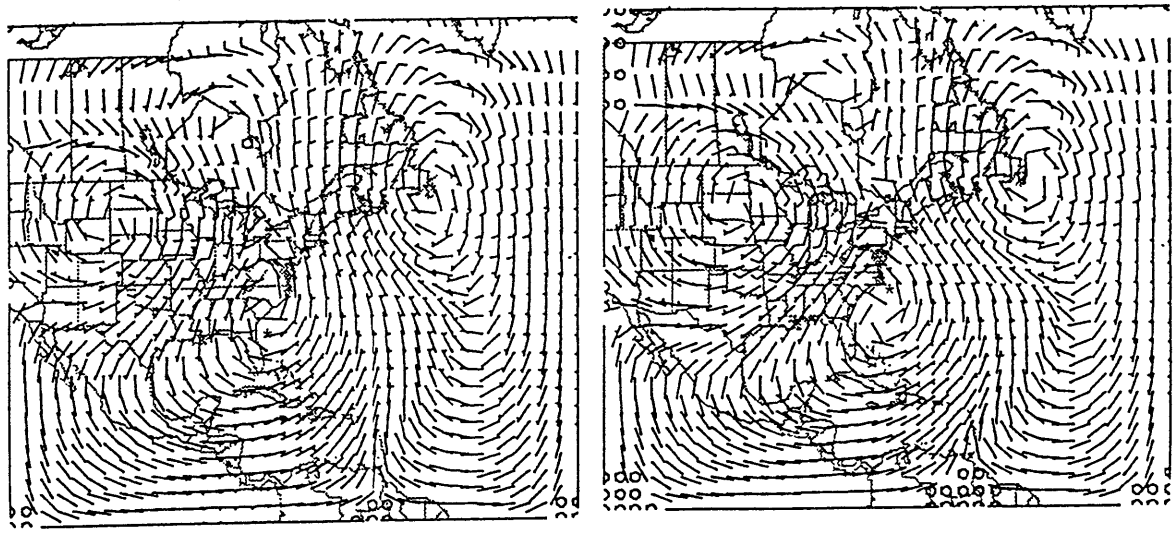

(c) 700 mb WIND (FROM U4 PERT. PV) 910703/0000

(d) 700 mb WIND (FROM U4 PERT. PV) 910703/1200

Figure 7.10 Time evolution of the 700-mb balanced wind field (wind barb plotted as in Fig. 6.4) associated with U4 from 0000 UTC 2 to 0000 UTC 5 July 1991. (a) 0000 UTC 2, (b) 1200 UTC 2, (c) 0000 UTC 3, (d) 1200 UTC 3, (e) 0000 UTC 4, (f) 1200 UTC 4, and (g) 0000 UTC 5. Tropical Storm Ana's best track positions are indicated by an asterisk (*).

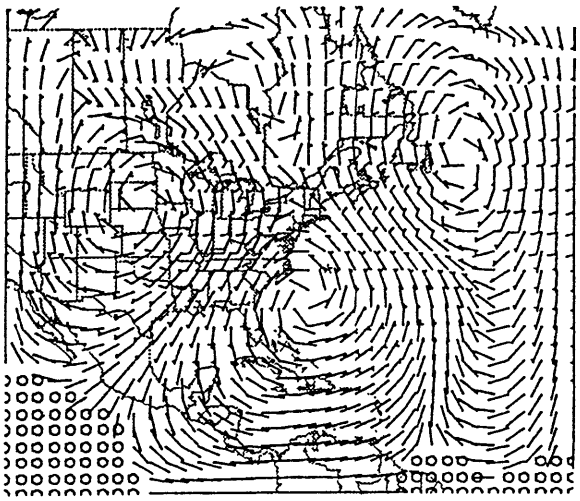

(e) 700 mb WIND (FROM U4 PERT. PV) 910704/0000

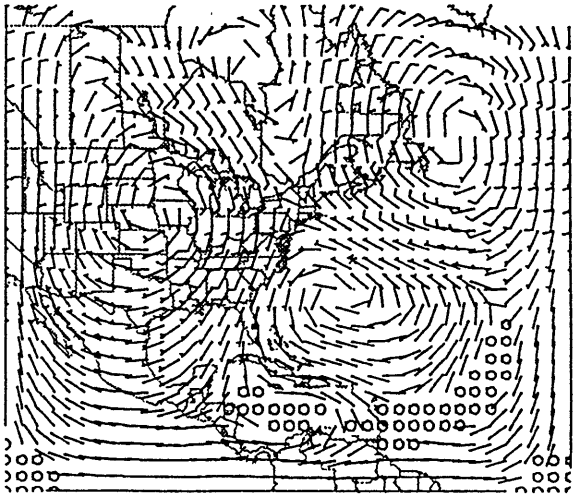

(f) 700 mb WIND (FROM U4 PERT. PV) 910704/1200

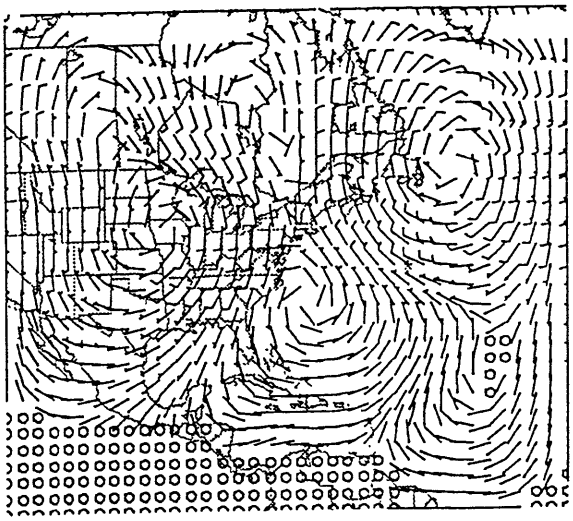

(g) 700 mb WIND (FROM U4 PERT. PV) 910705/0000

Figure 7.10 (Continued)

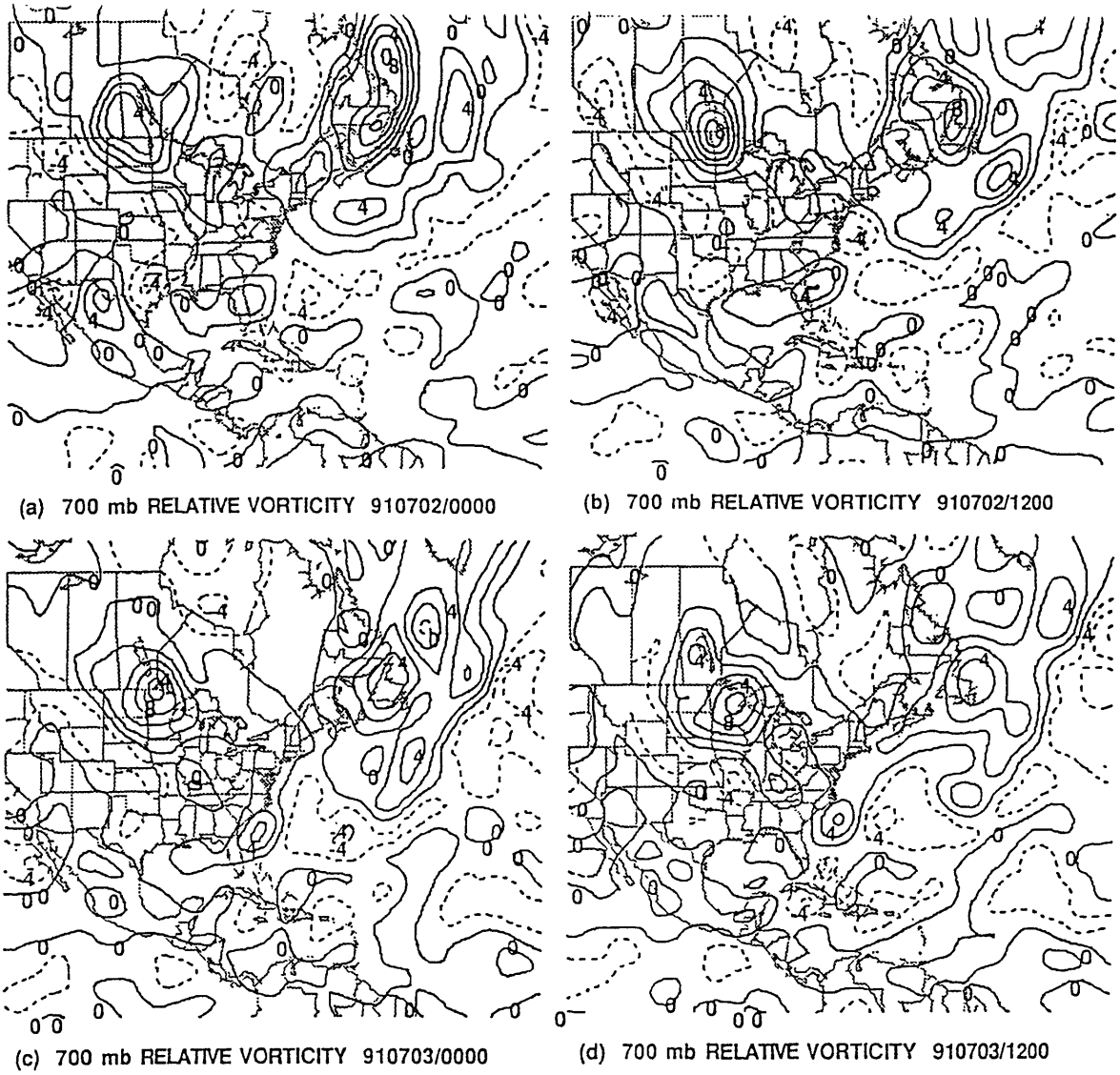

Figure 7.11 Time evolution of the relative vorticity field at 700 mb from 0000 UTC 2 to 0000 UTC 5 July 1991. (a) 0000 UTC 2, (b) 1200 UTC 2, (c) 0000 UTC 3, (d) 1200 UTC 3, (e) 0000 UTC 4, (f) 1200 UTC 4, and (g) 0000 UTC 5. The contour interval is 2×10^{-5} s^{-1}. All positive (negative) values are represented by solid (dashed) lines.

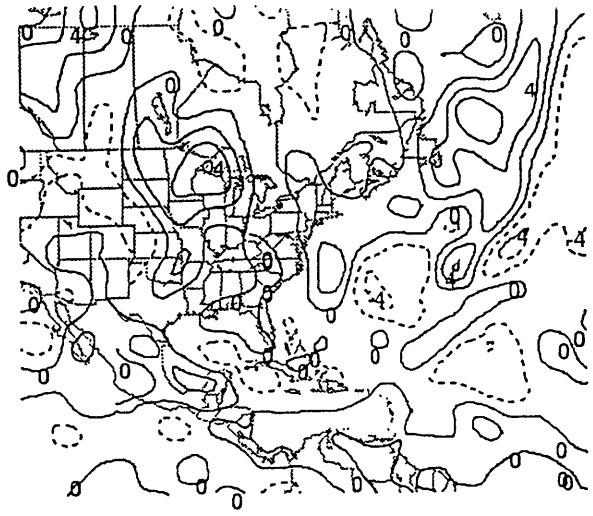

(e) 700 mb RELATIVE VORTICITY 910704/0000

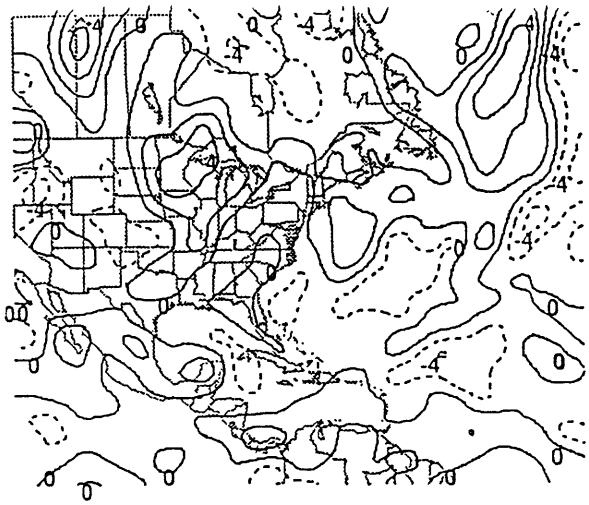

(f) 700 mb RELATIVE VORTICITY 910704/1200

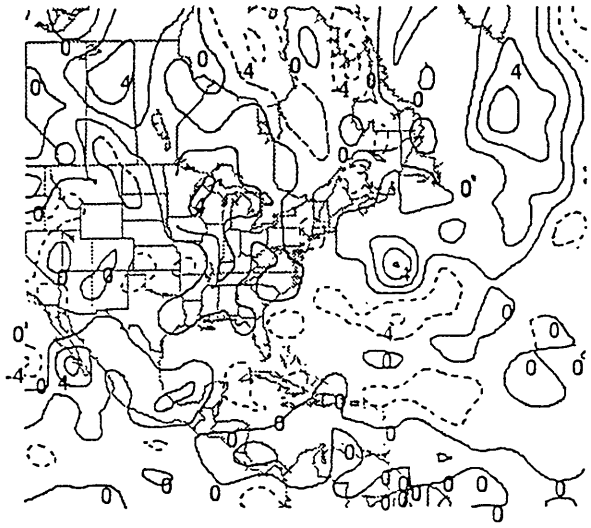

(g) 700 mb RELATIVE VORTICITY 910705/0000

Figure 7.11 (Continued)

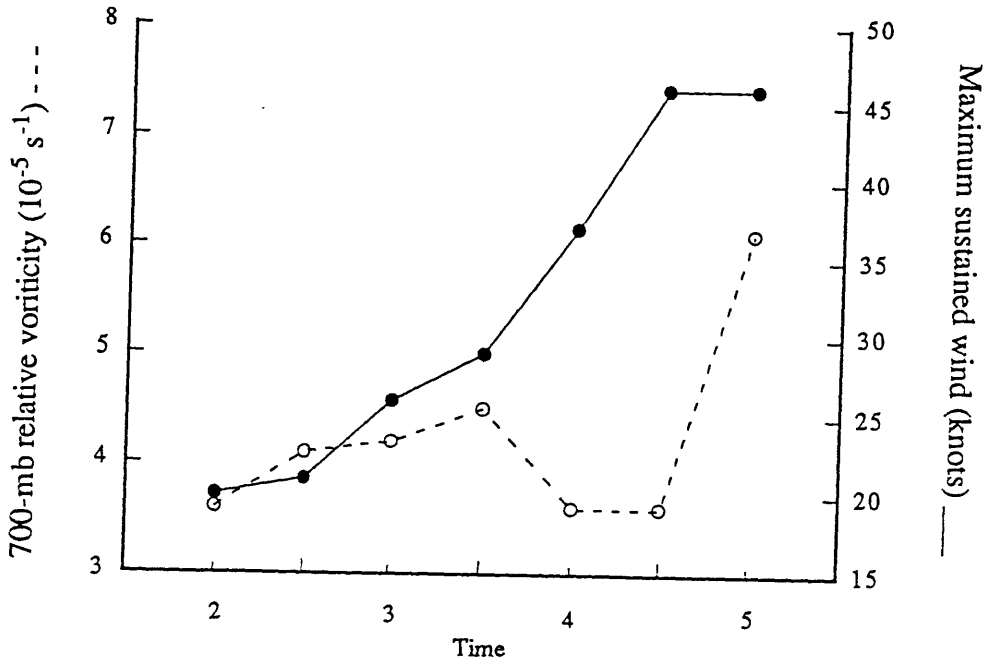

Figure 7.12 Analyzed maximum relative vorticity from NMC data (dashed) and best track maximum sustained wind speed curve (solid, from Preliminary Report) from 0000 UTC 2 to 0000 UTC 5 July 1991 for Tropical Storm Ana.

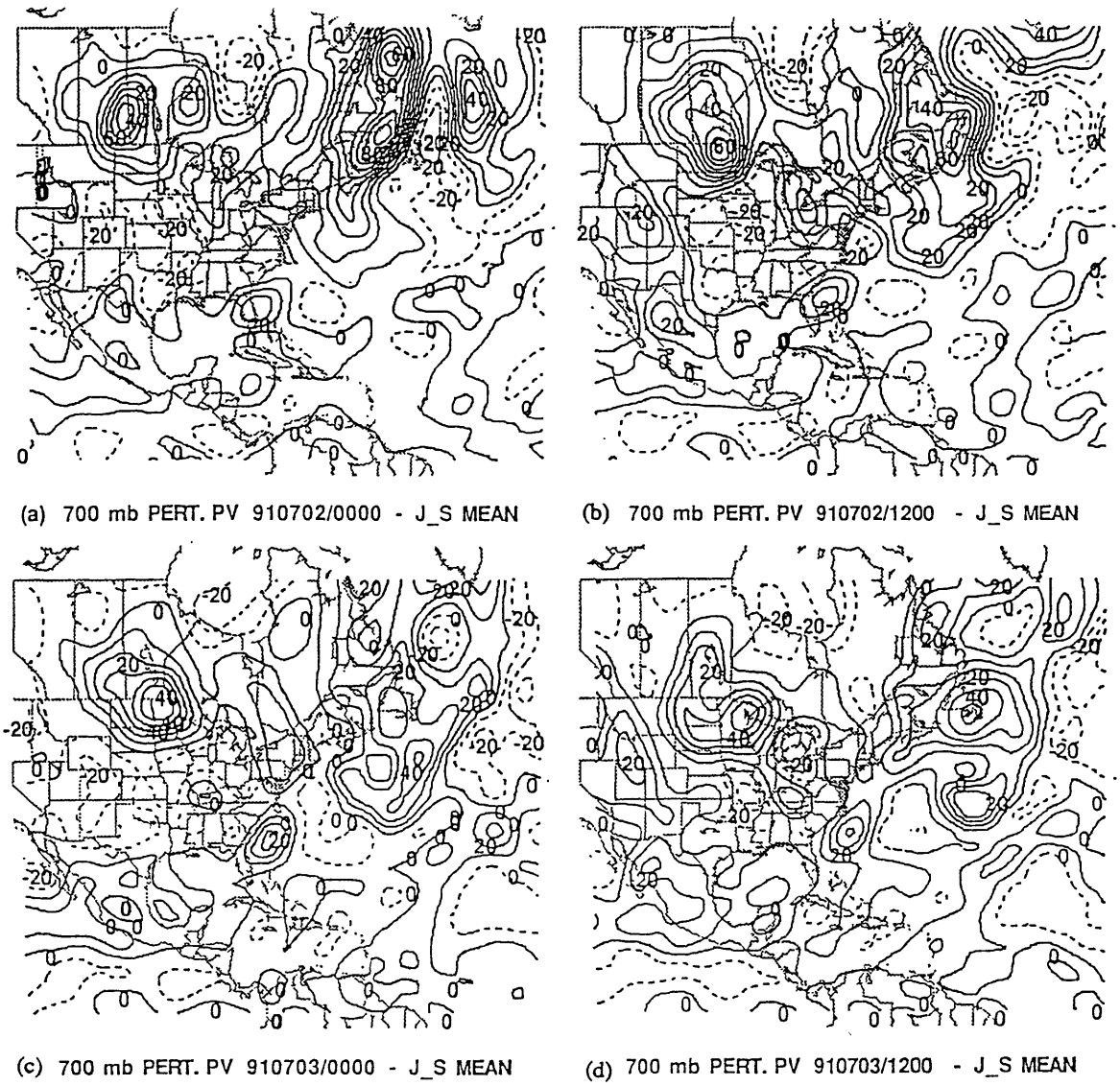

Figure 7.13 Time evolution of the Ertel's potential vorticity perturbation field at 700 mb from 0000 UTC 2 to 0000 UTC 5 July 1991. (a) 0000 UTC 2, (b) 1200 UTC 2, (c) 0000 UTC 3, (d) 1200 UTC 3, (e) 0000 UTC 4, (f) 1200 UTC 4, and (g) 0000 UTC 5. The unit is 0.01 PVU, and contour interval is 0.1 PVU. All positive (negative) values are represented by solid (dashed) lines.

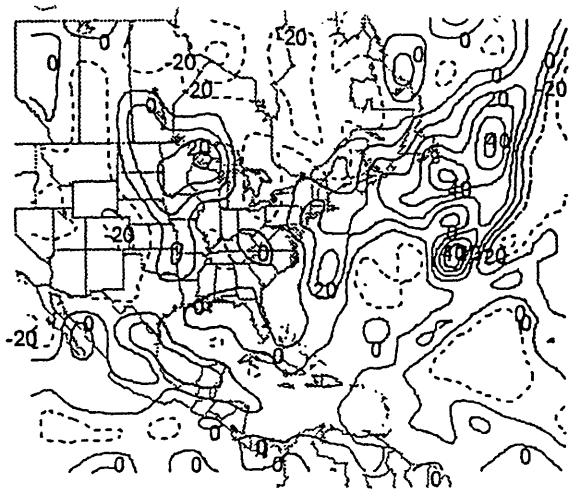

(e) 700 mb PERT. PV 910704/0000 - J_S MEAN

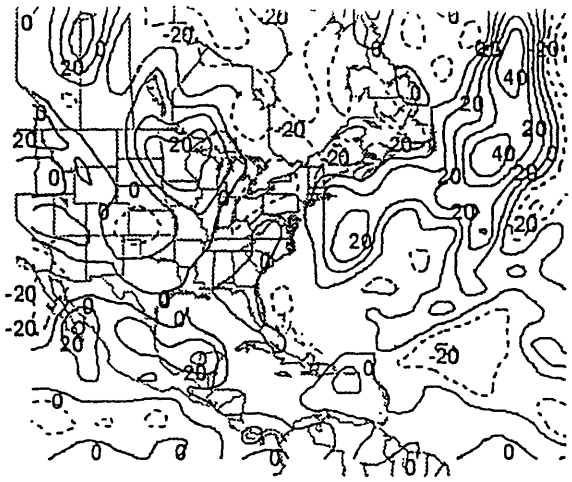

(f) 700 mb PERT. PV 910704/1200 - J_S MEAN

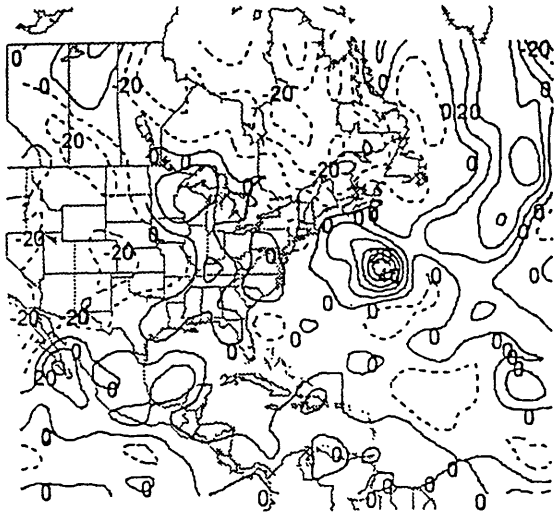

(g) 700 mb PERT. PV 910705/0000 - J_S MEAN

Figure 7.13 (Continued)

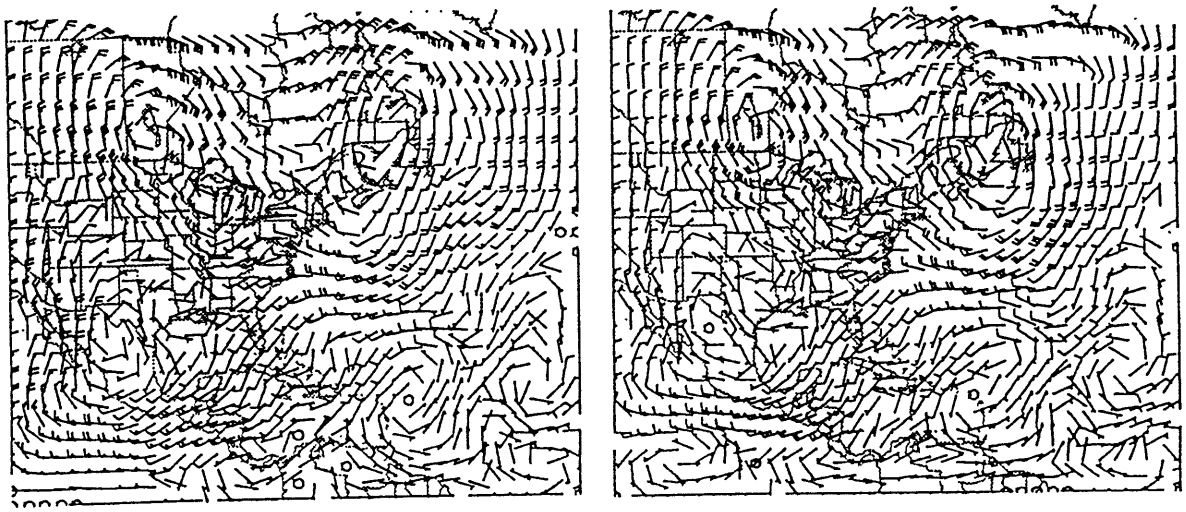

(a) 700 mb WIND (FROM L6E PERT. PV) 910702/0000 (b) 700 mb WIND (FROM L6E PERT. PV) 910702/1200

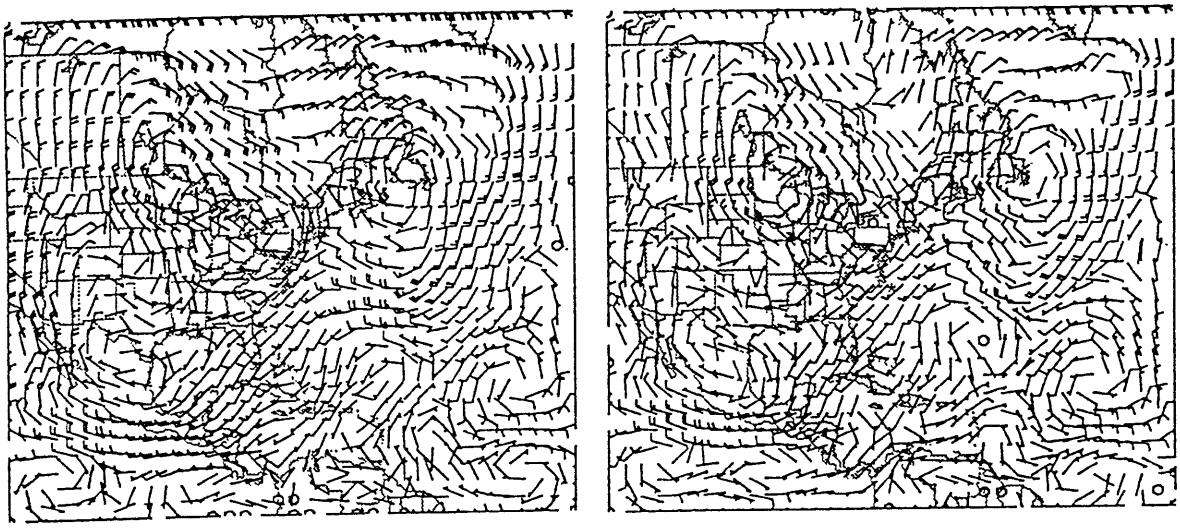

(c) 700 mb WIND (FROM L6E PERT. PV) 910703/0000 (d) 700 mb WIND (FROM L6E PERT. PV) 910703/1200

Figure 7.14 Time evolution of the 700-mb balanced wind field (wind barb plotted as in Fig. 6.4) associated with L6E from 0000 UTC 2 to 0000 UTC 5 July 1991. (a) 0000 UTC 2, (b) 1200 UTC 2, (c) 0000 UTC 3, (d) 1200 UTC 3, (e) 0000 UTC 4, (f) 1200 UTC 4, and (g) 0000 UTC 5. Tropical Storm Ana's best track positions are indicated by an asterisk (*).

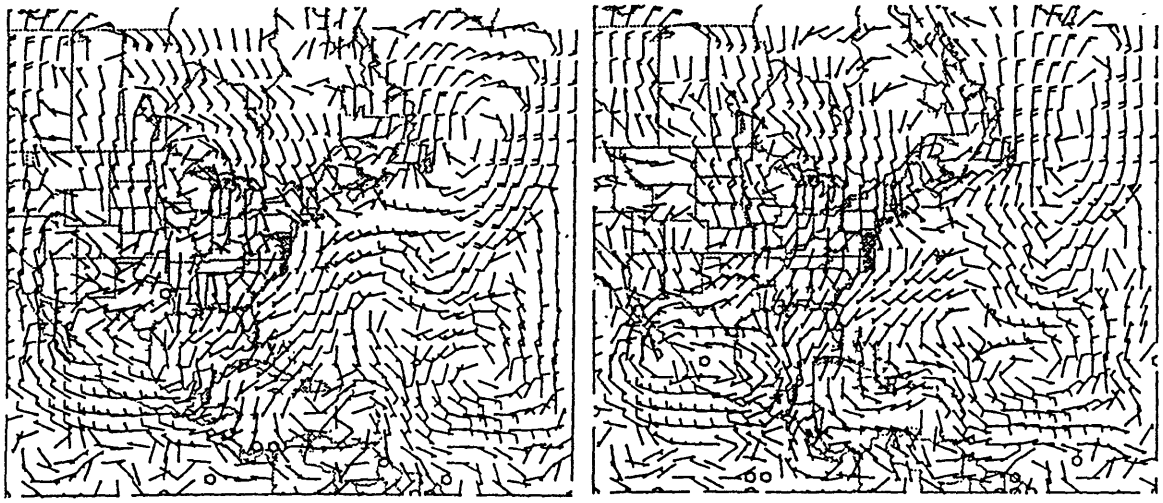

(e) 700 mb WIND (FROM L6E PERT. PV) 910704/0000 (f) 700 mb WIND (FROM L6E PERT. PV) 910704/1200

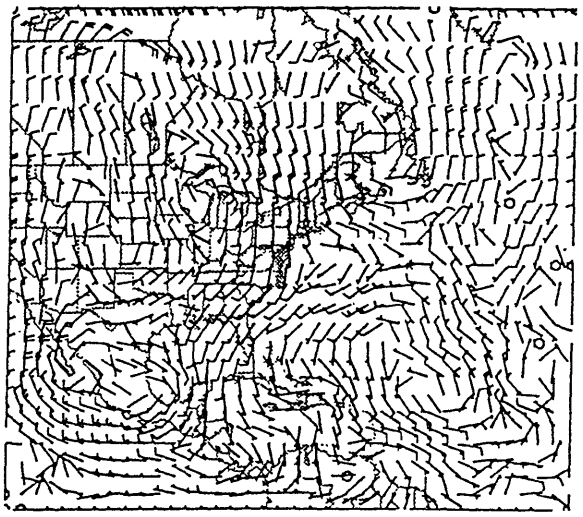

(g) 700 mb WIND (FROM L6E PERT. PV) 910705/0000

Figure 7.14 (Continued)

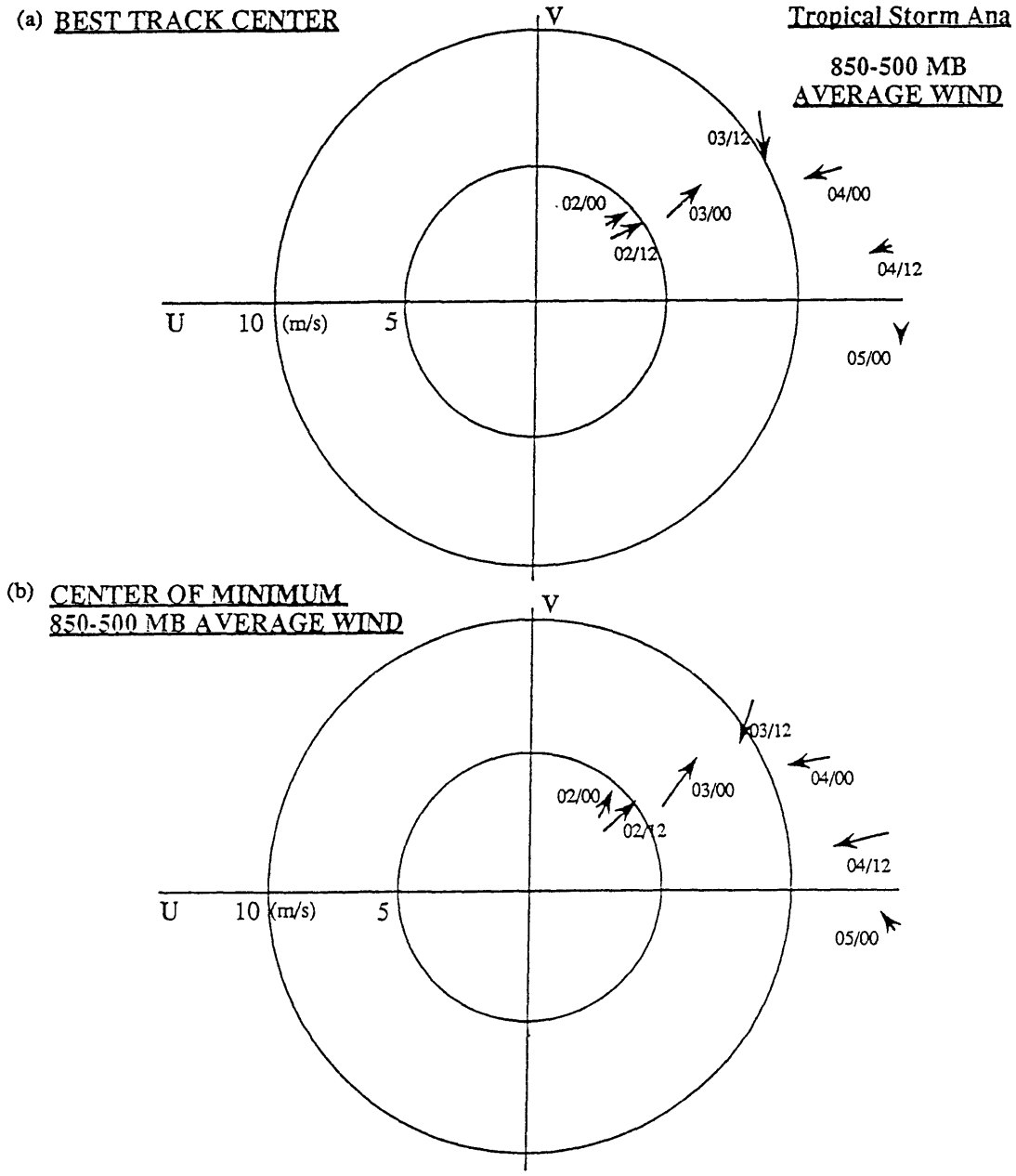

Figure 7.15 Velocity vector differences between the 850-500-mb pressure-averaged advection flow and Ana's motion from 0000 UTC 2 to 0000 UTC 5 July 1991. (a) Interpolation of the balanced wind fields at the best-track center; and (b) at the 850-500-mb pressure-averaged balanced vortex center.

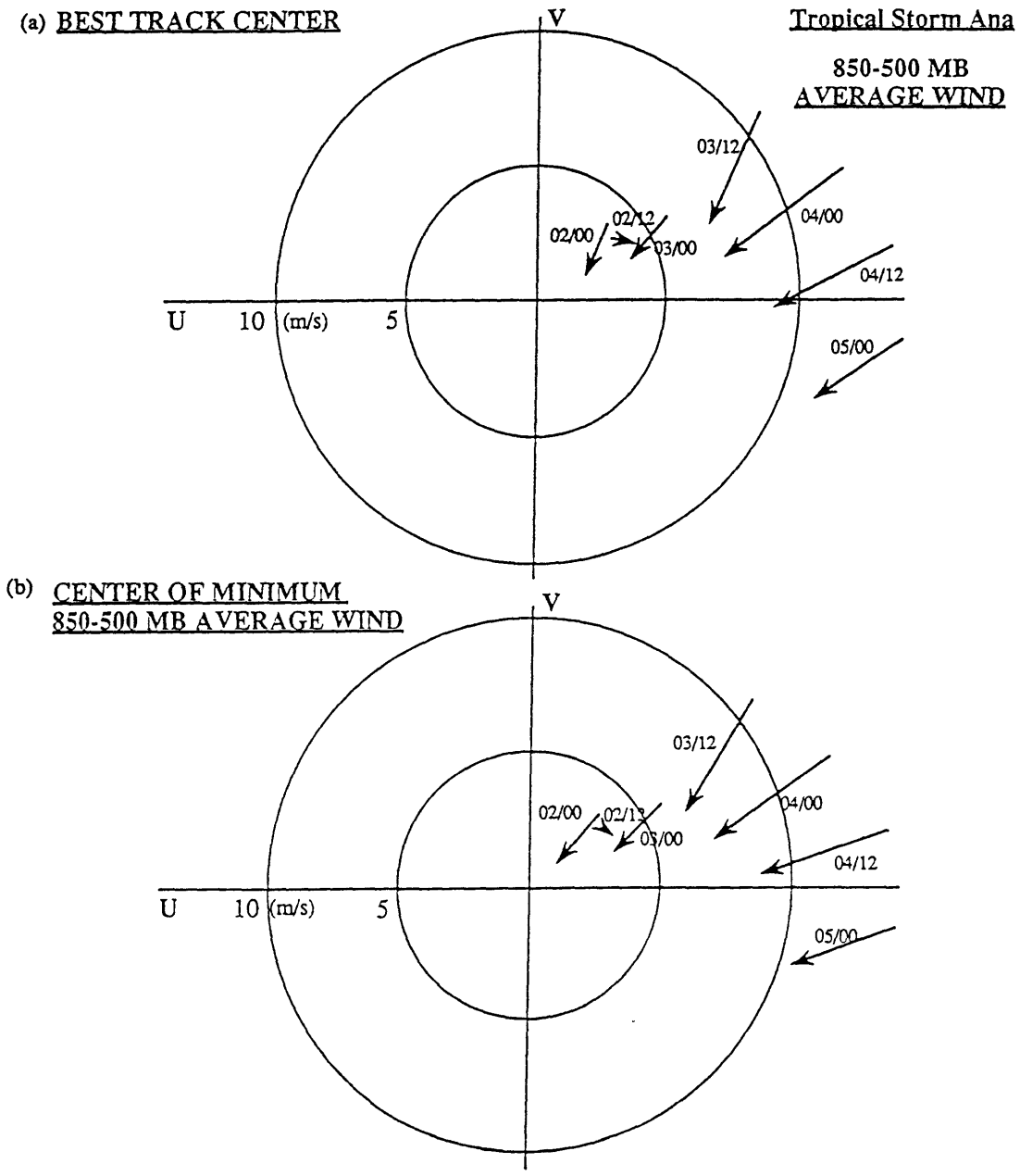

Figure 7.16 Velocity vector differences between the 850-500-mb pressure-averaged annular mean flow and Ana's motion from 0000 UTC 2 to 0000 UTC 5 July 1991. (a) Interpolation of the wind fields at the best-track center; and (b) at the 850-500-mb averaged balanced vortex center.

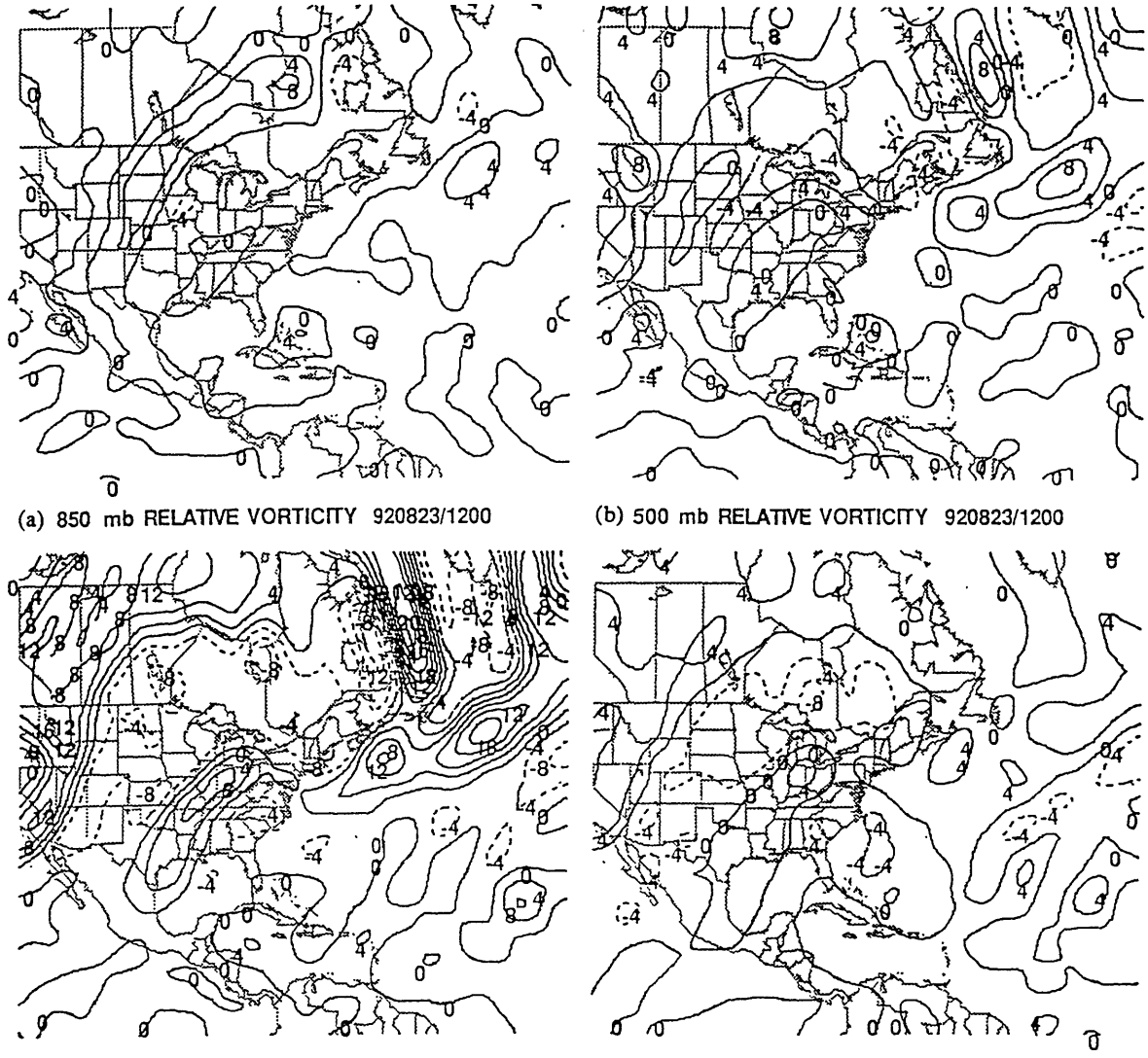

Figure 7.17 Relative vorticity field at 1200 UTC 23 August 1992 at (a) 850 mb, (b) 500 mb, (c) 300 mb, and (d) 150 mb. Solid (dashed) line indicates positive (negative) values. Contour interval is 4×10^{-5} s^{-1}.

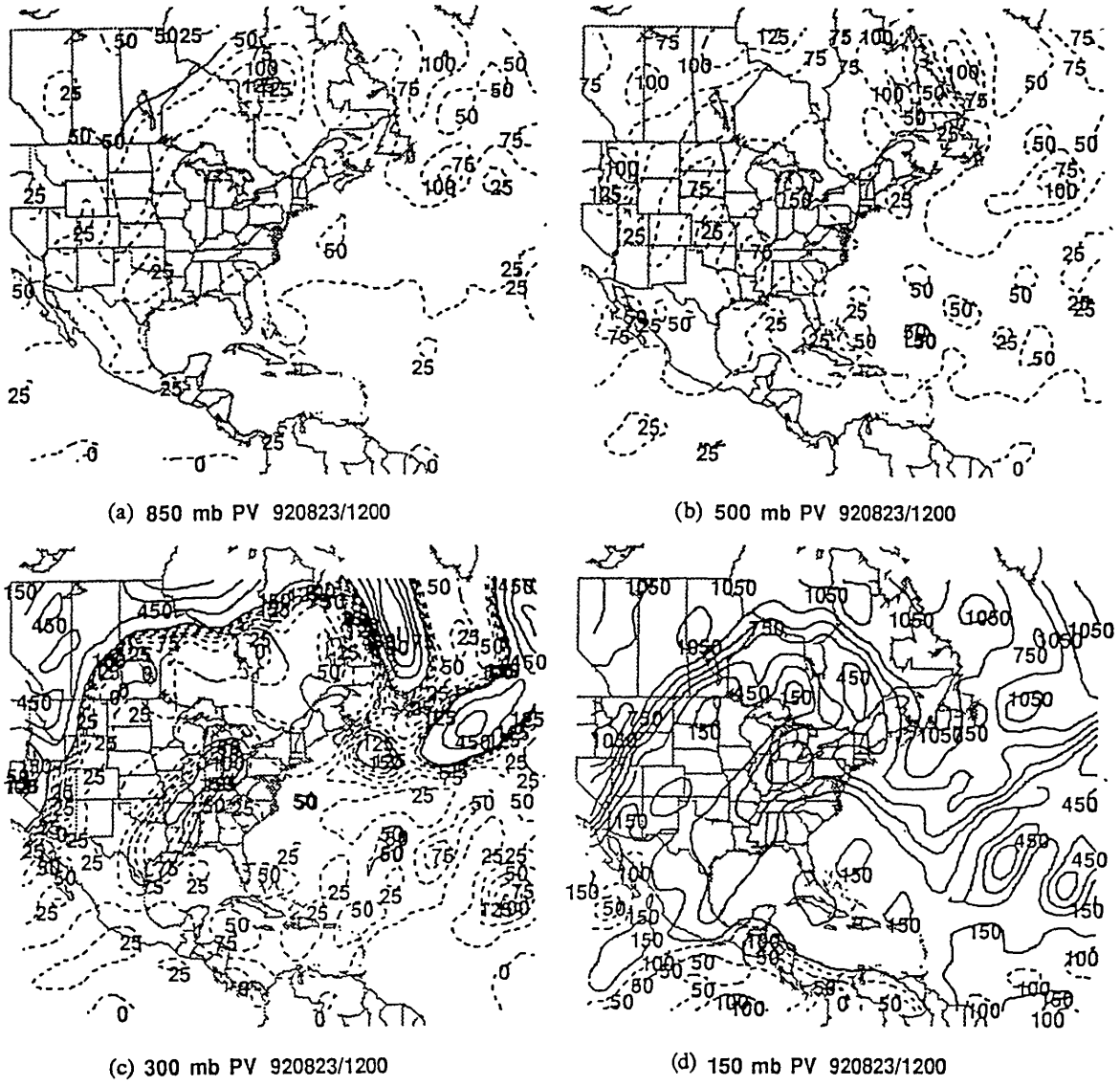

(a) 850 mb PV 920823/1200

(b) 500 mb PV 920823/1200

(c) 300 mb PV 920823/1200

(d) 150 mb PV 920823/1200

Figure 7.18 Ertel's potential vorticity field at 1200 UTC 23 August 1992. (a), (b), (c), and (d) are the perturbation PV maps for the 850, 500, 300 and 150 isobaric surfaces, respectively. The unit is 0.01 PVU. Potential vorticity values smaller than (larger than or equal to) 1.5 PVU are shown as solid (dashed) lines with contour intervals of 0.25 PVU (1.5 PVU).

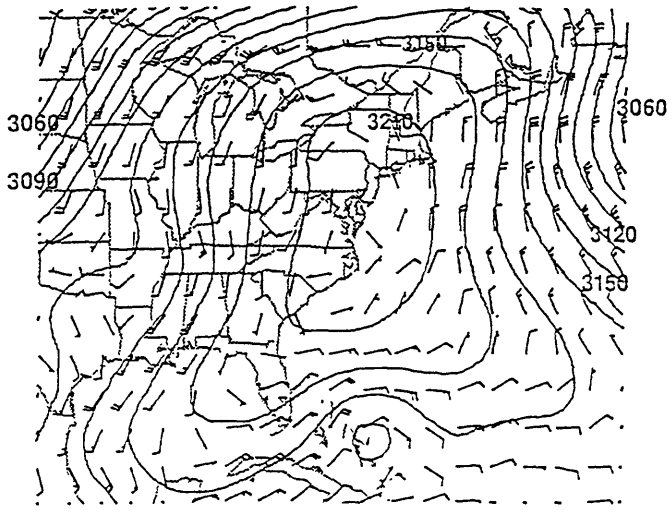

(a) 700 mb BAL H and NMC ANALYSIS WIND 920823/1200

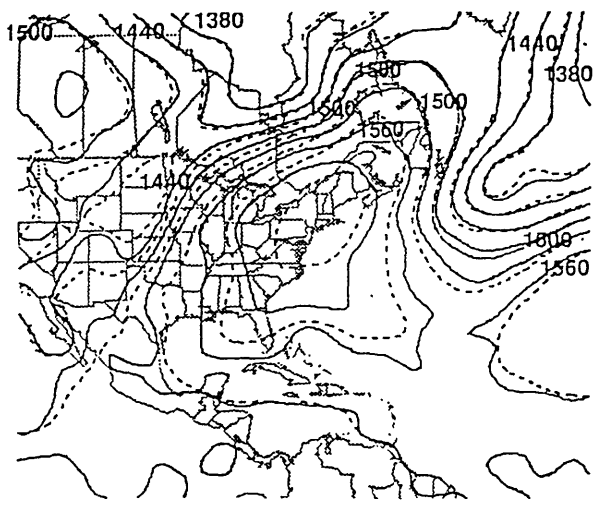

(b) 850 mb H AND BALANCED H 920823/1200

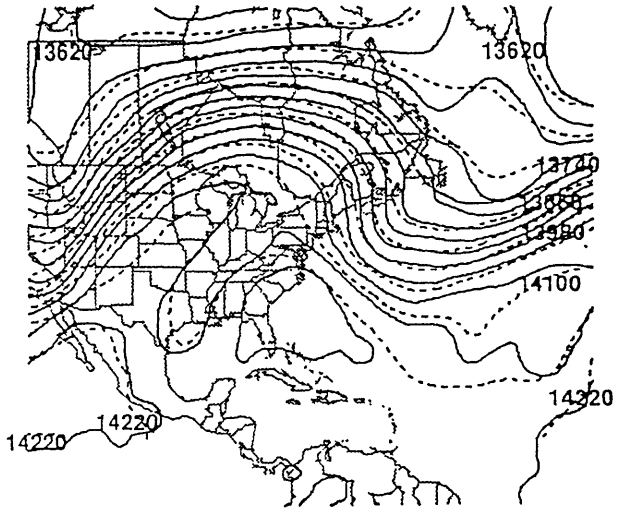

(c) 150 mb H AND BALANCED H 920823/1200

Figure 7.19 (a) Balanced height field (contour interval of 15 m) and NMC analyzed wind field (wind barb plotted as in Fig. 6.4) at 700 mb at 1200 UTC 23 August 1992. NMC analyzed height field (solid) and balanced height field (dashed) at 1200 UTC 18 August 1991 at (b) 850 mb, and (c) 150 mb. Contour intervals are 30 m for (b), 60 m (c).

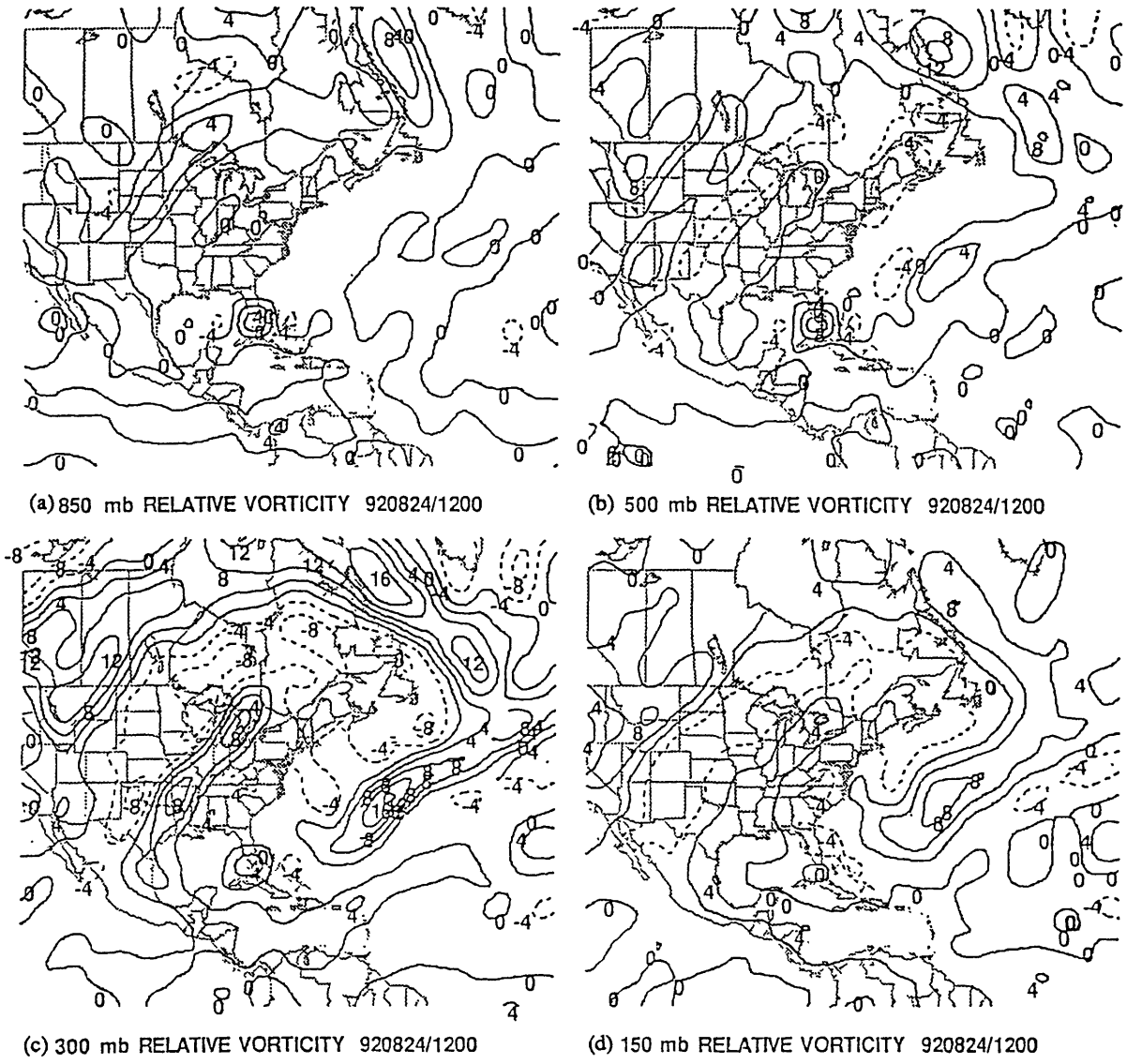

Figure 7.20 Relative vorticity field at 1200 UTC 23 August 1992 at (a) 850 mb, (b) 500 mb, (c) 300 mb, and (d) 150 mb. Solid (dashed) line indicates positive (negative) values. Contour interval is 4×10^{-5} s^{-1}.

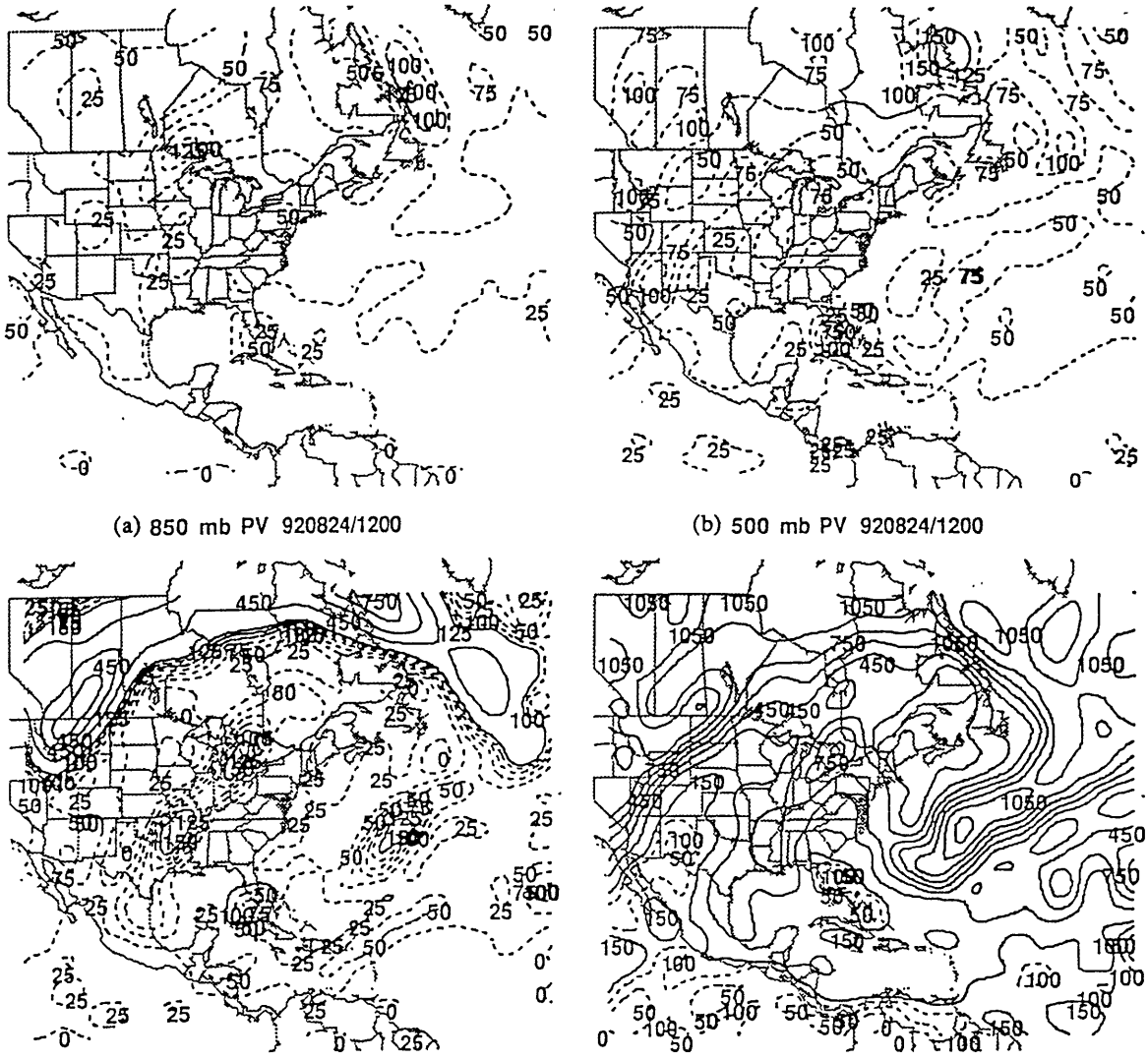

(a) 850 mb PV 920824/1200

(b) 500 mb PV 920824/1200

(c) 300 mb PV 920824/1200

(d) 150 mb PV 920824/1200

Figure 7.21 Ertel's potential vorticity field at 1200 UTC 23 August 1992. (a), (b), (c), and (d) are the perturbation PV maps for the 850, 500, 300 and 150 isobaric surfaces, respectively. The unit is 0.01 PVU. Potential vorticity values smaller than (larger than or equal to) 1.5 PVU are shown as solid (dashed) lines with contour intervals of 0.25 PVU (1.5 PVU).

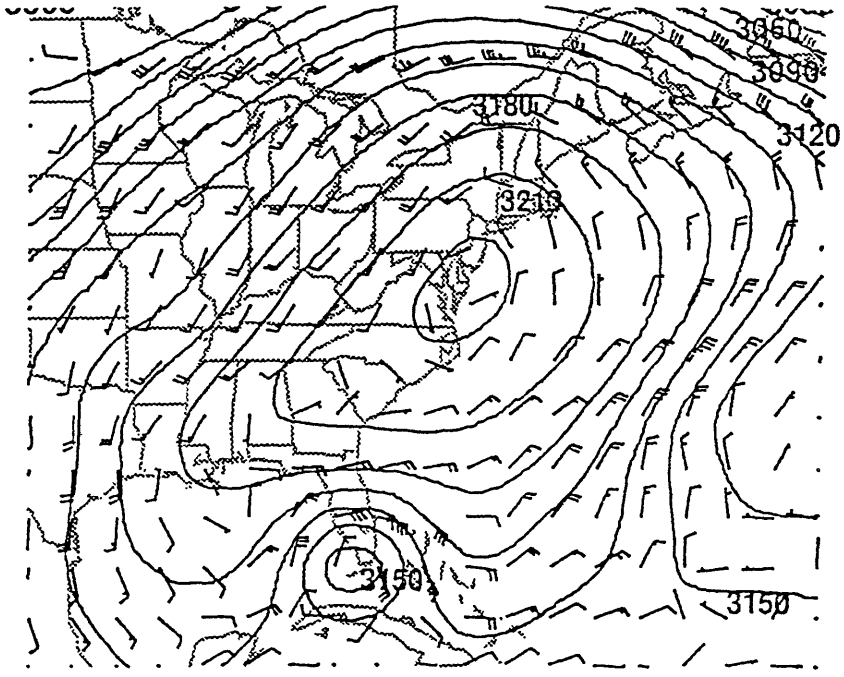

700 mb BAL H and NMC ANALYSIS WIND 920824/1200

Figure 7.22 Balanced height field (contour interval of 15 m) and wind analysis (wind barb plotted as in Fig. 6.4) at 700 mb at 1200 UTC 24 August 1992.

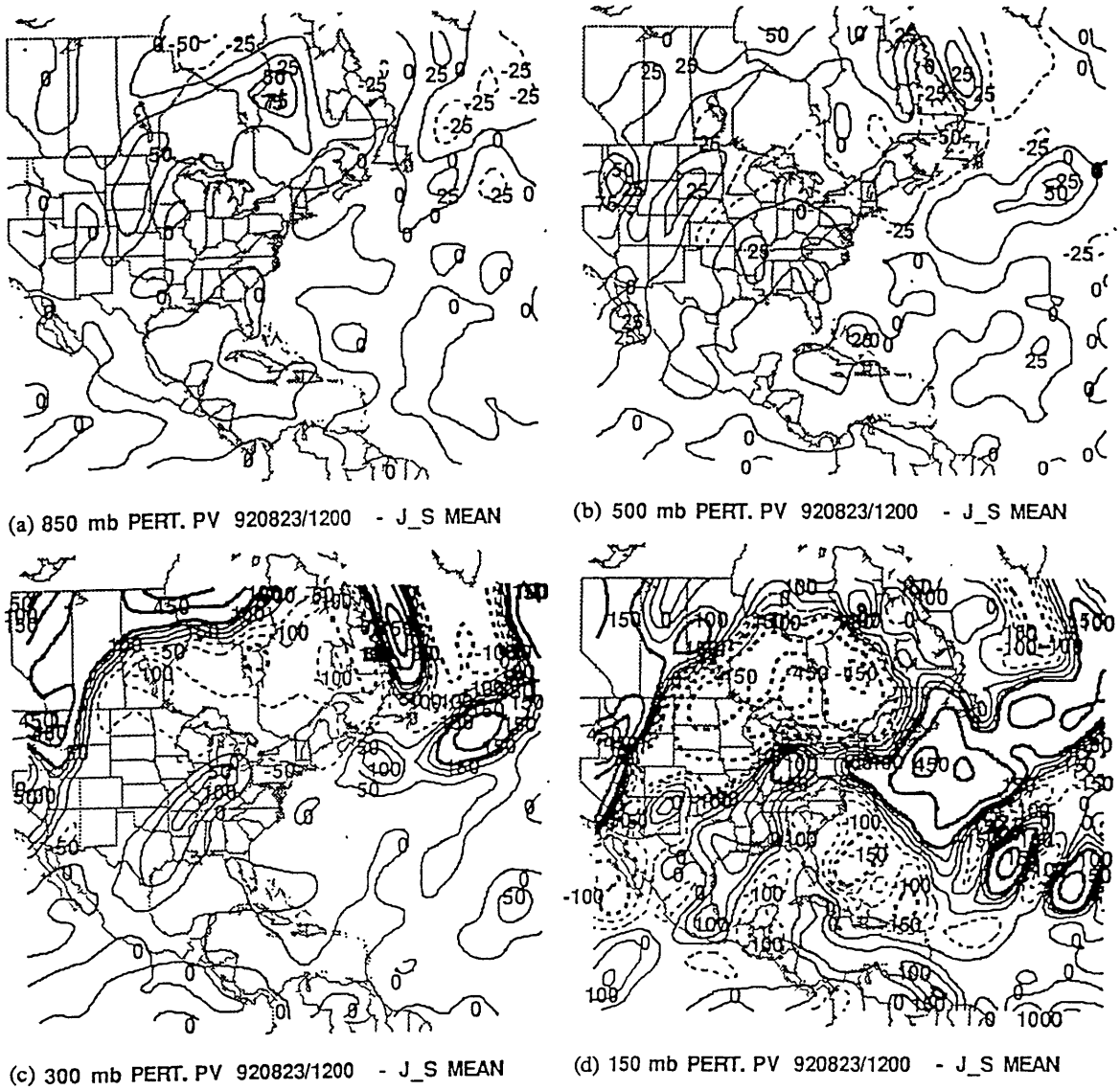

Figure 7.23 Ertel's potential vorticity perturbation field at 1200 UTC 23 August 1992. (a), (b), (c), and (d) are the perturbation PV maps for the 850, 500, 300 and 150 isobaric surfaces, respectively. The unit is 0.01 PVU. Potential vorticity values smaller than (larger than or equal to) 1.5 PVU are shown as thin lines (bold lines) with contour intervals of 0.25 PVU (1.5 PVU). Positive (negative) values are represented by solid (dashed) lines.

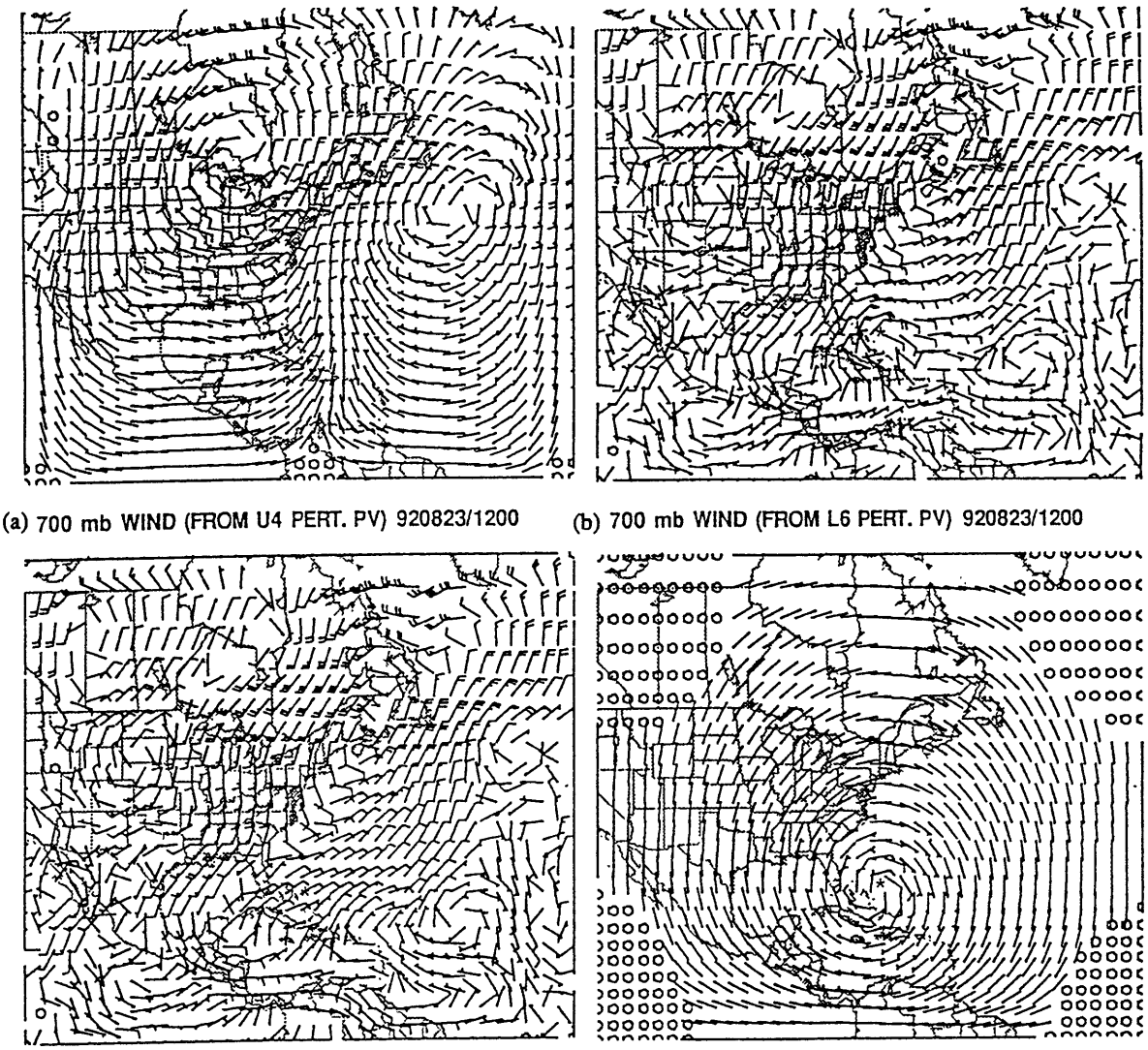

Figure 7.24 700-mb balanced wind fields (wind barb plotted as in Fig. 6.4) associated with (a) U4, (b) L6, (c) L6E, and (d) L6S at 1200 UTC 23 August 1992. Hurricane Andrew's best track positions are indicated by an asterisk (*).

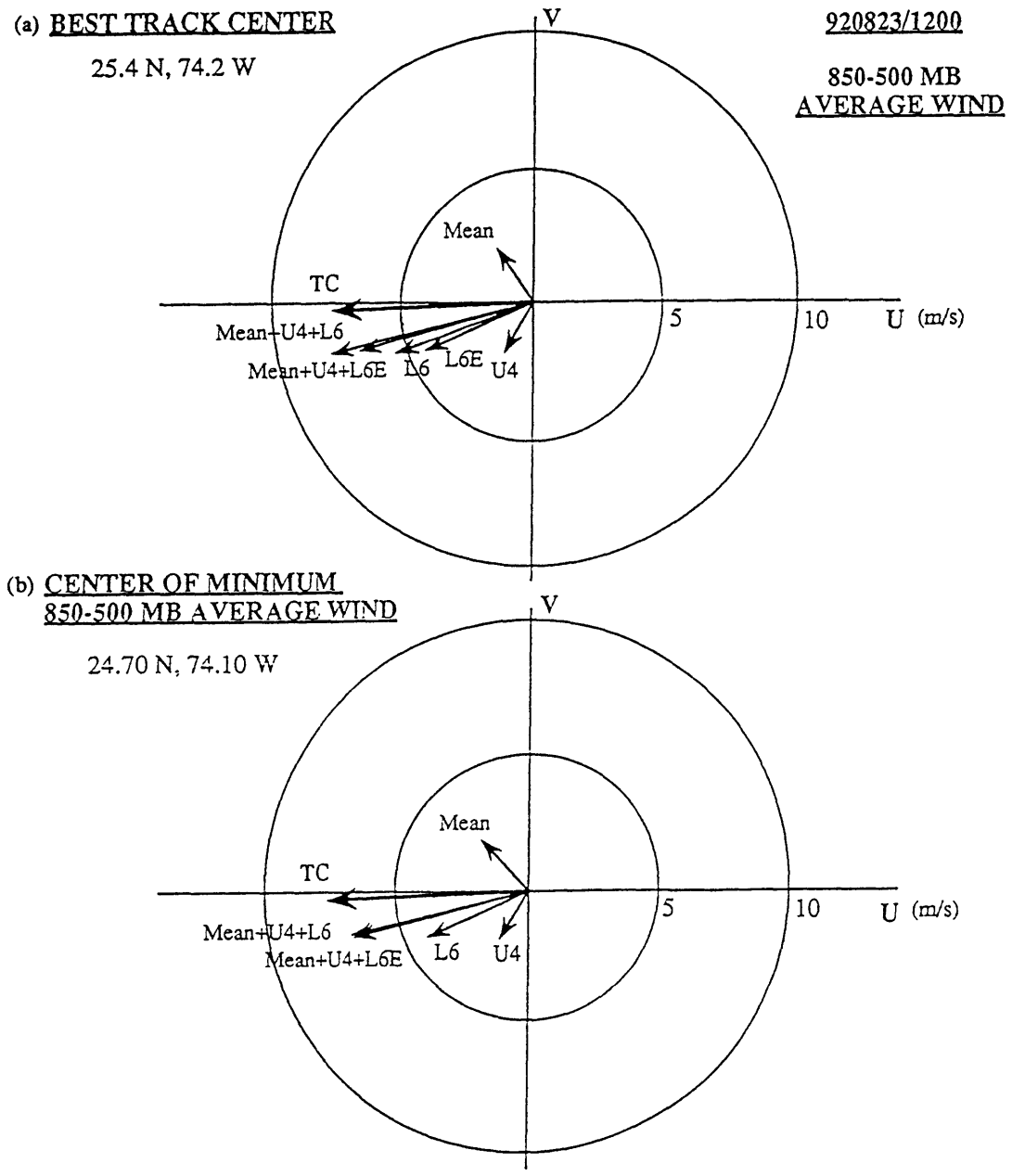

Figure 7.25 Velocity vectors of balanced flows and Hurricane Andrew's motion at 1200 UTC 23 August 1992. Mean, U4, L6, and L6E represent the 850-500-mb pressure-averaged balanced flows associated with mean potential vorticity, potential vorticity perturbations of U4, L6, and L6E, respectively. Mean+U4+L6E represents the total hurricane advection flow. TC indicates Andrew's motion estimated from every 6-hour best-track position. (a) Interpolation of the balanced wind fields at the best-track center; and (b) at the 850-500-mb pressure-averaged balanced vortex center.

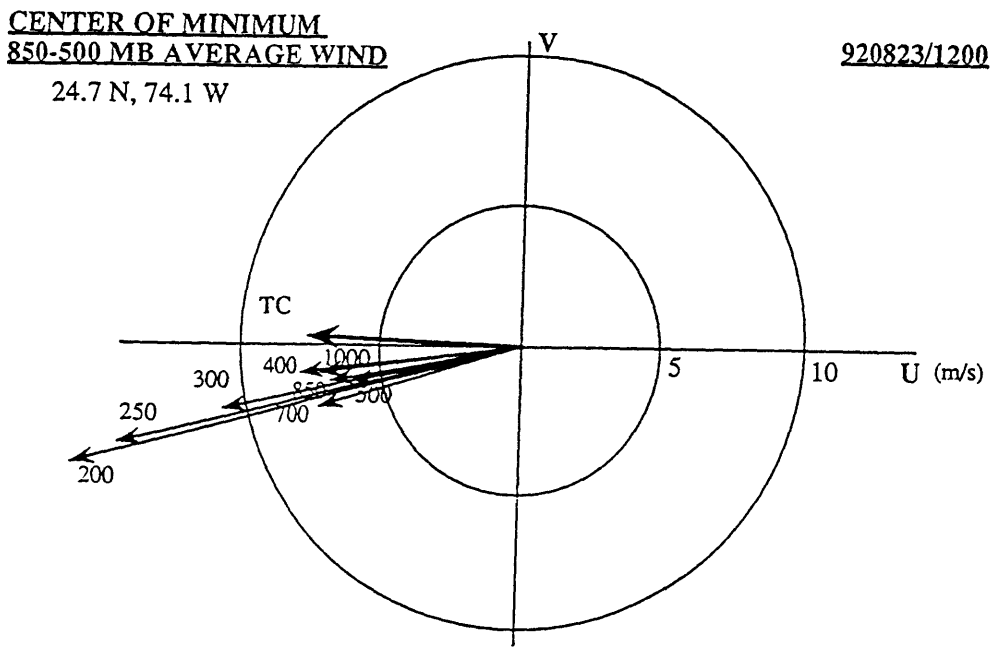

Figure 7.26 Velocity vectors of advection flow at each level and Hurricane Andrew's motion at 1200 UTC 23 August 1992. The hurricane advection flow is defined as the interpolation of the balanced flows associated with mean, U4, and L6E at the 850-500-mb pressure-averaged balanced vortex center. TC indicates Andrew's motion estimated from every 6-hour best-track position.

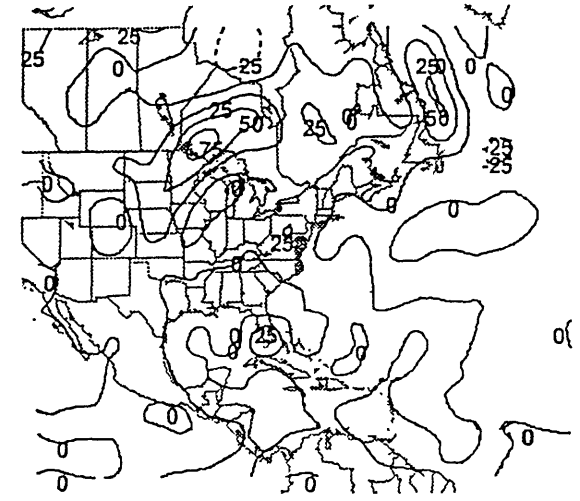

(a) 850 mb PERT. PV 920824/1200 - J_S MEAN

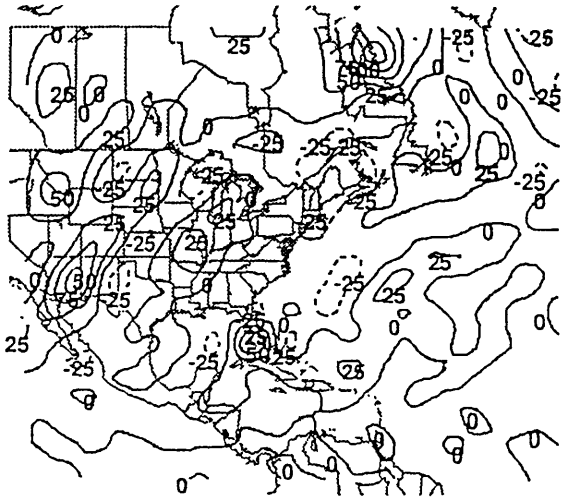

(b) 500 mb PERT. PV 920824/1200 - J_S MEAN

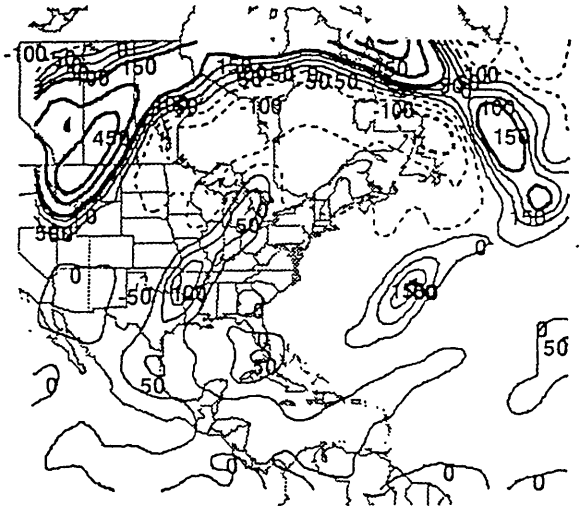

(c) 300 mb PERT. PV 920824/1200 - J_S MEAN

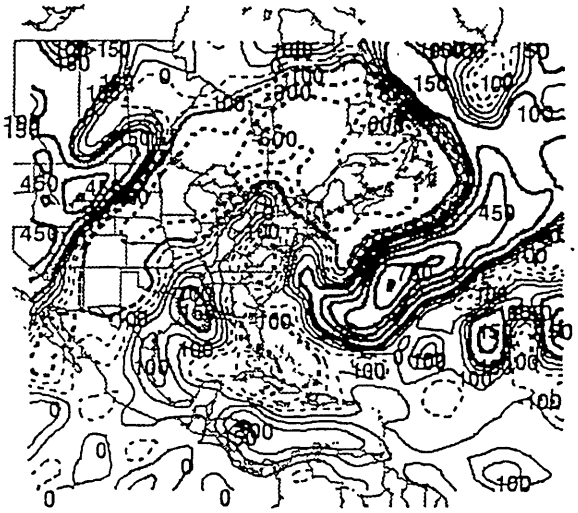

(d) 150 mb PERT. PV 920824/1200 - J_S MEAN

Figure 7.27 Ertel's potential vorticity perturbation field at 1200 UTC 24 August 1992. (a), (b), (c), and (d) are the perturbation PV maps for the 850, 500, 300 and 150 isobaric surfaces, respectively. The unit is 0.01 PVU. Potential vorticity values smaller than (larger than or equal to) 1.5 PVU are shown as thin lines (bold lines) with contour intervals of 0.25 PVU (1.5 PVU). Positive (negative) values are represented by solid (dashed) lines.

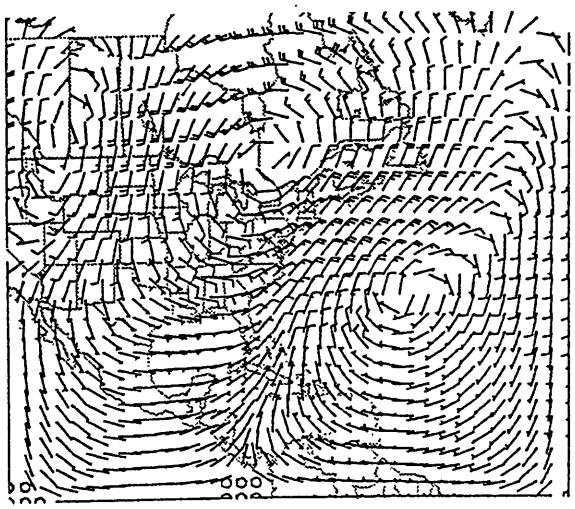

(a) 700 mb WIND (FROM U4 PERT. PV) 920824/1200

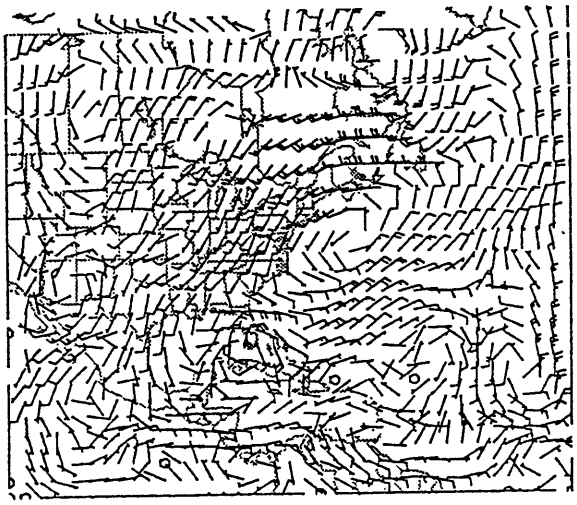

(b) 700 mb WIND (FROM L6 PERT. PV) 920824/1200

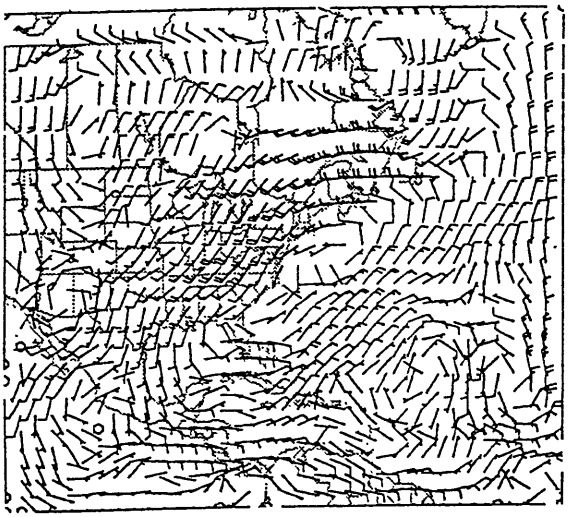

(c) 700 mb WIND (FROM L6E PERT. PV) 920824/1200

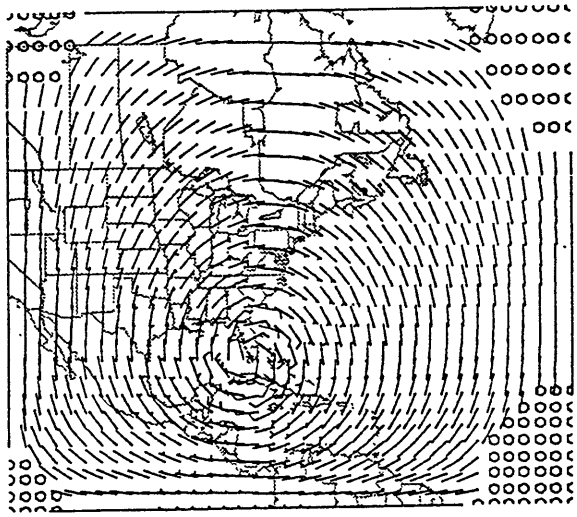

(d) 700 mb WIND (FROM L6S PERT. PV) 920824/1200

Figure 7.28 700-mb balanced wind fields (wind barb plotted as in Fig. 6.4) associated with (a) U4, (b) L6, (c) L6E, and (d) L6S at 1200 UTC 24 August 1992. Hurricane Andrew's best track positions are indicated by an asterisk (*).

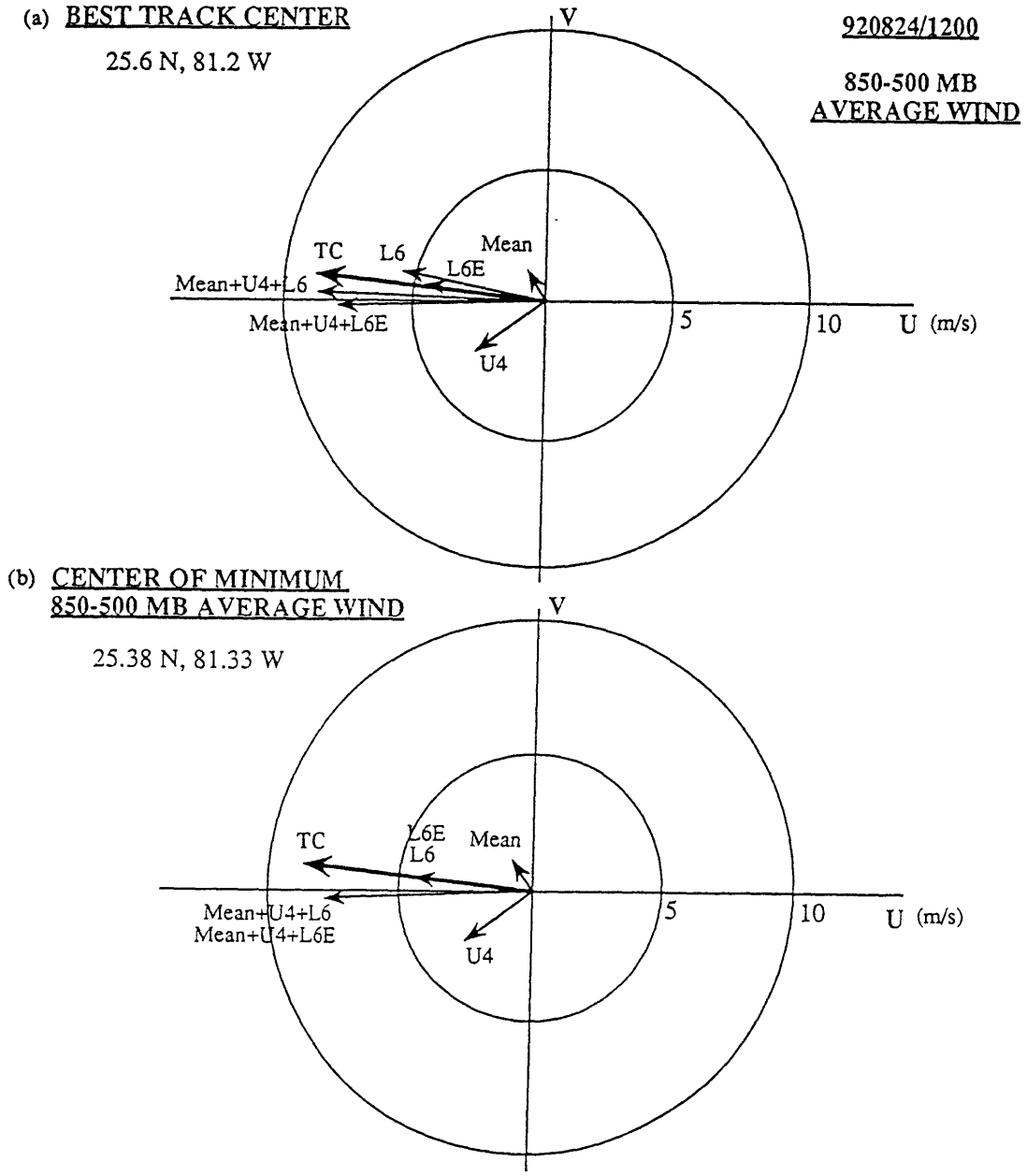

Figure 7.29 Velocity vectors of balanced flows and Hurricane Andrew's motion at 1200 UTC 24 August 1992. Mean, U4, L6, and L6E represent the 850-500-mb pressure-averaged balanced flows associated with mean potential vorticity, potential vorticity perturbations of U4, L6, and L6E, respectively. Mean+U4+L6E represents the total hurricane advection flow. TC indicates Andrew's motion estimated from every 6-hour best-track position. (a) Interpolation of the balanced wind fields at the best-track center; and (b) at the 850-500-mb pressure-averaged balanced vortex center.

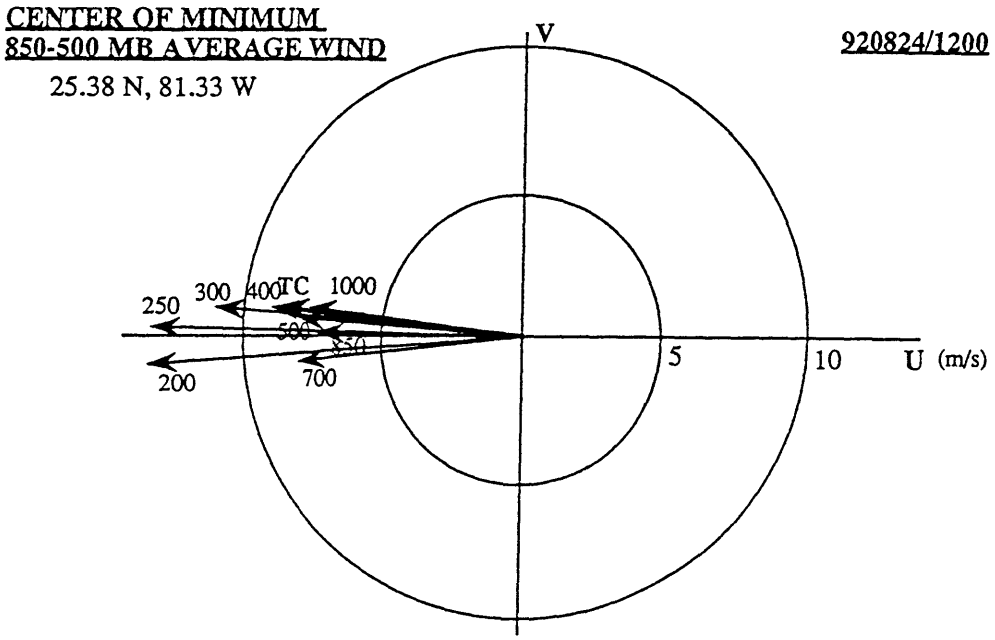

Figure 7.30 Velocity vectors of advection flow at each level and Hurricane Andrew's motion at 1200 UTC 24 August 1992. The hurricane advection flow is defined as the interpolation of the balanced flows associated with mean, U4, and L6E at the 850-500-mb pressure-averaged balanced vortex center. TC indicates Andrew's motion estimated from every 6-hour best-track position.

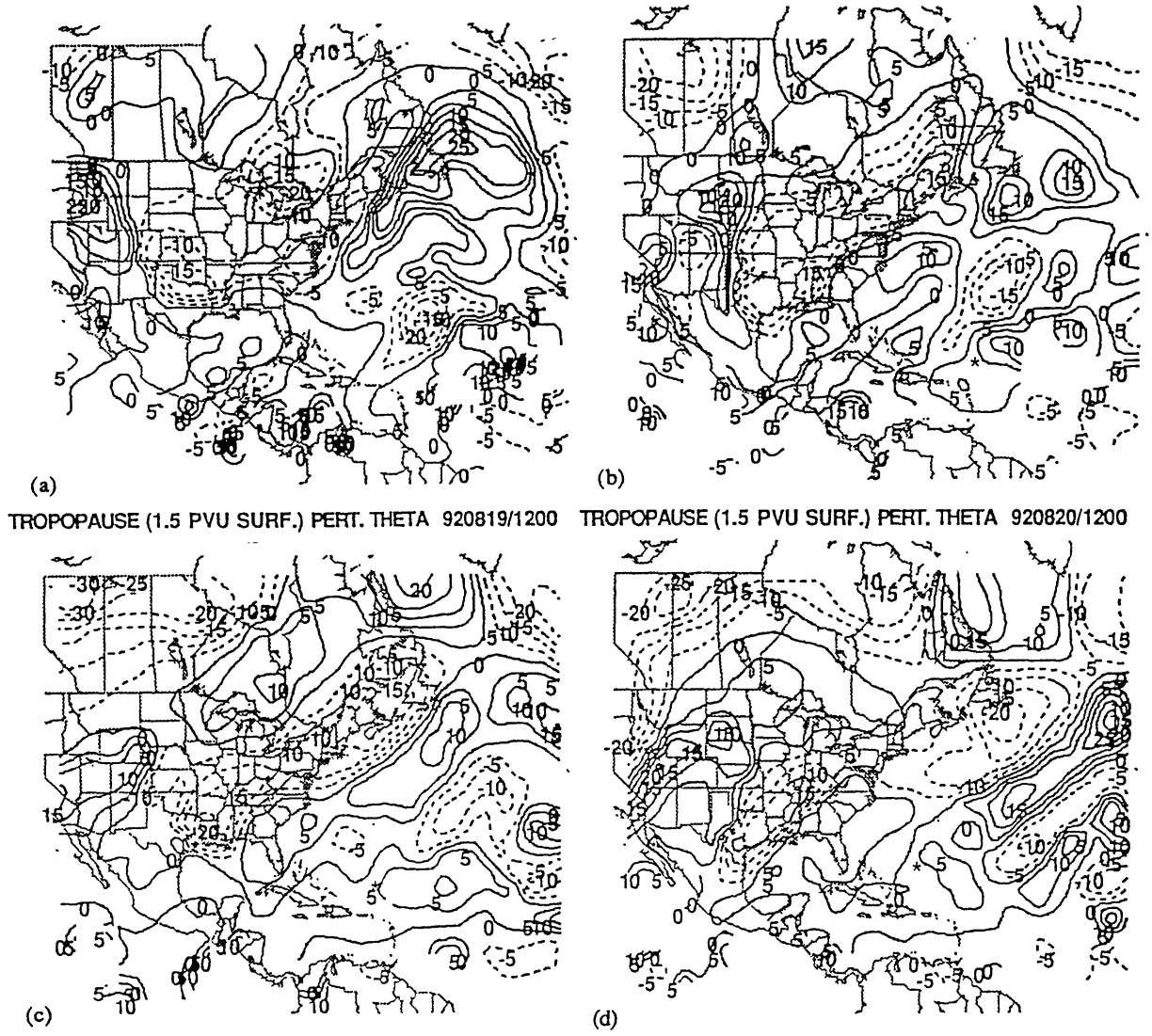

Figure 7.31 Time evolution of the tropopause potential temperature perturbation field (on the 1.5 PVU surface) from 1200 UTC 19 to 26 August 1992. (a) 1200 UTC 19, (b) 1200 UTC 20, (c) 1200 UTC 21, (d) 1200 UTC 22, (e) 1200 UTC 23, (f) 1200 UTC 24, (g) 1200 UTC 25, and (h) 1200 UTC 26. The contour interval is 5 K. All positive (negative) values are represented by solid (dashed) lines. Hurricane Andrew's best track positions are indicated by an asterisk (*).

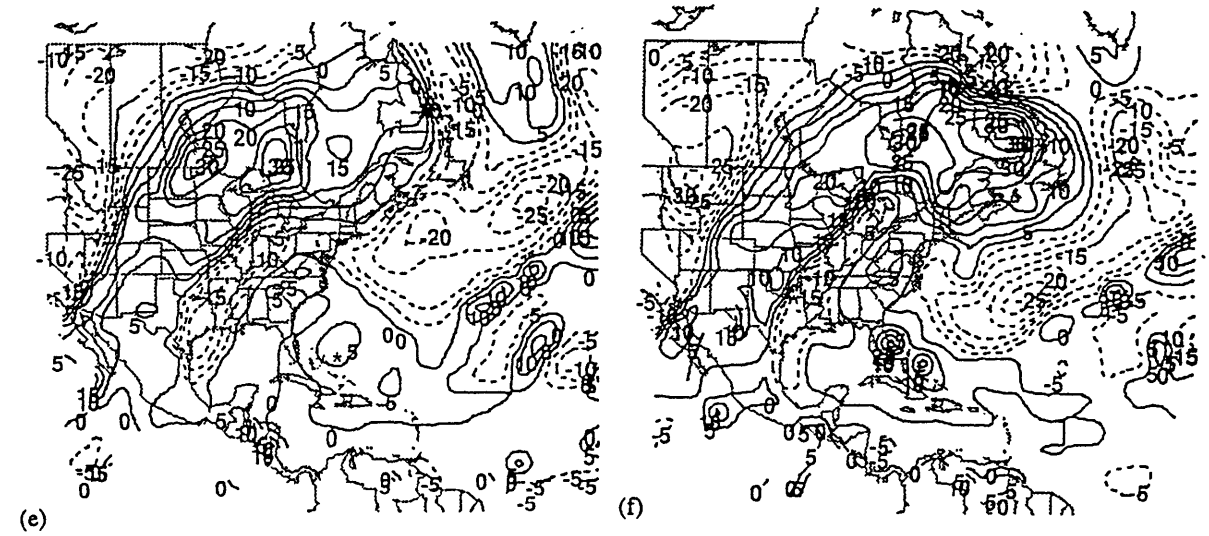

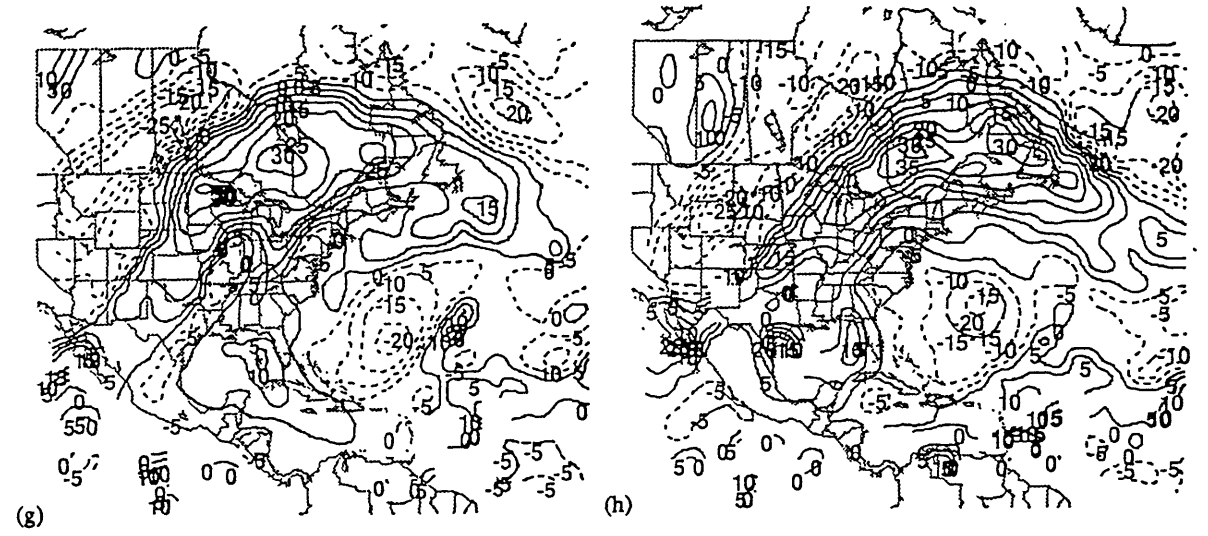

Figure 7.31 (Continued)

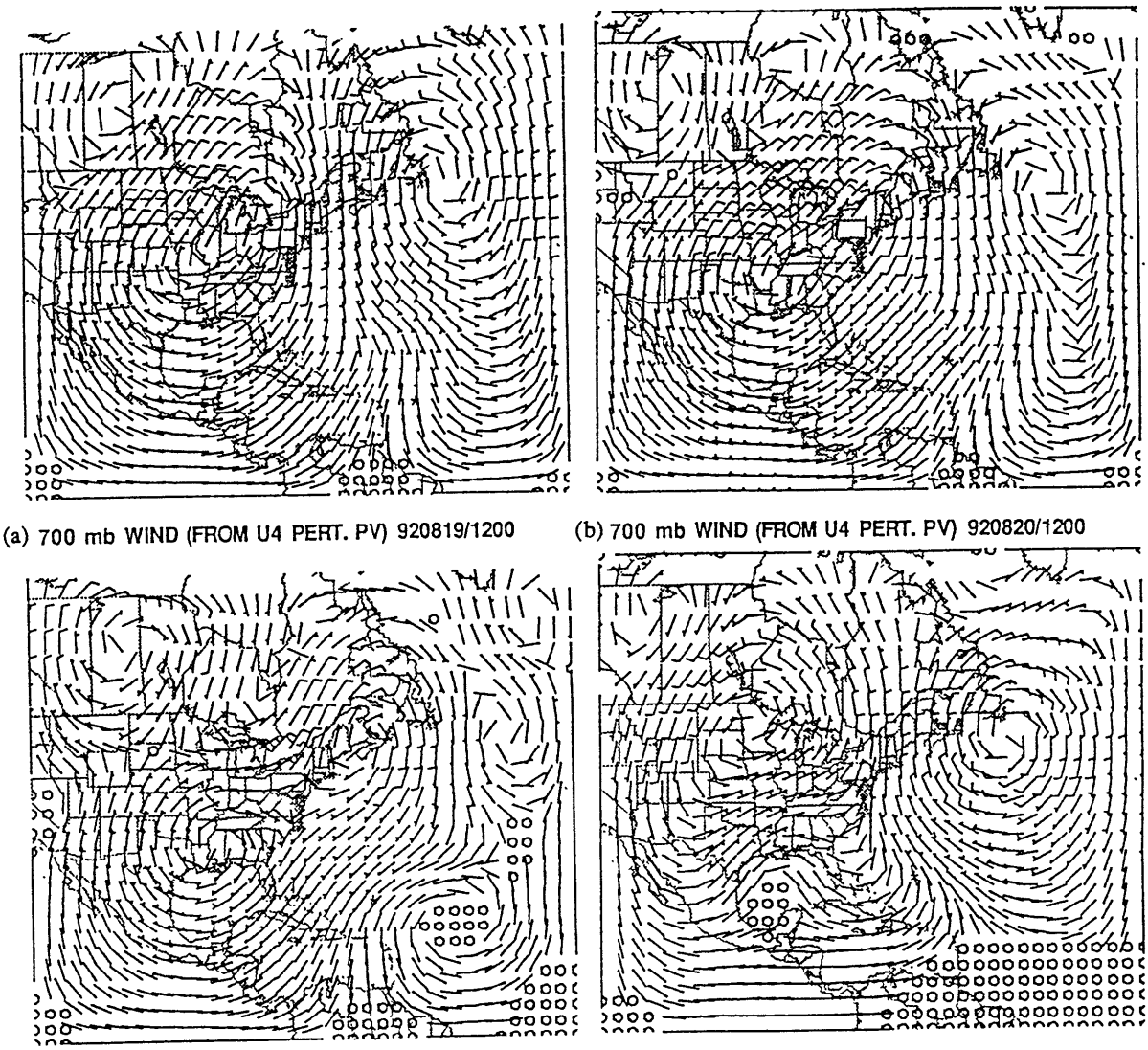

Figure 7.32 Time evolution of the 700-mb balanced wind field (wind barb plotted as in Fig. 6.4) associated with U4 from 1200 UTC 19 to 26 August 1992. (a) 1200 UTC 19, (b) 1200 UTC 20, (c) 1200 UTC 21, (d) 1200 UTC 22, (e) 1200 UTC 23, (f) 1200 UTC 24, (g) 1200 UTC 25, and (h) 1200 UTC 26. Hurricane Andrew's best track positions are indicated by an asterisk (*).

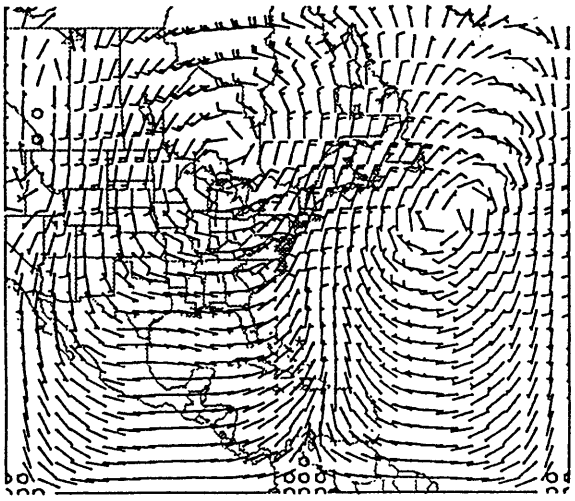

(e) 700 mb WIND (FROM U4 PERT. PV) 920823/1200

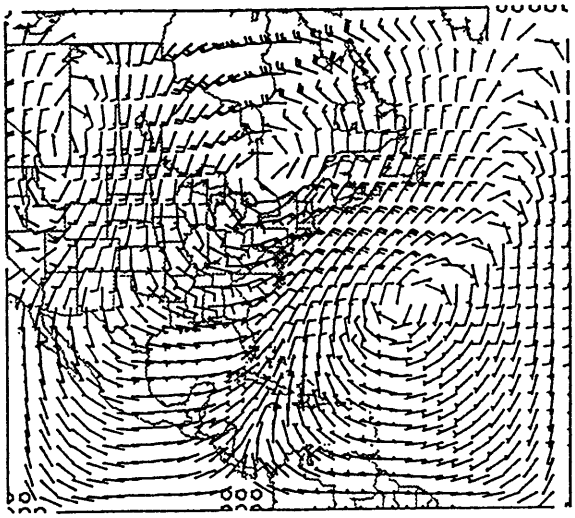

(f) 700 mb WIND (FROM U4 PERT. PV) 920824/1200

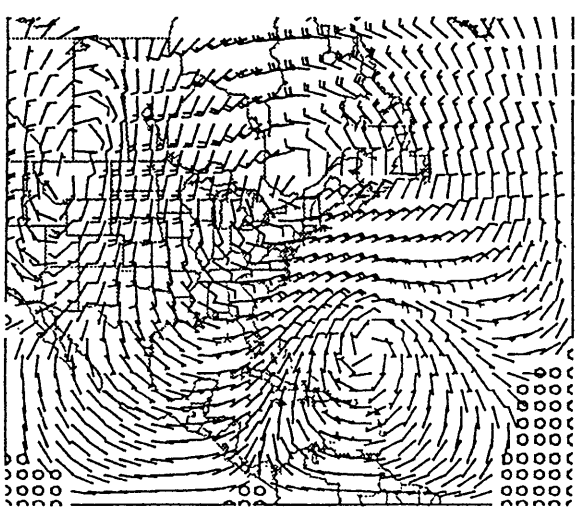

(g) 700 mb WIND (FROM U4 PERT. PV) 920825/1200

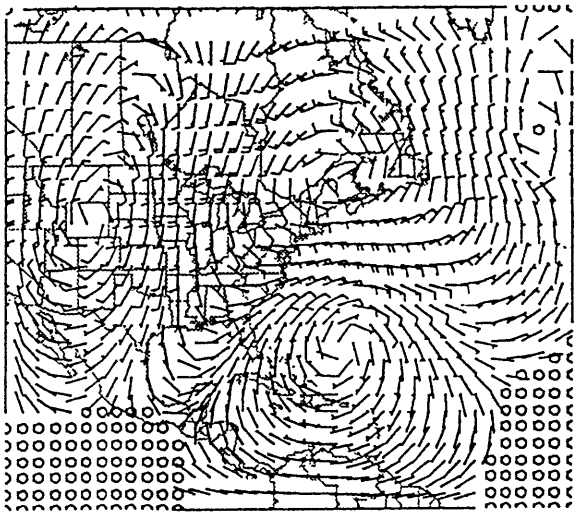

(h) 700 mb WIND (FROM U4 PERT. PV) 920826/1200

Figure 7.32 (Continued)

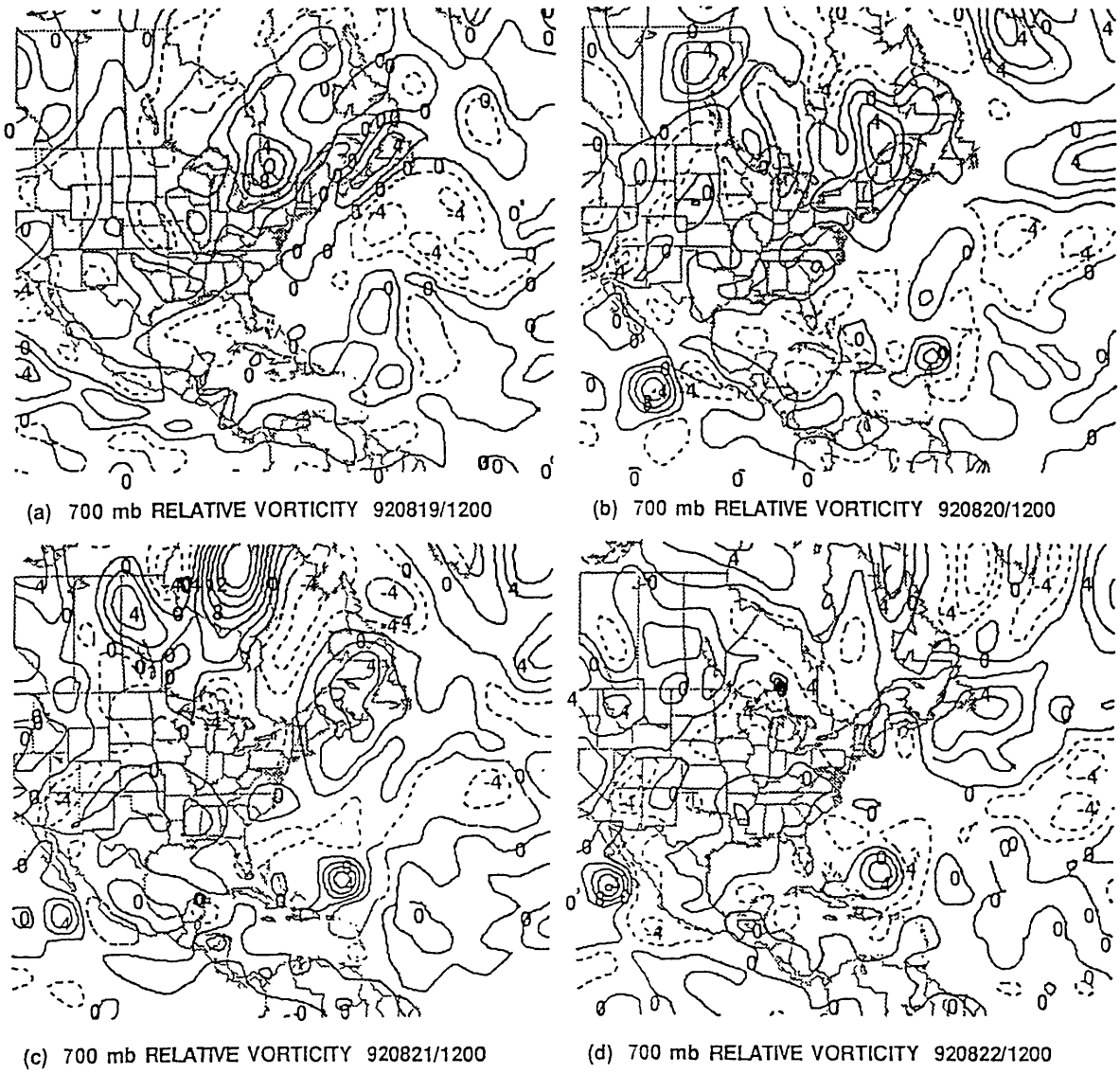

Figure 7.33 Time evolution of the relative vorticity field at 700 mb from 1200 UTC 19 to 26 August 1992. (a) 1200 UTC 19, (b) 1200 UTC 20, (c) 1200 UTC 21, (d) 1200 UTC 22, (e) 1200 UTC 23, (f) 1200 UTC 24, (g) 1200 UTC 25, and (h) 1200 UTC 26. The contour interval is 2×10^{-5} s^{-1}. All positive (negative) values are represented by solid (dashed) lines.

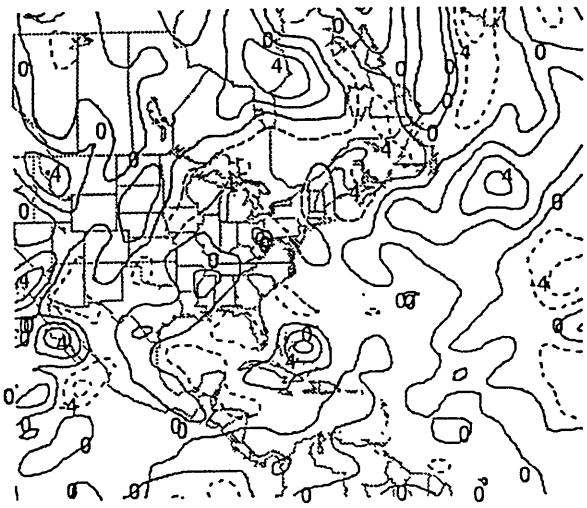

(e) 700 mb RELATIVE VORTICITY 920823/1200

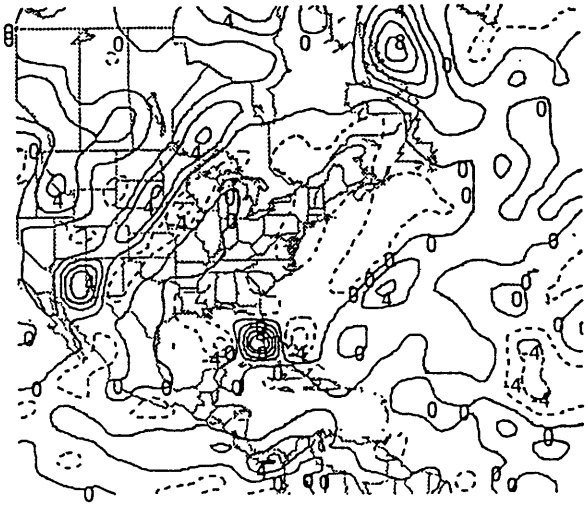

(f) 700 mb RELATIVE VORTICITY 920824/1200

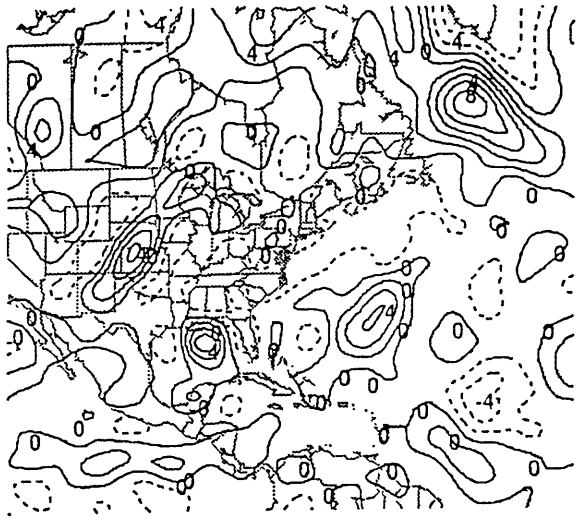

(g) 700 mb RELATIVE VORTICITY 920825/1200

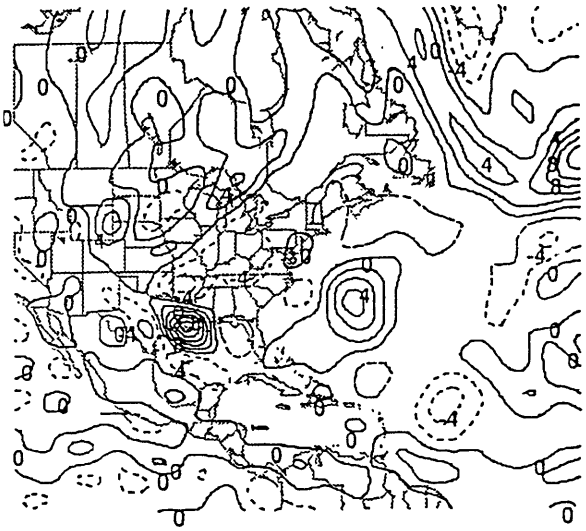

(h) 700 mb RELATIVE VORTICITY 920826/1200

Figure 7.33 (Continued)

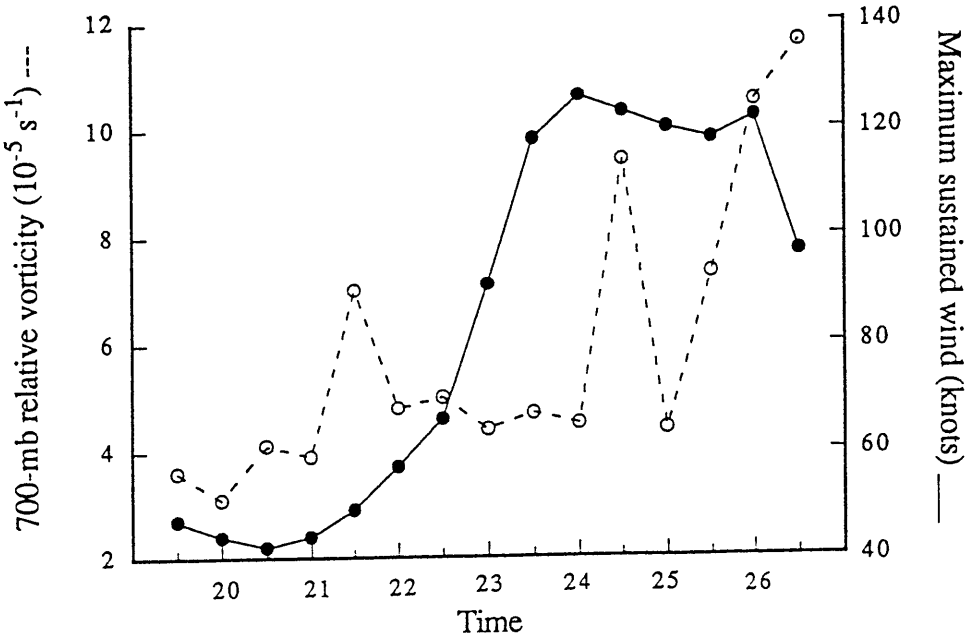

Figure 7.34 Analyzed maximum relative vorticity from NMC data (dashed) and best-track maximum sustained wind speed curve (solid, from Preliminary Report) from 1200 UTC 19 to 26 August 1992 for Hurricane Andrew.

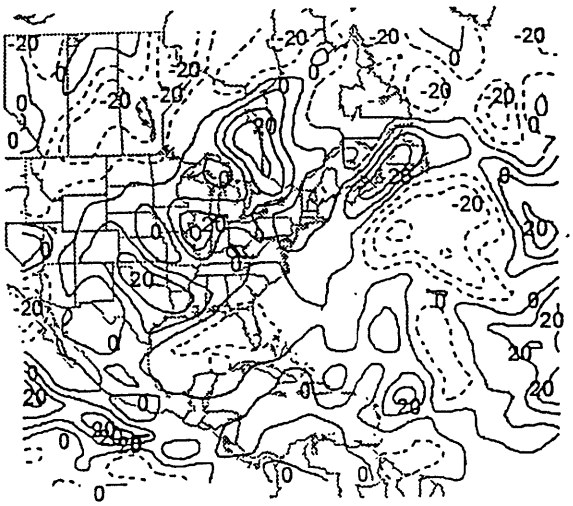

(a) 700 mb PERT. PV 920819/1200 - J_S MEAN

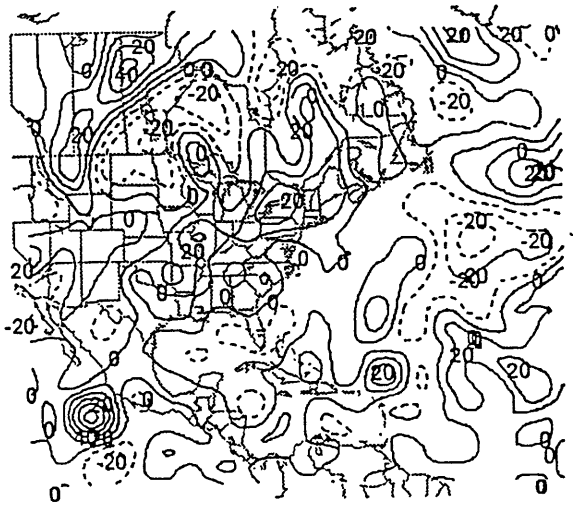

(b) 700 mb PERT. PV 920820/1200 - J_S MEAN

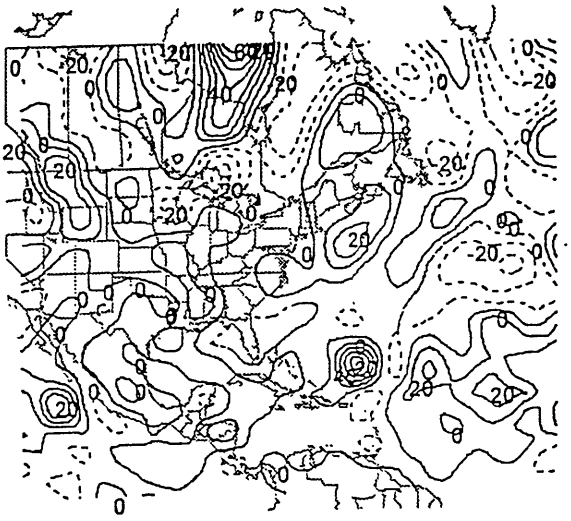

(c) 700 mb PERT. PV 920821/1200 - J_S MEAN

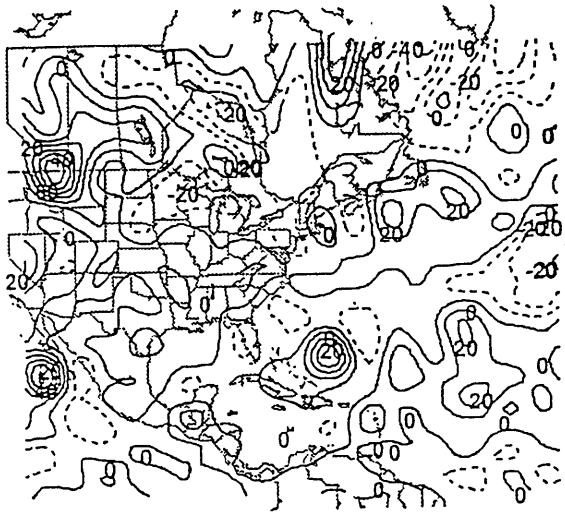

(d) 700 mb PERT. PV 920822/1200 - J_S MEAN

Figure 7.35 Time evolution of the Ertel's potential vorticity perturbation field at 700 mb from 1200 UTC 19 to 26 August 1992. (a) 1200 UTC 19, (b) 1200 UTC 20, (c) 1200 UTC 21, (d) 1200 UTC 22, (e) 1200 UTC 23, (f) 1200 UTC 24, (g) 1200 UTC 25, and (h) 1200 UTC 26. The unit is 0.01 PVU, and contour interval is 0.1 PVU. All positive (negative) values are represented by solid (dashed) lines.

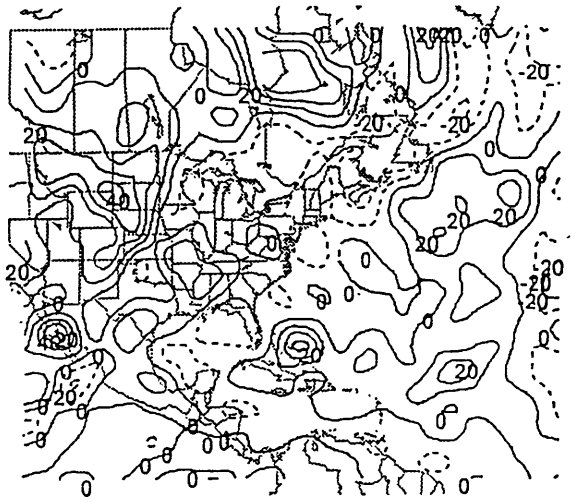

(e) 700 mb PERT. PV 920823/1200 - J_S MEAN

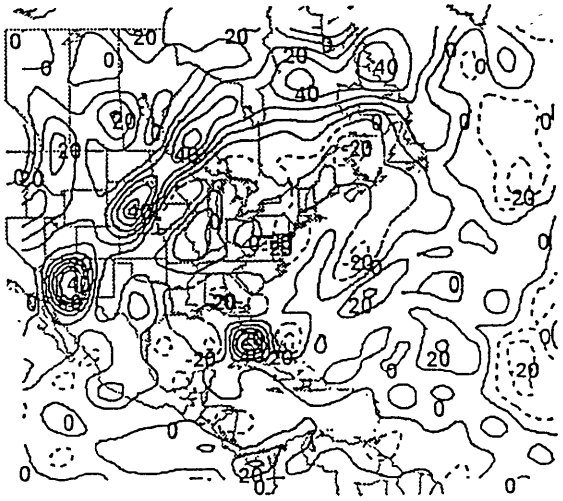

(f) 700 mb PERT. PV 920824/1200 - J_S MEAN

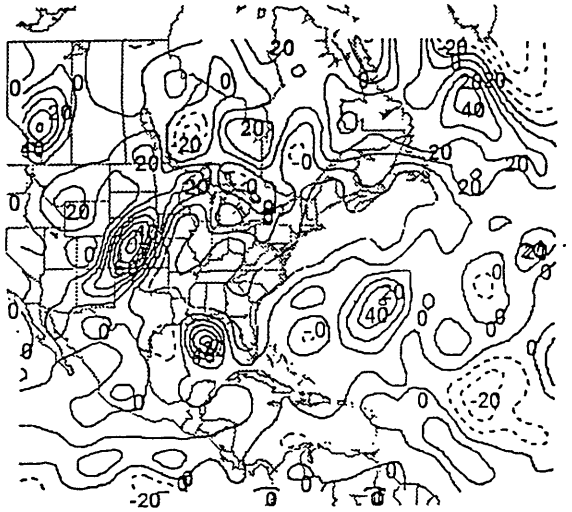

(g) 700 mb PERT. PV 920825/1200 - J_S MEAN

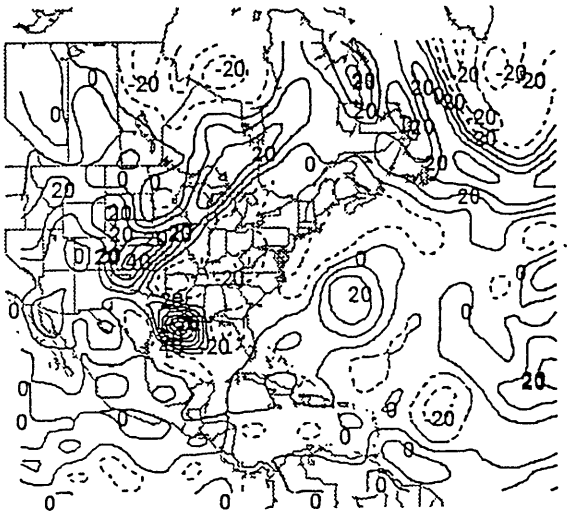

(h) 700 mb PERT. PV 920826/1200 - J_S MEAN

Figure 7.35 (Continued)

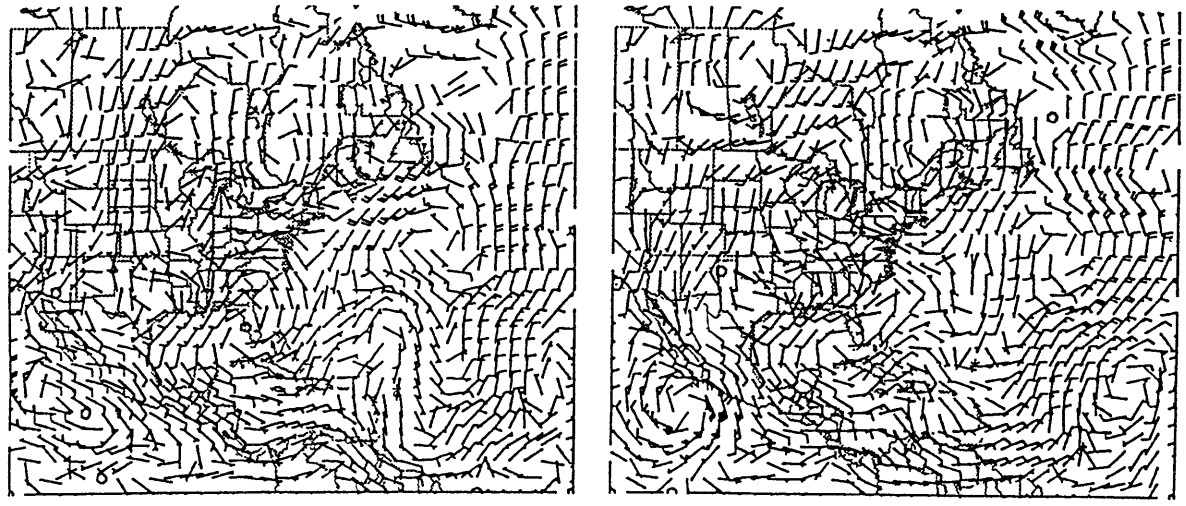

(a) 700 mb WIND (FROM L6E PERT. PV) 920819/1200 (b) 700 mb WIND (FROM L6E PERT. PV) 920820/1200

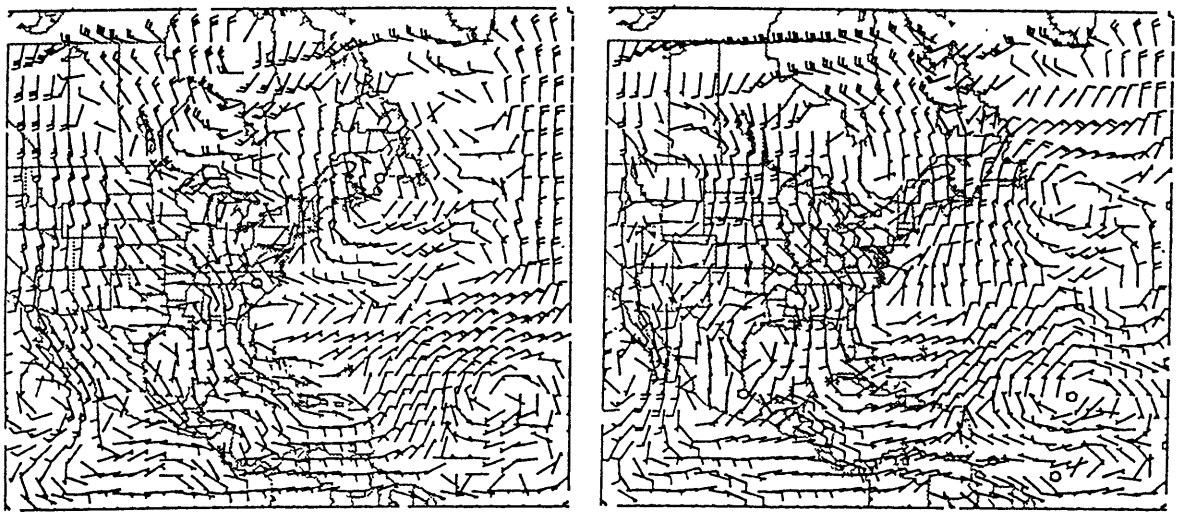

(c) 700 mb WIND (FROM L6E PERT. PV) 920821/1200 (d) 700 mb WIND (FROM L6E PERT. PV) 920822/1200

Figure 7.36 Time evolution of the 700-mb balanced wind field (wind barb plotted as in Fig. 6.4) associated with L6E from 1200 UTC 19 to 26 August 1992. (a) 1200 UTC 19, (b) 1200 UTC 20, (c) 1200 UTC 21, (d) 1200 UTC 22, (e) 1200 UTC 23, (f) 1200 UTC 24, (g) 1200 UTC 25, and (h) 1200 UTC 26. Tropical Storm Ana's best track positions are indicated by an asterisk (*).

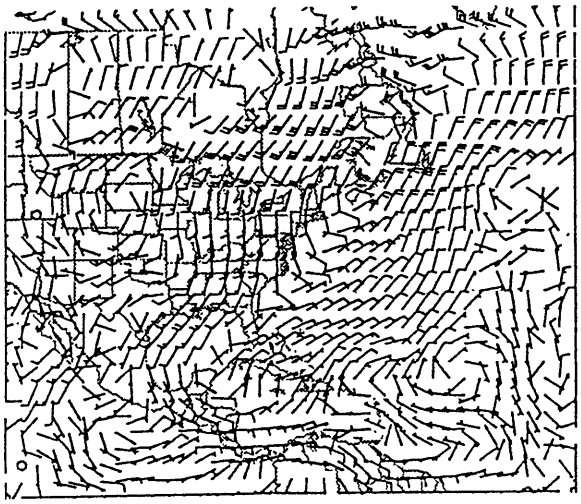

(e) 700 mb WIND (FROM L6E PERT. PV) 920823/1200

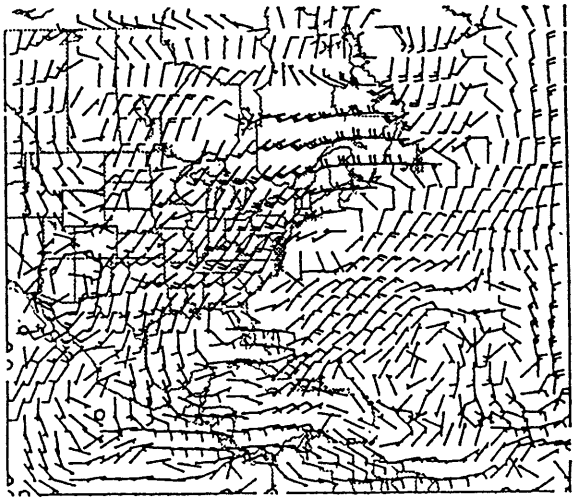

(f) 700 mb WIND (FROM L6E PERT. PV) 920824/1200

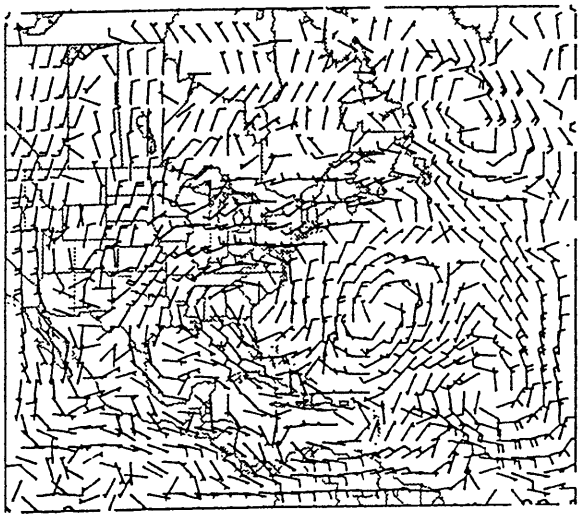

(g) 700 mb WIND (FROM L6E PERT. PV) 920825/1200

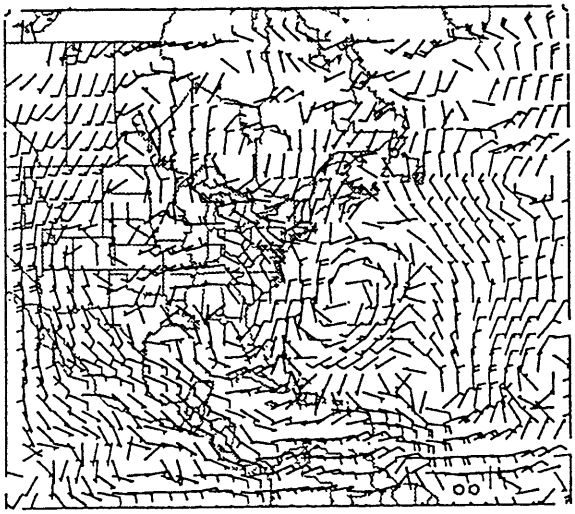

(h) 700 mb WIND (FROM L6E PERT. PV) 920826/1200

Figure 7.36 (Continued)

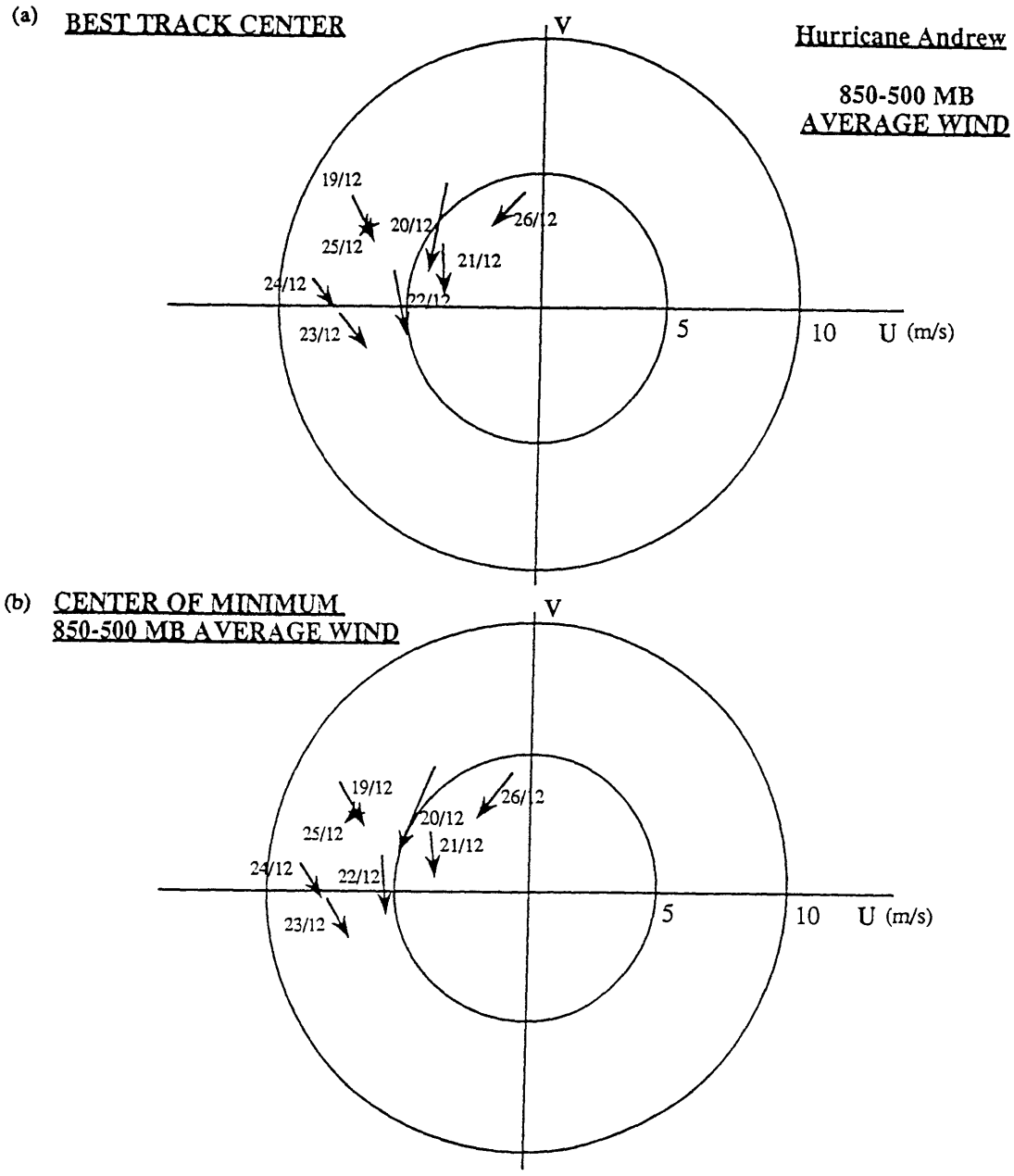

Figure 7.37 Velocity vector differences between the 850-500-mb pressure-averaged advection flow and Andrew's motion from 1200 UTC 19 to 1200 UTC 26 August 1992. (a) Interpolation of the balanced wind fields at the best-track center; and (b) at the 850-500-mb pressure-averaged balanced vortex center.

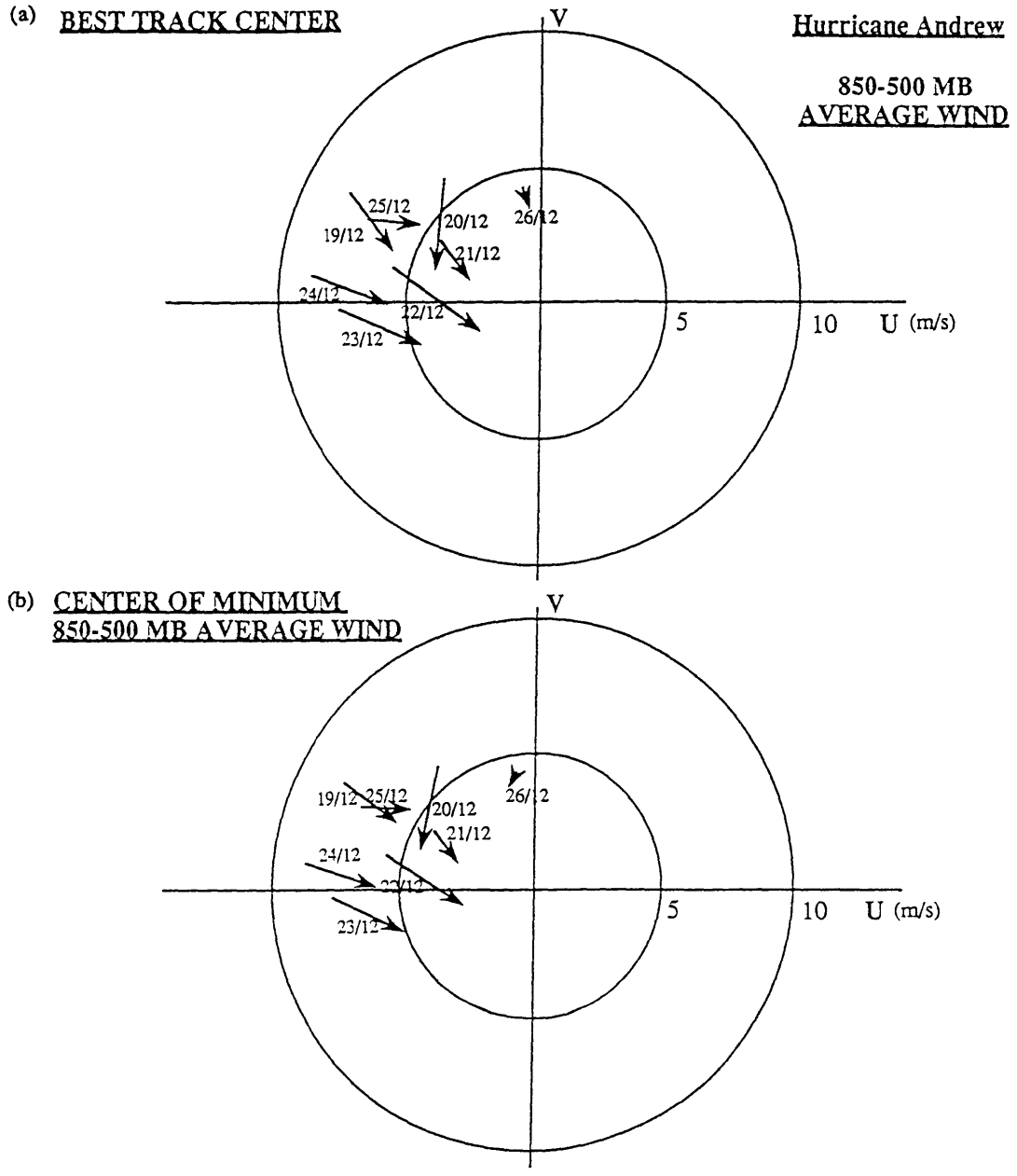

Figure 7.38 Velocity vector differences between the 850-500-mb pressure-averaged annular mean flow and Andrew's motion from 1200 UTC 19 to 1200 UTC 26 August 1992. (a) Interpolation of the wind fields at the best-track center; and (b) at the 850-500-mb averaged balanced vortex center.

8. Conclusions

a. Summary

Observations show that tropical cyclones have broad anticyclones aloft and that the distribution of the potential vorticity gradient in both the middle latitudes and tropical atmosphere is highly inhomogeneous. There is some indication that the potential vorticity gradients in the subtropical troposphere are very weak, perhaps having been rendered so by the action of synoptic-scale disturbances. To account for this and to isolate the direct effect of vertical wind shear on the motion of a baroclinic vortex, in the first part of this thesis, we have performed experiments with an idealized two-layer quasigeostrophic model in which there is no background potential vorticity gradient. The lower-layer potential vorticity anomaly is represented by a point vortex, while the upper-layer anomaly is represented by a patch of zero potential vorticity air, which is expanding in time owing to a point source of mass collocated with the lower-layer point potential vortex. The method of contour dynamics and contour surgery is used to integrate the upper-level pseudo-potential vorticity equation.

We find that the direct effect of ambient vertical shear is to displace the upper-level plume of anticyclonic relative potential vorticity downshear from the lower-layer cyclonic point potential vortex, thus inducing a mutual interaction between the circulations associated with each other. This results in a drift of the point vortex broadly to the left of the vertical shear vector (in the Northern Hemisphere). This drift is sensitive to the assumed relative thicknesses of the two layers, but its magnitude is generally comparable to that found in simulations of barotropic vortices on the β plane. It is also shown that such a drift is closely related to the thickness ratio of the two layers, and the strength of the upper negative PV anomaly. The numerical model produces features of the hurricane outflow,

and it also demonstrates that the redistribution of the upper-tropospheric potential vorticity by the hurricane outflow may have substantial effects on hurricane movement.

In the second part of this thesis, we conduct an observational study to explore the dynamics of hurricane movement using the potential vorticity framework. Three case studies (Hurricane Bob and Tropical Storm Ana of 1991 and Hurricane Andrew of 1992) have been made to demonstrate the use of PV diagnostics for the understanding of hurricane movement. The twice-daily National Meteorological Center Northern Hemisphere final analyses gridded datasets are used for these studies. Using the seasonal climatology as the mean reference state, piecewise potential vorticity inversions are performed under the nonlinear balance condition. This allows one to determine the balanced flow associated with any individual perturbation of PV. By examining the balanced flow at the hurricane center, one can identify which PV perturbation has the most influence on hurricane movement. We also define the hurricane advection flow as the balanced flow (at the center of the storm) associated with the whole PV in the troposphere, except for the PV anomaly of the hurricane itself.

Although the NMC analyses have a relatively coarse resolution and cannot capture the actual strength of hurricanes, the results show that such an advection flow is a very good approximation to the real storm motion. This steering flow derived from the PV perspective is much more consistent and dynamically meaningful than the traditional steering stream, which is generally taken as the tropospheric annular mean flow. The results also show that hurricane movement is dominated by the balanced flow associated with the mean PV and perturbation PV in both the lower and upper troposphere, but the data did not allow us to discuss the particular potential vorticity perturbations produced by the storms themselves. We believe that PV diagnostics are conceptually simpler and much more useful in quantitatively understanding how individual portions of the large-scale dynamics interact with the hurricane.

b. Suggestions for future work

In this thesis work, we have explored the dynamics of hurricane motion by using an idealized model which applies the method of contour dynamics. A key assumption in the model is that the background PV gradient is zero. We feel that it is necessary to examine the dynamics of hurricane movement using more comprehensive modeling and observational studies, with a view toward establishing the actual background potential vorticity gradients in the atmosphere.

It is crucial to develop more complete models that can realistically incorporate variable background potential vorticity gradients, and can also appropriately represent the effect of diabatic heating on the generation of the upper-level negative PV anomaly above a hurricane. We think that a nonlinear balance model may be adequate for such work.

In the observational study undertaken as part of this thesis, we do not find any evidence of the so-called β effect. Though the preliminary study of Bob suggests that an upper negative PV anomaly is generated above Bob, and acts to steer Bob, it is not clear whether this negative PV anomaly is generated diabatically by Bob or due to horizontal advection from other regions. The analyses of the other two cases (Ana and Andrew) do not show similar signals.

It appears that the study of these two effects is strongly influenced by the limitations of the NMC data. For example, the NMC analyses may have too coarse a resolution to resolve the β gyres (if existing); and the upper negative PV anomaly diabatically generated by the hurricane over the oceanic area may not be well detected from the raw observations and thus may be underestimated or lost in the NMC analyses. Also it should be remembered that the analyzed flow fields may have errors that are comparable to the signals of these effects (e.g., 2 m s^{-1}), which makes the evaluation of the individual influence of these dynamical processes on hurricane motion even more difficult.

We find that it is necessary to perform further observational studies using data with a higher resolution, which better represent the hurricane's strength. For example, since the GFDL model is shown (Kurihara 1990) to be able to capture the structure, intensity and storm movement very well, this model output data may be a good candidate for our analysis. It is also possible that the quality of the measurements above a storm system can be substantially improved by unmanned aircraft (Langford and Emanuel 1993) in the future. If this new technology for observation can be successfully employed, we will have better data (especially better upper-tropospheric information over the oceans) for the study of this problem in the future.

In order to examine the β effect, we can use the balanced flow associated with the PV anomaly of the hurricane itself to perturb the environmental PV. Then we can invert the perturbed PV to understand its feedback on hurricane motion. From these PV diagnostics, we shall be able to better understand the β effect.

To understand the effect of the upper-level negative PV anomaly on hurricane motion, it is crucial to be able to distinguish from the data that PV anomaly that is diabatically generated by the storm. As discussed previously, it is very difficult to do so using the actual data. One possibility involves running a comprehensive model with two experiments: one initially includes a hurricane, but the other does not. Then we may take the difference between the two runs to understand the influence of the hurricane. By doing so, perhaps we can evaluate the amount of upper negative PV anomaly generated by the storm. Then by applying piecewise inversion, we can examine our hypothesis.

It has been well established that the Fujiwhara effect does occur, but there is need for a quantitative operational definition of this effect that could be used in practical forecasting. It should also be possible to use the piecewise inversion technique to understand the binary interaction of tropical cyclones.

We believe that the findings from this work will aid in improving our understanding on the dynamics of hurricane movement and perhaps lead to better observational strategies for future forecasts of tropical cyclone motion.

References

Adem, J, 1956: A series solution for the barotropic vorticity equation and its application in the study of atmospheric vortices. Tellus, **8**, 364-372.

_____, and P. Lezama, 1960: On the motion of a cyclone embedded in a uniform flow. Tellus, **12**, 255-258.

Anthes, R. A., and J. E. Hoke, 1975: The effect of horizontal divergence and latitudinal variation of the Coriolis parameter on the drift of a model hurricane. Mon. Wea. Rev., **103**, 757-763.

Bengtsson, L. O., 1976: Initial data and some practical aspects of weather forecasting. NCAR colloquium, "Weather Forecasting and Weather Forecasts: Models, Systems, and Users "Volume 1. 254-419.

Brand, S., C. A. Buenafe and H. D. Hamilton, 1981: Comparison of tropical cyclone motion and environmental steering. Mon. Wea. Rev., **109**, 908-909.

Brand, S., 1970: Interaction of binary tropical cyclones of the western North Pacific Ocean. J. Appl. Meteor., **9**, 433-441.

Bretherton, F. P., 1966: Critical layer instability in baroclinic flows. Quart. J. Roy. Meteor. Soc., **92**, 325-334.

Carr, L. E., III, and R. L., Elsberry, 1990: Observational evidence for tropical cyclone propagation relative to environmental steering. J. Atmos. Sci., **47**, 542-546.

Chan, J. C.-L., and W. M. Gray, 1982: Tropical cyclone movement and surrounding flow relationship. Mon. Wea. Rev., **110**, 1354-1376.

Chan, J. C. L., 1985: Identification of the steering flow for tropical cyclone motion from objectively analyzed wind fields. Mon. Wea. Rev., **113**, 106-116.

_____, and R. T. Williams, 1987: Analytic and numerical studies of the beta-effect in tropical cyclone motion. Part 1. Zero mean flow. J. Atmos. Sci., **44**, 1257-1264.

Charney, J. G., 1955: The use of primitive equations of motion in numerical prediction. Tellus, **7**, 22-26.

Davis, C. A., and K. A. Emanuel, 1991: Potential vorticity diagnostics of cyclogenesis. Mon. Wea. Rev., **119**, 1929-1953.

Davis, C. A., 1992a: A potential-vorticity diagnosis of the importance of initial structure and condensational heating in observed extratropical cyclogenesis. Mon. Wea. Rev., **120**, 2409-2428.

_____, 1990: Cyclogenesis diagnosed with potential vorticity. Ph. D. thesis. Massachusetts Institute of Technology. 194pp.

_____, 1992b: Piecewise potential vorticity inversion. J. Atmos. Sci., **49**, 1397-1411.

DeMaria, M., 1985: Tropical cyclone motion in a nondivergent barotropic model. Mon. Wea. Rev., **113**, 1199-1210.

Dey, C. H., 1989: The evolution of objective analysis methodology at the National Meteorological Center. Wea. Forecasting, **4**, 297-312.

Dong, K., and C. J. Neumann, 1986: The relation between tropical cyclone motion and environmental geostrophic flows. Mon. Wea. Rev., **114**, 115-122.

Dritschel, D. G., 1989: Contour dynamics and contour surgery: Numerical algorithms for extended, high resolution modelling of vortex dynamics in two-dimensional inviscid compressible flows. Computer Phys. Rep., **10**, 77-146.

Elsberry, R. L., and R. F. Abbey, Jr., 1991: Recent advances in understanding tropical cyclone motion. Tech. Rep. NPS-MR-91-003, Naval Postgraduate School, Monterey, CA 93943, 93pp.

Elsberry, R. L., B. C. Diehl, J. C.-L. Chan, P. A. Harr, G. J. Holland, M. Lander, T. Neta, and D. Thom, 1990: ONR Tropical cyclone motion research initiative: Field experiment summary. Tech. Rep. NPS-MR-91-001, Naval Postgraduate School, Monterey, CA 93943, 107pp.

Elsberry, R. L., 1988: ONR Tropical cyclone motion research initiative: Mid-year review, discussion and working group reports. Tech. Rep. NPS 63-86-005, Naval Postgraduate School, Monterey, CA 93943, 85pp.

Evans, J. L., G. J. Holland, and R. L. Elsberry, 1991: Interactions between a barotropical vortex and an idealized subtropical ridge. Part I: Vortex motion. J. Atmos. Sci., **48**, 301-314.

Feur, S. E., and J. L. Franklin, 1991: Nested analysis of Hurricane Gloria from dropwindsonde and Doppler radar data. Preprint, 19th Conference on Hurricanes and Tropical Meteorology, Amer. Meteor. Soc., 130-133.

Fiorino, M., and R. L. Elsberry, 1989: Some aspects of vortex structure related to tropical cyclone motion. J. Atmos. Sci., **46**, 975-990.

Flatau, M., and Schubert, W. H., 1991: The role of baroclinic processes in a tropical cyclone motion. Part I: The influence of vertical tilt. Submitted to J. Atmos. Sci .

Flierl, G. R., M. E. Stern, and J. A. Whitehead, Jr., 1983: The physical significance of modons: Laboratory experiments and general integral constraints. Dyn. Atmos. Oceans, **7**, 233-263.

Frank, W. M., 1977: The structure and energetics of the tropical cyclone. I. Storm structure. Mon. Wea. Rev., **105**, 1119-1135.

Franklin, J. L., 1990: Dropwindsonde observations of the environmental flow of Hurricane Josephine (1984): Relation to vortex motion. Mon. Wea. Rev., **118**, 2732-2744.

Fujiwhara, S., 1923: On the growth and decay of vortical systems. Quart. J. Roy. Meteor. Soc., **49**,75-104.

George, J. E., and W. M. Gray, 1976: Tropical cyclone motion and surrounding parameter relationships. J. Appl. Meteor, **15**, 1252-1264.

Gryanik, V. M., 1983: Dynamics of singular geostrophic vortices in a two-level model of the atmosphere (or ocean). Bull. (Ivz.). Acad. Sci. USSR. Atmospheric and oceanic physics, **19**, 171-179.

Haltiner, G. J., and R. T. Williams, 1980: Numerical Prediction and Dynamic Meteorology. 2d ed. Wiley and Sons, 477pp.

Holland, G. J., 1984: Tropical cyclone motion: A comparison of theory and observation. J. Atmos. Sci., **41**, 68-75.

_____, 1983: Tropical cyclone motion: Environmental interaction plus a beta effect. J. Atmos. Sci., **40**, 328-342.

Holland, G. J., L. M. Leslie, and B. C. Diehl, 1992: Comments on "The Detection of Flow Asymmetries in the Tropical Cyclone Environment." Mon. Wea. Rev., **120**, 2394-2400.

Hoskins, B. J., M. E. McIntyre, and A. W. Robertson, 1985: On the use and significance of isentropic potential-vorticity maps. Quart. J. Roy. Meteor. Soc., **111**, 877-946.

Jordan, E. S., 1952: An observational study of the upper wind-circulation around tropical storms. J. Meteor., **9**, 340-346.

Kanamitsu, M., 1989: Description of the NMC global data assimilation and forecast system. Wea. Forecasting, **4**, 335-342.

Kanamitsu, M., J. C. Alpert, K. A. Campana, P. M. Caplan, D. G. Deaven, M. Iredell, B. Katz, H.-L. Pan, J. Sela, and G. H. White, 1991: Recent changes implemented into the global forecast system at NMC. Wea. Forecasting, **6**, 425-435.

Kaplan, J., and L. Franklin, 1991: The relationship between the motion of Tropical Storm Florence (1988) and its environmental flow. Preprint, 19th Conference on Hurricanes and Tropical Meteorology, Amer. Meteor. Soc., 93-97.

Kasahara, A., 1957: The numerical prediction of hurricane movement with the barotropic model. J. Meteor., **14**, 386-402.

_____, and G. W. Platzman, 1963: Interaction of a hurricane with the steering flow and its effect upon the hurricane trajectory. Tellus, **25**, 321-335.

Kasahara, A., 1960: The numerical prediction of hurricane movement with a two-level baroclinic model. J. Meteor., **17**, 357-370.

Kitade, T., 1980: Numerical experiments of tropical cyclones on a plane with variable Coriolis parameter. J. Meteor. Soc. Japan, **58**, 471-488.

Kurihara, Y., M. A., Bender, R. E. Tuleya, and R. J. Ross, 1990: Prediction experiments of Hurricane Gloria (1985) using a multiply nested moveable mesh model. Mon. Wea. Rev., **118**, 2185-2198.

Langford, J. S., and K. A. Emanuel, 1993: An unmanned aircraft for dropwindsonde depolyment and hurricane reconnaissance. Bull. Amer. Meteor. Soc., **74**, 367-375.

Madala, R. V., and S. A. Piacsek, 1975: Numerical simulation of asymmetric hurricanes on a β-plane with vertical shear. Tellus, **27**, 453-468.

Marks, F. D., Jr., R. A. Houze, Jr. and J. F. Gamache, 1992: Dual-aircraft investigation of the inner core of Hurricane Norbert. Part I. Kinematic structure. J. Atmos. Sci., **49**, 919-942.

McIntyre, M. E., and W. A. Norton, 1991: Potential-vorticity inversion on a hemisphere. Submitted to J. Atmos. Sci..

Miller, B. I., and P. L. Moore, 1960: A comparison of hurricane steering levels. Bull. Amer. Meteor. Soc., **41**, 59-63.

Miller, B. I., 1958: The use of mean layer winds as a hurricane steering mechanism. U.S. National Hurricane Research Project, Rep. No. 18, 24 pp.

Molinari, J. 1992: Environmental controls on eye wall cycles and intensity change in Hurricane Allen (1980). ICSU/WMO International Symposium on Tropical Cyclone Disasters.

Montgomery, M. T., and B. F. Farrell, 1993: Tropical cyclone formation. J. Atmos. Sci., **50**, 285-310.

Neumann, C. J., 1979: On the use of deep-layer mean geopotential height fields in statistical prediction of tropical cyclone motion. Preprint, Sixth Conf. on Probability and Statistics in Atmosphere Sciences, Amer. Meteor. Soc., 32-38.

Nielsen, J. W., C. A. Davis and D. Keyser, 1991: Upper-level frontogenesis made easy? Preprint, First Int. Winter Storm Symp., Amer. Meteor. Soc., 82-88.

Peng, M. S., and R. T. Williams, 1990: Dynamics of vortex asymmetries and their influence on vortex motion on a beta-plane. J. Atmos. Sci., **47**, 1987-2003.

Polvani, L. M., Zabusky, N. J. and Flierl, G. R., 1989: Two-layer geostrophic vortex dynamics. Part I. Upper layer V-states and merger. J. Fluid Mech., **205**, 215-242.

Polvani L. M., and Plumb R. A., 1992: Rossby wave breaking, filamentation and secondary vortex formation: the dynamics of a perturbed vortex. J. Atmos. Sci., **49**, 462-476.

Raymond, D. J., and H. Jiang, 1990: A theory for long-lived mesoscale convective systems. J. Atmos. Sci., **47**, 3067-3077.

Reeder, M. J., R. K. Smith, and S. J. Lord, 1991: The detection of flow asymmetries in the tropical environment. Mon. Wea. Rev., **119**, 848-855.

Reilly, D. H., 1992: On the role of upper-tropospheric potential vorticity advection in tropical cyclone formation: Case studies from 1991. Master's thesis. Department of Earth, Atmospheric, and Planetary Sciences. Massachusetts Institute of Technology. 124 pp.

Rossby, C.-G., 1948: On displacement and intensity changes of atmospheric vortices. J. Marine. Res., **7**, 38-54.

_____, 1949: On a mechanism for the release of potential energy in the atmosphere. J. Meteor., **6**, 163-180.

_____, 1939: Relation between variations in the intensity of the zonal circulation of the atomsphere and the displacements of semipermanent centers of action. J. Marine. Res., **2**, 175-187.

Rotunno, R., and K. A. Emanuel, 1987: An air-sea interaction theory for tropical cyclones: Part II. J. Atmos. Sci., **44**, 542-561.

Roux, F., and F. D. Marks, Jr., 1991: Eyewall evolution in Hurricane Hugo deduced from successive airborne Doppler observations. Preprint, 19th Conference on Hurricanes and Tropical Meteorology, Amer. Meteor. Soc., 558-563.

Schubert, W. H., B. T. Alworth, 1987: Evolution of potential vorticity in tropical cyclones. Quart. J. Roy. Meteor. Soc., **113**, 147-162.

Schubert, W. H., and J. J. Hack, 1983: Transformed Eliassen balanced vortex model. J. Atmos. Sci., **40**, 1571-1583.

Schubert, W. H., P. E., Ciesielski, D. E. Stevens, and H. C. Kuo, 1991: Potential vorticity modeling of the ITCZ and the Hadley circulation. J. Atmos. Sci., **48**, 1493-1509.

Shapiro, L. J., and K. V. Ooyama, 1990: Barotropic vortex evolution on a beta plane. J. Atmos. Sci., 47, 170-187.

Shapiro, L. J., 1992: Hurricane vortex motion and evolution in a three-layer model. J. Atmos. Sci., **49**, 140-153.

Smith, R. K., W. Ulrich, and G. Dietachmayer, 1990: A numerical study of tropical cyclone motion using a barotropic model. I: The role of vortex asymmetries. Quart. J. Roy. Meteor. Soc., **116**, 337-362.

Smith, R. K., W. Ulrich, 1993: Vortex motion in relation to the absolute vorticity gradient of the vortex environment. Quart. J. Roy. Meteor. Soc., **119**, 207-215.

_____, 1990: An analytical theory of tropical cyclone motion using a barotropic model. Quart. J. Roy. Meteor. Soc., **47**, 1973-1986.

Sutyrin, G. G., 1988: Motion of an intense vortex on a rotating globe. Ivz. Akad. Nauk SSSR. Mekh. Zhidk. Gaza. 215-223.

_____, and Flierl, G. R., 1991: Intense vortex motion on the beta-plane. Part I. Development of the beta-gyres. Submitted to J. Atmos. Sci..

Talbert, K. M., 1987: The effect of vertical wind shear on tropical cyclone movement. Masters Thesis, Department of Atmospheric Sciences, North Carolina State University. Available from NTIS, Accession No. ADA-197-218.

Thorpe, A. J., and K. A. Emanuel, 1985: Frontogenesis in the presence of small stability to slantwise convection. J. Atmos. Sci., **42**, 1809-1824.

Thorpe, A. J., 1985: Diagnosis of balanced vortex structure using potential vorticity. J. Atmos. Sci., **42**, 397-406.

Trenberth, K. E., and J. G. Olson, 1988: Evaluation of the NMC global analysis: 1979-1987. NCAR Tech. Note/TN-299+STR.

Ulrich, W., and R. K. Smith, 1991: A numerical study of tropical cyclone motion using a barotropic model. II: Motion in spatially-varying large-scale flows. Quart. J. Roy. Meteor. Soc., **117**, 107-124.

Velden, C. S., And L. M. Leslie, 1991: The basic relationship between tropical cyclone intensity and the depth of the environmental steering layer in the Australian region. Wea. and Fcst., **6**, 244-253.

Wang, B., and X, Li, 1992: The beta drift of three dimensional vortices: A numerical study. Mon. Wea. Rev., **120**, 579-593.

Waugh, D. W., and R. A. Plumb:, 1992: Contour advection with surgery: A technique for investigating fine scale structure in tracer transport. Submitted to J. Atmos. Sci..

Willoughby, H. E., 1988: Linear motion of a shallow-water, barotropic vortex. J. Atmos. Sci., **45**, 1906-1928.

_____, 1990: Linear normal modes of a moving, shallow-water barotropic vortex. J. Atmos. Sci., **47**, 2141-2148.

_____, 1992: Linear motion of a shallow-water barotropic vortex as an initial-value problem. J. Atmos. Sci., **49**, 2015-2031.

Wu, C.-C., and K. A. Emanuel, 1993: Interaction of a baroclinic vortex with background shear: Application to hurricane movement. J. Atmos. Sci., **50**, 62-76.

Xu, K., and K. A. Emanuel, 1989: Is the tropical atmosphere conditional unstable? Mon. Wea. Rev., **117**, 1471-1479.

6194-52